Cu Nanoparticles on TiO_2: Growth, Oxidation and Interaction with Amino Acids

Dissertation
zur Erlangung des Doktorgrades
an der Fakultät für Mathematik, Informatik und Naturwissenschaften
Fachbereich Physik
der Universität Hamburg

vorgelegt von

Daniel Silvan Dolling

Hamburg

2026

Gutachter/innen der Dissertation:	Prof. Dr. Andreas Stierle Dr. Heshmat Noei
Zusammensetzung der Prüfungskommission:	Prof. Dr. Andreas Stierle Dr. Heshmat Noei Prof. Dr. Wolfgang J. Parak Prof. Dr. Alf Mews Prof. Dr. Robert H. Meißner
Vorsitzender der Prüfungskommission:	Prof. Dr. Wolfgang J. Parak
Datum der Disputation:	15.09.2026
Vorsitzender des Fach-Promotionsausschusses PHYSIK:	Prof. Dr. Johannes Haller
Leiter des Fachbereichs PHYSIK:	Prof. Dr. Markus Drescher
Dekan der Fakultät MIN:	Prof. Dr.-Ing. Norbert Ritter

Eidesstattliche Versicherung

Hiermit versichere ich an Eides statt, die vorliegende Dissertationsschrift selbst verfasst und keine anderen als die angegebenen Hilfsmittel und Quellen benutzt zu haben.

Sofern im Zuge der Erstellung der vorliegenden Dissertationsschrift generative Künstliche Intelligenz (gKI) basierte elektronische Hilfsmittel verwendet wurden, versichere ich, dass meine eigene Leistung im Vordergrund stand und dass eine vollständige Dokumentation aller verwendeten Hilfsmittel gemäß der Guten wissenschaftlichen Praxis vorliegt. Ich trage die Verantwortung für eventuell durch die gKI generierte fehlerhafte oder verzerrte Inhalte, fehlerhafte Referenzen, Verstöße gegen das Datenschutz- und Urheberrecht oder Plagiate.

24-06-2026 

Datum Unterschrift der Doktorandin / des Doktoranden

Zusammenfassung

Diese Dissertation untersucht das Wachstum und die Oxidation von Cu Nanopartikeln (NPs) auf Rutil TiO_2(110) und Anatase TiO_2(101) Einkristallen, sowie deren Interaktion mit der Aminosäure Cystein. Die Arbeit entstand im Rahmen des Helmholtz Projekts CORAERO (KA1-Co-06), welches die Verbreitung von SARS-CoV-2 Viren durch Luft sowie deren Inaktivierung untersucht hat. Das Modellsystem von Cu NPs auf TiO_2 wurde aufgrund der bekannten Effektivität bei der Deaktivierung von Viren und Bakterien ausgewählt. Im Gegensatz zu reinem Titandioxid, welches aufgrund seiner Bandlücke nur unter UV-Licht photokatalytisch aktiv ist, ist für Cu/TiO_2 Aktivität im sichtbaren Licht bekannt. Auch wenn somit grundlegende Fähigkeiten des Systems bereits bestätigt sind, bleiben weiterhin viele Fragen offen, insbesondere bezüglich der Optimierung der Nanopartikel hinsichtlich Größe, Bedeckung und Oxidationszustand sowie hinsichtlich der Interaktion mit adsorbierten organischen Molekülen. Die Nutzung des Modellsystems aus Cu Nanopartikeln auf TiO_2 Einkristallen ermöglicht einen hohen Grad an Kontrolle über die Oberfäche und die Nanopartikel und erlaubt die Nutzung präziser Messtechniken der Oberflächenphysik. Die Nanopartikel wurden mittels Molekularstrahlepitaxie (MBE) auf die Einkristelle gewachsen. Die Epitaxie der Partikel wurde mit Röntgenbeugung unter streifendem Einfall (GIXRD), Hochenergieröntgenbeugung (HEXRD), Kleinwinkelröntgenstreuung unter streifendem Einfall (GISAXS) und Rasterelektronenmikroskopie (SEM) untersucht. Die Oxidation der Cu Nanopartikel wurde mit Röntgen-Photoelektronenspektroskopie (XPS) und UV-Vis Spektroskopie untersucht. Schließlich wurde die Adsorption und Interaktion der Aminosäure Cystein mit dem System mittels XPS und Infrarotspektroskopie (IRRAS) untersucht. Auf Rutil TiO_2(110) Einkristallen wurde die Cu[110]||TiO_2[001] Epitaxie mit einer [111]-Orientierung des Kupfers bestätigt. Im Gegensatz zum bisherigen Wissensstand wurde eine Abhängigkeit der Epitaxie von der Wachstumstemperatur gefunden: Mit steigender Wachstumstemperatur (von 100 °C auf 400 °C) wurde ein wachsender Anteil einer leicht gedrehten Cu[110]||TiO_2[112] Epitaxie beobachtet. Die Kinetik der Oxidation der NPs bei Raumtemperatur und atmosphärischem Sauerstoffdruck ließ sich, im Einklang mit der Oxidationstheorie von Cabrera und Mott, für kurze Zeiten mit einem linearen Wachstum der Oxidschicht und für längere Zeiten mit einem invers logarithmischen Wachstum der Oxidschicht beschreiben. Auch nach mehreren Wochen an Luft konnte für manche NPs noch ein metallischer Kern nachgewiesen werden. Epitaktisches Oxid wurde hingegen nur für sehr große Nanopartikel und hohe Bedeckungen gefunden. Für das Wachstum von Cu NPs auf Anatas TiO_2(101) Einkristallen wurde eine Cu[001]||TiO_2[010] Epitaxy mit einer Cu[470]-Orienterung gefunden. Wie auf Rutilsubstraten wurde epitaktisches Oxid nur für große Nanopartikel gefunden (etwa $\geq$20 nm Durchmesser). Die Stabilität des metallischen Kupfers bei hohen Bedeckungen von NPs wurde durch eine plasmonische Cu Resonanz bestätigt, welche nach mehreren Monaten der Lagerung an Luft gefunden wurde.

Für die Adsorption von Cystein auf dem Cu/TiO_2 system wurde gefunden, dass diese hauptsächlich von der Cu Bedeckung und dem Oxidationszustand des Kupfers abhängt. Auf Cu NPs auf Anatas TiO_2(101) ist die Interaktion der Oberfläche mit dem Cystein durch Cu-S Bindungen geprägt. Innerhalb

der Auflösung der Messungen sind auch S-Ti Bindungen nicht auszuschließen. Ein Teil der Aminosäure zerbricht bei der Adsorpption, was durch Nitrilsignale in IRRAS-Spektren gefunden wurde. Für Cu NPs auf Rutil TiO_2(110) wurden andere Adsorbptionsmodi gefunden. So ist die Aminogruppe des Cysteins meist im molekularen Zustand (d.h. ohne zusätzliches H-Atom), wodurch eine Interaktion dieser Gruppe mit der Oberfläche angenommen wird. Des Weiteren wurden neben Signalen von Cu-S Bindungen auch ähnlich starke Signale von molekularen Thiol-Gruppen (S-H) gemessen. Im Gegensatz zu der Adsorption von Cystein auf Cu/Anatase, wurden keine Anhaltspunkte für Bindungen zwischen Titan und Schwefel (S-Ti) gefunden. Wie auch auf Anatas-Substraten, war ein Teil der Thiolgruppen direkt nach der Adsorption oxidiert und Nitril-Signale wurden gefunden. Zusätzlich wurden aber auch Signale von molekularen Carboxyl-Gruppen entdeckt, welche auf weniger stark an die Oberfläche gebundene Adsorptionsmodi schließen lassen.

Der photokatalytische Abbau von Cystein wurde für Cu Nanopartikel auf Anatas- und Rutil-Substraten untersucht, indem die Oxidation der Thiolgruppe für verschiedene Expositionszeiten unter Luft- und Lichteinfluss geprüft wurde. Es wurde gefunden, dass die Menge an oxidiertem Schwefel sowohl von der Bedeckung mit Cu Partikeln sowie dem Oxidationszustand dieser abhängt, da die Bindung von starken Cu-S Bindungen im Wettstreit mit der Oxidation steht. Die Oxidation des Schwefels wiederum schritt linear mit der Zeit an Luft voran, unabhängig von den Lichtbedingugen (Dunkelheit, weißes Licht, UV-Licht). Eine Ausnahme bildet hier eine Cu/TiO_2(110) Probe mit hoher Cu Bedeckung und einem hohen Antail an CuO, für welche die Oxidation des Cysteins klar vom sichtbaren Licht abhängig war, was wiederum eine starke photokatalytische Aktivität nahelegt.

Die durchgeführten Messungen und gewonnenen Erkenntnisse tragen zum besseren Verständnis des Cu/TiO_2 Systems bei, sowohl im Hinblick auf die Struktur der Nanopartikel als auch auf die photokatalytische Aktivität.

Abstract

This doctoral thesis investigates the growth and oxidation of Cu nanoparticles (NPs) on rutile TiO_2(110) and anatase TiO_2(101) single crystals, as well as their interaction with the amino acid cysteine. This work was initiated within the CORAERO project (Grant KA1-Co-06), which investigated airborne transmission routes of the SARS-CoV-2 to explore photocatalytic strategies for viral inactivation. Cu NPs on TiO_2 have been chosen because their effectiveness in degrading organic substances, including viruses and bacteria, has already been proven. In contrast to pristine TiO_2, which has a bandgap in the UV-light region and thus is not active under visible light, the research for Cu/TiO_2 indicates visible light activity. Nevertheless, several open questions remain regarding the optimization of the NPs size, coverage, and oxidation state, as well as the molecular dynamics of the interaction with organic molecules. The model system of Cu NPs on TiO_2 single crystals enables precise control over the surfaces and interfaces and allows for the use of surface-science techniques for investigation. The nanoparticles were grown by molecular beam epitaxy (MBE) and the epitaxy was investigated with grazing-incidence X-ray diffraction (GIXRD), high-energy X-ray diffraction (HEXRD), grazing-incidence small angle scattering (GISAXS) and scanning electron microscopy (SEM). The oxidation was additionally investigated with X-ray photoelectron spectroscopy (XPS) and ultra-violet-visible spectroscopy (UV-Vis). Finally, the interaction with cysteine (an amino acid) was studied using infrared reflection absorption spectroscopy (IRRAS) and XPS. For the growth of Cu on rutile TiO_2(110), the main epitaxy was confirmed to be Cu[110] || TiO_2[001] with a [111]-orientation of Cu. In contrast to previous reports, a dependency of epitaxy on growth temperature could be established. An increase of the growth temperature from 100 °C to 400 °C led to an increase in the signal of a Cu[110]||TiO_2[112] epitaxy (tilted 12° in-plane with respect to the main epitaxy Cu[110] || TiO_2[001]). The oxidation kinetics at room temperature and ambient O_2 pressure followed an inverse logarithmic oxide growth rate after an initial linear phase, in line with the oxidation theory of Cabrera and Mott. Though it was found that metallic Cu NPs were still present after one week of oxidation, epitaxial oxide was found only for very large NPs and high coverage.

For the growth of Cu NPs on the anatase TiO_2(101) surface, the main epitaxy was found to be Cu[001]||TiO_2[010] with a Cu[470]-orientation, independent of the growth temperature. Similar to the oxidation of Cu on rutile, epitaxial Cu_2O was found only for relatively large NPs (diameters of about 20 nm). The long-term stability of Cu/oxide core-shell particles with diameters of about 20 nm was confirmed by a strong plasmonic resonance (originating from metallic Cu) found after several months in air.

The adsorption of cysteine on the Cu/TiO_2 system depends on the Cu coverage as well as the oxidation state. For Cu on anatase TiO_2(101), the dominant adsorption mechanism is Cu-S bonding and interaction of copper and the deprotonated carboxyl group. Within the limits of experimental resolution, adsorption of sulfur on titanium can not be ruled out. In the presence of Cu-Oxide, parts of the thiol group of cysteine are oxidized directly upon adsorption in UHV. In addition, the presence of nitrile signals suggests that parts of the thiol groups in cysteine are decomposed upon adsorption. On Cu NPs on rutile TiO_2(110),

the dominant adsorption mechanisms are different. The amino group appeared mostly unprotonated and was assumed to interact with the surface, whereas the thiol group was found both in molecular state (S-H) as well as adsorbed on Cu (S-Cu). In contrast to the anatase substrates, no sign of sulfur adsorption on Ti was found. As for the anatase substrates, parts of the thiol groups were oxidized upon adsorption and some samples showed nitrile signals, corresponding to the decomposition of cysteine. In addition, a new adsorption mode with protonated carboxyl group was observed for several samples, indicating limited surface interaction of the carboxyl group.

The light-induced (photo-)oxidation of cysteine was studied for Cu NPs on both anatase and rutile, following oxidation of the thiol group of cysteine. The amount of oxidized sulfur was found to depend both on the Cu coverage and the oxidation state of the copper, revealing competition between the formation of strong Cu-S bonds and sulfur oxidation. Moreover, the oxidation of the thiol group progressed linearly with the time of exposure to air, independent of the light conditions, for all but one sample. For this high-Cu-coverage sample on rutile, featuring mostly of CuO in XPS, the oxidation of cysteine was found to only appear under white light, indicating photoactivity.

Overall, these findings enhance our understanding of the Cu/TiO_2 system regarding NP growth and oxidation as well as cysteine adsorption and degradation.

List of Publications - Main Articles

This thesis is based on the following three articles:

Article I: In-Situ Growth and Oxidation of Cu Nanoparticles on Rutile TiO_2(110)

Daniel Silvan Dolling, Miguel Blanco Garcia, Mona Kohantorabi, Yufeng Zhai, Benedikt Sochor, Mohammad Ebrahim Haji Naghi Tehrani, Jan-Christian Schober, Ming-Chao Kao, Jagrati Dwivedi, Arno Jeromin, Olof Gutowski, Dmitri V. Novikov, Thomas F. Keller, Stephan V. Roth, Andreas Stierle and Heshmat Noei

Journal of Physical Chemistry C 2026, 130, 20, 7136–7147, doi: 10.1021/acs.jpcc.6c00835

I performed sample preparation, design and realization of experiments at PETRAIII P23 (GIXRD), P03 (GISAXS) and P07 (HEXRD) as well as XPS experiments, all data analysis and manuscript writing.

Article II: Structure and Reactivity of Cu and Cu Oxide Nanoparticles on Anatase TiO_2(101) for Cysteine Degradation

Daniel Silvan Dolling, Miguel Blanco Garcia, Ming-Chao Kao, Mona Kohantorabi, Lydia J. Bachmann, Luis-Felipe Mochalski, Luisa K. Wartner, Eleonora Spurio, Arti Dangwal, Joris W. Fuchs, Mais Jamil A. Ahmad, Arno Jeromin, Ying Kong, Dmitri Novikov, Thomas F. Keller, Volkmar Koller, Olof Gutowski, Paola Luches, Vedran Vonk, Andreas Stierle, Heshmat Noei

Manuscript in Preparation

I performed sample preparation, design and realization of experiments at PETRAIII P23 (GIXRD), P22 (HAXPES) and P07 (HEXRD) as well as all XPS and IRRAS experiments, all data analysis and manuscript writing.

Article III: Cysteine Degradation Facilitated by Cu Nanoparticles Supported on TiO_2(110)

Daniel Silvan Dolling, Miguel Blanco Garcia, Arno Jeromin, Thomas F. Keller, Andreas Stierle, Heshmat Noei

Manuscript in Preparation

I performed all sample preparation, design and realization of XPS and IRRAS experiments, all data analysis and manuscript writing.

List of Publications - Co-Authored Articles

Furthermore, I have contributed to the following publications during the doctoral studies:

Article IV: Light-Induced Transformation of Virus-Like Particles on TiO_2

Mona Kohantorabi, Aldo Ugolotti, Benedikt Sochor, Johannes Roessler, Michael Wagstaffe, Alexander Meinhardt, E. Erik Beck, Daniel Silvan Dolling, Miguel Blanco Garcia, Marcus Creutzburg, Thomas F. Keller, Matthias Schwartzkopf, Sarathlal Koyiloth Vayalil, Roland Thuenauer, Gabriela Guédez, Christian Löw, Gregor Ebert, Ulrike Protzer, Wolfgang Hammerschmidt, Reinhard Zeidler, Stephan V. Roth, Cristiana Di Valentin, Andreas Stierle, Heshmat Noei*
ACS Applied Material Interfaces 2024, 16, 28, 37275–37287, doi:10.1021/acsami.4c07151
I participated in the acquisition of GISAXS data at PETRA III P03 beamline.

Article V: Unraveling the Role of the Multifunctional Groups in the Adsorption of L-Cysteine on Rutile TiO_2(110)

Miguel Blanco Garcia, Daniele Perilli, Chiara Daldossi, Aldo Ugolotti, Martina Giordano, Daniel Silvan Dolling, Michael Wagstaffe, Mona Kohantorabi, Andreas Stierle, Cristiana Di Valentin, Heshmat Noei
Journal of the American Chemical Society, 2025, 147, 44, 40158–40170, doi: 10.1021/jacs.5c07119
I participated in sample preparation and IRRAS measurements.

Article VI: Coherent X-ray Diffraction Imaging of a Twinned PtRh Catalyst Nanoparticle under Operando Conditions

Lydia J. Bachmann, Dmitry Lapkin, Jan-Christian Schober, Daniel Silvan Dolling, Young Yong Kim, Dameli Assalauova, Nastasia Mukharamova, Jagrati Dwivedi, Tobias U. Schulli, Thomas F. Keller, Ivan A. Vartanyants, Andreas Stierle
ACS Nano 2025, 19, 26, 23552–23563, doi:10.1021/acsnano.4c15457
I participated in the acquisition of Bragg CDI data at ESRF beamline ID01.

Article VII: Equilibrium Shape and Surface Termination of Supported Magnetite Nanoparticles

Mohammad Ebrahim Haji Naghi Tehrani, Daniel Silvan Dolling, Jan-Christian Schober, Esko Erick Beck, Mona Kohantorabi, Arno Jeromin, Ludwig J. V. Ahrens-Iwers, Thomas F. Keller, Vedran Vonk, Gregor B. Vonbun-Feldbauer, Heshmat Noei, Andreas Stierle
Communications Chemistry 9, 158, 2026, doi: 10.1038/s42004-026-02008-4
I participated in the acquisition of IRRAS data.

Article VIII: Adsorption and Sulfur-Selective Photooxidation of Cysteine on Anatase TiO_2(101)

Miguel Blanco Garcia, Daniele Perilli, Chiara Daldossi, Aldo Ugolotti, Daniel Silvan Dolling, Andreas Stierle, Annabella Selloni, Cristiana Di Valentin, Heshmat Noei
Journal of the American Chemical Society, 2026, doi: 10.1021/jacs.6c07370
I participated in the acquisition of IRRAS data.

Danksagung

An dieser Stelle möchte ich allen Menschen danken, die mich während meiner Promotionszeit unterstützt und begleitet haben. Zunächst gilt mein herzlicher Dank Dr. Heshmat Noei, die mich über die letzten vier Jahre hinweg mit Geduld und Fachkenntnis betreut hat. Ihre stets offene Tür und Bereitschaft zu konstruktiven Diskussionen, das sorgfältige Korrigieren unzähliger Manuskriptversionen sowie ihre optimistische Haltung waren für mich nicht nur fachlich bereichernd, sondern auch menschlich sehr wertvoll. Ebenso möchte ich Prof. Dr. Andreas Stierle herzlich danken. Seine stets hilfreichen und zielgerichteten Anmerkungen sowie seine klare wissenschaftliche Perspektive haben wesentlich zum Gelingen dieser Arbeit beigetragen. Mein Dank gilt außerdem allen aktuellen und ehemaligen Mitgliedern des NanoLab für die angenehme Arbeitsatmosphäre sowie die große Hilfsbereitschaft während der vergangenen Jahre. Mohammad Ebrahim Haji Naghi Tehrani danke ich für die gemeinsame Zeit im Labor, insbesondere für das Instandhalten von MBEI und des alten IR sowie für die vielen hilfreichen Diskussionen über XRD und IRRAS. Besonders bedanken möchte ich mich auch bei Artem Zaidman, mit dem ich über die gesamte Promotionszeit hinweg das Büro geteilt habe. Die zahlreichen fachlichen Diskussionen, aber auch die vielen Gespräche abseits der Wissenschaft haben den Arbeitsalltag stets bereichert und meinen Horizont immer wieder erweitert. Miguel Blanco Garcia wiederum danke ich für die enge Zusammenarbeit im COREARO-Projekt sowie für die wertvollen wissenschaftlichen Diskussionen, die wesentlich zum Fortschritt dieser Arbeit beigetragen haben. Luisa Wartner möchte ich dafür danken, mir das Schwimmen nahegebracht zu haben, das insbesondere in der bürolastigen Schreibphase einen willkommenen Ausgleich zur Arbeit darstellte. Ein besonderer Dank gilt außerdem Dennis Renner, der das UHV-Labor stets einwandfrei funktionsfähig gehalten und dabei immer zu einer angenehmen Arbeitsatmosphäre beigetragen hat. Schließlich möchte ich mich bei meinen Eltern, Elke und Klaus, für ihre Unterstützung während der gesamten Promotionszeit bedanken. Ohne ihren Rückhalt wäre vieles nicht möglich gewesen.

Contents

Eidesstattliche Erklärung **v**

Zusammenfassung **vii**

Abstract **ix**

List of Publications **xi**

Danksagung **xiii**

Table of Contents **1**

1 Introduction **3**

2 Current Knowledge **7**
2.1 Cu Growth on TiO_2 . . . 7
2.2 Cu Oxidation . . . 8
2.3 Cu and TiO_2 for Organic Degradation . . . 8
2.4 Cysteine on TiO_2 and Cu . . . 9

3 Basic Principles & Theoretical Background **11**
3.1 Crystal Lattices . . . 11
3.2 X-ray Diffraction from the Lattice . . . 12
3.3 Bragg's Law . . . 13
3.4 Grazing-Incidence X-Ray Diffraction . . . 13
3.5 High-Energy X-Ray Diffraction (HEXRD) . . . 14
3.6 Rutile and Anatase Structure . . . 14
3.7 X-ray Photoelectron Spectroscopy (XPS) . . . 16
3.8 Infrared Reflection Absorption Spectroscopy (IRRAS) . . . 20
3.9 Scanning Electron Microscopy (SEM) . . . 23
3.10 Scanning Auger Microscopy (SAM) . . . 24
3.11 Grazing-Incidence Small Angle X-ray Diffraction (GISAXS) . . . 24
3.12 Ultra-High Vacuum (UHV) . . . 26
3.13 Molecular Beam Epitaxy (MBE) . . . 27
3.14 Low Energy Electron Diffraction (LEED) . . . 28
3.15 Photocatalysis . . . 28

4 Experimental Setups **31**
4.1 DESY NanoLab: UHV lab 31
4.1.1 IRRAS 34
4.1.2 XPS 36
4.1.3 Growth Chamber 37
4.2 SEM 38
4.3 SAM 39
4.4 PETRA III P23 40
4.5 Petra III P07 41
4.6 Petra III P22 42
4.7 Sample Preparation 43
4.8 Photocatalysis & Light Exposure 45

5 Article I: In-Situ Growth and Oxidation of Cu Nanoparticles on Rutile TiO_2(110) **47**
5.1 High-Coverage Oxidation 60

6 Article II: Structure and Reactivity of Cu and Cu Oxide Nanoparticles on Anatase TiO_2(101) for Cysteine Degradation **63**

7 Article III: Cysteine Degradation Facilitated by Cu Nanoparticles Supported on TiO_2(110) **95**

8 Conclusions **117**

9 SI Article I **127**

10 SI Article II **179**

11 SI Article III **231**

Chapter 1

Introduction

In the aftermath of the recent coronavirus pandemic, it became clear that we must be prepared for possible future pandemics. Especially in public spaces, efficient disinfection of surfaces is crucial to avoid mass infection. The normal procedure, cleaning with a solvent, is both cost- and work-intensive (solvent is used and a worker has to apply it). Concerning possible future pandemics and the overall reduction of infection risk for diseases transmitted via surfaces, these work-intensive procedures could be circumvented by using photo-catalytically self-cleaning surfaces. The general working principle can be seen in Figure 1.1: the virus adsorbs on the surface. In combination with (visible) light, the surface catalyzes reactions that damage the virus, ultimately leading to its inactivation.

Photocatalysis in general describes the use of a semiconductor material which adsorbs light and thus creates electron-hole-pairs. These pairs can interact with the surrounding, enabling and catalyzing

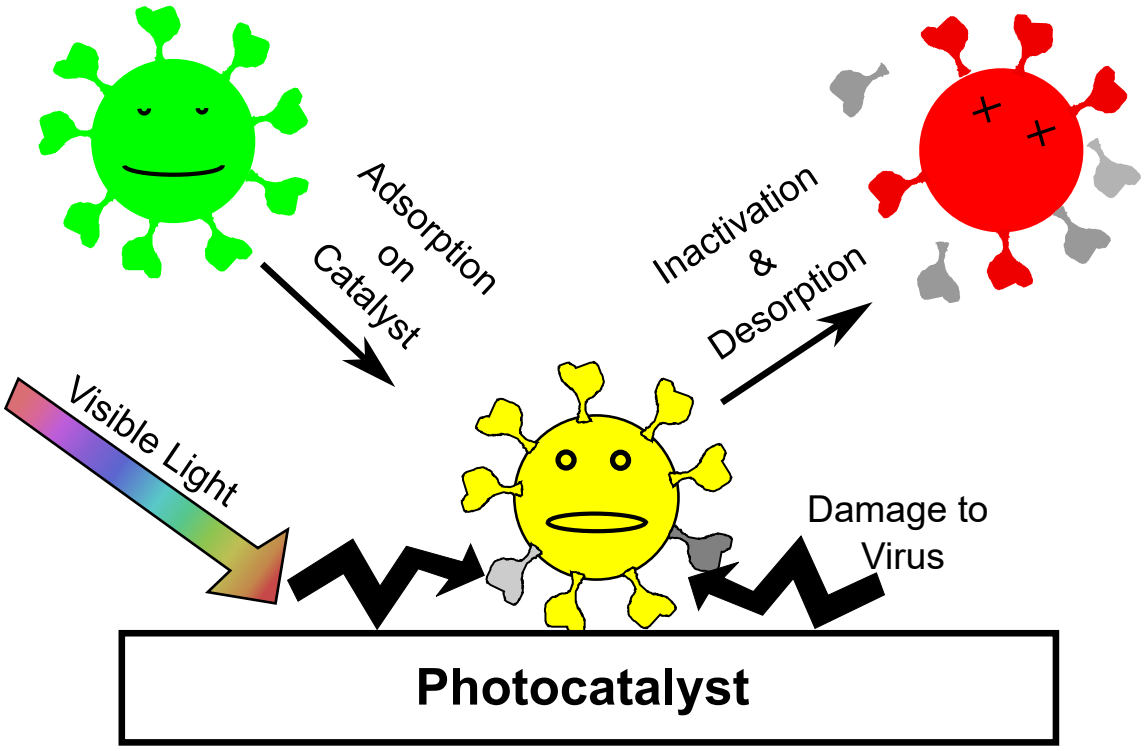


Figure 1.1: Working principle of photocatalytic virus inactivation: the virus adsorbs on the surface. By adsorption of (visible) light, the photocatalyst becomes active and deconstructs / damages the virus. The damaged virus detaches, but is not infectious anymore.

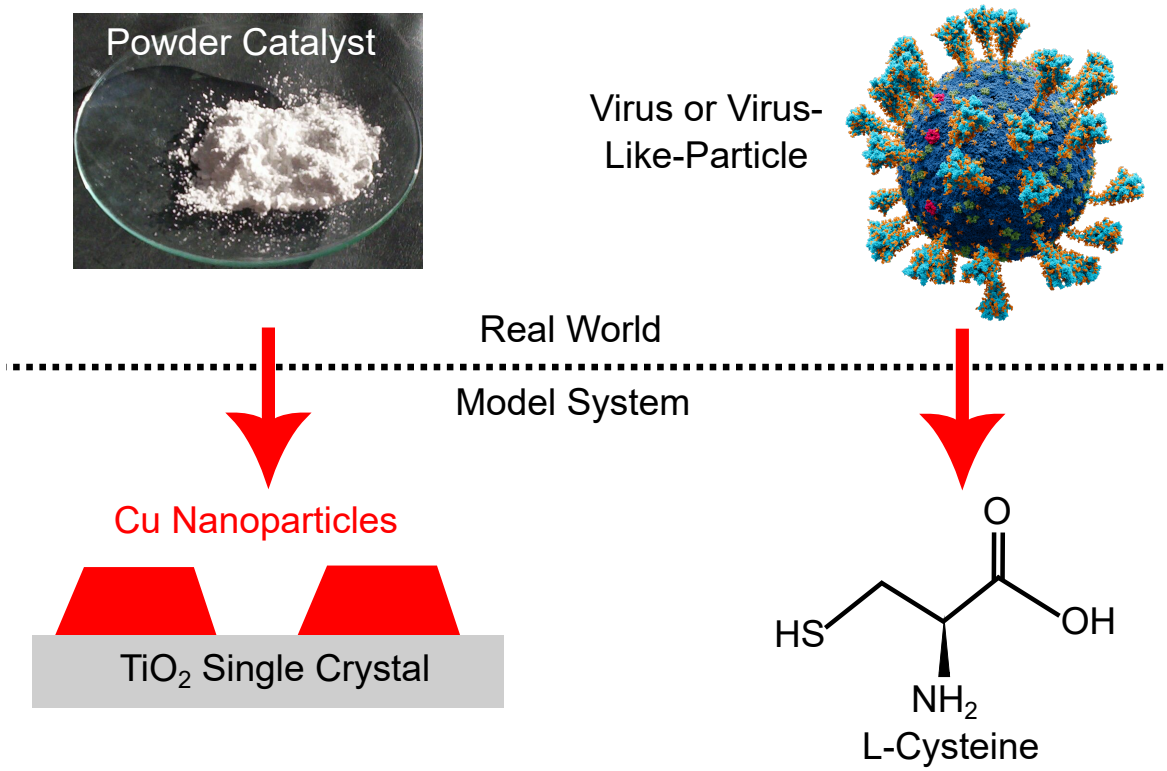


Figure 1.2: From the real world to a model system: the usage of a model system of Cu(-oxide) NPs on single crystalline TiO_2 provides a high degree of control over the system, whereas the usage of L-cysteine instead of real viruses ensures that the data can be meaningfully analyzed. The TiO_2 powder image was adapted from Wikimedia Commons, CC0. The virus graphic was adapted from "Scientifically accurate atomic model of the external structure of SARS-CoV-2" by Alexey Solodovnikov and Valeria Arkhipova, Wikimedia Commons, CC BY-SA 4.0. Both accessed 08.06.2026.

reactions. For a material to be photocatalytic, it needs to have a bandgap in the visible, infrared or UV light region - anything with very small or very large bandgap is not considered (as it would either need extreme-UV irradiation or the recombination of electron-hole pairs would be to fast). Of all photocatalysts, TiO_2 is the best known, having been extensively researched since the discovery of its photocatalytic activity in 1972 [2]. It is an abundant [52, 8] and cheap material and offers good chemical stability [3], hence being an excellent starting point for self-cleaning surfaces. The drawback of TiO_2 is its bandgap of about 3 eV, resulting in the need for UV light (about 380 nm) for photo-activity. In the context of self-cleaning surfaces, this is a serious disadvantage: the typical light in everyday environments is in the visible range (400 nm to 800 nm). As a result, a TiO_2 photocatalyst needs a UV lamp to function. As this is very impractical for surface coatings in communal spaces, a different solution is needed. This is where the Cu(-oxide) enters the playing field: recently, it was shown that a mixture of CuO and Cu_2O on TiO_2 inactivates various strains of the coronavirus both in light and in dark conditions [33], highlighting the effectiveness of this system as well as its visible-light activity. Moreover, combinations of Cu-oxide and TiO_2 have been used effectively in various studies for the degradation of organic substances [15, 27, 30]. The mechanism for visible-light-activity of the Cu(-oxide)/TiO_2 system is found in the surface interaction between Cu and TiO_2 [31, 37, 30] and it is dependent on the oxide composition.

The effectivity of the Cu(-oxide) NPs on TiO_2 has thus been proven. Nevertheless, major questions remain, as most studies focus on powder systems interacting with bacteria and viruses. Even though such an approach yields good results on the overall activity, it is not sufficient for an atomic level understanding

of the interactions between catalyst and virus. Moreover, a systematic study of the Cu NP features (size, oxidation state,...) and their impact on the catalytic properties is missing. This thesis aims to close those knowledge gaps. To this cause, a model system is investigated instead of the real catalyst and virus, see Figure 1.2: Instead of a powder catalyst, Cu NPs are grown onto TiO_2 single crystals and instead of viruses, L-Cysteine is used. The use of single crystalline TiO_2 with Cu NPs enables the use of the highly precise surface science techniques, like grazing-incidence X-ray diffraction and X-ray photoelectron spectroscopy, as well as a high degree of control over the NPs. Cysteine is used instead of real viruses, as real viruses and bacteria are very large (about 100 nm diameter for SARS-CoV-2) and contain a high number of different molecules, making it difficult to draw direct conclusions about specific interactions with the surface. In contrast, cysteine features three different functional groups (amino-, carboxyl- and thiol-group). This means different interactions can be probed while resulting spectra and data will be 'clean' enough to relate signal to specific interactions. Additionally, cysteine is known to be present in large numbers in the spike proteins of SARS-CoV-2 [54].

This thesis is structured as follows: Chapter 2 reviews the state-of-the-art knowledge regarding Cu growth on TiO_2, the oxidation of Cu (NPs), the antiviral properties of Cu and TiO_2, and the specific case of cysteine adsorption on Cu and TiO_2. Open questions regarding the different topics are highlighted. Chapter 3 provides background information on the measurement techniques and basic principles that were used, whereas Chapter 4 offers an overview of the actual setups. Chapter 5 explores the growth and oxidation of Cu NPs on rutile $TiO_2(110)$, based on an article that has been published in the Journal of Physical Chemistry C [10]. Chapter 6 investigates the growth and oxidation of Cu NPs on anatase $TiO_2(101)$ as well as the adsorption and degradation of cysteine on the system. It is based on an article in preparation. In Chapter 7, the adsorption and degradation of cysteine on Cu NPs supported on rutile $TiO_2(110)$ are investigated, based on an article in preparation. Finally, in Chapter 8 the work is summarized and conclusions are drawn, thereby relating the open questions from Chapter 2 to the results.

Chapter 2

Current Knowledge

2.1 Cu Growth on TiO_2

The growth of Cu nanoparticles on single crystalline rutile $TiO_2(110)$ by physical vapor deposition has been studied by three different research groups [51, 9, 56]. Diebold et al. [51] used X-ray photoelectron spectroscopy and low energy ion scattering to find that Cu grows in island (Volmer-Weber) mode and is commensurate along the $TiO_2[110]$ axis. Moreover, they found that the effect of defects in the TiO_2 crystal on the growth of Cu is negligible. Chen et al. [9] employed scanning tunneling microscopy (STM) to study the growth mode as well as the effects of substrate temperature on the resulting NPs. They confirmed that copper grows in island (Volmer-Weber) growth mode, nucleating especially at step edges. Higher growth temperatures led to larger particles, and it did not matter if the temperature was used during growth or during annealing afterwards. Wilson et al. [56] investigated the epitaxy by using X-ray diffraction methods. They found that the particles are (111)-oriented and form hemispherical shapes.

No direct study is available for the growth of Cu NPs on anatase $TiO_2(101)$. The closest approximation of this is either found in the growth of Cu on other high-index substrates (approximating the stepped anatase $TiO_2(101)$ surface) or in the growth of other metals on $TiO_2(101)$. The former was studied by Gleißner et al., growing Cu NPs on vicinal ZnO surfaces [12]. They found Volmer-Weber growth mode and an alignment of the Cu[111] axis with the ZnO[0001] axis on the ZnO$(10\bar{1}4)$ surface, creating a 'tilted' epitaxy. Gong et al. studied the growth of Au and Pt NPs on anatase $TiO_2(101)$ via vapor deposition [14], finding island growth of the NPs. Additionally, they discovered that Pt mostly nucleates at terraces, whereas Au grows at step edges. The Volmer-Weber growth mode of Pt on anatase was also confirmed by Zhou et al. [58]. In their work they also concluded that the Pt atoms have a high mobility along the Anatase[010] axis as compared to the $[10\bar{1}]$ axis.

In total, the open questions regarding the growth of Cu NPs on rutile and anatase TiO_2 are:

- Are all Cu NPs (111)-oriented on rutile $TiO_2(110)$?
- What is the orientation of the NPs on anatase $TiO_2(101)$?
- Does growth temperature affect the resulting epitaxy?

The questions regarding the growth of Cu on rutile $TiO_2(110)$ will be addressed in Chapter 5, while the questions regarding the growth of Cu NPs on anatase $TiO_2(101)$ will be addressed in Chapter 6.

2.2 Cu Oxidation

The oxidation of metal has been studied for a long time and the modern theories of oxidation date back about 90 years when Wagner published a theoretical work on the oxidation of metals in O_2 atmosphere in 1936 [53]. He proposed that for the oxidation Cu→Cu_2O the rate is governed by the diffusion of Cu^+ atoms to the surface of the oxide and described a parabolic growth law for the oxide thickness with time. About 20 years later, Cabrera and Mott presented a differentiation between a thin oxide film ($\leq$ 10 Å) and a relatively thick oxide film ($\geq$10 Å). For the latter, they agree with the parabolic growth law of the oxide thickness and the assumption that either metal or oxygen diffuses through the other. For the case of a thin oxide film, they find that the oxidation is governed by an inverse logarithmic law. Moving from the oxidation of bulk Cu to the case of Cu NPs, the situation becomes more difficult. The oxidation of the NPs does not only depend on the oxygen pressure and the temperature, but can also be influenced by the nanoparticle size and shape as well as the substrate. Additionally, the oxide can either be epitaxial or polycrystalline. It can have the same orientation as the metal or exhibit a different one. For the oxidation of Cu NPs on ZnO at ambient conditions Gleißner et al. [13] reported the emergence of epitaxial Cu_2O after a few days. When heating the NPs under argon atmosphere to 500 K, the particles sintered and in the case of a vicinal ZnO substrate different orientations of Cu were observed. More differences for the NPs on the different substrates were found when reducing the NPs in H_2 gas: on basal Zn-ZnO substrates, the NPs were reversibly reduced and maintained their epitaxy. On vicinal ZnO they formed Cu powder. Pedersen et al. [38] investigated the oxidation of small Cu NPs (3 nm diameter) on glass substrates under dry air and at ambient conditions. They reported that at temperatures below 220 °C a Cu_2O shell formed, which prevented further oxidation. When heating to higher temperatures, CuO was found. Moreover, it was reported that the initial Cu NPs as well as the Cu_2O NPs were well-ordered, but the CuO NPs were powder-like (not ordered). Similarly, slow or self-limited oxide growth on Cu NPs was also reported in other publications [35, 29, 40, 41]. When heated to higher temperatures under oxygen, the creation of Kirkendall voids is reported for Cu NPs [34, 41]: By diffusion of the Cu towards the outer oxide layer, the NPs become hollow shells of Cu_2O. This high degree of different results for the oxidation of Cu NPs shows that it is inherently dependent on the specific conditions.

The open questions regarding the oxidation of Cu NPs on TiO_2 thus are:

- How fast do the NPs oxidize?
- Which oxides are formed?
- Are the oxides epitaxial?

These questions are addressed in Chapters 5 and 6.

2.3 Cu and TiO_2 for Organic Degradation

Various studies have investigated TiO_2 for the degradation of organic substances [1, 11, 16, 21, 24, 25], finding the system to be effective under UV-light. Though catalytic activity is reported both for anatase and rutile, anatase TiO_2 is often considered to be more active [44, 36]. In recent times, especially the antiviral properties of TiO_2 have attracted interest. It was shown that SARS-CoV-2 viruses and virus-like-particles are degraded under UV light on the surface of anatase TiO_2(101) [24, 25]. Structural degradation of the virus was observed, attributed to reactive oxygen species attacking the virus. In general, the creation of reactive oxygen species is considered the mechanism causing the antiviral activity of TiO_2 [4, 26, 50, 57]. Reactive oxygen species are molecules produced by the oxidation and reduction

of water or oxygen molecules present at the TiO_2 surface and include molecules like hydrogen peroxide (H_2O_2) and the superoxide anion (O_2^-).

Cu NPs have been investigated for various applications including waste degradation, water cleaning and for antibacterial and antiviral surfaces. For pure CuO and Cu_2O powder on glass substrates, Sunada et al. [47] showed that only Cu_2O achieves a significant degradation of pathogens (specifically bacteriophage Qβ and E.coli). Notably, these experiments were done under dark conditions. In contrast, several reports exist for CuO/TiO_2 systems, describing their catalytic efficiency under visible light for the degradation of organic substances [19, 28, 32, 30]. Moreover, Cu_2O supported on TiO_2 has also been shown to be effective for the degradation of organic substances under visible light [15]. Several studies focus on Cu_xO, a mixture of CuO and Cu_2O, deposited on powder TiO_2 [39, 33]. This system was found not only to effectively degrade SARS-CoV-2 under visible light, but with reduced effectivity also under dark conditions [33]. That behavior was attributed to an interplay of both oxides, effectively acting as storage for (photo-) electrons produced under light conditions. Additionally, they showed that both the spike proteins of the virus (which are located on the outer shell) as well as the RNA were attacked, resulting ultimately in the complete fragmentation of the virus.

In contrast to pure TiO_2, the mechanism which deactivates viruses and bacteria on Cu/TiO_2 systems is debated. Three main routes are possible: (1) Reactive oxygen species, generated at the surface, attack viruses or bacteria [18]. These are molecules like hydrogen peroxide (H_2O_2) and the superoxide anion (O^{2-}), generated from photo-excited electrons and holes interacting with surrounding water and air. (2) Direct interactions between adsorbed molecules and Cu or TiO_2 lead to organic degradation [47] by oxidation or reduction. (3) Cu ions are released, which are known to be harmful to organic molecules [49]. For the Cu/TiO_2 system, recent studies indicate that direct interaction with Cu constitutes the dominant pathway for antiviral activity: Investigations of CuO/TiO_2 powder for propanol degradation revealed the possibility of CuO to be reduced in the absence of O_2, degrading the propanol [19]. For CuO powder, the degrading properties for organic substances were found to remain untouched by the absence of oxygen [47]. The release of Cu ions is only possible in aqueous media. For CuO powder, it was shown that it contributes to the catalytic activity [47]. For this thesis, it is not of interest as only solid-state samples are investigated.

In total, the research situation regarding $Cu(Oxide)/TiO_2$ clearly shows its high effectiveness for the degradation of viruses, bacteria or organic waste. Nevertheless, the working mechanism and the optimal configuration are not yet known and different studies come to opposite conclusions, e.g. regarding the need for CuO to achieve activity. Hence, the open questions are:

- How do the interactions between the NPs and the organic molecules work on a microscopic level?
- Can specific NP geometries, coverages or epitaxies affect the activity?
- Which oxidation state of Cu is best?

These questions are addressed in Chapters 6 and 7.

2.4 Cysteine on TiO_2 and Cu

Cysteine consists of of three different functional groups, see Figure 2.1: a thiol group, an amino group and a carboxyl group. These distinct groups allow for distinction between different adsorption geometries, e.g. with XPS or IRRAS.

The adsorption of amino acids in general and cysteine in particular has been studied both on single crystalline TiO_2 and metallic Cu. On rutile $TiO_2(110)$ single crystals, a recent study found that several

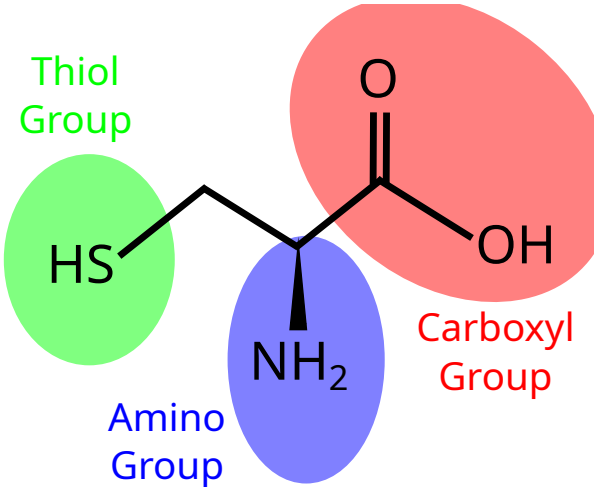


Figure 2.1: Skeletal structure of l-cysteine, the constituting functional groups are marked.

adsorption geometries are possible [6]: a combination of IRRAS, XPS and DFT calculations leads to the conclusion that cysteine almost exclusively adsorbs in a bridging configuration (on two Ti atoms) and with de-protonated carboxyl group. The interaction with the Ti is realized either by the carboxyl group or by a combination of the carboxyl group and a second functional group. Moreover, a stabilization of the protonated amino group NH_2^+ by residual water molecules is reported. A very similar study was conducted for cysteine adsorption on anatase $TiO_2(101)$ [5]. As for rutile, the adsorption is found to favor a bridging configuration between two Ti atoms. In contrast to the adsorption on rutile, the amino group is found to be rarely protonated, indicating a stronger interaction with the surface and binding through the thiol group is common. On Cu, it is known that organic molecules with a thiol group will form Cu-S bonds [22, 23, 20]. Moreover, for the adsorption of thiol-containing molecules on CuO it was reported that the oxide became partially reduced by Cu-S bond formation [55]. No studies for the adsorption of cysteine on Cu/TiO_2 systems exist, leaving the following open questions:

- How does Cysteine adsorb on Cu/TiO_2?
- Does the adsorption depend on the Cu coverage and oxidation state or on the TiO_2 substrate?

These questions will be addressed in Chapters 6 and 7.

Chapter 3

Basic Principles & Theoretical Background

3.1 Crystal Lattices

We are surrounded by a lot of 'hard' material - things that are not gas-phase (like air) or liquid-phase (like water). Most of these fall into the category of so-called 'solid state' systems. What they have in common (and what constitutes their 'solidness'), is a long-range order of their building blocks. Where the gas-phase features no order at all between the gas molecules and where the liquid-phase allows only a short-range order (that is: neighboring molecules have preferred orientations toward each other, but a few molecules away it does not matter anymore), solid-state systems are ordered at large scales. Considering single crystals, this order can extend as far as having all atoms in a crystal aligned in a specific direction, where the crystal can be of macroscopic size (of the order of centimeters).

The specific order of the solid-state systems can vary a lot, depending on the actual system. Considering a material that has long-range order of macroscopic scales (at least a few micrometer), one often talks of 'crystals'. This will be done from here onward.

A crystal can be described as a system of ordered minimal building blocks. Mathematically, this is described by a Bravais lattice: Each point in the lattice can be reached by integer multiples of basis vectors. For a 3-dimensional case, this means

$$\vec{R} = \mathbf{n}_1\vec{a} + \mathbf{n}_2\vec{b} + \mathbf{n}_3\vec{c} \tag{3.1}$$

with integers $\mathrm{n_i}$. An example of such a lattice can be seen in Figure 3.1: every point of this lattice can be reached by a combination of the vectors $\vec{a}$, $\vec{b}$ and $\vec{c}$.

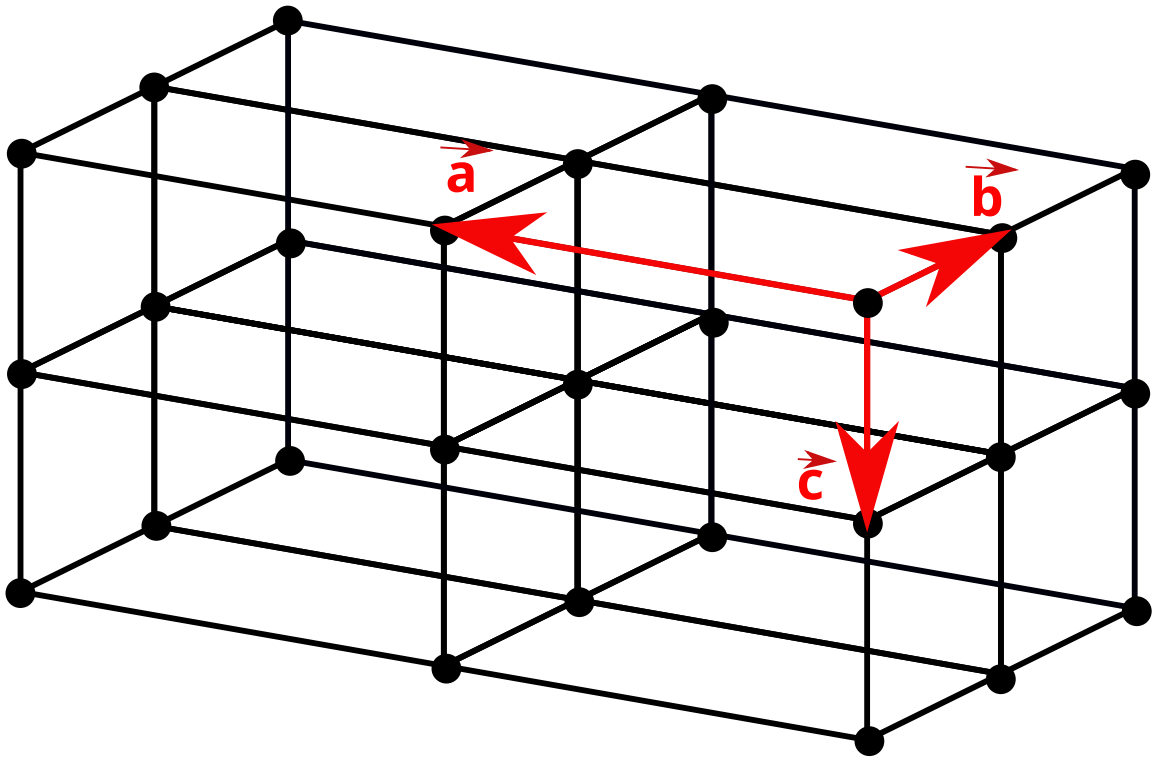


Figure 3.1: Simple Bravais lattice. By adding basis vectors $\vec{a}$ and $\vec{b}$, every point can be reached.

3.2 X-ray Diffraction from the Lattice

For the interaction of X-rays with matter, we can consider plane waves interacting with each lattice point. At each lattice point, a new wave is created, according to Huygen's principle. We can describe the wave by

$$\vec{w}(\vec{r}) = e^{i\vec{k}\vec{r}} \tag{3.2}$$

neglecting the amplitude and temporal dependencies, with $\vec{r}$ being the distance to the origin. For constructive interference to appear, we need

$$\vec{w}(\vec{r}) = \vec{w}(\vec{r} + \vec{R}) \tag{3.3}$$

with an arbitrary Bravais lattice vector $\vec{R}$. This means

$$e^{i\vec{k}\vec{r}} = e^{i\vec{k}(\vec{r}+\vec{R})} = e^{i\vec{k}\vec{r}} e^{i\vec{k}\vec{R}} \tag{3.4}$$

which demands

$$e^{i\vec{k}\vec{R}} = 1 \tag{3.5}$$

meaning

$$\vec{k}\vec{R} = 2\pi\dot{N} \tag{3.6}$$

with $n \in \mathbb{N}$. Using a set of basis vectors to describe the wave vector

$$\vec{k} = \vec{b_1}m_1 + \vec{b_2}m_2 + \vec{b_3}m3 \tag{3.7}$$

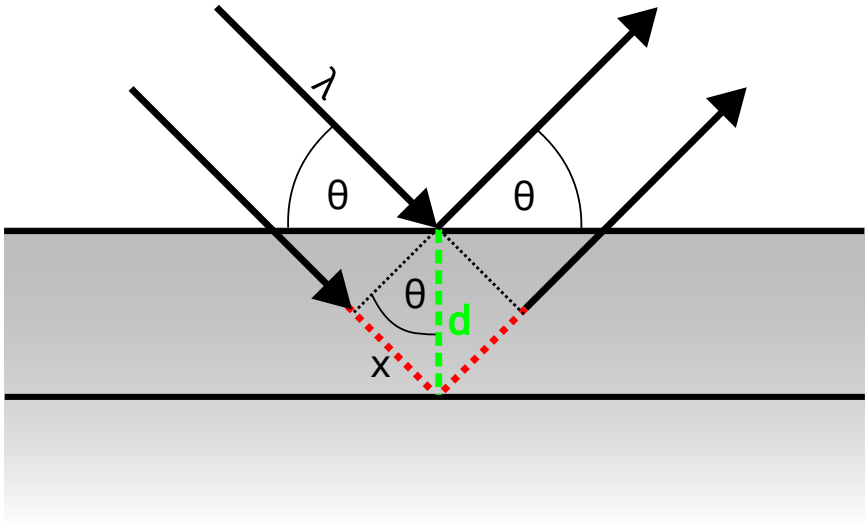


Figure 3.2: X-ray diffraction in geometric terms: The incident beam enters the sample at an angle θ. Inside the sample, the distance between lattice planes is d.

with integer m_i leads to

$$a_i b_j = \delta_{ij} \tag{3.8}$$

The b_i describe the so-called reciprocal lattice. Mathematically, it is the Fourier transform of the Bravais lattice in real-space. Physically, it represents the allowed scattering wave vectors. Moreover, each point in the reciprocal lattice represents a set of planes in the real lattice that diffract the X-rays. Now, for arbitrary scattering of X-rays with initial wavevector k_i and final wavevector k_f, the Laue condition

$$k_f - k_i = G_{HKL} \tag{3.9}$$

has to be fulfilled, that is the scattering vector needs to be part of the reciprocal lattice.

3.3 Bragg's Law

A different way to approach the diffraction of X-rays with matter is the geometric approach taken in Bragg's Law: Consider a surface, and underneath it several layers with uniform distance d, see Figure 3.2. Considering monochromatic radiation with wavelength λ, and an incoming angle θ equal to the outgoing angle. The incoming and the outgoing waves need to have a path difference equal to integer multiples of λ to achieve constructive interference. With $\sin\theta = \frac{x}{d}$, this means

$$n \times \lambda \stackrel{!}{=} 2 \times \mathbf{d} \times \sin\theta \tag{3.10}$$

which is Bragg's Law. It can be shown that Bragg's Law and the Laue condition are equivalent.

3.4 Grazing-Incidence X-Ray Diffraction

When studying model systems of nanoparticles on single crystals, only the surface of the sample is of interest (where the NPs are). Very high surface sensitivity can be reached by utilizing grazing-incidence

for X-ray diffraction. For X-rays, the refractive index n is given by:

$$\mathbf{n} = 1 - \delta + \mathbf{i}\beta \tag{3.11}$$

Here, δ describes the refraction and β the adsorption. Both are positive-valued. When the X-rays pass the barrier from one medium with index n_1 to another medium with index n_2, they have to fulfill Snell's Law,

$$n_1 \times \sin\alpha_1 = n_2 \times \sin\alpha_2 \tag{3.12}$$

where α_i are the angles between the radiation and the surface normal in both media. When the quotient $\frac{n_1}{n_2}$ becomes larger than 1, there is an angle $\alpha_{1,crit}$ above which this equation can no longer be fulfilled. This angle is called the critical angle. At the critical angle, the wave does not move into the second medium, but it travels along the surface. This is exploited in GIXRD, as such a wave is only sensitive to the surface of the material.

3.5 High-Energy X-Ray Diffraction (HEXRD)

The diffraction on a crystal can be visualized with an Ewald Sphere, see Figure 3.3. In this 2D visualization, the reciprocal lattice points (gray) that lie on the Ewald Sphere (purple) are accessible to the experimental setup. the length of the wavevectors k is determined by the wavelength, $k \propto \frac{1}{\lambda}$. As a result, when decreasing the employed wavelength, the radius of the Ewald Sphere increases. In standard XRD setups, the detector has to be moved around the Ewald Sphere to detect different peaks on it. When the Ewald sphere becomes almost flat, however, a large 2D detector is able to probe large parts of the reciprocal space at once. This effect is exploited in High-Energy X-Ray Diffraction (HEXRD): beam energies typically above 60 keV allow probing large parts of the reciprocal space at once. This has the benefit of being able to study reactions in-situ or probe large amounts of the reciprocal space in relatively short time.

3.6 Rutile and Anatase Structure

Titanium dioxide exists in several polymorphs, representing different crystal structures for the same combination of elements. The most common are rutile and anatase. Rutile features a tetragonal crystal structure, with lattice constants a=b=4.59308 and c=2.95889 [7]. A drawing of its most stable surface, [110], can be seen in Figure 3.5. The lattice constants for rutile are [7]: a=b=4.59308 and c=2.95889

The lattice constants for anatase are [7]: a=b=3.78479, c=9.50226

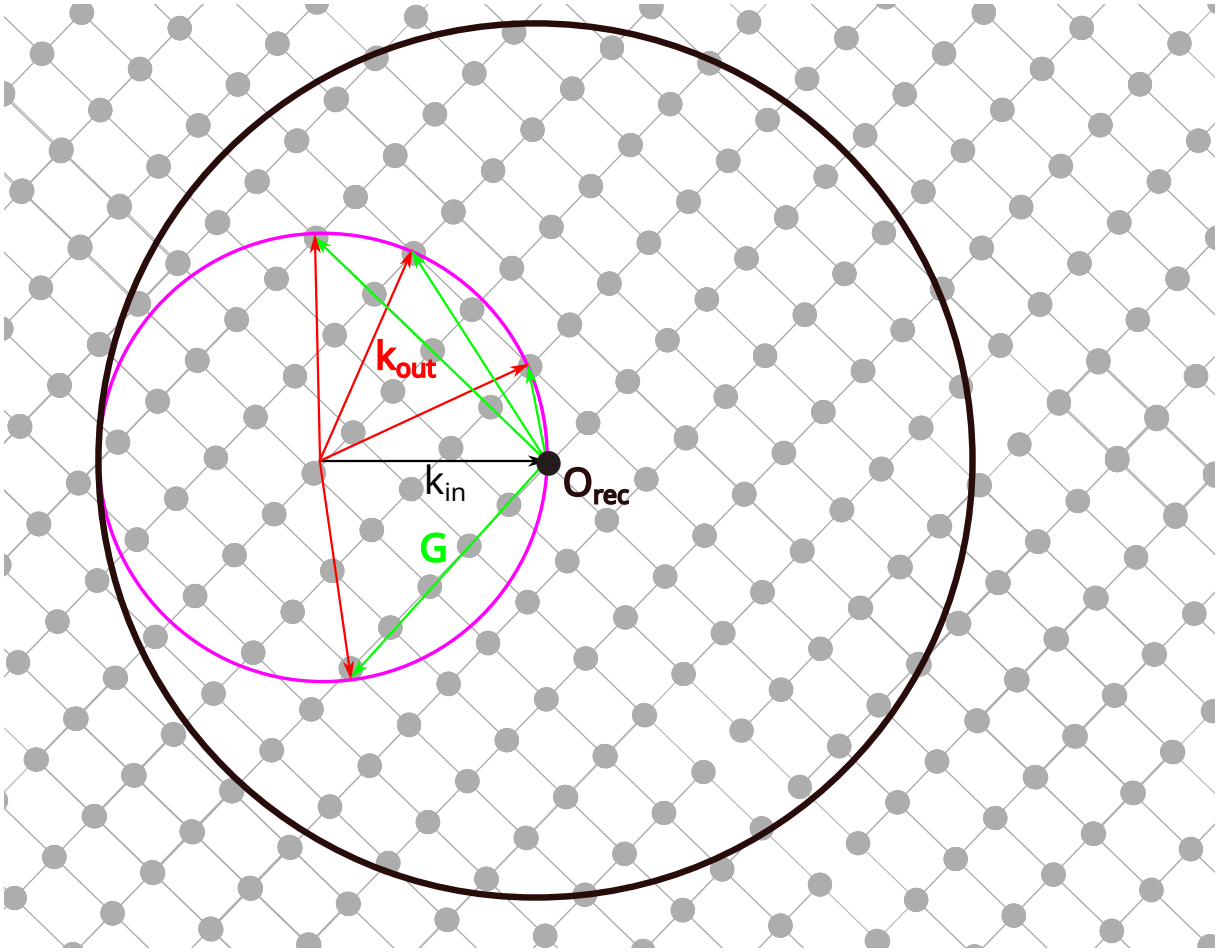


Figure 3.3: Ewald Sphere: The reciprocal space is represented by the gray lattice points with its origin at the black lattice point. The incoming wavevector $\mathbf{k_{in}}$ ends at the origin of the reciprocal space. Considering elastic scattering, where the lengths of both incoming and outgoing wavevectors are the same, all allowed outgoing wavevectors (red) have to connect to a lattice point on the Ewald circle (purple). Thus, all momentum transfer vectors (green) are part of the reciprocal lattice. When the real-space crystal is turned, the reciprocal space is also turned around its origin. As a result, all peaks that can be probed lie within the black circle with a radius of double the wavevector.

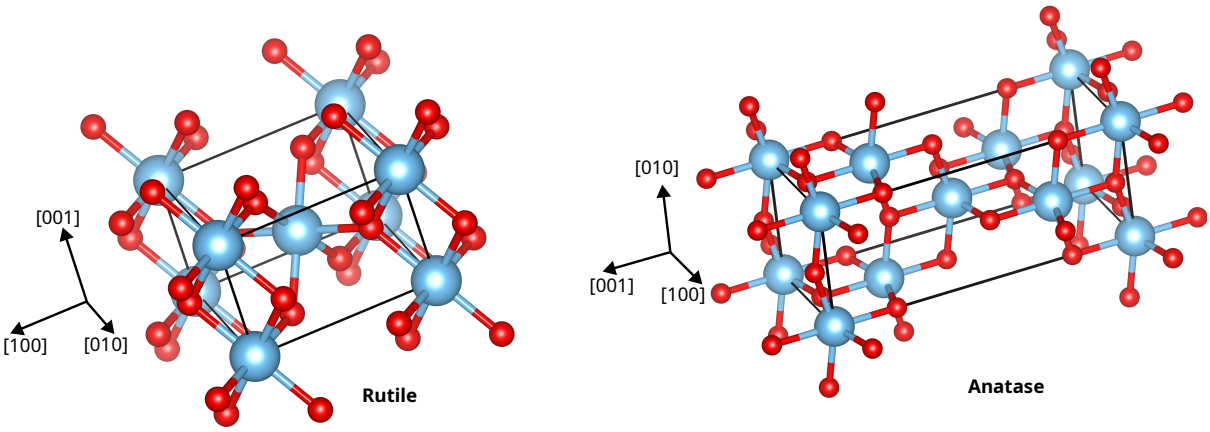


Figure 3.4: Unit cells of Rutile and Anatase TiO_2. Oxygen atoms are represented in red, titanium atoms in grey.

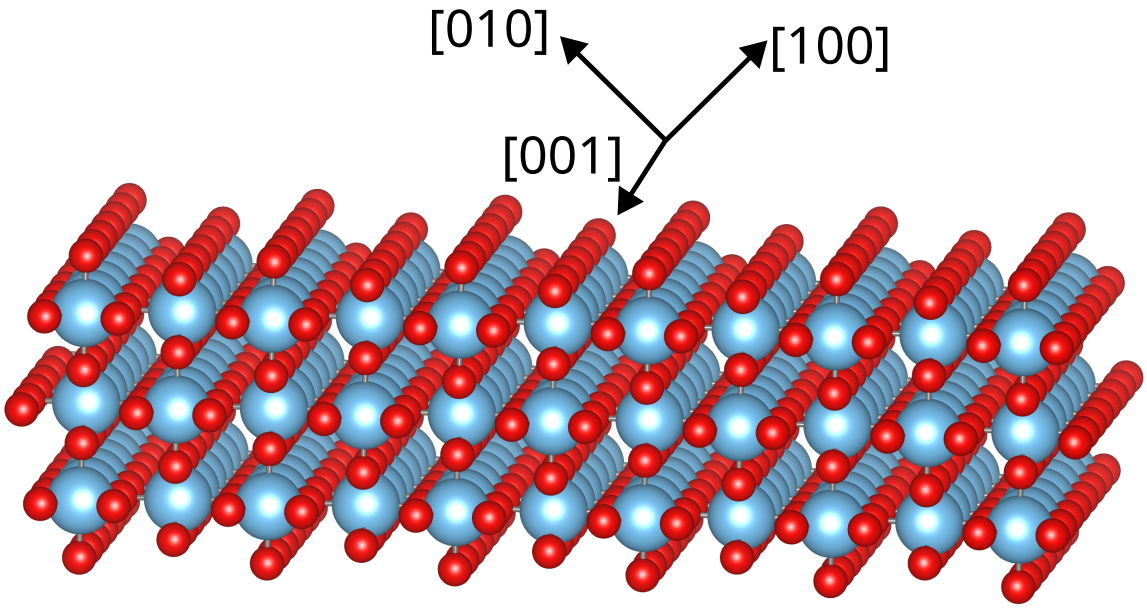


Figure 3.5: Schematic drawing of the rutile $TiO_2(110)$ surface. Oxygen atoms are represented by red balls, Titanium atoms by grey balls.

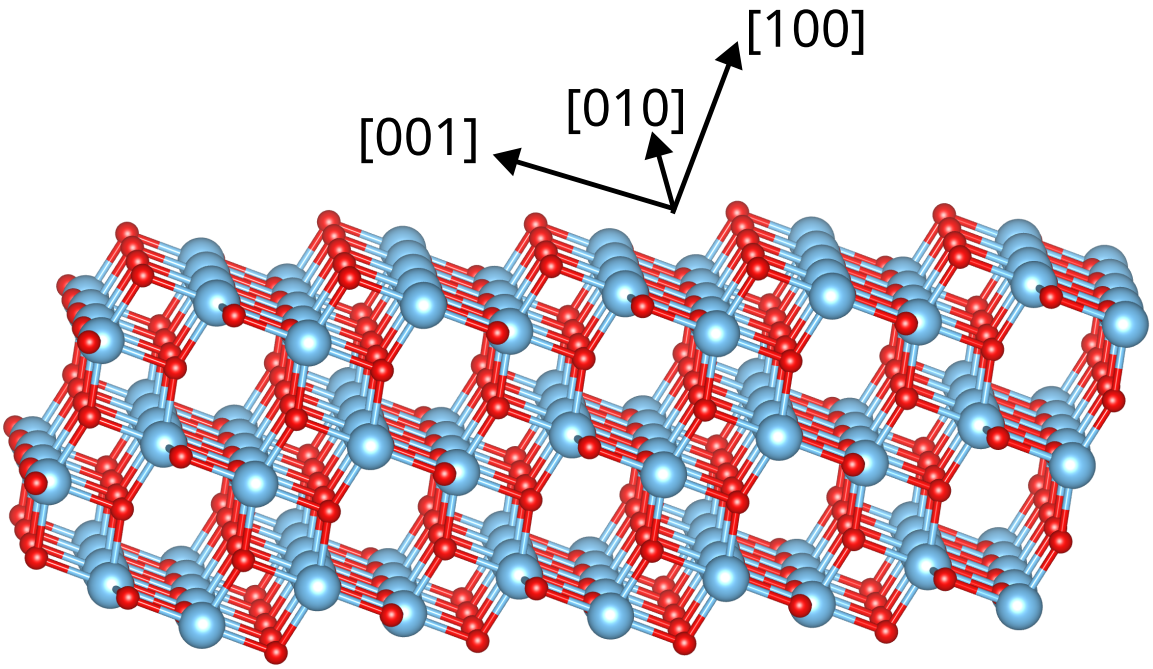


Figure 3.6: Schematic drawing of the anatase $TiO_2(101)$ surface. Oxygen atoms are represented by red balls, Titanium atoms by grey balls.

3.7 X-ray Photoelectron Spectroscopy (XPS)

With X-ray photo-electron spectroscopy (XPS), the elemental and chemical composition of the surface of a sample is probed. To this end, the surface is illuminated with X-rays. The X-ray source, in conventional XPS setups, is typically Al K_α or Mg K_α radiation. The spot size depends on the setup, but is typically

in the range of μm to mm. A schematic view of the XPS working principle can be seen in Figure 3.7: The X-rays are absorbed by electrons in the material. As the typical X-ray energies are around 1 keV, the electrons are easily removed from their atoms, with the kinetic energy of the electron determined by the difference between binding energy and photon energy (neglecting setup-dependent offsets):

$$E_{kinetic} = E_{photon} - E_{binding} \tag{3.13}$$

The kinetic energy of the ejected electrons is detected. By knowing the kinetic energy of the electron and the energy of the photon, the binding energy is calculated. The binding energy depends on the individual element, the chemical bindings the element has and the surroundings that may influence energy levels. As a result, the spectra reveal detailed information about the sample. In addition to the XPS working principle, it is also possible to detect Auger electrons. These follow a different generation mechanism, see Figure 3.7 b) and c): The X-rays eject an inner-shell electron. The created vacancy is filled by a higher shell electron. This still leaves energy in the system. This energy is used to eject another higher shell electron. The kinetic energy of this electron is independent of the photon energy and only depends on the energy levels of the participating electrons. Like XPS, the resulting spectra are sensitive to the atomic species they were ejected from. Though Auger electrons are sensitive to chemical bonds, their dependence on inner shell reactions causes this sensitivity to be low compared to core-level spectra from outer shell electron in XPS. Instead of photons, Auger electrons can also be created by bombarding the surface with high-energy electrons (Auger Electron Spectroscopy, AES).

The naming of XPS peaks is based on the quantum numbers: for example, the Cu $2p_{3/2}$ peak means the peak for the element Cu, principal quantum number n=2, p-orbital (which means that angular momentum quantum number is l=1), and the total angular momentum quantum number j=3/2. Peaks from all shells except the s-shell exhibit peak splitting due to spin-orbit coupling: j=l$\pm$s, where different total angular momentum results in different energy levels. The splitting is distinct for each element. The magnitude of it can range from barely detectable (two overlapping peaks) to two separate peaks (as it is the case for Cu 2p). The intensity ratio is governed by the degeneracy of each state. From quantum mechanics, it is known that each of the total angular momentum states can be filled with $2j+1$ different electrons, corresponding to all possible magnetic quantum numbers m_z for a given total angular momentum j, $m_z \in [j, j, j-1, ..., 0, ..., -j+1, -j]$. For the 2p peaks, this results in a ratio of 1:2 for $2p_{1/2)} : 2p_{3/2)}$.

The probing depths of both XPS and AES is defined by the mean free path of electrons in the material. The mean free path of electrons can be calculated by a formula only dependent on the electron energy [45]:

$$\lambda = \frac{A}{E_{kinetic}^2} + B\sqrt{E_{kinetic}} \tag{3.14}$$

with A and B as constants, depending on the specific material. With the kinetic energy given in eV and λ in nm, A is typically $\sim$100 nm$\cdot$(eV)^2 and B is typically$\sim$0.05 nm/(eV)$^{\frac{1}{2}}$. The resulting dependency can be seen in Figure 3.8. It can be seen that typical XPS electron energies have inelastic mean free paths of below 5 nm. Hence, XPS and AES are inherently surface sensitive.

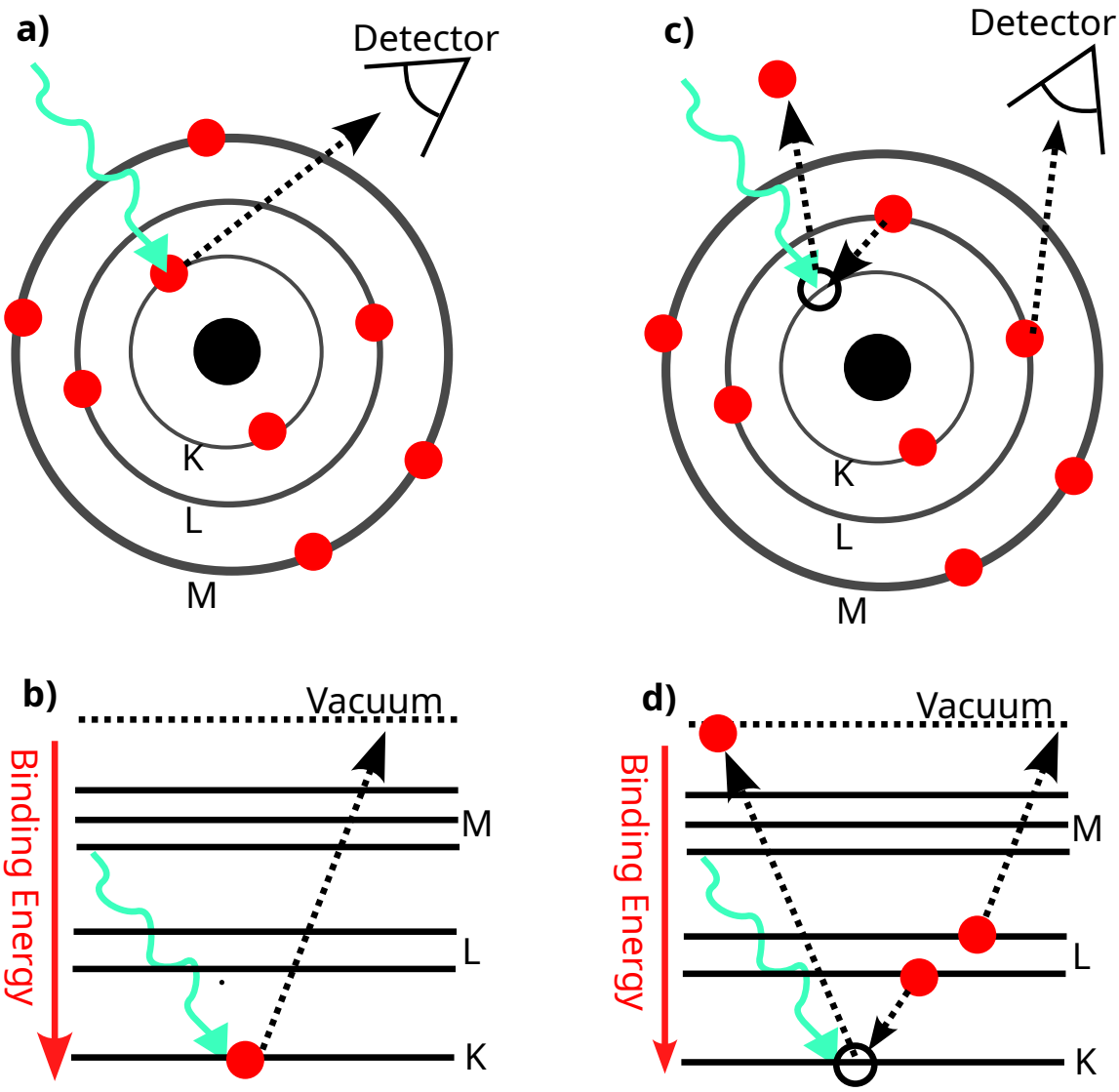


Figure 3.7: Working principle of XPS and AES. a) Schematic view on an atom for XPS measurements: X-rays are adsorbed by an electron, which in turn is ejected and detected. b) The same XPS working principle, but from point of view of energy levels. c) Schematic view on an atom for Auger spectroscopy: By adsorption of the X-rays, an inner shell electron is ejected. To fill the vacancy, a higher shell electron takes its place. By the remaining energy, a different electron is ejected. d) The same Auger spectroscopy prnciple, but from point of view of energy levels.

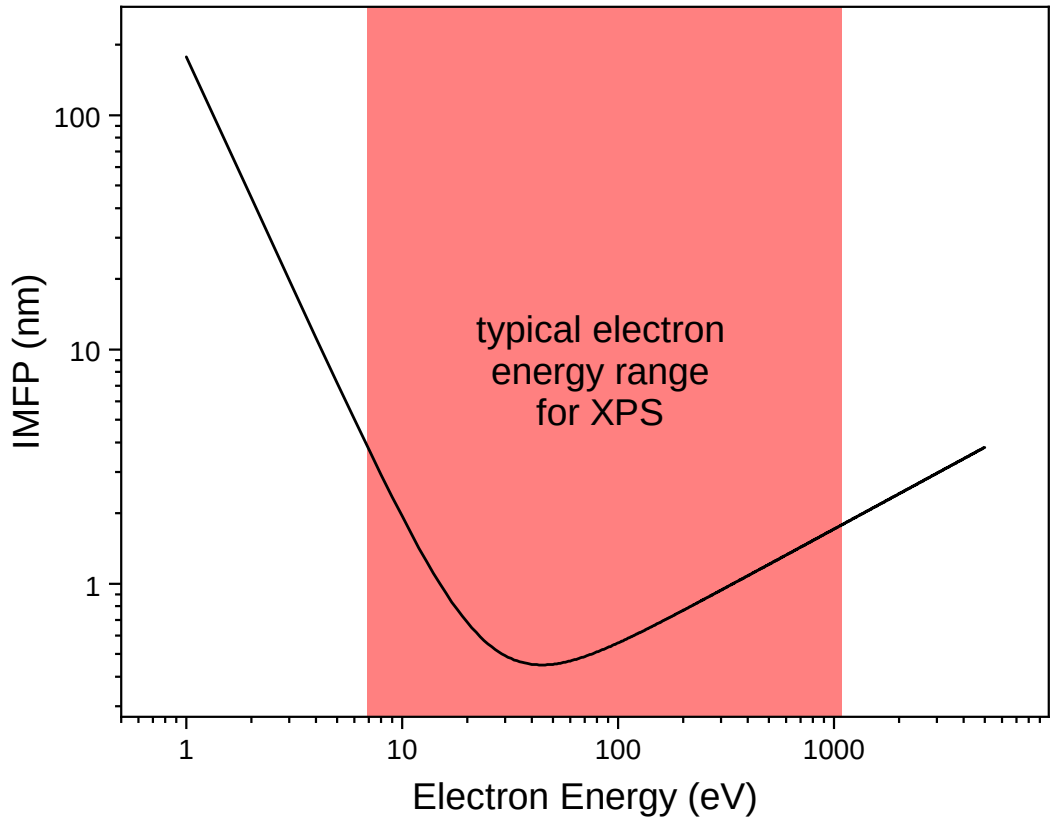


Figure 3.8: Inelastic mean free path (IMFP) for electrons in a solid. Produced with the formula and the values from Seah&Dench [45].

3.8 Infrared Reflection Absorption Spectroscopy (IRRAS)

The individual atoms in a molecule can be described as being in a potential, where the energy depends on the specific positions of the atoms with respect to each other. In the simple case of carbon monoxide, this breaks down to the distance between carbon and oxygen. Especially in this example it is apparent that a description similar to a spring can be used: the atoms are in a harmonic potential, in which the energy is proportional to the square of the distance to the equilibrium, r:

$$V(r) \propto r^2 \tag{3.15}$$

Considering this system as a quantum mechanical harmonic oscillator, the well-known energy levels are:

$$V_{harmonic} = h\nu(n + \frac{1}{2}) \tag{3.16}$$

Here, E is the energy, h Planck's constant, ν the frequency associated with the vibration and n is the vibrational quantum number.
The harmonic oscillator description is useful, but a more realistic description uses a Morse potential:

$$V_{Morse} = V_{harmonic} + h\nu k_e(n + \frac{1}{2})^2 \tag{3.17}$$

The constant k_e is called the anharmonicity constant. A comparison of both potential types can be seen in Figure 3.10.
This simple model describes the CO vibration well, but the basic principles are also shared with more complex vibrations (see Figure 3.9).

When such a molecule has a dipole moment (which it possesses as long as not all atoms are identical), it can absorb electromagnetic radiation and change its vibrational energy level. The photons needed for this typically lie in the infrared light region (wavenumbers between 4000 cm^{-1} and 500 cm^{-1}, where the wavenumber is the inverse of the photon wavelength). Considering a pure harmonic oscillator, only energy transitions with $\Delta n = \pm 1$ are possible. In a Morse-type potential, also larger energy differences are allowed, the so-called overtones.

The potential the molecule experiences is influenced by its surroundings and chemical bonds. Thus, the photon energy needed to excite the vibration is sensitive to the surroundings. This effect is used in infrared spectroscopy: The position of the absorbed light on the spectrum allows for conclusions on which molecules are present in which surroundings. In this thesis, this principle is applied by investigating the gas-phase adsorption of molecules on single-crystals and NPs. In this case, the resulting absorption lines are very weak, as only the surface of the system allows for adsorption of molecules. The signals are identified by dividing the spectra with adsorbed molecules by the spectra measured before adsorption.

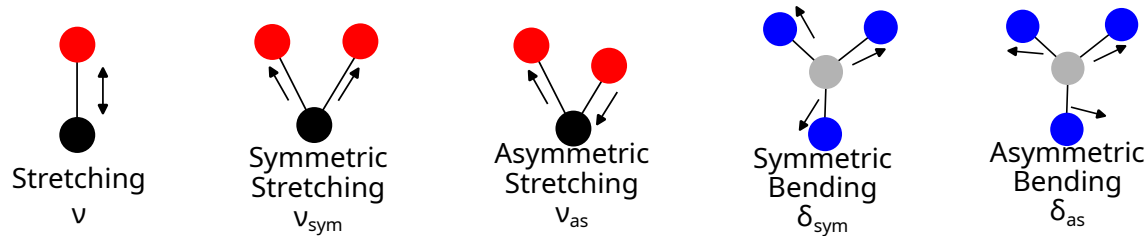


Figure 3.9: Examples of molecular vibrations. From left to right: CO stretching, CO_2 symmetric stretching, CO_2 asymmetric stretching, NH_3^+ symmetric bending (all blue H molecules move in and out of the page layer), NH_3^+ asymmetric bending (the blue H atoms do not move in the same directions).

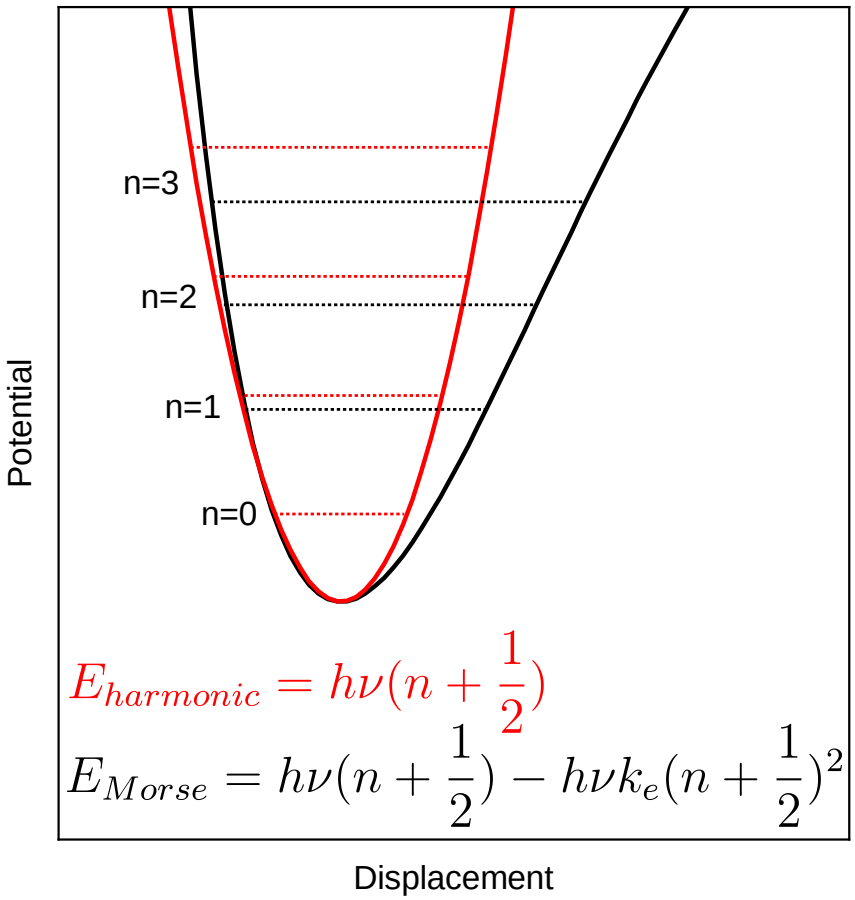


Figure 3.10: The potential describing vibrational modes: The harmonic potential works as an approximation for a more realistic, anharmonic model, e.g. Morse type. The vibrational modes are marked by horizontal lines. The energy levels are labeld by their quantum number n.

To probe the response of a system to infrared light, the easiest approach would be to use a single wavelength of light and to measure its absorption, probing one wavelength after another. Even though this is how the first infrared spectrometers operated, this is not optimal. On the one hand, it is very slow to probe one wavelength after another, considering typical probing ranges of a few thousand cm^{-1}. On the other hand, it requires the use of a complicated monochromator to achieve IR light of a single, specific wavelength. A solution to this difficulty is found in the Michelson interferometer. A Michelson interferometer, see Figure 3.11, uses a beam-splitter to split a beam of light into two. Each of these rays runs a specific length and is reflected back via a mirror. Both rays re-unite at the detector, forming an interference pattern. The interference depends on the path difference for the split light rays, δ. When this path difference is an integer multiple of the light wavelength λ, $\delta/\lambda = n$, $n \in \mathbb{N}$, constructive interference is formed. Destructive interference (extinction) occurs for $\delta/\lambda = \frac{2n+1}{2}$. The path difference can be adjusted by moving one of the mirrors. When light of multiple wavelengths λ and respective frequencies $\nu = \frac{c_0}{\lambda}$ (with the speed of light c_0) is used, the full intensity of all wavelengths combined is:

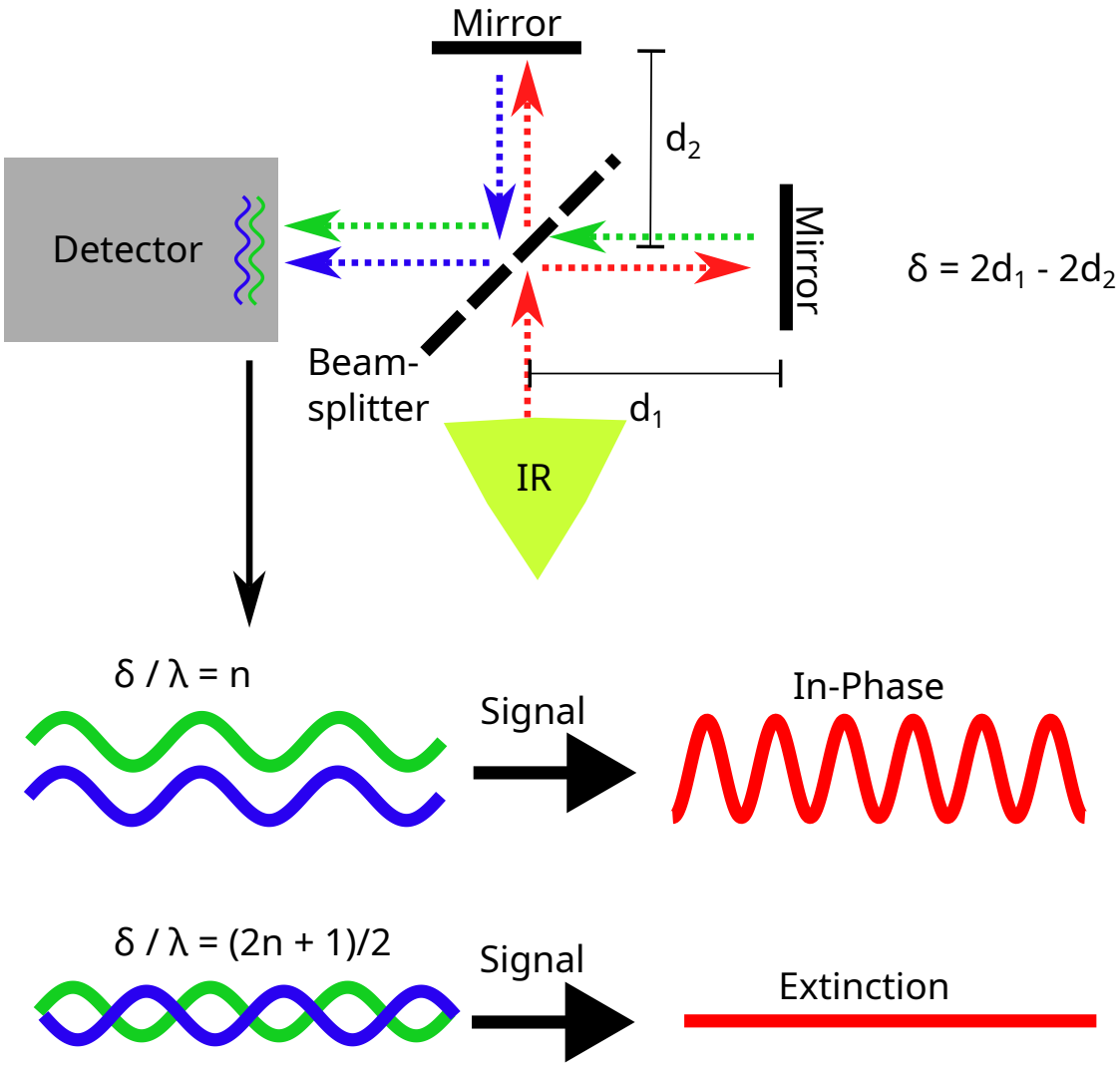


Figure 3.11: Schematic representation of a Michelson interferometer and the creation of the IRRAS signal.

$$S(\delta) = \int_{\nu_{min}}^{\nu_{max}} S_\nu(\delta) d\nu \tag{3.18}$$

Here, $S(\delta)$ is the detected signal, S_ν is the signal corresponding to light of the frequency ν. It is integrated over the range of light frequencies that are used: ν_{min} to ν_{max}. The intensity of a single wavelength of light is known to vary periodically with the path difference. Hence, the expression can be rewritten as:

$$S(\delta) = \int_{\nu_{min}}^{\nu_{max}} S_\nu \cos(2\pi\delta\frac{\nu}{c_0}) d\nu \tag{3.19}$$

Here, S_ν contains all information of the intensity for a given light frequency ν, including experimental variables. This expression has the form of the Fourier transform of S_ν. Hence, the reverse Fourier transform of $S(\delta)$ will produce $S(\nu)$. By this principle, a white light infrared source can be used to probe a whole set of wavelengths at once when using the Michelson interferometer. Instead of "moving" through different light wavelengths, the interferometer "moves" through different path differences, which can be done efficiently.

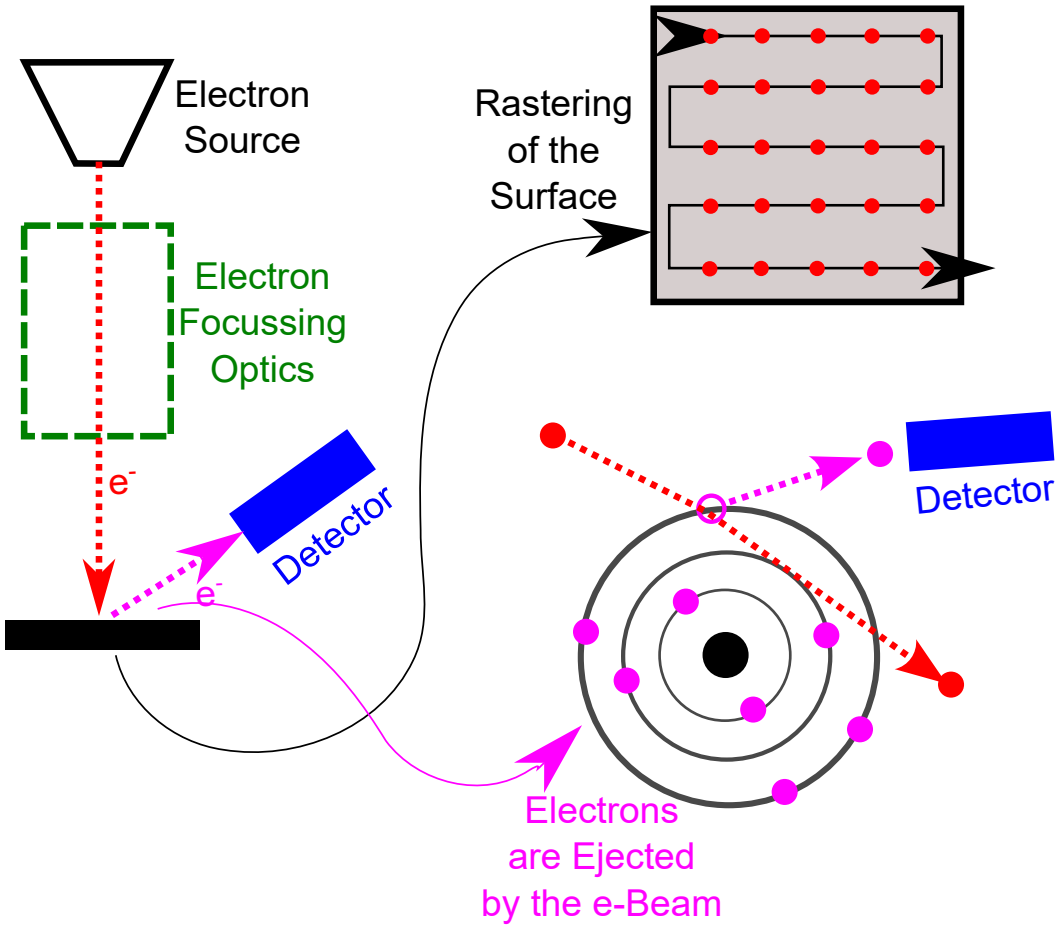


Figure 3.12: Working principle of the SEM: an electron beam is focussed on the sample. The sample is rastered point by point. At each point, the high-energy e-beam kicks out electrons from the sample. These are detected.

3.9 Scanning Electron Microscopy (SEM)

Scanning electron microscopy is used to get high-resolution real-space images of the samples. The working principle of scanning electron microscopy can be seen in Figure 3.12: electrons are focused and accelerated onto a sample (with about 5 keV to 20 keV). These can create a multitude of interactions, but the most important one is the creation of secondary electrons: these are electrons, which are kicked out by the beam. They typically have low energies (below 100 eV) and are thus very surface sensitive. They are detected by an electron detector, placed above the sample. Other interactions that occur are the creation of Auger electrons, back-scattering of the beam electrons, creation of X-ray fluorescence and Bremsstrahlung. Specialized setups make use of these to obtain information about the sample. The secondary electrons are used in most setups as they offer a high surface sensitivity. Moreover, as they are only ejected from the surface, they are also affected by changes in the morphology. This is beneficial for SEM, allowing for good depth resolution. The surface is subsequently rastered with the electron beam, collecting (secondary) electron signal at each spot, thus creating a real-space image of the sample.

3.10 Scanning Auger Microscopy (SAM)

Scanning Auger Microscopy (SAM) is very similar to SEM, but instead of detecting secondary electrons, Auger electrons are detected. In practice, this means that the detector for scanning Auger measurements resolves the energy of the electrons, enabling the measurement of spectra. While SEM measures the absolute intensity of ejected electrons at each raster point, SAM takes an energy spectrum at each raster point. Hence, for each point a full elemental analysis is possible. This allows for element-resolved maps and linescans.

3.11 Grazing-Incidence Small Angle X-ray Diffraction (GISAXS)

Grazing-Incidence Small Angle Scattering (GISAXS) is used to probe structures of thin films and nanoparticles. In contrast to X-ray diffraction, which probes Bragg peaks, GISAXS probes the electron density modulations on the surface. As a result, it is sensitive not only to crystalline structures but also to amorphous layers and NPs. The basic principle can be seen in Figure 3.13: the X-ray beam is set to grazing incidence. This causes the X-rays to travel as an evanescent wave over the surface, where they can be scattered by the NPs (or other density modulations). Scattering from an array of NPs causes interference patterns on the detector. As the detector captures two-dimensional images, information about the particle height as well as the lateral dimensions and ordering can be obtained. A typical feature of the scattering pattern is the so-called Yoneda peak (or the Yoneda wings) which appear around the critical angle of the substrate. The analysis of the diffraction patterns is often not straightforward, as many contributions create the actual image. In the case of NPs, the height, diameter, roughness, typical interparticle distance, and material can influence the pattern. As a result, theoretical calculations are

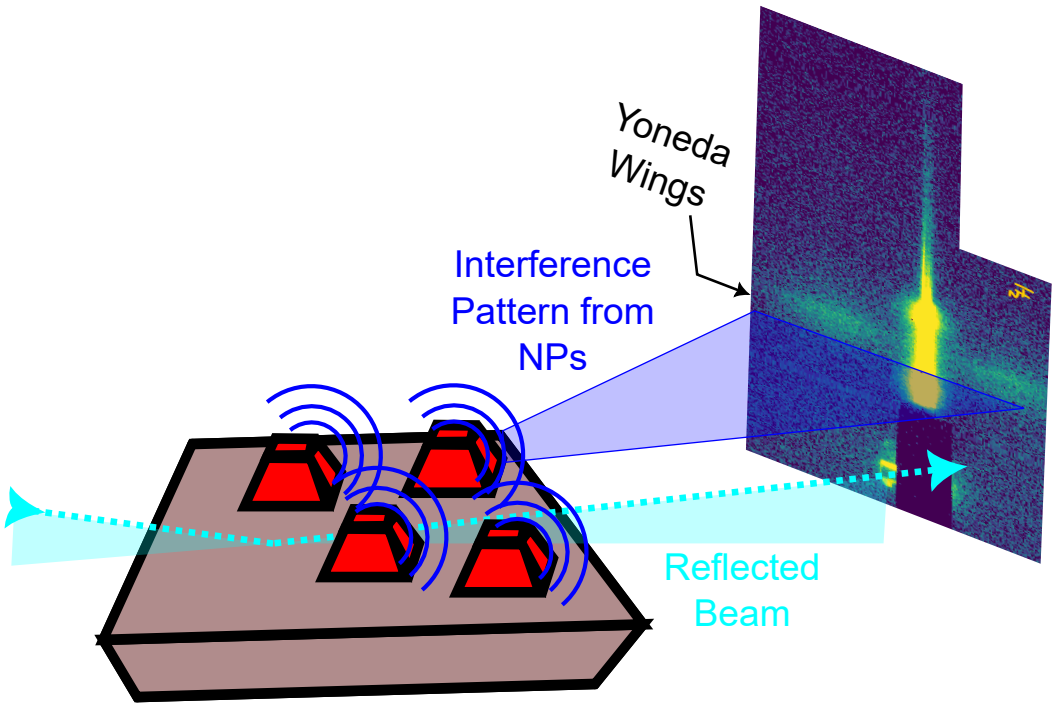


Figure 3.13: GISAXS working principle: the X-ray beam is set to hit the sample below (or at) the critical angle, thus creating an evanescent wave. This is scattered by the NPs on the sample. An interference pattern from the scattering of the NPs is formed on the detector.

often needed for the analysis, comparing the actual images with expected images.

3.12 Ultra-High Vacuum (UHV)

Most of the experiments in this thesis are performed in ultra-high vacuum (UHV). This means that the pressure in the corresponding chamber is below 10^{-7} mbar, see Figure 3.14 - for the setups used in this thesis the base pressures were on the order of 10^{-10} mbar. This offers distinct advantages: samples stay clean (no contamination with carbon), Cu NPs do not oxidize, and the low pressure enables the use of techniques like XPS, which depend on low pressures for a long mean-free path of electrons.

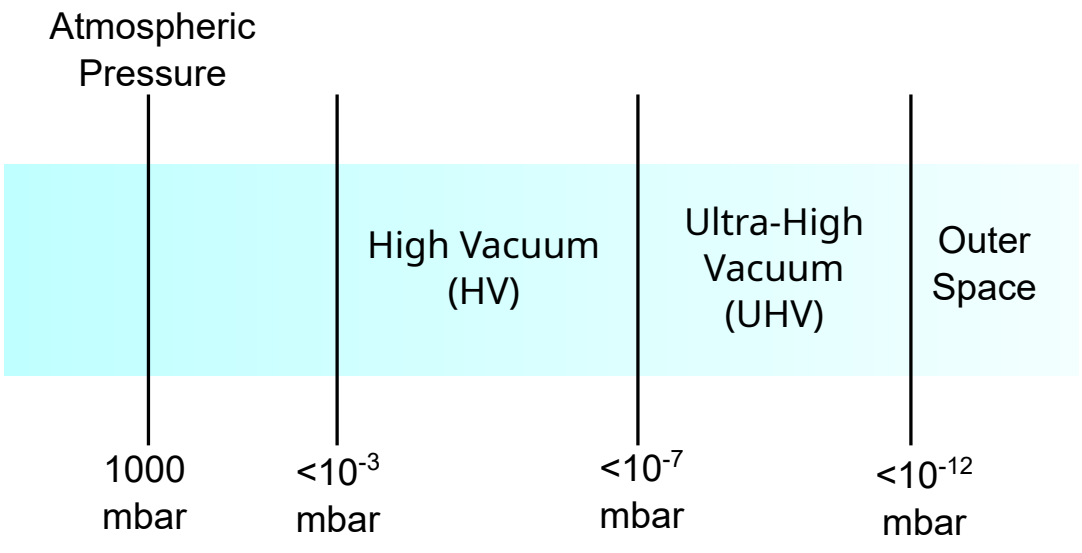


Figure 3.14: Comparison of pressure ranges for UHV.

3.13 Molecular Beam Epitaxy (MBE)

Molecular beam epitaxy (MBE) is a method to grow thin films and NP systems in UHV. A rod of the material that should be deposited is heated, such that it partially sublimates and gas-phase material is created. The jet of gas is directed at the sample. A typical MBE setup can be seen in Figure 3.15, for the case of Cu evaporation. The evaporator consists of a Cu rod, which is heated by applying high voltage between the rod and a filament (a separate current is running through the filament). This bombards the Cu rod with electrons, heating it. A droplet of Cu can be seen at the tip of the rod, indicating its liquid form upon heating. To keep the surroundings cool, water cooling and a cooling shroud are used. The Cu beam can be controlled by a movable shutter, enabling precise deposition times. Growth rates for MBE evaporators are typically round 1 Ångstrom per minute. Instead of a Cu rod, a crucible can be used, in which Cu pellets are melted.

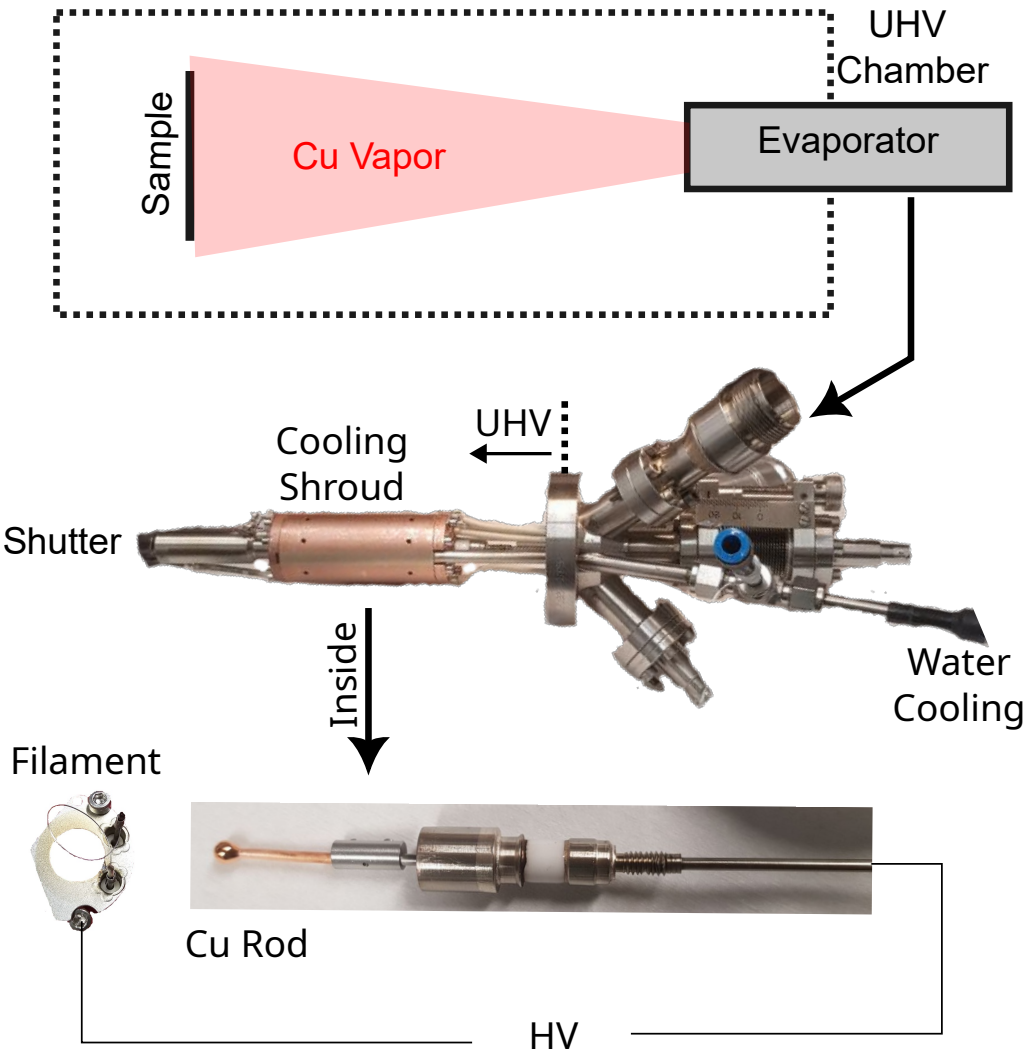


Figure 3.15: MBE evaporation of Cu: by applying a voltage between the filament and the Cu rod, the rod is heated. This creates gas-phase Cu. The jet of Cu is directed at the sample.

3.14 Low Energy Electron Diffraction (LEED)

Low-energy electron diffraction (LEED) is used to identify surface structures and probe if a sample is clean. The working principle can be seen in Figure 3.16. Electrons are shot at the sample at about 100 eV kinetic energy. They are elastically diffracted. This happens according to the Laue condition, represented by the Ewald sphere. On the fluorescent screen, the diffracted electrons create patterns resembling the reciprocal space of the sample's surface. The appearance of the pattern signifies that the surface is clean, as any dirt would block the signal due to the short mean free path of the electrons (see Figure 3.8). Moreover, as the diffraction signal is dependent on the surface structure, it can be used to confirm that a crystal has a specific surface or to find superstructures.

3.15 Photocatalysis

Electronic Structure of Solids The ordered structure of crystals also affects their electronic structure. Considering a single atom, the allowed energy states for electrons are described by the well-known solutions to the Schrödinger equation, with energy levels given by the main quantum number, the spin, and the orbital quantum numbers. The energy levels are discrete and sharp. When introducing a second atom, the molecular orbitals may overlap, producing a different set of allowed states for both atoms, with a higher number of energy levels. When going from a few atoms to a bulk crystal (with about 10^{23} atoms), the spacing between energy levels becomes very small and they effectively form bands of certain dimensions (a continuum of allowed energy levels). Restrictions on these energy levels come from the crystalline nature, determining the position of the bands. The energy level up to which bands are filled with electrons is called the Fermi energy E_f. Typically, three different cases emerge, see Figure 3.17.

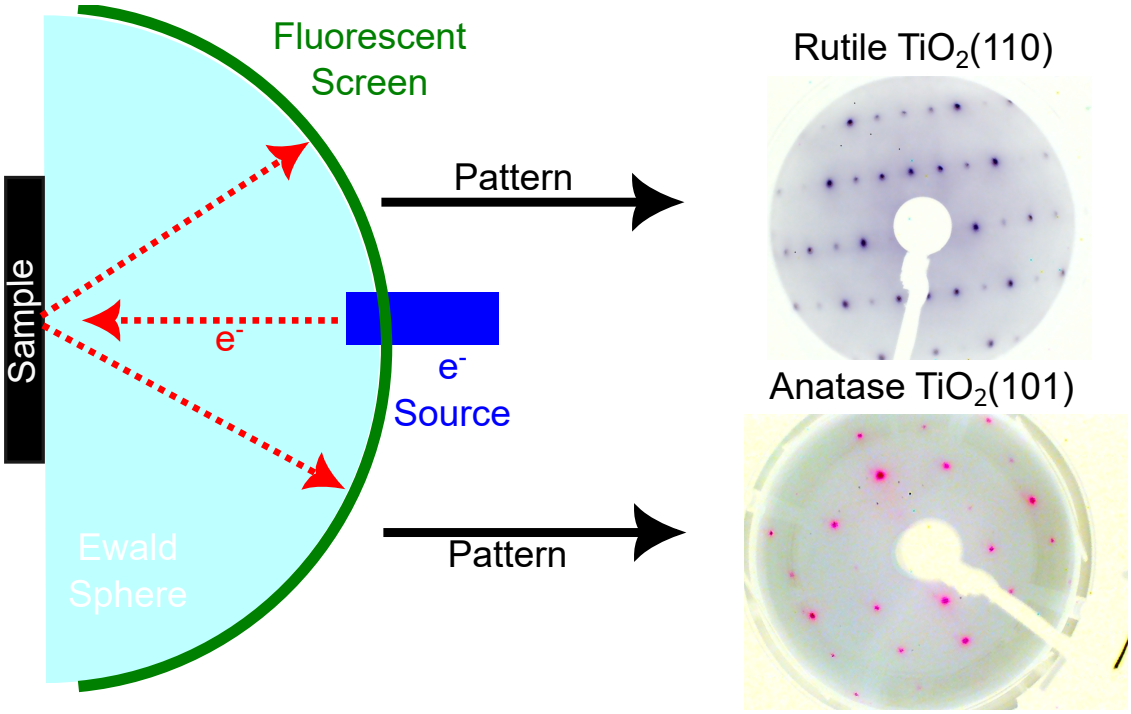


Figure 3.16: Working principle of LEED: Electrons are shot on the sample. There, they are diffracted according to the Ewald sphere (see also Figure 3.3). The fluorescent screen detects the scattered electrons. The pattern shows the reciprocal lattice at the surface and is indicative of specific structures, e.g. rutile and anatase.

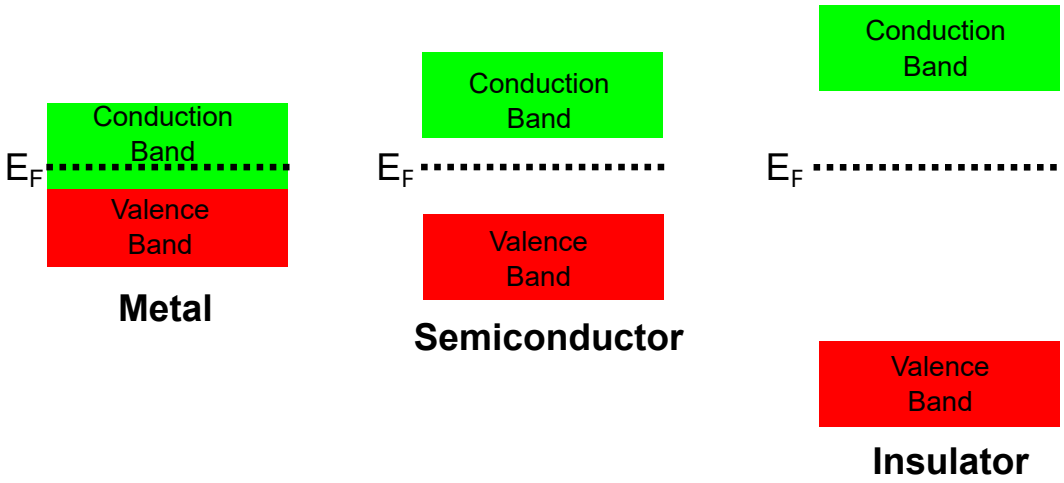


Figure 3.17: Schematic drawings of the energy levels for semiconductors, metals and insulators.

When the Fermi level lies in a band, electrons can conduct charge as they can move freely through the crystal, and the structure is called a metal. When the Fermi energy is in-between two bands, the lower one (fully filled) is called the valence band and the upper one (fully empty) is called the conduction band. In this state, the electrons cannot conduct charge, as all allowed levels are full. The space between valence band and conduction band is the bandgap. If the bandgap is small, the thermal energy distribution may allow for a certain number of electrons to be in the conduction band. This effect can be enhanced by applying an electric potential. Materials which can thus be made conductive is called a semiconductor. When the bandgap is large, this does not occur and the material is an insulator.

Photoexcitation and Photocatalysis For a semiconductor, the absorption of light by an electron in the valence band can lead to the promotion of the electron into the conduction band if the photon energy is at least as large as the bandgap, see Figure 3.18. Both the electron in the conduction band and the hole in the valence band can interact with the surroundings of the semiconductor, allowing the catalysis of certain reactions at the surface (which use either electrons, holes or both). The electron-hole pair can also recombine, however, which is not beneficial for photocatalysis. To avoid recombination, the charge carriers can be separated, for example by the introduction of metal nanoparticles on top of the semiconductor, by doping or by the addition of molecules that either scavenge electrons or holes, leaving no options for recombination.

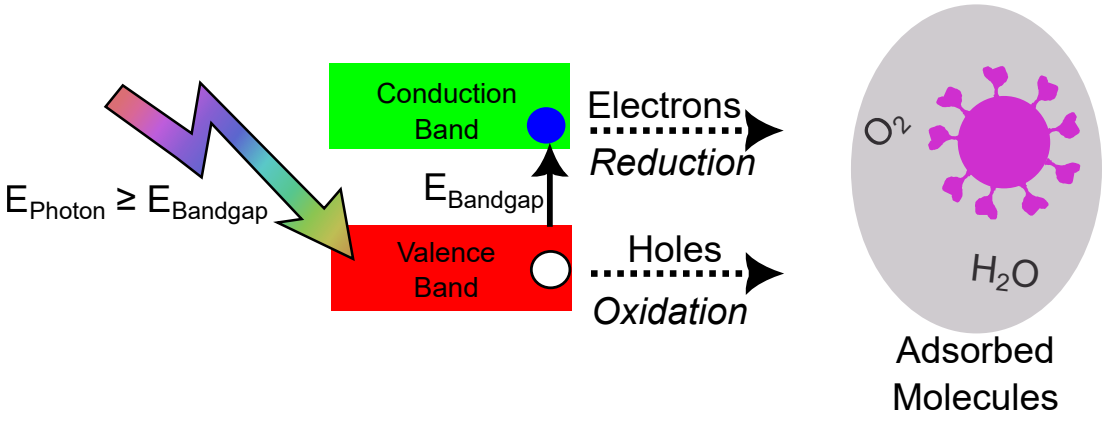


Figure 3.18: Schematic depiction of photocatalysis: Light of sufficient energy is absorbed by an electron in the semiconductor valence band. As a result, the electron is promoted to the conduction band, and a hole is left in the valence band. Both electron and hole can interact with molecules on the surface of the semiconductor, either acting as a reducing or oxidizing agent.

Chapter 4

Experimental Setups

4.1 DESY NanoLab: UHV lab

The DESY NanoLab [46] is part of the Centre for X-Ray and Nano Science (CXNS) at DESY. It comprises different laboratories: A UHV laboratory, an electro-chemistry laboratory, a chemistry laboratory, an X-ray laboratory and a microscopy laboratory. For the work conducted for this thesis, the UHV laboratory was used for the majority of the experiments. An image and schematic drawing of the UHV laboratory can be seen in Figure 4.1. The UHV laboratory is built around the concept of being able to do various measurements and treatments on a sample without leaving the UHV. To this end, it is set up such that all instruments and chambers are connected to a tunnel (which is also pumped to UHV). The samples can be brought from the individual chambers onto a trolley in the tunnel, which in turn can be moved to switch from one chamber to another. In this way, samples can be kept inside UHV all the time.

The UHV laboratory hosts several instruments: Two chambers are equipped with several molecular beam evaporators (and hence called 'MBE' chambers). In addition to the evaporators, they feature a sputter gun, a LEED/AES system, sample heating (resistive heating and e-beam heating) and gas-dosing systems (e.g. for oxygen). Two infrared spectrometers are available for adsorption studies, either at room temperature or cooled to liquid nitrogen or liquid helium temperature. An XPS is combined with a UPS, as is an STM combined with an AFM. Finally, there is a dedicated chamber for zinc evaporation and free space to connect mobile chambers to the UHV system. The samples are mounted on sample holders made of molybdenum, typically by spot-welding with tantalum clips, see Figure 4.2.

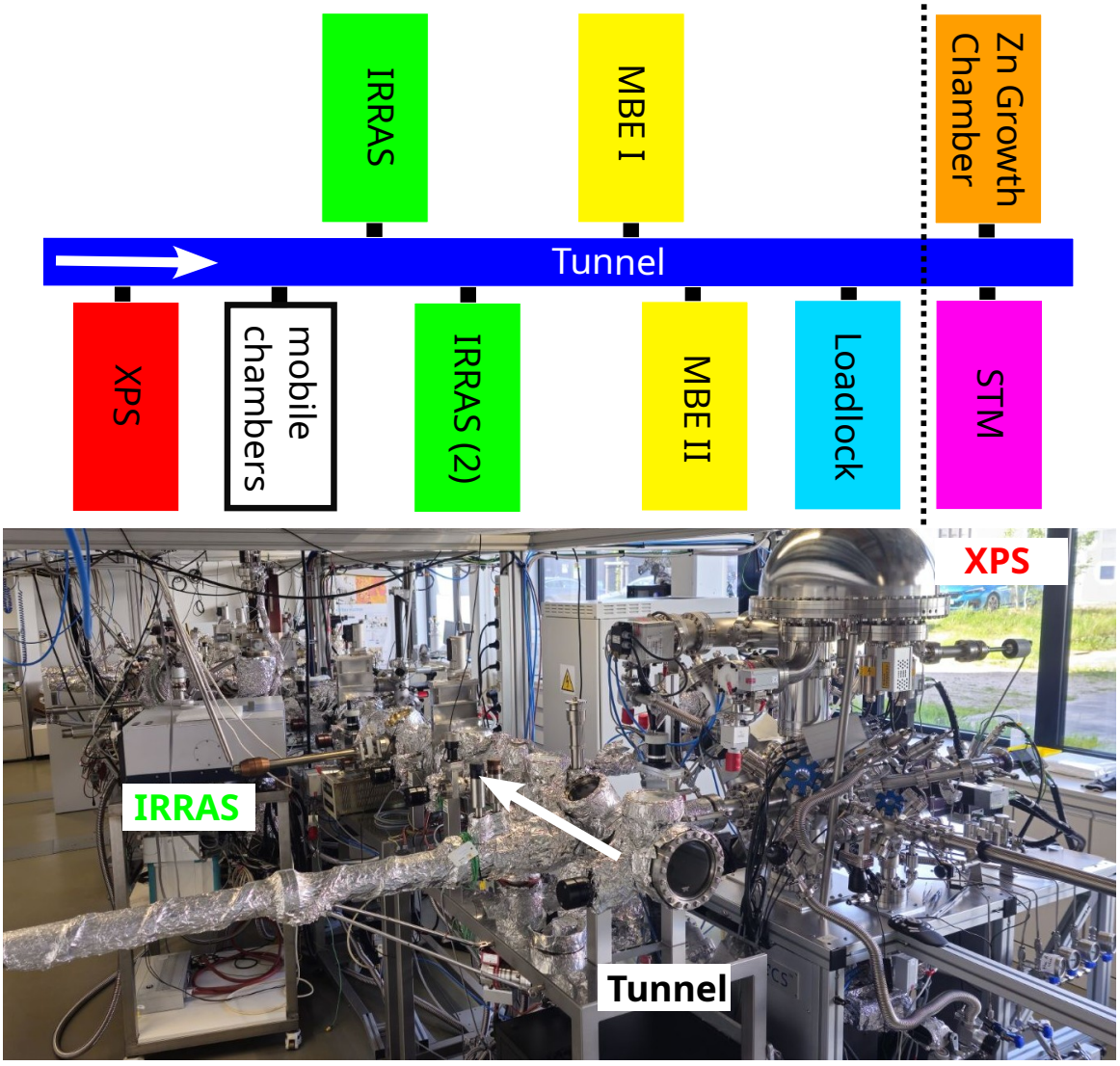


Figure 4.1: The DESY NanoLab UHV laboratory. top: schematic view on the different end-stations connected to the tunnel. Bottom: image of the UHV laboratory, facing the XPS.

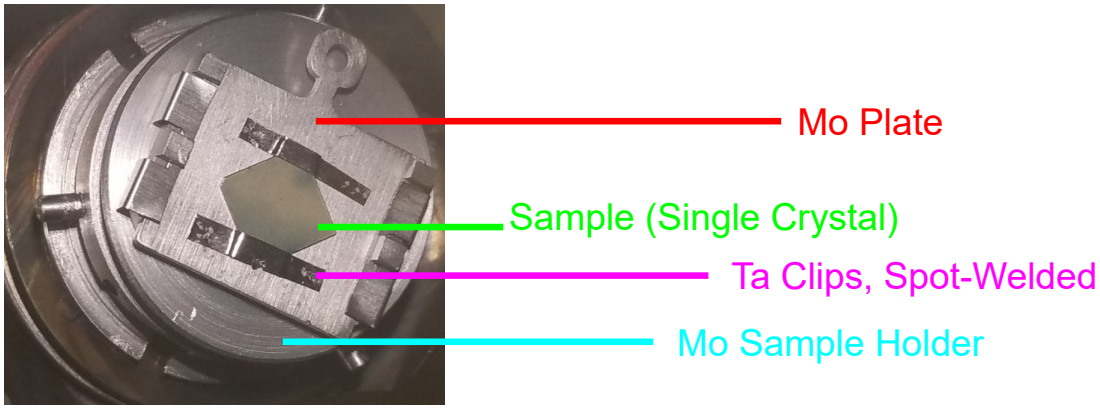


Figure 4.2: A sample holder used in the UHV lab: The sample (single crystal, here: rutile $TiO_2(110)$) is fixed by spot-welded tantalum clips to a molybdenum plate. This plate is on a molybdenum sample holder.

4.1.1 IRRAS

The IRRAS setup of NanoLab can be seen in Figure 4.3. The spectrometer and the detector are separated and the IR light is led through an UHV chamber, containing the sample. Measurements are done in reflectance mode, over 512 scans with a resolution of 2 cm^{-1} and a measurement time of 5 minutes. The spectrometer is a Bruker Vertex 80V, employing a liquid-nitrogen-cooled mercury cadmium telluride (MCT) detector. The UHV chamber was kept at a base pressure of 10^{-9} mbar. A gasline with separate pumping is connected to the chamber for cysteine dosing.

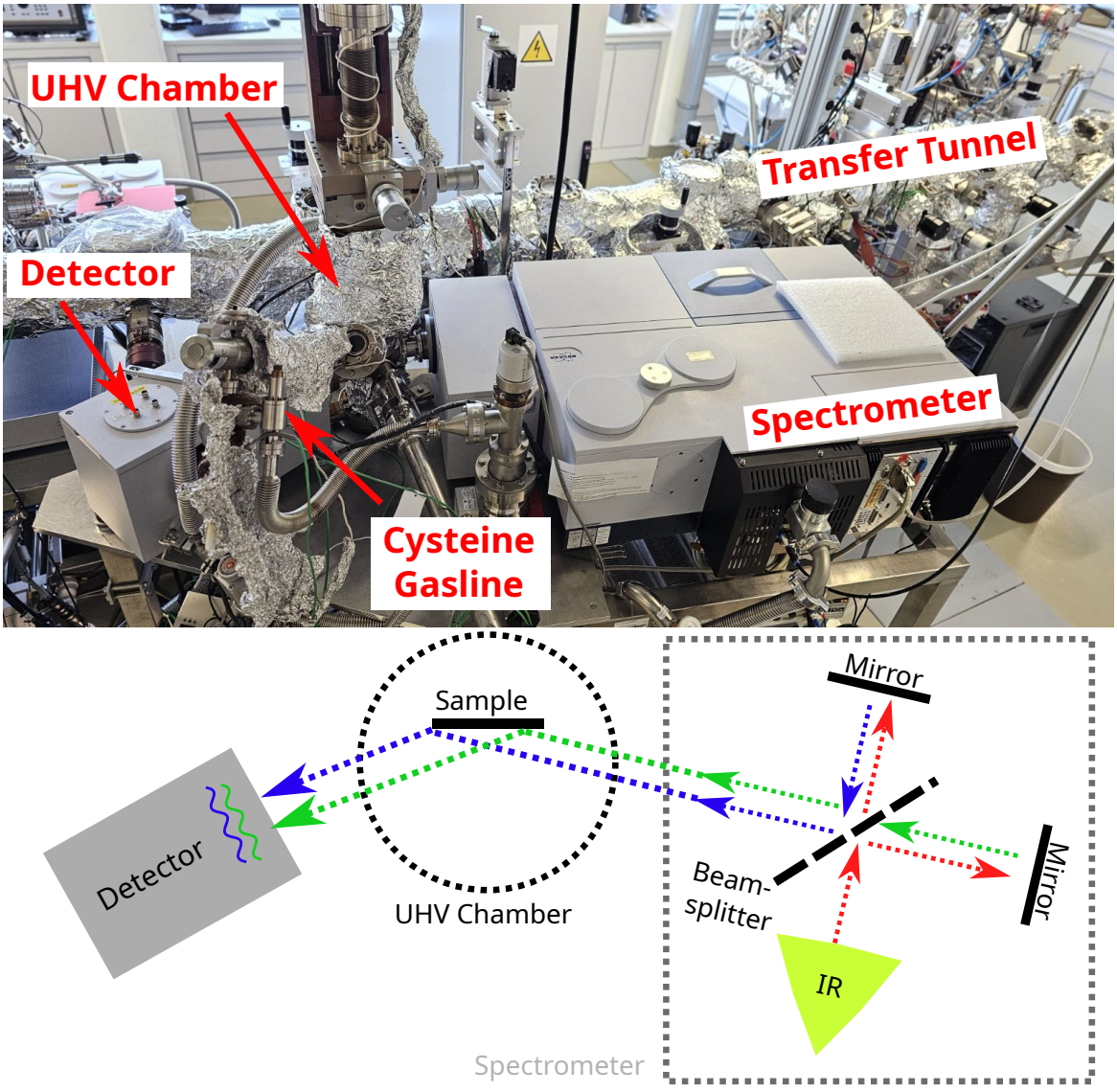


Figure 4.3: The IRRAS setup in the UHV lab of DESY NanoLab. The schematic view at the bottom is roughly alingned with the actual setup on-top. A detailed description of the principles can be found in the corresponding theory section, Section 3.8

.

Cysteine Dosing Cysteine is dosed in the IRRAS chamber by evaporation, the specific setup can be seen in Figure 4.4. Cysteine powder is in a glass vial, which is connected to a pumping line as well as to a leak valve towards the IRRAS UHV chamber. It can be heated via a heating tape. Before usage in IRRAS measurements, the cysteine is degassed by heating it to 100 °C for two hours, leaving the valve to the vacuum pump open. In this way, residue of water is removed. For dosing cysteine to the main chamber, it is heated to 120 °C to 140 °C and the valve to the pumping line is closed. Cysteine is dosed via the leak valve to the main chamber.

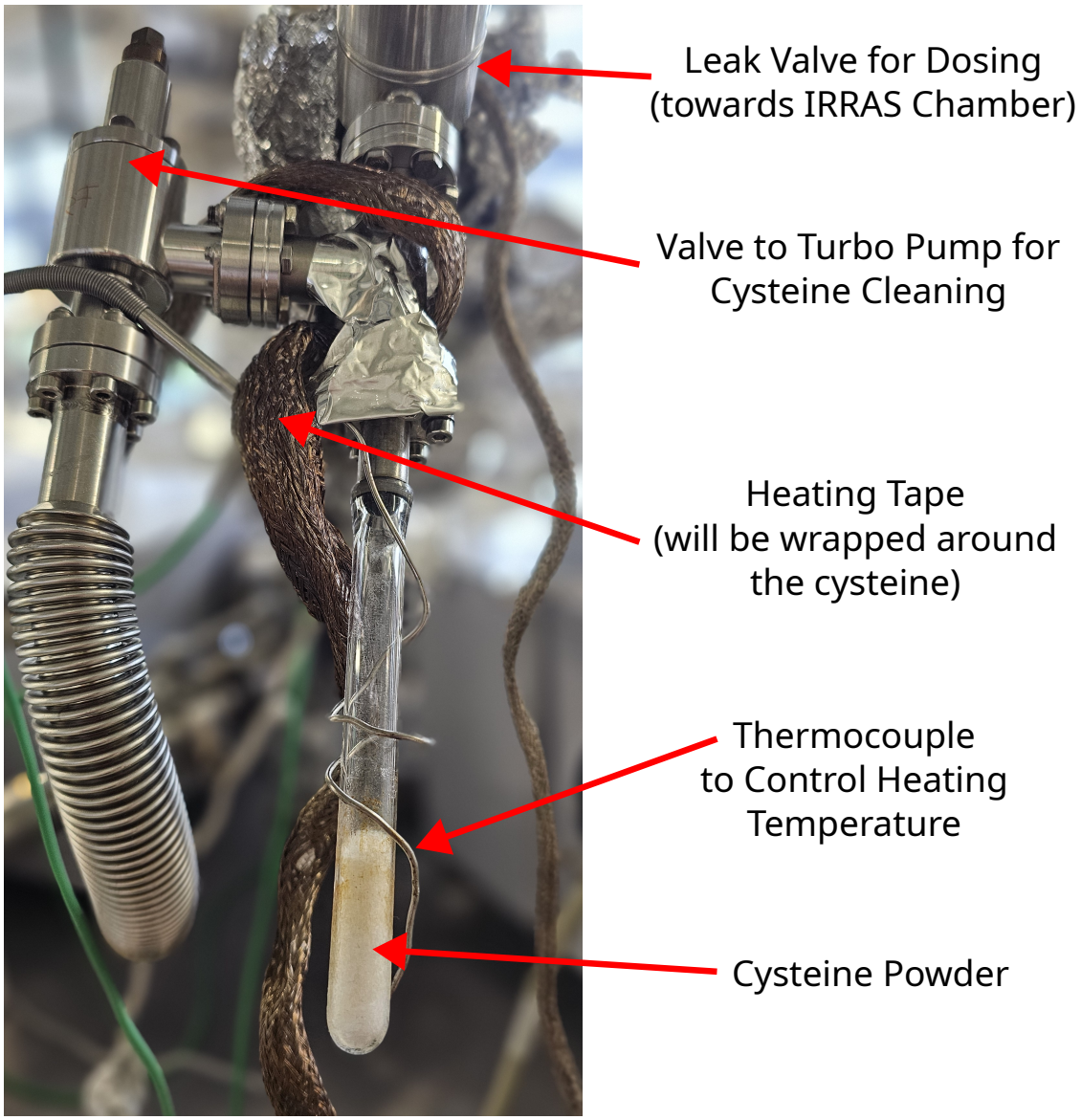


Figure 4.4: Cysteine dosing setup: Cysteine is in a glass vial, connected to a UHV pumping system. The valve to the pump can be closed, and cysteine can be dosed via a leak valve into the main IRRAS chamber. The heating of the powder is done by wrapping the vial with a heating tape and controlling the temperature via a thermocouple.

4.1.2 XPS

The XPS setup at DESY NanoLab [46] can be seen in Figure 4.5. A SPECS FOCUS 500 Al Kα source (1486 eV) is used in combination with a SPECS PHOIBOS 150 2D-DLD hemispherical analyzer. The UHV chamber is kept at a base pressure of less than 10^{-10} mbar.

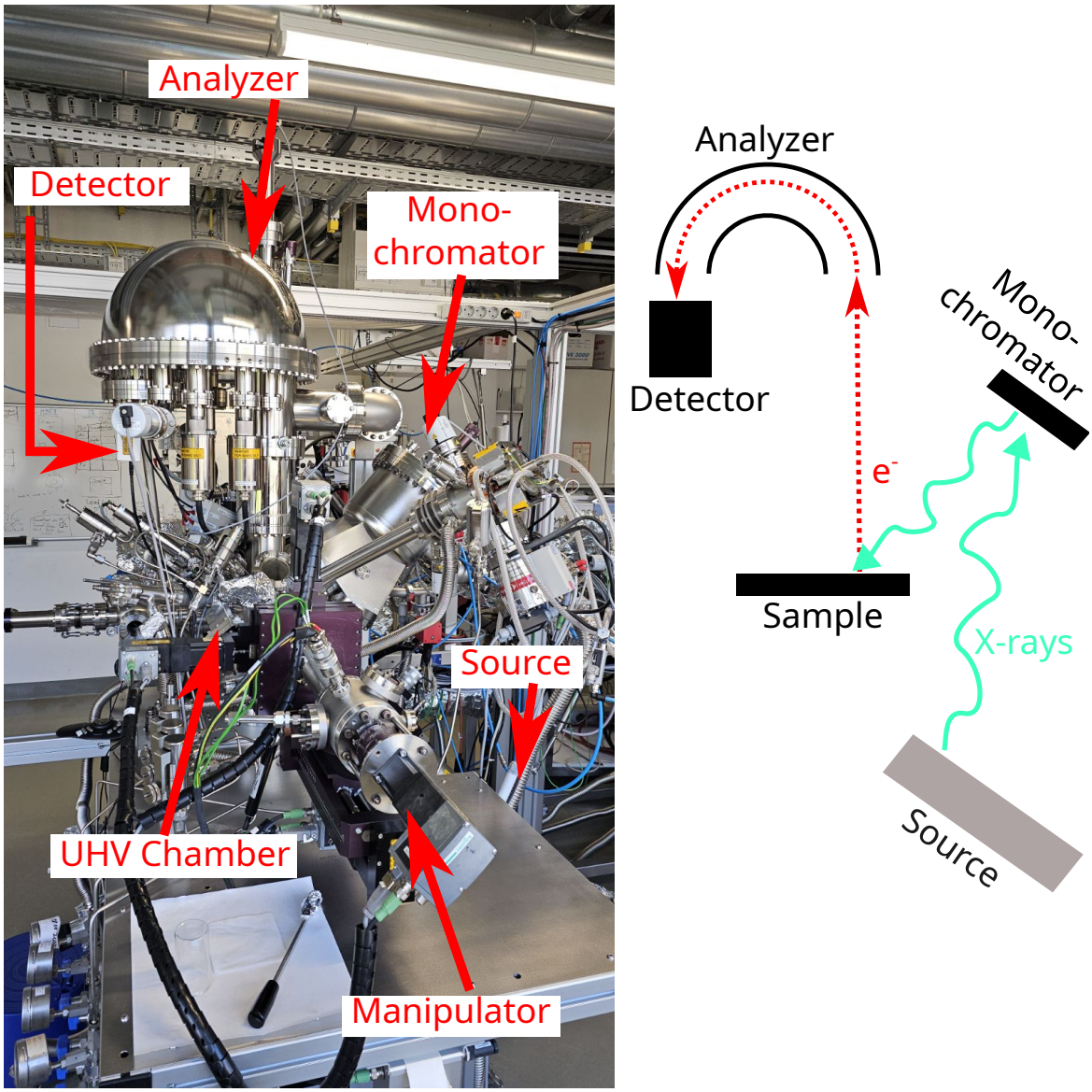


Figure 4.5: The XPS Setup in the UHV lab at DESY NanoLab [46], actual image and schematic drawing.

4.1.3 Growth Chamber

The sample preparation and NP growth are done in one of the two growth chambers at NanoLab. Both feature sample heating up to 1100 °C, gas dosing systems for Ar and O_2, low energy electron diffraction (LEED) and Auger electron spectroscopy (AES) setups and several differently loaded molecular beam epitaxy (MBE) evaporators. The evaporators used in this thesis are of type FOCUS EFM3, either employing a Cu rod or Cu in a crucible. Sample heating is done either by filament heating or by e-beam heating. The former applies electrical current through a thin tungsten filament behind the sample holder, heating it resistively. The latter applies a voltage between the filament and the sample holder. This leads to electrons being ejected from the filament, accelerated and then absorbed by the sample holder, producing heat by their kinetic energy.

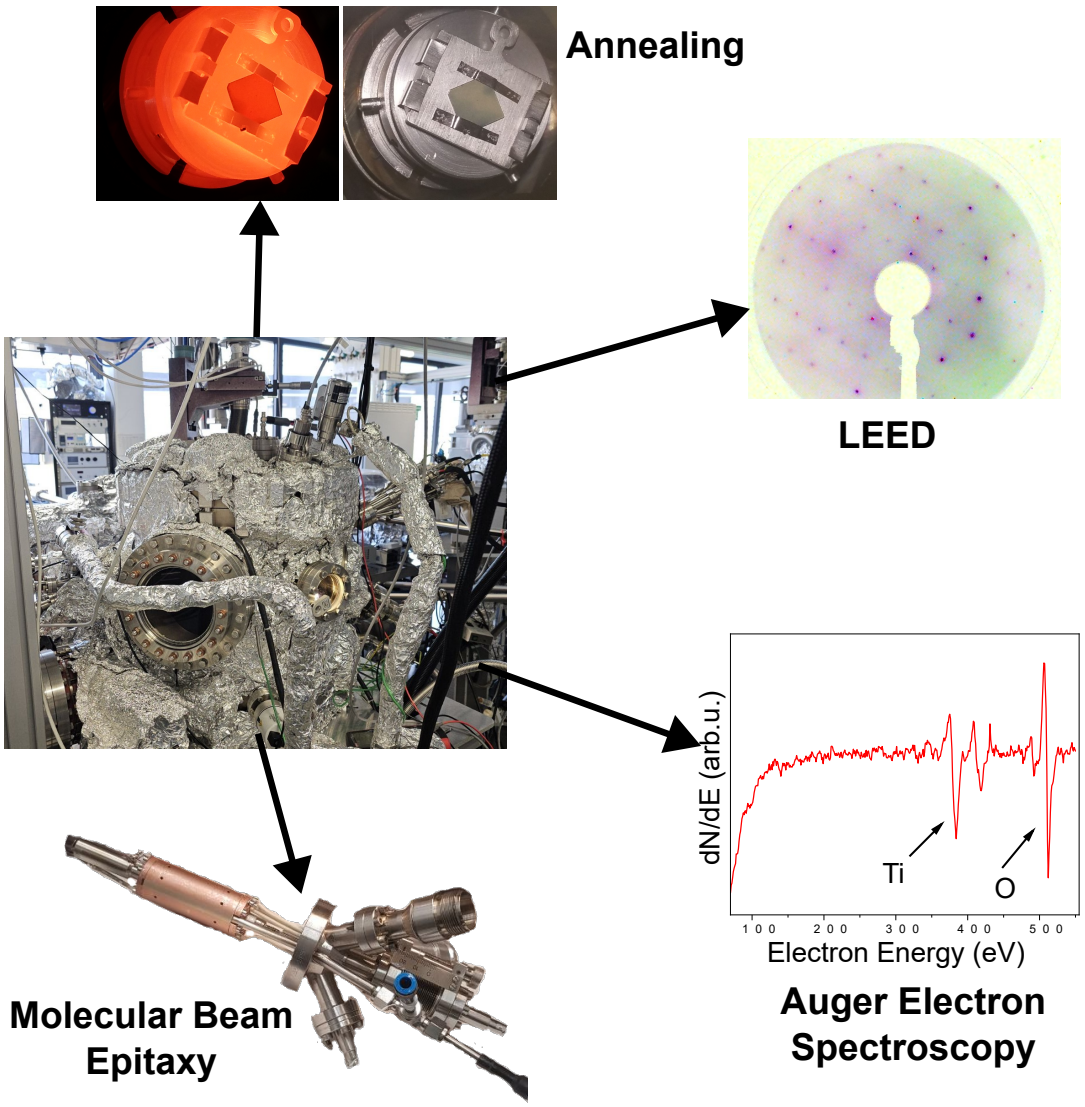


Figure 4.6: One of both growth chambers at NanoLab. The chamber is equipped with a LEED/AES system, a sputter gun, a sample heating station, several gaslines (typically used for O_2 and Ar) and three different MBE evaporators (Cu, Fe and Pd/Pt/Rh).

4.2 SEM

SEM images were obtained in the secondary electron mode with a field emission instrument at an accelerator voltage of 5 kV, providing a nominal lateral resolution of 1.3 nm.

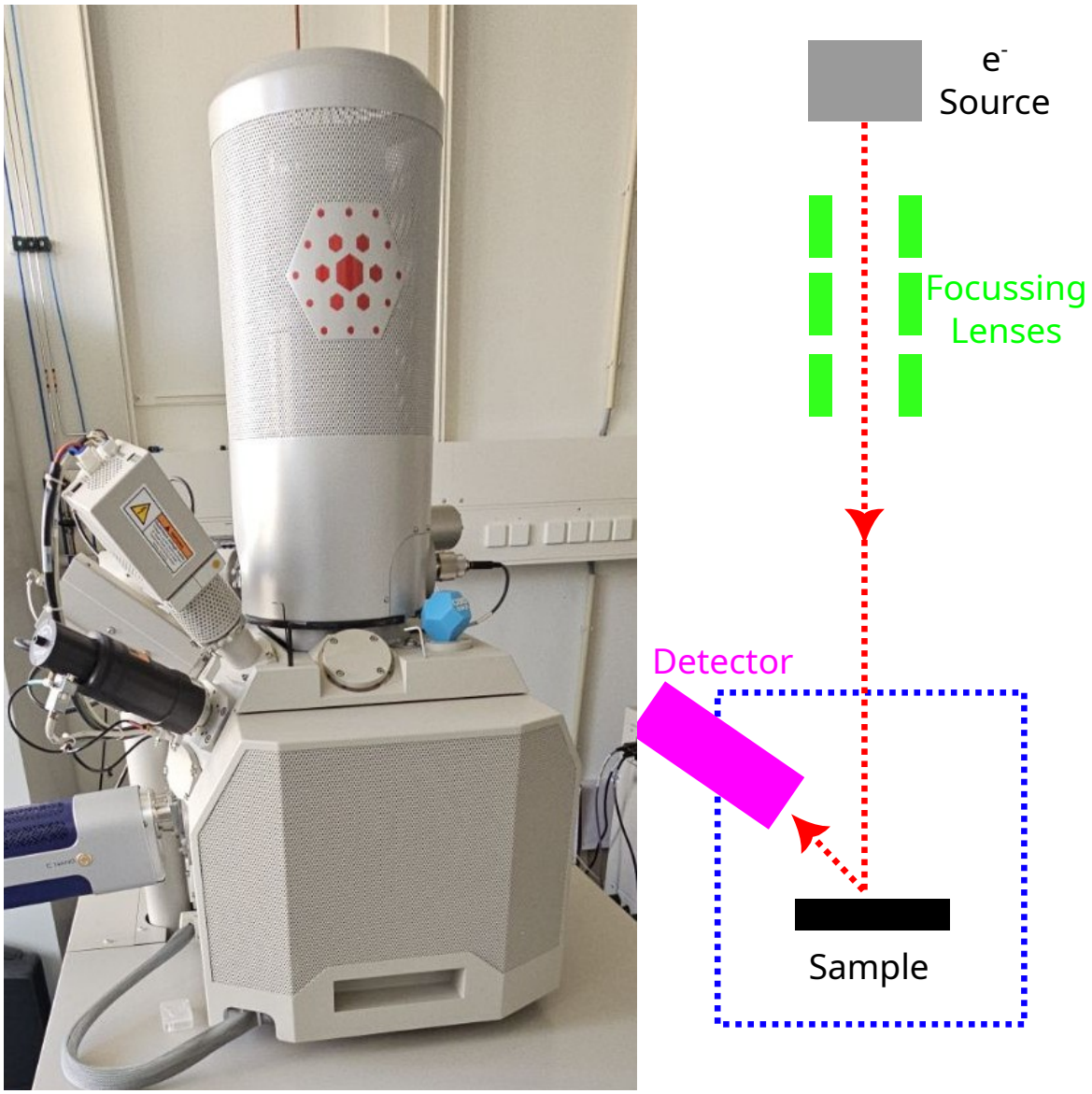


Figure 4.7: SEM setup at DESY NanoaLab [46], along with a schematic drawing.

4.3 SAM

SAM measurements were done using a PHI 710 Scanning Auger Nanoprobe instrument at an acceleration voltage of 20 kV with a nominal lateral resolution of 8 nm. An image of the instrument can be seen in Figure 4.8.

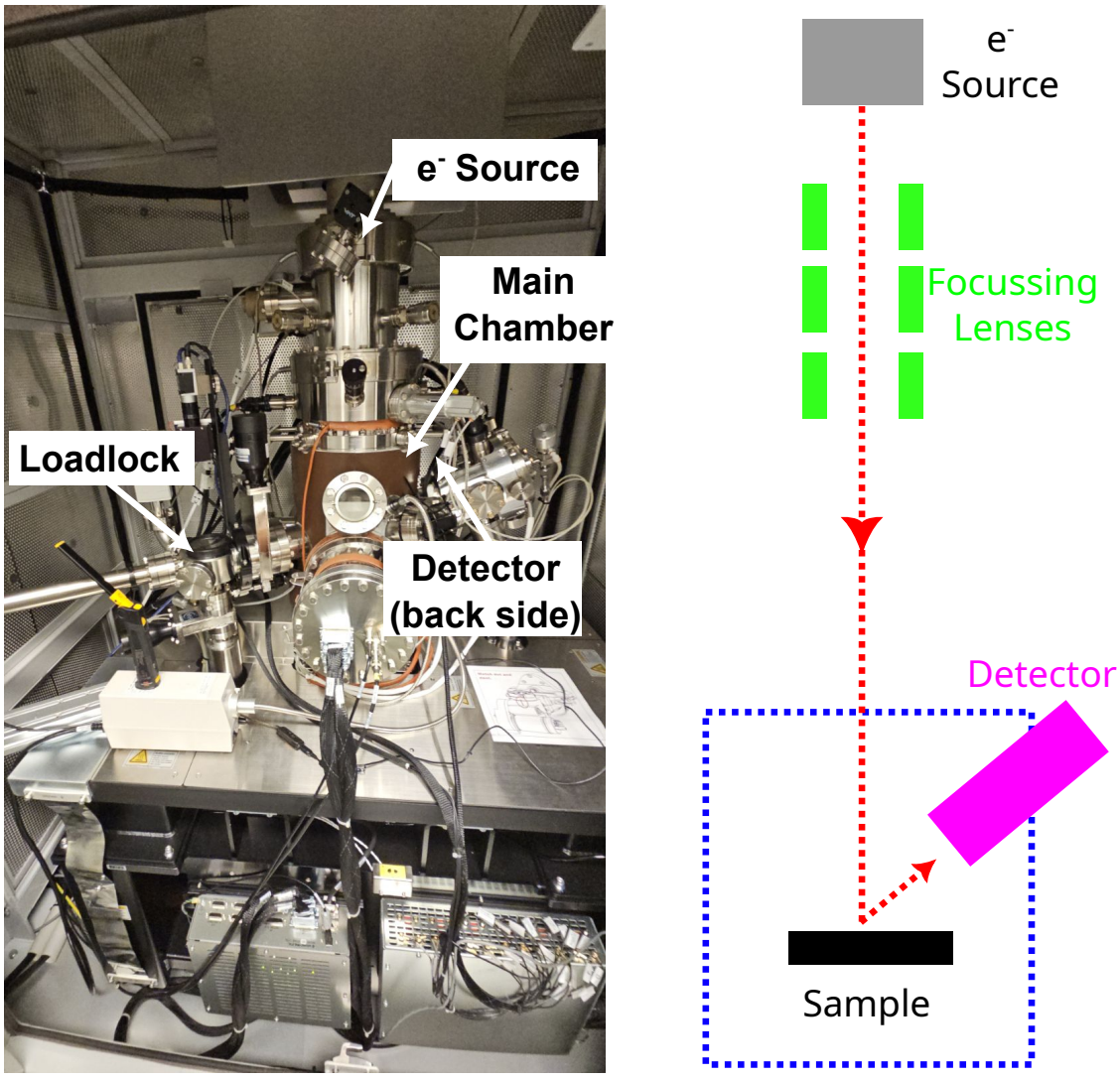


Figure 4.8: The SAM setup at DESY NanoLab and a schematic drawing.

4.4 PETRA III P23

The PETRA III beamline P23 is dedicated to surface and grazing-incidence X-ray diffraction. It features photon energies between 5 keV and 30 keV, a heavy-duty six-circle diffractometer and a 2D LAMBDA pixel detector with GaAs sensor. For the experiments conducted throughouth this thesis, a mobile UHV chamber from NanoLab was placed on the heavy duty diffractometer, see Figure 4.9. The chamber is equipped with a Be window (beryllium is transparent to X-rays) and a Cu MBE evaporator. Moreover, the chamber features sample heating and can be flooded with gases up to ambient pressure (about 1 bar). As a result, this setup enabled the study of Cu NP growth under UHV by GIXRD, as well as the subsequent oxidation under controlled O_2 pressure.

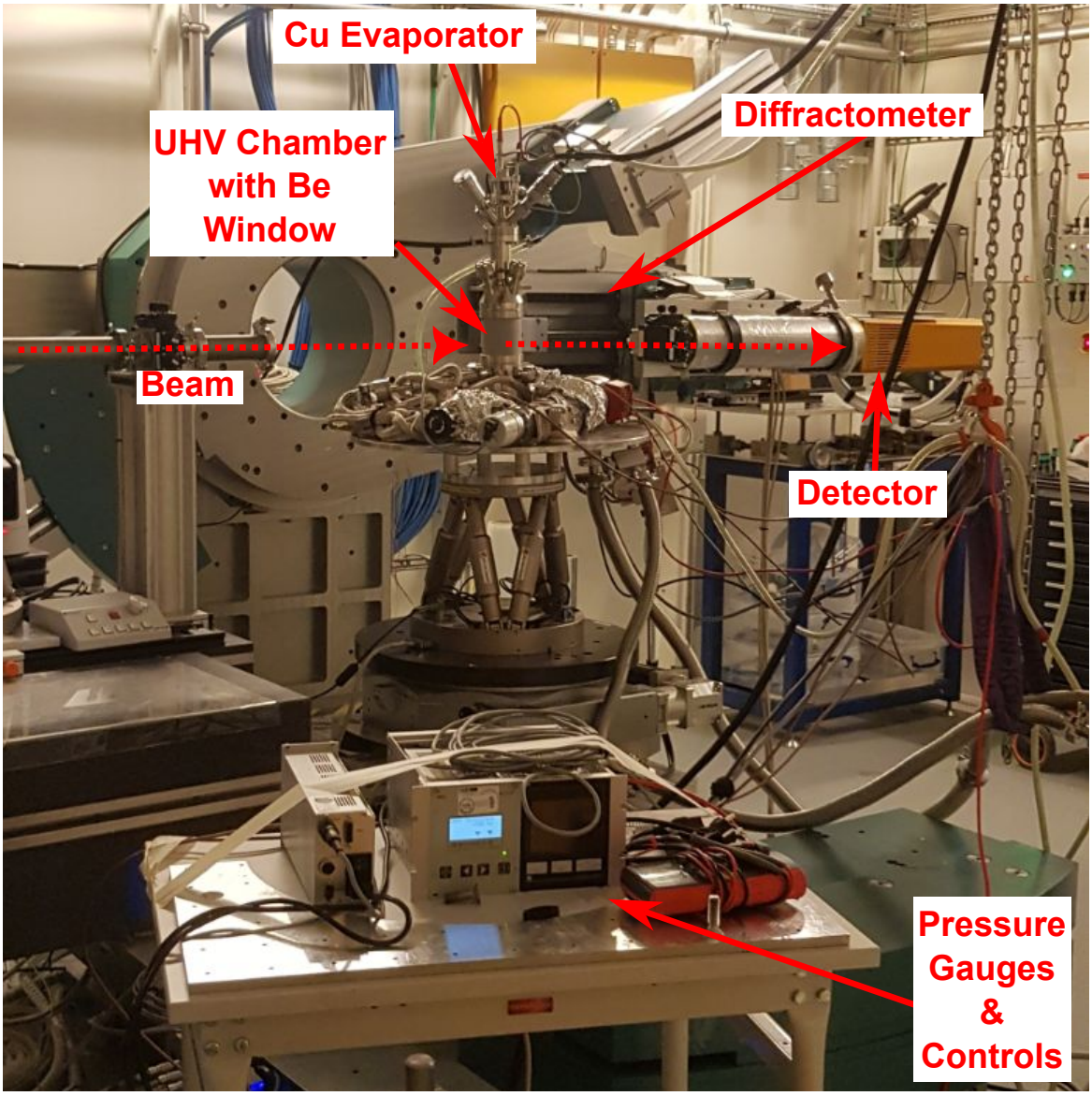


Figure 4.9: Experimental setup at PETRA III beamline P23: a mobile UHV chamber is placed on the diffractometer. The chamber has a Beryllium window (transparent to X-rays) and a Cu MBE evaporator is mounted on-top. The diffracted signal is detected with a 2D GaAs detector.

4.5 Petra III P07

Beamline P07 at PETRA III is dedicated to HEXRD [42]. To this cause, photon energies of 40 keV to 150 keV are used in combination with a large 2D-detector, see Figure 4.10. For the studies in this thesis, a Varex XRD4343CT amorphous silicon flat panel detector with CsI scintillator was used and the samples were placed in air on the diffractometer.

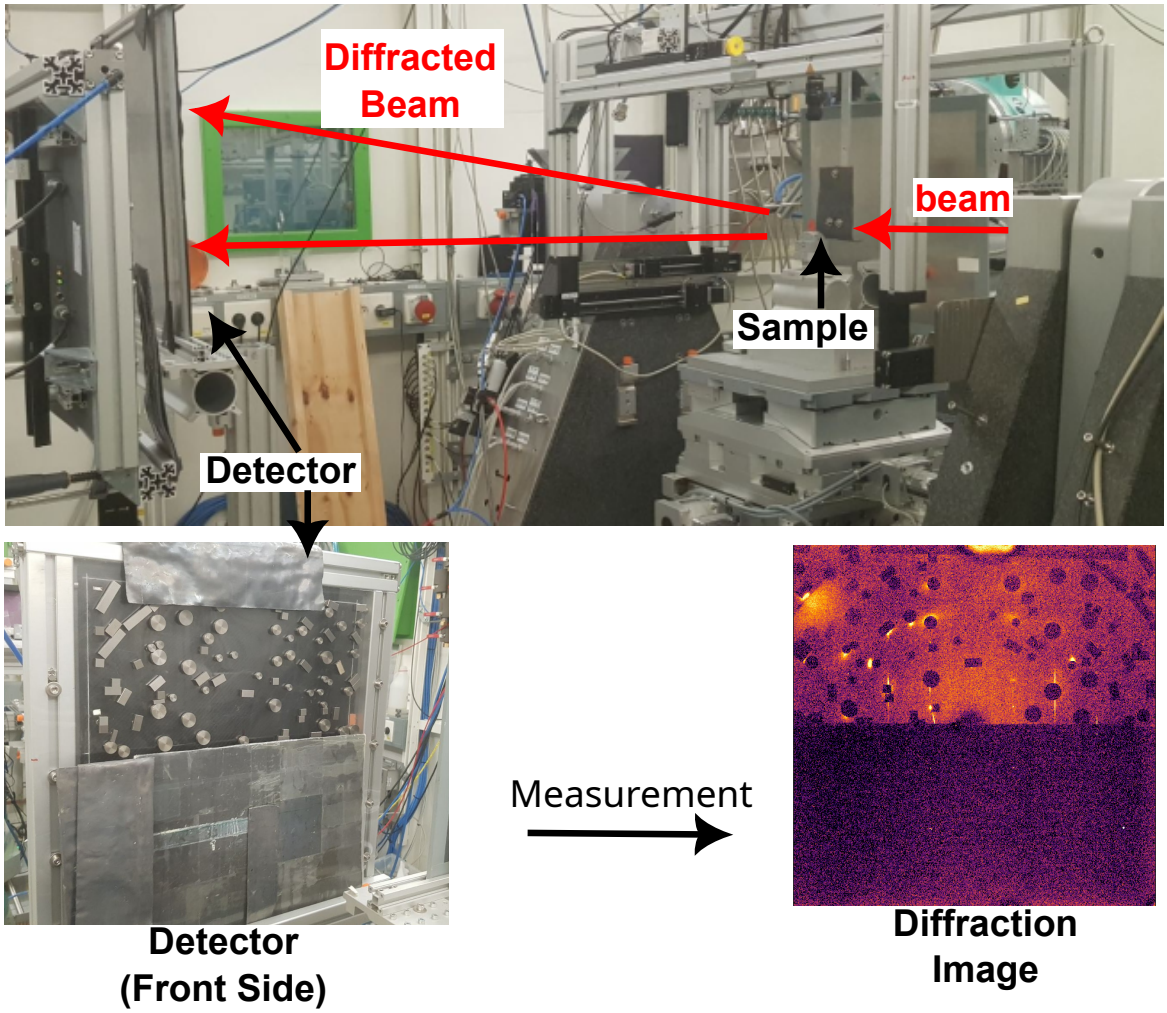


Figure 4.10: The HEXRD setup at PETRA III beamline P07: The sample is placed in air on a movable stage. The detector is a Varex pixel detector. The substrate Bragg peaks have to be covered with lead or tungsten beamblocks on the detector to avoid oversaturation.

4.6 Petra III P22

Beamline P22 at PETRA III features a Hard X-ray Photo Electron Spectroscopy (HAXPES) endstation. The setup and working principle are almost the same as for a conventional XPS, see Figure 4.11, but instead of an Al K_α source the radiation is produced in the synchrotron, with photon energies between 2.4 keV to 15 keV [43].

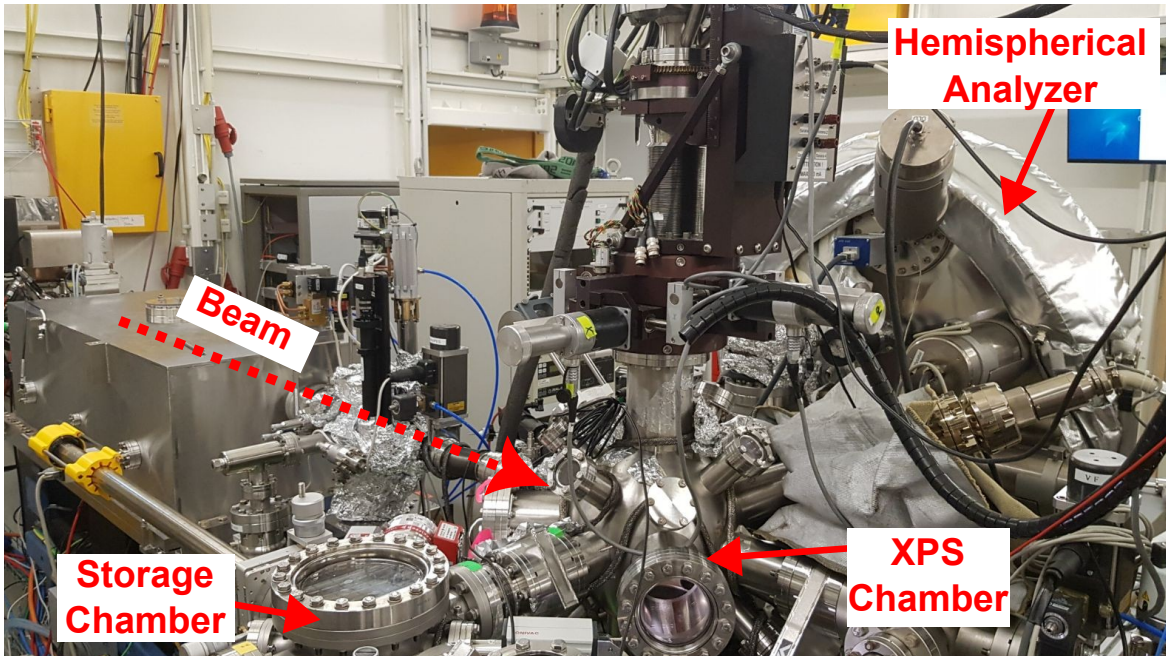


Figure 4.11: The experimental setup at PETRA III beamline P22, HAXPES endstation. The setup is very similar to a conventional XPS (see Figure 4.5, but instead of an Al K_α source synchrotron radiation is used. The setup features a hemispherical analyzer and a storage chamber for samples in UHV.

4.7 Sample Preparation

The sample preparation followed the same formula for all samples, with differences found for rutile and anatase substrates. An overview can be seen in Figure 4.12.

Pre-Cleaning of the Crystals The rutile and anatase crystals used are commercially available and are cut and polished to a nominal miscut smaller than 0.5 °. Before the samples were inserted into the UHV system, they were cleaned in an ultrasonic bath in acetone, ethanol, isopropanol and de-ionized water for 15 minutes in each solvent. Following this cleaning procedure, they were mounted on molybdenum sample holders by spot welding them with tantalum clips.

Sputter-Annealing In the UHV system, the single crystals were sputter-annealed to produce clean and flat surfaces. Sputtering was always done at 1 kV acceleration voltage, 10 mA emission current, 10^{-6} mbar Ar pressure and about 2 μA drain current, for 10 minutes. Sputtering and annealing were always done alternating. For anatase substrates, annealing was done by heating the crystal to 400 °C in 2×10^{-7} mbar O_2 for 10 minutes, then to 650 °C in UHV for 15 minutes. This cycle was repeated six times. For rutile substrates, the samples were annealed to 800 °C for 15 minutes in UHV for two cycles. Then, annealing to the same temperature for the same time was done in 10^{-6} mbar O_2, followed by another cycle of UHV annealing. The fifth annealing cycle was in UHV again (to 800 °C), but after 15 minutes 10^{-6} mbar O_2 were introduced during the sample cool down. After the fifth cycle, the rutile crystals were not sputtered again, but annealed in UHV for 10 minutes to 420 °C.

Crystal Check After the sputter-annealing, the success of the preparation was evaluated by LEED or by scanning tunneling microscopy. The LEED signal should yield the corresponding clean surface pattern (see Figure 3.16) and the STM image should show monolayer steps and terraces.

Cu Growth When the crystal was prepared and tested, Cu was grown via MBE. The relevant growth parameters, sample temperature and the amount of deposited Cu (which is the product of deposition time and the Cu flux) were varied for different samples. After growth, the Cu NPs could be investigated via scanning tunneling microscopy or XPS before oxidation.

Oxidation The oxidation of the NPs was done in different ways. The samples coud be taken out of UHV and be stored in air for hours or days to oxidize the NPs, or a UHV chamber could be flooded with up to 1 bar molecular O_2 for hours. Finally, some samples were annealed in a tube furnace in air to achieve even stronger oxidation.

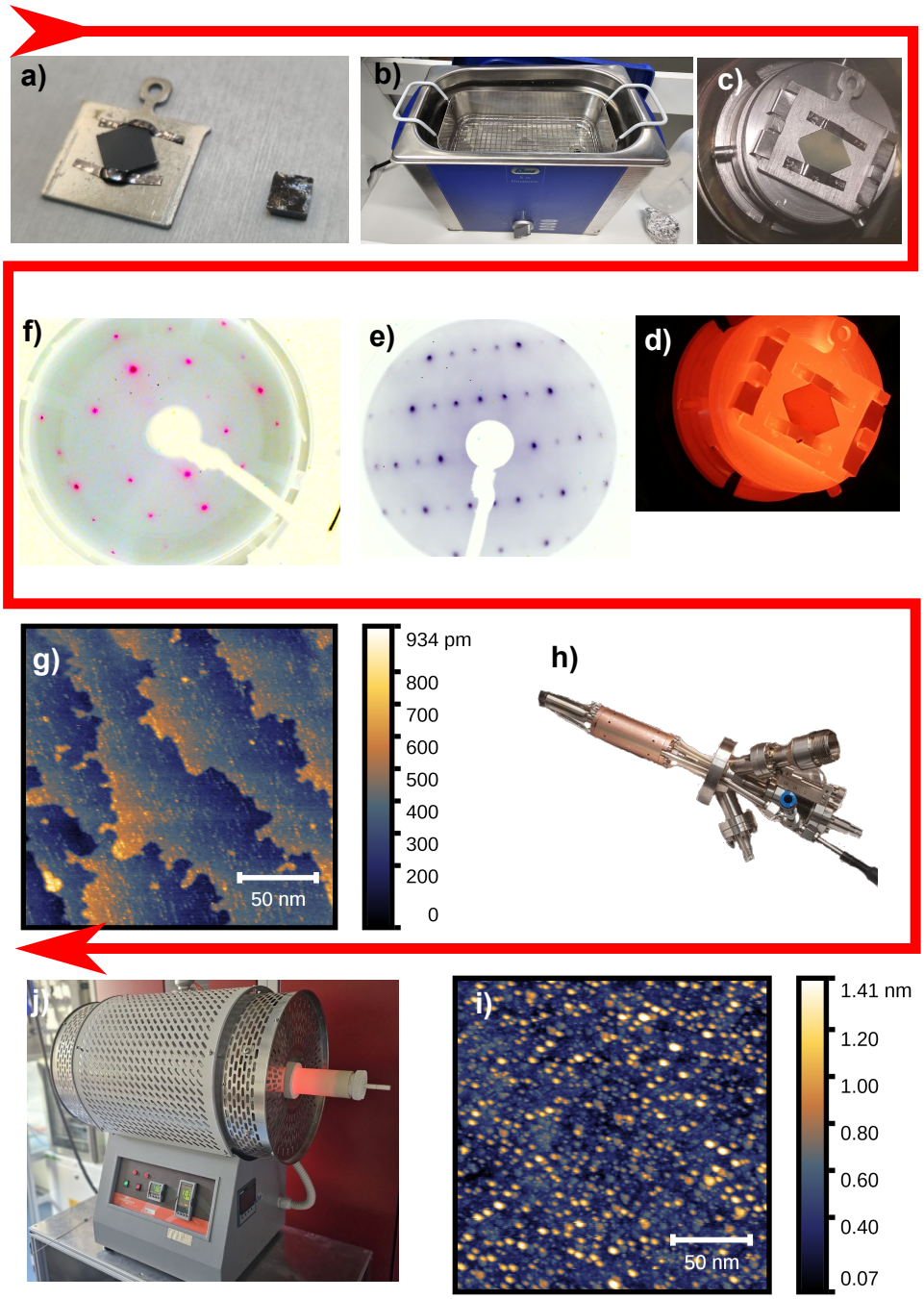


Figure 4.12: The sample preparation procedure - the red line is the timeline the procedure follows. a) A rutile TiO_2 crystal mounted with Ta clips on a Mo sample holder plate (the crystal appears black in the image, but is actually transparent) and an anatase $TiO_2(110)$ crystal. b) Ultrasonic bath for cleaning of the crystals. c) Mounted rutile $TiO_2(110)$ crystal inside an UHV chamber. d) The same crystal during annealing in a sputter-annealing cycle. e) LEED pattern of a clean rutile $TiO_2(110)$ crystal. f) LEED pattern of a clean anatase $TiO_2(101)$ crystal. g) Scanning tunneling microscopy image of the clean rutile surface with monolayer steps visible. h) MBE evaporator for Cu deposition. i) STM image of Cu NPs after deposition. j) The tube furnace used for annealing in air.

4.8 Photocatalysis & Light Exposure

For the photocatalytic experiments, the samples were taken out of UHV and exposed to ambient conditions. This was done in steps of 30 minutes exposure to air. The samples were either kept in dark conditions during their time in air, or were specifically exposed to either white light or UV light. The setup for the ambient exposure consisted of a box with an aluminum lid, where the samples could be placed to avoid the influence of ambient light. Inside the box, either a UV lamp (HeroLab UV-6L) or a white broadband LED (ThorLabs MBB1L3 with a 450 nm cutoff filter) could be directed at the sample. The setup can be seen in Figure 4.13. The lamp spectra can be seen in Figure 4.14.

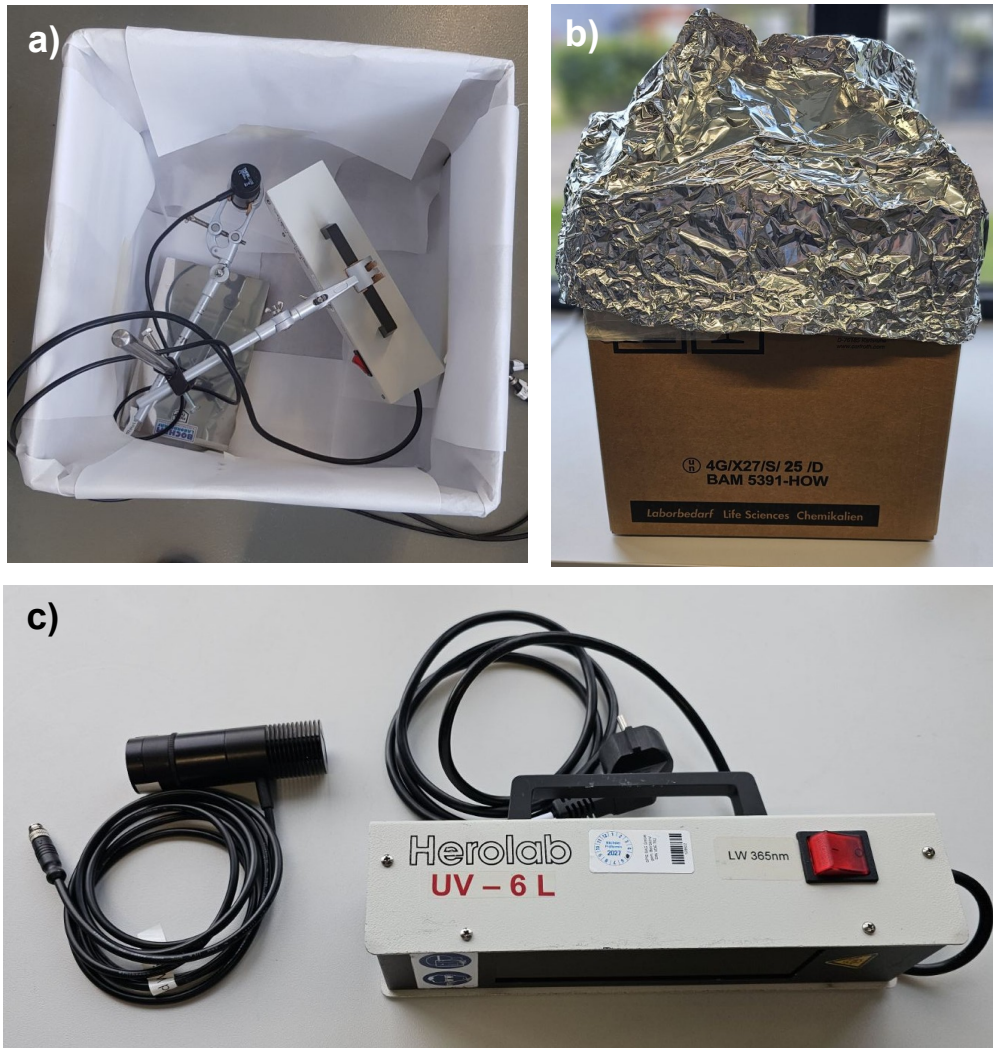


Figure 4.13: The setup used for photocatalytic light-exposure experiments. a) Top-down look into the box for light exposure: the sample is placed at the bottom, light sources can be directed at it. b) The box is closed with an aluminum cover once the sample is in to avoid exposure to ambient light. c) The two lamps used: ThorLabs MBB1L3 broadband LED and HeroLab UV-6L.

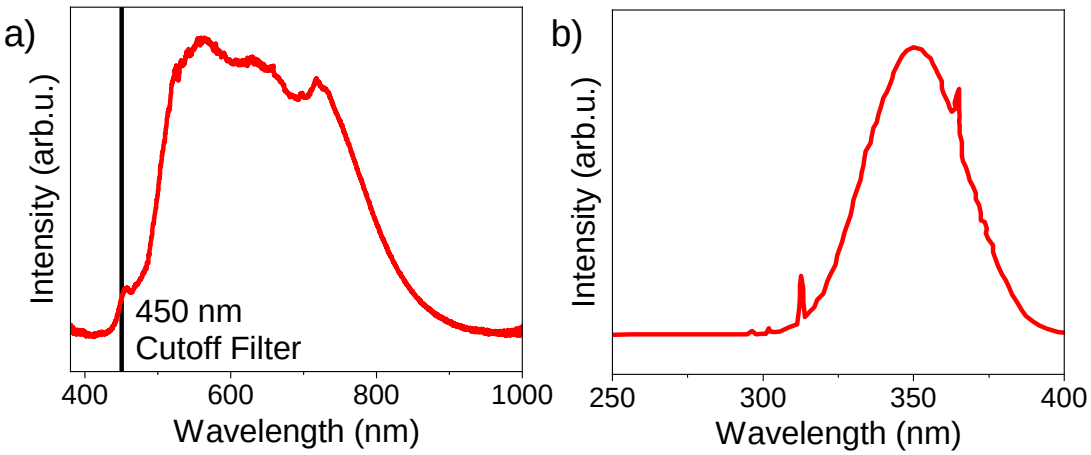


Figure 4.14: Spectra of the two light sources used. a) ThorLabs MBB1L3 Broadband LED, spectra reproduced from [48]. A 450 nm cutoff filter was used additionally to avoid light close to the TiO_2 bandgap (∼380 nm). b) Herolabs UV-6L, spectrum reproduced from [17].

Chapter 5

Article I: In-Situ Growth and Oxidation of Cu Nanoparticles on Rutile TiO_2(110)

THE JOURNAL OF PHYSICAL CHEMISTRY C
A JOURNAL OF THE AMERICAN CHEMICAL SOCIETY

Open Access
This article is licensed under CC-BY 4.0

pubs.acs.org/JPCC
Article

In-Situ Growth and Oxidation of Cu Nanoparticles on Rutile TiO_2(110)

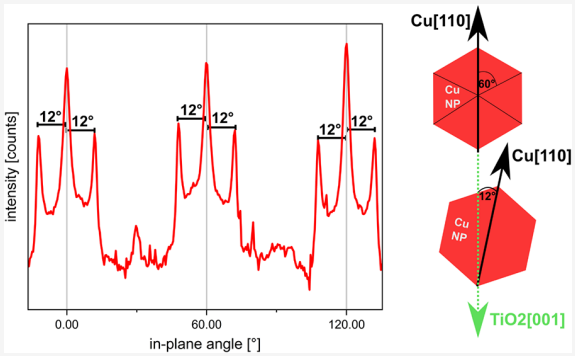
Daniel Silvan Dolling, Miguel Blanco Garcia, Mona Kohantorabi, Yufeng Zhai, Benedikt Sochor, Mohammad Ebrahim Haji Naghi Tehrani, Jan-Christian Schober, Ming-Chao Kao, Jagrati Dwivedi, Arno Jeromin, Olof Gutowski, Dmitri V. Novikov, Thomas F. Keller, Stephan V. Roth, Andreas Stierle,* and Heshmat Noei*

Cite This: J. Phys. Chem. C 2026, 130, 7136−7147

Read Online

ACCESS | Metrics & More | Article Recommendations | Supporting Information

ABSTRACT: Copper (oxide) nanoparticles on TiO_2 substrates are of interest for various applications, ranging from waste cleaning to photocatalytic virus inactivation. We studied the growth and oxidation of Cu nanoparticles (NPs) on single crystalline rutile TiO_2(110) using X-ray grazing incidence diffraction and small angle scattering (GIXRD, GISAXS) and X-ray photoelectron spectroscopy (XPS) methods, complemented by scanning Auger electron microscopy (SAM) and scanning electron microscopy (SEM). Cu NPs were grown via physical vapor deposition under ultrahigh vacuum (UHV) conditions at different temperatures. We found that higher growth temperatures result in not only larger NPs but also different NP epitaxy. The particle's shape and size were studied with SAM, SEM, GIXRD, and GISAXS, revealing homogeneous size distributions and oxidation states across the whole surface. It was found that the particles either fully oxidize to a mixture of CuO and Cu_2O or form core−shell particles with a metallic Cu core and an oxide shell after oxidation at 1 bar O_2 and exposure to ambient (atmospheric) conditions. With the exception of minor amounts of Cu_2O(111), all of the other oxides are amorphous. Testing the long-term stability of the NPs revealed that their oxidation state at different oxidation times (beyond the initial oxidation) did not change, confirming the stability of the NPs under ambient conditions.



1. INTRODUCTION

Copper and copper oxide nanoparticles (NPs) on TiO_2 are of interest for various applications, especially for photocatalytic inactivation of viruses and bacteria as well as for the degradation of environmental pollutants.[1−6] It has been shown that visible light activity can be achieved by the addition of Cu and Cu oxide nanoparticles to TiO_2 and that these systems can be used for bacteria and virus inactivation.[2,5,7−11] TiO_2 itself is one of the most well-known photocatalysts and has been extensively studied since the discovery of its photocatalytic activity in 1972.[12] It is an abundant material[13] and offers good chemical stability.[13] The use of TiO_2 in coatings and as a catalyst is safe, as dermal contact poses no risks to humans.[14] The use of Cu and Cu oxide NPs for visible light activity, especially in contrast to the more frequently used combination of noble metal NPs such as Au and Ag[15−17] with TiO_2, provides the distinct advantage of significantly greater availability,[18] which is particularly critical for potential large-scale applications. The oxidation state of Cu is a crucial factor for the performance of the catalyst,[4,7,19,20] resulting in the need for precise control over it. The oxidation of Cu has been extensively studied for thin films and bulk Cu over the past 90 years. Wagner (1936)[21] described the parabolic growth of the oxide layer governed by the diffusion of ions and vacancies through the growing oxide film. Later, Cabrera and Mott (1949)[22] presented the inverse logarithmic rate law for Cu oxidation in thin layers (below 10−20 nm), where the electric potential across the oxide controls the diffusion rate of ions. They estimated that at room temperature, a Cu_2O layer of approximately 3 nm will form before further oxidation is inhibited. The size of the oxide layer was later confirmed.[23,24] A more recent study focusing on the oxidation of a Cu thin film under standard ambient conditions finds a stable Cu_2O layer after 122 days with 5 nm thickness. For nanoparticles, the oxidation behavior can be different: the outcome shows strong dependencies on the NP size, substrate,

Received: February 6, 2026
Revised: April 9, 2026
Accepted: April 10, 2026
Published: May 6, 2026



ACS Publications
© 2026 The Authors. Published by American Chemical Society

https://doi.org/10.1021/acs.jpcc.6c00835
J. Phys. Chem. C 2026, 130, 7136−7147

Downloaded via DEUTSCHES ELEKTRONEN-SYNCHROTRON on May 24, 2026 at 10:13:47 (UTC).
See https://pubs.acs.org/sharingguidelines for options on how to legitimately share published articles.

and temperature, ranging from disordered CuO[25] over Kirkendall voids[26,27] to stable core−shell particles.[25,27] To date, no study has explicitly investigated the oxidation of Cu NPs on oxide surfaces.

Rutile TiO_2 features a body-centered tetragonal unit cell with a_{rutile} = 4.59 Å, c_{rutile} = 2.95 Å,[28] space group $P4_2/mnm$. The rutile $TiO_2(110)$ surface has a rectangular face-centered surface lattice with lattice constants $a_{rutile,surface} = \sqrt{2} \times a_{rutile}$ = 6.49 Å and $c_{rutile,surface} = c_{rutile}$ = 2.95 Å. Cu features a face-centered cubic (fcc) crystal system with the lattice parameter a_{Cu} = 3.62 Å,[29] space group $FM\bar{3}m$. (111)-oriented Cu can be described in a hexagonal surface system, where $a_{Cu,hexagonal\ surface} = \frac{a_{Cu}}{\sqrt{2}}$ = 2.56 Å and $c_{Cu,hexagonal\ surface} = \sqrt{3} \times a_{Cu}$ = 6.27 Å. Cu_2O crystallizes in a cubic lattice, where oxygen atoms are at the lattice points and the Cu atoms form an inset fcc lattice shifted by $\left(\frac{1}{4}, \frac{1}{4}, \frac{1}{4}\right)$ (cuprite structure), space group $Pn\bar{3}m$. The lattice constant is a_{Cu_2O} = 4.27 Å.[30] CuO forms a monoclinic lattice with a = 4.67 Å, b = 3.48 Å, c = 5.12 Å, $\alpha = \gamma = 90°$, and β = 98.60°,[31] space group $C2/c$.

It is known that Cu exhibits 3D island growth on several oxide single crystals[32−35] and that the NP size can be controlled via growth temperature.[36] At 187 °C growth temperature, Cu on rutile $TiO_2(110)$ results mostly in (111)-oriented particles with $Cu(220)/TiO_2(001)$ epitaxy and minor amounts of (112) orientation.[37] Similar results are reported for the growth of Cu on ZnO(0001),[38] where Cu was found to grow mainly (111)-oriented. In contrast to the growth of other 3d metals on metal oxide surfaces,[39] Cu is not known to form subsurface species.[35,40]

The key unresolved questions regarding the Cu(oxide)/TiO_2 system include, on one hand, how growth conditions influence the resulting epitaxy of the NPs and, on the other hand, how the epitaxy of the NPs impacts their oxidation. To systematically study the effect of the growth parameters on the Cu NPs and subsequently their oxidation, we employ in situ grazing incidence X-ray diffraction (GIXRD) at beamline *P*23 at the PETRA III synchrotron inside a vacuum growth chamber.[41] This chamber can be flooded with up to 1 bar of pure O_2, allowing the study of nanoparticle oxidation by using X-ray diffraction. Furthermore, to understand the oxidation over time scales of several days at ambient conditions, we employ high-energy X-ray diffraction (HEXRD) at the high energy materials science beamline P07 at the PETRA III,[42] grazing-incidence small-angle X-ray diffraction (GISAXS) at the micro- and nanofocus X-ray scattering beamline P03[43] at PETRA III, and X-ray photoelectron spectroscopy (XPS), scanning Auger microscopy (SAM), and scanning electron microscopy (SEM) at DESY NanoLab.[44]

2. METHODS

All experiments were performed at DESY Nanolab,[44] PETRA III beamline *P*23, PETRA III beamline P03,[43] and PETRA III beamline P07-DESY.[42] The nanoparticles were grown in a mobile UHV chamber with an electron beam evaporator by using a Cu rod at beamline *P*23. The rutile $TiO_2(110)$ crystals were prepared in a UHV system before being inserted into the mobile UHV chamber.[41] They were cleaned four times in an ultrasonic bath: first in acetone, then in ethanol, afterward in isopropyl, and finally in deionized water and then introduced to a UHV system. They were sputtered at 1 kV acceleration voltage, 10 mA emission current, and 10^{-6} mbar Ar and subsequently annealed at 800 °C six times: three times with UHV annealing, once with annealing in 1×10^{-6} mbar O_2, once with annealing in UHV, and finally once with annealing in UHV and cooling down in 1×10^{-6} mbar O_2. Afterward, the sample was flashed to 420 °C in UHV. The substrate crystals were brought to the mobile UHV chamber under ambient conditions and were degassed for 5 min at 450 °C after inserting them into UHV again. High-purity oxygen (99.999%) was used for sample preparation. The XRD measurements at beamline *P*23 were done at a photon energy of 18 keV. High Energy X-ray Diffraction (HEXRD) measurements were performed at the PETRA III beamline P07 at 73.34 keV and an incidence angle of 0.03°. Scanning electron microscopy (SEM) images were obtained in the secondary electron mode with a field emission instrument at an accelerator voltage of 5 kV, providing a nominal lateral resolution of 1.3 nm. For XPS measurements, the X-ray source employed was Al Kα at 1.486 keV and a hemispherical energy analyzer with a base pressure of 1.2×10^{-10} mbar. All XPS spectra were fitted by CasaXPS software[45] with a Shirley background and a Gaussian−Lorentzian line profile, employing the Marquardt fitting algorithm. Peak position and fwhm were constrained; see SI for details. All spectra were normalized by setting the Ti $2p_{3/2}$ position to 458.7 eV. GISAXS measurements were performed at the Petra III P03 beamline at a photon energy of 12.1 kV with a 30 μm beam diameter at a detector distance of 4.18 m and an incidence angle of 0.4°. In order to study the NP morphology, different spots of the sample were imaged, moving the sample perpendicular to the beam and using 0.1 s illumination. The data were analyzed by using a convolutional neural network (CNN); details can be found in the SI. Scanning Auger Microscopy (SAM) measurements were done using a PHI 710 Scanning Auger Nanoprobe instrument at an acceleration voltage of 20 kV with a nominal lateral resolution of 8 nm.

3. RESULTS

3.1. Cu Nanoparticle Growth

We investigated the epitaxial growth of Cu NPs on rutile $TiO_2(110)$ single crystals by in situ GIXRD. Cu was thermally evaporated onto the crystal in an ultrahigh vacuum (UHV) chamber with a base pressure of 3×10^{-10} mbar. Three Cu nanoparticle samples were grown at different temperatures to evaluate the influence of the growth temperature on the epitaxy and shape of the resulting NPs. Sample A was grown at a 100 °C substrate temperature, sample B at 200 °C, and sample C at 400 °C. After growth, X-ray reflectivity (XRR) measurements were performed to evaluate the amount of deposited Cu. From fits to the reflectivity curves, the NP coverage was evaluated (Table 1). Samples A and B show coverages of about 40%, while sample C shows a coverage of about 10%.

Table 1. Cu Growth and Characterization Parameters[a]

sample	growth temperature [°C]	nominally deposited material [nm]	coverage [%]
A	100	1.2	44
B	200	0.79	38
C	400	0.27	10

[a]The coverage and the nominally deposited material are calculated from XRR data; see Figures S1 to S5.

The epitaxy of the NPs was investigated by in-plane rocking scans, searching for signals from Cu(220), Cu(200), and Cu(111); see Figure 1 and S6−S8. A signal from these scans means that the corresponding crystal planes exist perpendicular to the substrate surface. The combination of the three scans allows for the identification of out-of-plane growth directions as well as in-plane epitaxies, as specific epitaxies feature

https://doi.org/10.1021/acs.jpcc.6c00835
J. Phys. Chem. C 2026, 130, 7136−7147

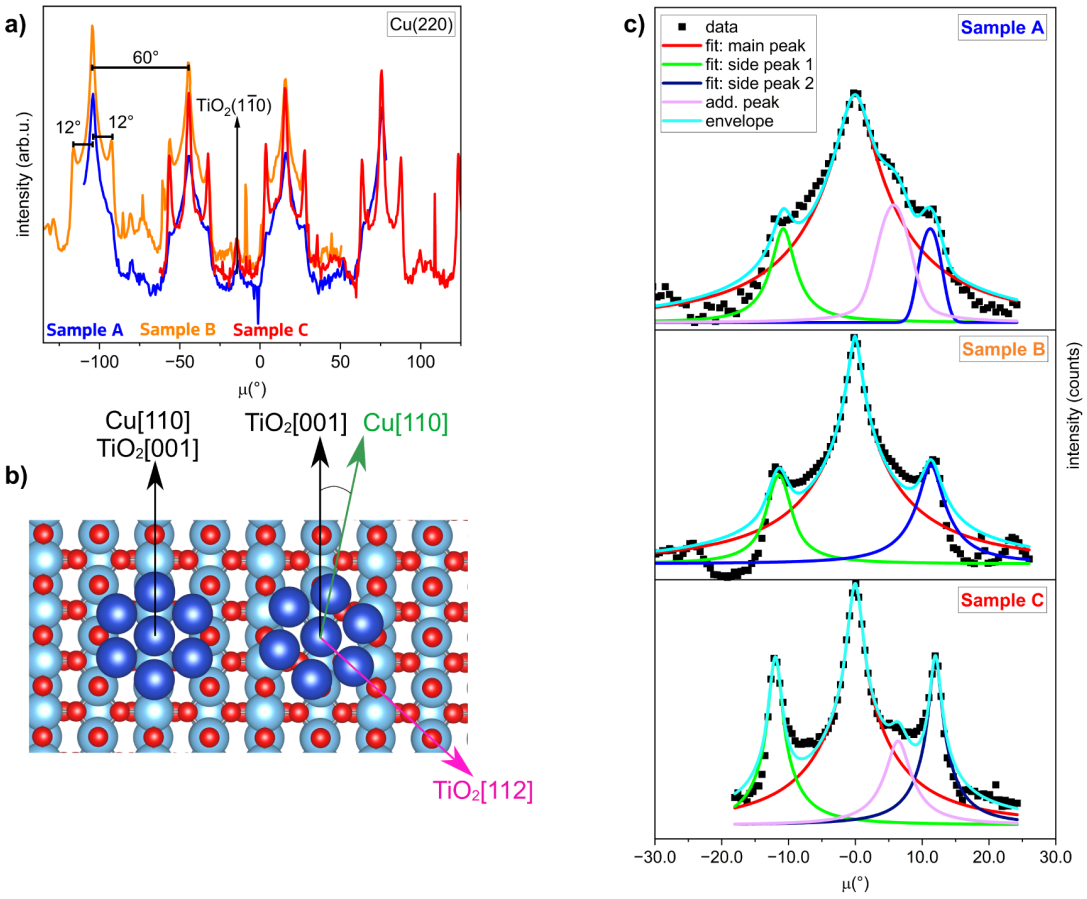


Figure 1. a) In-plane rocking scans set to detect Cu(220) planes. The measurements were taken at a photon energy of 18 keV. For sample B, a different setting of beam slits was used below $\mu = 0$, resulting in a different background and an extra peak at $\sim\mu = -15°$, as well as a higher intensity for the peaks. b) Real-space atomic model of the system: The TiO_2(110) surface (Ti: silver, O: red) and Cu (blue). The left Cu island is oriented in the main growth direction Cu[110]||TiO_2[001], while the right island is 12° tilted away, resulting in the orientation Cu[110]||TiO_2[112]. c) Fits for the "trident" peaks for samples A, B, and C. For samples A and C, a fourth peak (in magenta) had to be used, as the "trident" contains a peak from [100]-oriented NPs (for sample B, the used "trident" peak does not contain this peak).

characteristic angular patterns in the different scans. The scans sensitive to Cu(220) feature a set of peaks with a 60° spacing for all samples. Together with the absence of strong (111) in-plane Bragg peaks, this is characteristic of a Cu[111] out-of-plane orientation with a hexagonal in-plane lattice. Compared to peaks in rocking scans set to detect different planes (Figure S6–S8), this peak exhibits the highest intensity and peak-to-background ratio, supporting its assignment as the primary out-of-plane growth direction for the Cu NPs. The in-plane growth direction, with respect to the substrate crystal, is Cu[110]||TiO_2[001]. Both are in agreement with the literature.[36,37] For all samples, each Cu(220) peak features two distinct new smaller peaks, resembling a "trident", with the outer peaks being ∼12° away from the main peaks. The real-space representation of the corresponding Cu and TiO_2 lattice can be seen in Figure 1. The turning angle of 12° shows a good alignment of the Cu[110] direction with the TiO_2[112] direction. The theoretical angle between TiO_2[112] and TiO_2[001] is 47.7°, which is well in line with the experimental results for the tilted epitaxy angle, 60°−47.7° = 12.3° ≈ 12°. To evaluate the extent of [111]-oriented particles with the previously unreported 12° tilted epitaxy, a "trident" was fitted with three peaks for each sample; see Figure 1. Comparing the area of the main peak with 60° spacing to the side peaks with 12° spacing results in 7.9% ± 4.9% side-peak area for sample A, 7.3% ± 0.9% for sample B, and 21.8% ± 0.8% for sample C. Hence, sample C features the highest fraction of Cu particles showing the tilted epitaxy. Regarding the effect of the growth temperature on the epitaxy, it can be seen that it mainly influences the extent to which the "tilted" particles appear but not which epitaxies occur in general. It should be noted that the Cu(220) in-plane peaks feature not only a "trident" but also a shoulder approximately 6° off the main peaks. This is most likely not related to another in-plane tilt of the [111]-oriented particles, as it is asymmetric with respect to the turning angle and can be attributed to [100]-oriented NPs; see Figure S10. In addition to the primary out-of-plane growth direction of Cu[111], several minor growth directions are found in the in-plane rocking scans: Cu[112], Cu[100], and Cu[110]; details are found in the Supporting Information.

The in-plane and out-of-plane diameters of the particles with Cu[111] out-of-plane orientation and Cu[110]||TiO_2[001] epitaxy on sample A were investigated further by radial scans (see Figure 2 and S26) and linescans through Bragg peaks. For the analysis, hexagonal surface coordinates are introduced for the [111]-oriented Cu. They are denoted by a subscript s in (HKL) notations; the transformation matrix can be found in the SI. The particle sizes resulting from fits of these peaks were calculated with Scherrer's formula $D \approx \frac{2\pi}{\Delta Q}$ and can be seen in

https://doi.org/10.1021/acs.jpcc.6c00835
J. Phys. Chem. C 2026, 130, 7136−7147

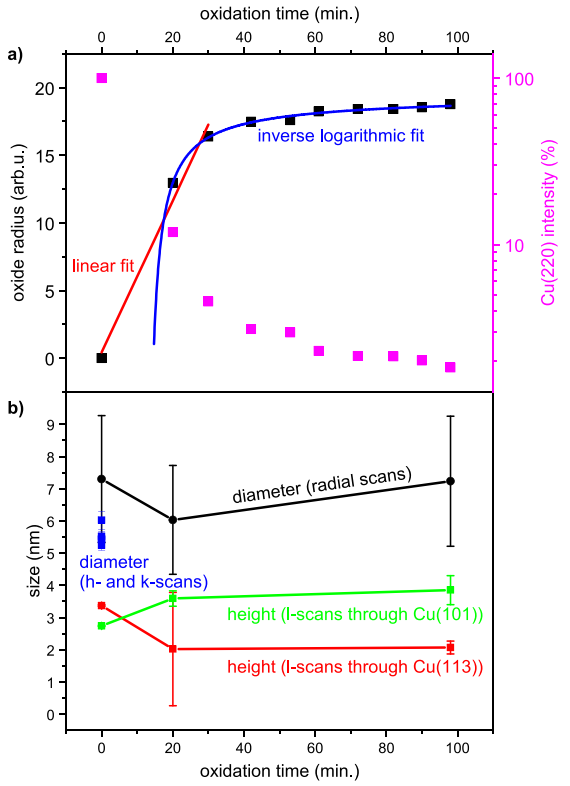


Figure 2. Oxidation kinetics and NP size changes for sample A: a) The oxide radius, as estimated by the intensity of the Cu peak and the percentage intensity of the Cu(220) peak. The fitting parameters can be found in Table S6 and S7. b) Nanoparticle diameter and heights, calculated from (in-plane) radial scans (through Cu(220)) and linescans through Bragg peaks for different oxidation times.

Table 2. The fits can be found in Figure S21, and details on the fitting are provided in the Supporting Information. The

Table 2. Particle Sizes for Sample A, Calculated from Fits of Linescans through the Cu(101)$_s$ and Cu(113)$_s$ Bragg Peak[a]

	particle size (nm)		aspect ratio height/diameter (111)	
scan direction	(101)$_s$ Bragg peak	(113)$_s$ Bragg peak	(101)$_s$ Bragg peak	(113)$_s$ Bragg peak
H_s	6.02 ± 0.28	5.44 ± 0.15	0.46 ± 0.02	0.62 ± 0.02
K_s	5.42 ± 0.07	not measured	0.51 ± 0.01	not measured
$(HK)_s$	5.52 ± 0.15	5.24 ± 0.15	0.50 ± 0.01	0.64 ± 0.03
L_s	2.74 ± 0.02	3.37 ± 0.02	–	–

[a]The L_s scan is orthogonal to the surface, and the other scans are parallel to it.

particles feature diameters (D) between 5.44 ± 0.15 and 6.02 ± 0.28 nm and heights (H) between 2.74 ± 0.02 and 3.37 ± 0.02 nm. From the linescans through the (101)$_s$ Bragg peak, the aspect ratio is calculated to be roughly H/D = 0.5 (see Table 2). A similar aspect ratio is achieved when employing the NP diameters calculated from radial scans; see Table 3. Employing the linescans through the (113)$_s$ Bragg peak, the ratio H/D is approximately 0.6. To evaluate possible size differences for the different epitaxies, a radial scan was done through the large center peak in the Cu(111) rocking scan (attributed to [112]-oriented Cu). Fitting the data results in an average particle size of 6.3 ± 1.0 nm; see the SI for details on

Table 3. Particle Sizes Obtained from Fits for Radial Scans through Cu(220) In-Plane Bragg Peaks as well as the Particle Height as Calculated from Linescans in Out-Of-Plane Direction through the Cu(101)$_s$ Bragg Peak (See Table S3)[a]

	diameter D (nm) (radial scan)	height H (nm)	H/D
before oxidation	7.30 ± 1.97	2.74 ± 0.02	0.38 ± 0.10
20 min in 1 bar O_2	6.03 ± 1.69	3.59 ± 0.24	0.59 ± 0.17
100 min in 1 bar O_2	7.23 ± 2.02	3.85 ± 0.49	0.53 ± 0.16

[a]The corresponding fits can be found in Figures S21 to S27.

the fitting. No significant difference in diameter was observed between the main epitaxy Cu[110]||TiO_2[001] and the minor epitaxy with Cu[112] out-of-plane orientation.

3.2. Nanoparticle Oxidation

The oxidation of the nanoparticles is of particular interest for two reasons: first, metallic Cu is highly susceptible to oxidation under ambient conditions; second, the various oxidation states of Cu nanoparticles on TiO_2 lead to distinct pathways for visible light activity. Therefore, we investigated the oxidation process of Cu NPs under ambient conditions following growth in UHV. The UHV chamber was then exposed to 1 bar of pure oxygen gas for 20−30 min to evaluate the oxidation behavior. Afterward, the chamber was pumped to UHV (base pressure of 1.2×10^{-10} mbar) again, and the samples were analyzed with GIXRD. Samples A and C were exposed to the same oxygen pressure for an additional time, resulting in a total of 100 min exposure. Sample C was heated to 100 °C during this second oxidation. Sample A was analyzed a third time, and all three samples were subsequently brought to ambient atmospheric conditions afterward. The detailed oxidation times for each sample can be found in Table S1.

The existence of the oxide was confirmed by comparing XRR measurements before and after oxidation: for all samples, the nominal thickness increased, indicating that the oxide is formed; see Table S2. To evaluate the possibility of epitaxial oxide, multiple in-plane rocking scans were set to detect different oxide epitaxies; see Figures S16 and S17. In contrast to investigations of similar systems where epitaxial Cu_2O was detected,[46] epitaxial oxide was not found here.

The change in the Cu signal was monitored for each oxidation step. In-plane rocking scans for samples A and C after the oxidation steps can be seen in Figures S12−S15, following the change in the signal corresponding to metallic Cu. The 60° spaced peaks corresponding to [111]-oriented Cu (in the Cu(220) rocking scan) are still visible after the first oxidation, as are the "trident" peaks, but decreased significantly in intensity. All other signals in the rocking scans vanished, indicating a complete oxidation of all "minor epitaxies". For the second oxidation of sample A, the Cu signals decrease even further (see Figure S12), but they remained detectable. The second oxidation of sample C (at 100 °C) resulted in the complete loss of all Cu signals (see Figure S15).

For sample A, in-plane radial and linescans were conducted for the main epitaxy, [111]-oriented Cu[110]||TiO_2[001], to track changes of the metallic Cu particle size. The results of the fits can be seen in Table 3 and Figure 2. No clear shift in the NP diameter is detected. The height of the NPs decreases by about one-third in the scans through the Cu(113)$_s$ Bragg peak,

https://doi.org/10.1021/acs.jpcc.6c00835
J. Phys. Chem. C 2026, 130, 7136−7147

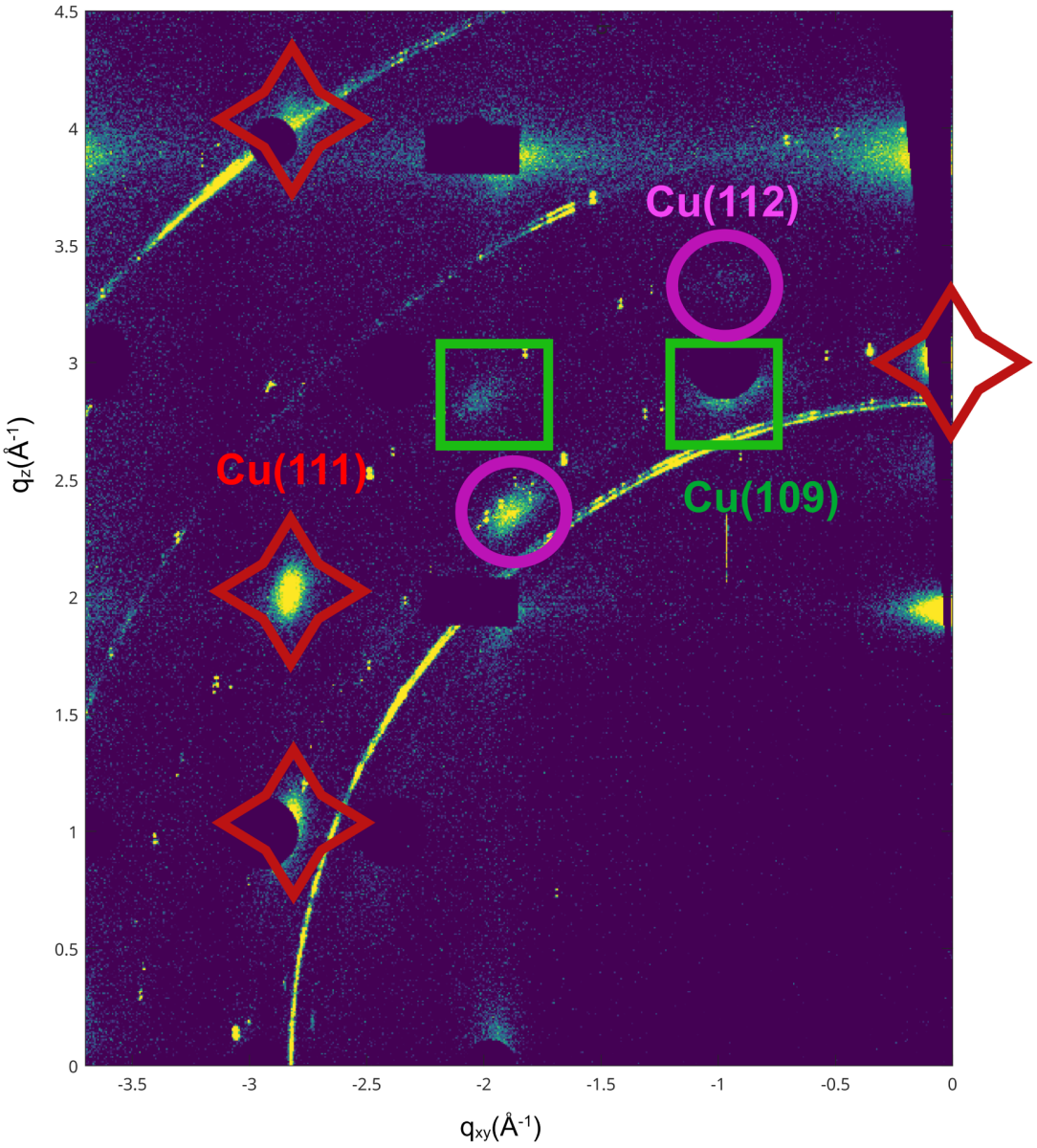


Figure 3. HEXRD data for sample B with a photon energy of 73.34 keV. The image is a sum of 40 images, while the sample was in-plane rotated 1° around the $TiO_2[1\bar{1}0]$ direction. The red star markers correspond to peaks from [111]-oriented Cu with $Cu[110]\|TiO_2[001]$ epitaxy. The pink circle markers correspond to [112]-oriented Cu, and the green square markers correspond to [109]-oriented Cu.

but increases by the same amount in the scans through the $Cu(101)_s$ Bragg peaks. $(113)_s$ is a higher index Bragg peak, thus being more sensitive to strain broadening.[47] Hence, an internal strain distribution is present. As a result, the discrepancies in the calculated size may be attributed to strain on the particle. As the loss of Cu signal intensity clearly indicates the oxidation of the NPs, the lack of any change in the calculated NP dimensions implies that the NP ensemble is evolving: smaller nanoparticles undergo complete oxidation more rapidly and are no longer detected in the ensemble, leading to an apparent increase in the average particle diameter. This effect is partially offset by the ongoing oxidation of larger nanoparticles, resulting in an overall relatively stable average NP size. This effect has been observed in the oxidation of Pd NPs.[48] The oxidation kinetics were investigated by following the change in Cu Bragg peak intensity during the oxidation for sample A; see Figure 2. Compared to the signal intensity before oxidation, about 98% of the Cu signal is lost at 1 bar O_2 in 100 min. The Cu signal intensity is proportional to the metallic Cu volume, which is proportional to the third power of the metallic Cu radius, $I_{Cu} \propto r_{Cu}^3$. An approximation of the oxide thickness can be reached by taking $r_{oxide} = r_{Cu,\, t=0} - r_{Cu}$. The resulting oxide radius is shown in Figure 2. The oxide radius was fitted with the Cabrera & Mott inverse logarithmic function $r = \frac{1}{A + B \times \log t} + C$ (the constant C is an offset used here, as we do not have real oxide thickness). The model reproduces the oxidation kinetics very well at times beyond 20 min, whereas the early stage is more accurately captured by a linear growth regime. Similar behavior has been reported in the literature,[49] where the initial oxidation is attributed to a limitation by oxygen dissociation at the surface. In our case, the transition to the plateau-like oxide growth

https://doi.org/10.1021/acs.jpcc.6c00835
J. Phys. Chem. C 2026, 130, 7136−7147

occurs after approximately 30 min, consistent with previous reports.[22]

3.3. High Energy XRD Characterization

After the in situ growth and oxidation measurements, the samples were stored at ambient conditions for up to 1 week; see Table S1. The most notable difference is that sample A was only 2 h at ambient conditions, whereas sample B was exposed to air for more than a week. Sample C was heated to 100 °C in 1 bar O_2. High-energy X-ray diffraction (HEXRD) was used to further elucidate the mechanisms of long-term oxidation.

Diffraction images for all samples can be seen in Figure 3 and Figures S18−S20. All samples feature a smeared-out specular peak that can be attributed to $Cu_2O(111)$. Considering that the Bragg angle of the reflection is ∼ 1° at the used photon energy (73.34 keV), it can be assumed that the samples contain [111]-oriented Cu_2O NPs with a few degrees of misalignment. Sample C features a faint Cu(111) powder ring; sample A shows no signs of metallic copper. Sample B, however, features various Bragg peaks from several Cu epitaxies; see Figure 3 and Table S3. The strongest peaks belong to the [111]-oriented Cu[110]||TiO_2[001] epitaxy, in agreement with the in situ measurements (see Figure 1). Similarly, the signals from the 12° tilted epitaxy are found as well as [112]-oriented Cu and [100]-oriented Cu. Even though the in situ measurements suggested the existence of three different in-plane epitaxies (Cu[110]||TiO_2[1$\bar{1}$0] and Cu[110]|| ± 24° TiO_2[1$\bar{1}$0]) of [001]-oriented Cu, only two of them are found in the HEXRD data. This may be due to low signal intensity, as it would be unlikely that one of the two tilted epitaxies for Cu[001]-orientation exists, while the other one does not. In addition, two high-index NP epitaxies are seen in the HEXRD data that were not found before: [109]-oriented NPs are present, as well as one type of high-index-oriented Cu particles. The exact orientation for the latter is not clear, as only two Cu(111) peaks can be attributed to them, fitting with several possible out-of-plane orientations, e.g., [105], [134], and [239]. Line integrations were done through the Bragg peaks, and the NP diameters and heights were calculated with Scherrer's formula. The averaged sizes for all fits of a specific epitaxy can be seen in Table S3, and the complete set of fits can be seen in the SI. For the [111]-oriented Cu particles with Cu[110]||TiO_2[001], the fits result in an average diameter of 14.53 nm ± 0.76 nm and an average height of 7.15 nm ± 0.68 nm; see Figure 4. The other epitaxies feature similar sizes with two exceptions: the [111]-oriented Cu NPs with the 12° tilted Cu[110]||TiO_2[001] epitaxy have a significantly smaller diameter of 9.39 nm ± 1.45 nm, while maintaining the same height. Similarly, the [109]-oriented NPs have a comparable height but a reduced diameter of 9.43 ± 1.58 nm.

3.4. SEM

Scanning electron microscopy (SEM) images of the samples were taken after the samples were exposed to ambient conditions for about a week. For each sample, five images were taken: one at the center of the sample and four toward the four sides. From the SEM images, the coverage and the average particle size were calculated, approximating the NPs as half-spheres; see Table 4 and Figure 5 and Figure S28. Samples A and B have almost identical coverages of ∼52%, whereas sample C has only 20% coverage. These coverages match the pattern seen before oxidation with XRR, but all samples show a larger coverage. On the one hand, this can be attributed to Cu oxidation and, on the other hand, to the fact that SEM image analysis may overestimate sizes due to shadowing. The particle sizes were calculated by taking the mode (the bin with the highest counts) of each of the five SEM images per sample and

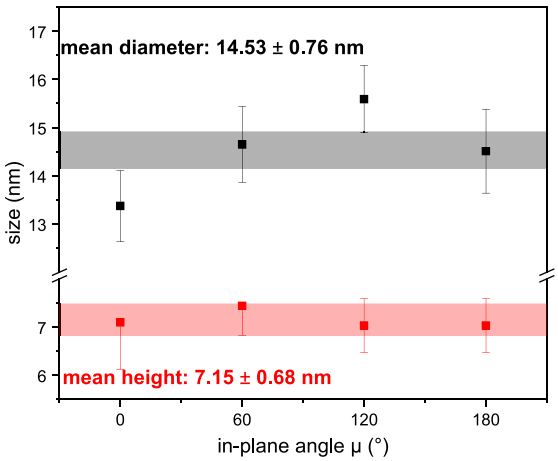


Figure 4. Nanoparticle height and diameter of [111]-oriented Cu on sample B, calculated from linescans of Cu(200) Bragg peaks at several in-plane angles μ from HEXRD data.

Table 4. Particle Diameters and Coverage as Determined from SEM Images Taken about 1 Week after the Samples Were Introduced to Ambient Conditions[a]

sample	A	B	C
diameter [nm]	10.0 ± 0.8	13.4 ± 1.1	10.8 ± 1.2
coverage [%]	52 ± 5	53 ± 2	20 ± 5

[a]The corresponding SEM data can be seen in Figure S28; the size is the average of the mode of the individual SEM images and the coverage is the mean coverage of the individual SEM images.

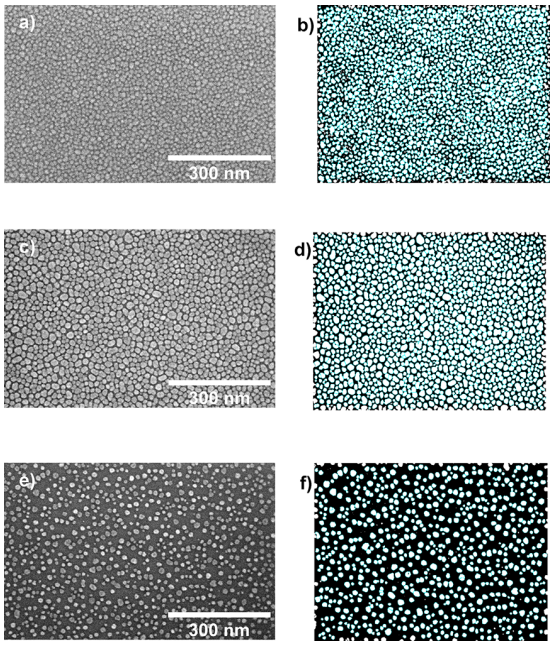


Figure 5. Raw SEM images and the masks used to identify individual particles for the size calculations. a and b for sample A, c and d for sample B, and e and f for sample C. The images and masks correspond to the SEM images from the central region of the samples.

https://doi.org/10.1021/acs.jpcc.6c00835
J. Phys. Chem. C 2026, 130, 7136−7147

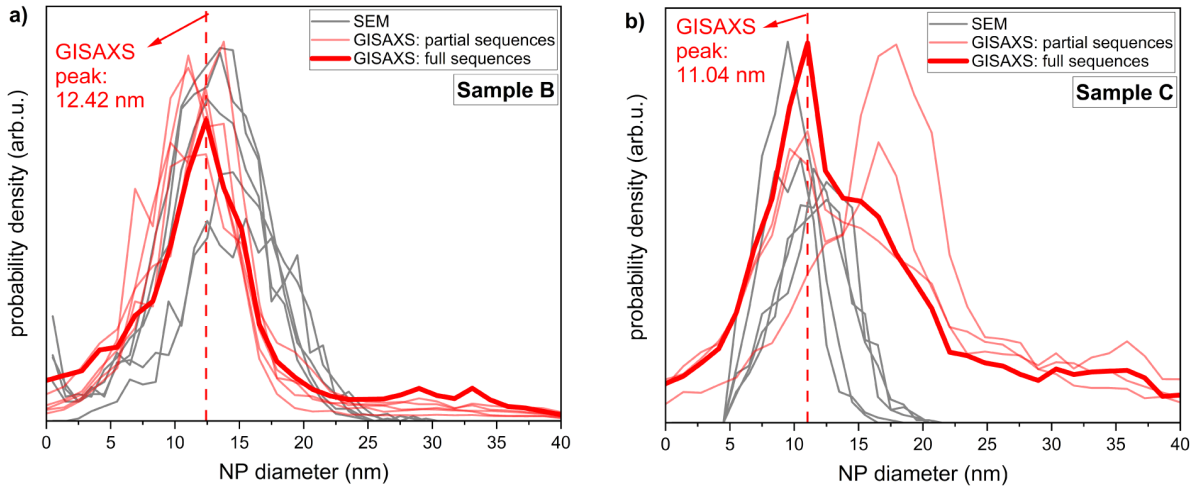


Figure 6. NP diameter distribution for a) sample B and b) sample C as determined by GISAXS (red) and SEM (gray). The thick red line corresponds to the size calculated from all GISAXS images combined, whereas the thinner red lines correspond to partial sections of the sample.

averaging them, revealing particle sizes of around 10 nm for sample A, 13 nm for sample B, and 11 nm for sample C. The comparison of samples A and B is particularly helpful for understanding the influence of growth conditions on the diameters, as both samples experienced similar treatments (whereas sample C was heated in oxygen, resulting in different oxidation conditions). The data clearly show that the higher growth temperature resulted in overall larger particles, even at the same coverage. As shown by the in situ in-plane rocking scans in Figure 1 and Figures S6–S8, all samples exhibit the same Cu epitaxies before oxidation, so the size differences cannot be related to differing epitaxies. Hence, the different NP sizes are solely related to the growth temperature.

The comparison of samples B and C highlights the influence of the coverage on the resulting NP size: Sample C was grown at a higher temperature (400 °C) than sample B (200 °C), yet it exhibits more than double the coverage. Consequently, sample B has significantly larger particles, even though the higher growth temperature of sample C would normally suggest larger particles.

3.5. GISAXS

To further investigate the particle size distribution, grazing-incidence X-ray diffraction (GISAXS) was employed on samples B and C using a 12.1 keV beam. These measurements were performed after the samples had been stored under ambient conditions for six months. Measurements were taken at several positions across the sample. To evaluate the detector images, we trained a convolutional neural network (CNN) to evaluate the NP size distribution based on the detector image. To this cause, pregenerated data were used for training. Full details of the procedure can be found in Section 2. For each image, the diameter distribution was calculated. The resulting NP diameter distribution for both full sums over all scans and partial sequences can be seen in Figure 6. For samples B and C, the diameter distribution obtained from GISAXS, featuring particle diameters of 12.4 nm for sample B and 11.0 nm for sample C, fits closely with those obtained from SEM (13.4 nm for sample B and 10.8 nm for sample C). For sample C, the GISAXS analysis also detects larger particles (about 20 nm diameter) for two sequences. The corresponding sequences are related to scans close to the single crystal edge (unlike sequences that did not exhibit these larger particles). Overall, the GISAXS results confirm the homogeneity of the particle size distributions across the single crystal surface and the particle diameters.

3.6. Long-Term Oxidation of Cu NPs

To investigate the long-term oxidation and stability of the nanoparticles, XPS measurements were taken after 2 months of storage at ambient conditions. The results can be seen in Figure 7 and Table 5. Samples A and B feature approximately the same ratio of CuO and Cu_2O as determined from their Cu 2p spectra (88% and 84%), whereas sample C features significantly more CuO (97%). The Cu 2p spectra do not allow the differentiation of Cu_2O and metallic Cu, as both peaks are separated only by 0.1 eV.[50,51] For this reason, the Cu LMM Auger peak was measured, which provides clear identification of Cu_2O at ∼916.5 eV and Cu at ∼918.5 eV.[51,52] Due to a large background TiO_2 signal and broad peaks, consistent fitting was impossible for these spectra. From the position of the peak, it is clear for all samples, however, that no metallic Cu is present (in the area probed by XPS).

These measurements were repeated after a combined 6–8 months of storage under ambient conditions. The results can be seen in Table S5 and Figure S30. The spectra reveal no significant changes with respect to the measurements after 2 months of storage, thus showing that the oxidation state is stable and no full oxidation to CuO takes place in air. The information depths of the XPS measurements can be approximated by employing the well-known mean free path for electrons:[53] for Cu $2p_{3/2}$, it is about 1 nm, while for Ti 2p and Cu LMM, it is roughly 2 nm. Compared to the particle heights of 5–10 nm, this indicates that only the outer layers are being probed.

3.6.1. Homogeneity of the Oxidation. Both XRD and XPS techniques can distinguish different oxidation states through lattice parameters or the kinetic energy of the photoelectrons, but both techniques probe ensembles of particles. Since individual NPs may feature different oxidation states, we employed surface-sensitive scanning Auger spectroscopy (SAM) with high spatial resolution to evaluate the oxidation state of individual NPs on sample B. The results of the SAM measurements can be seen in Figure 8: an SEM image of the sample was taken to determine a suitable measurement area; see Figure 8a. Next, a linescan was

https://doi.org/10.1021/acs.jpcc.6c00835
J. Phys. Chem. C 2026, 130, 7136−7147

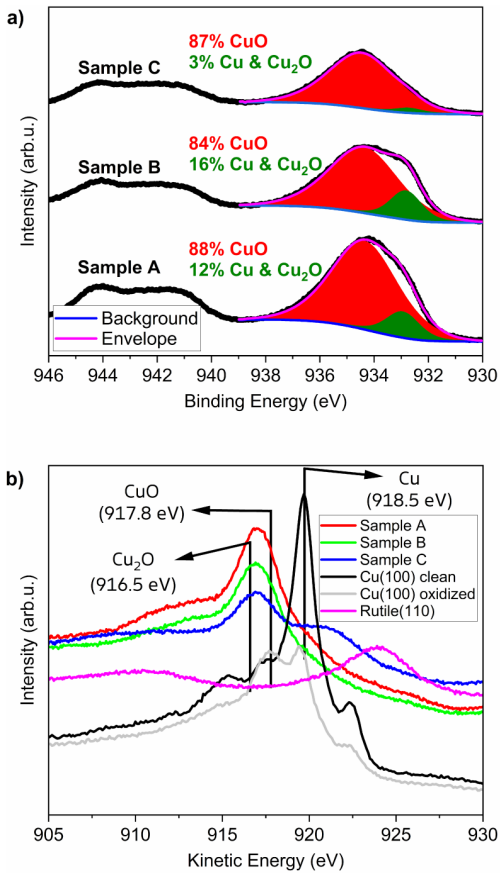


Figure 7. a) Deconvoluted XPS spectra of Cu 2p core levels obtained after the samples were stored at ambient conditions for two months. The Cu $2p_{3/2}$ peaks were deconvoluted into the CuO and Cu_2O and Cu contributions. The percentages represent the part of the whole Cu 2p area that is attributed to one of the peaks. b) Cu LMM XPS spectra after the samples were stored at ambient conditions for two months. For peak identification, reference spectra for a Cu(100) single crystal in metallic state (UHV annealed) and in an oxidized state (1 h in 1 bar O_2) are included.

Table 5. Parameters from Fitting the Cu $2p_{3/2}$ XPS Peak after the Samples Were Stored under Ambient Conditions for Two Months[a]

	CuO			Cu & Cu_2O		
sample	Binding Energy [eV]	fwhm [eV]	Area [%]	Binding Energy [eV]	fwhm [eV]	Area [%]
A	934.37	2.88	87.70	932.95	1.41	12.30
B	934.40	2.98	84.11	932.82	1.31	15.89
C	933.00	2.88	97.24	932.73	1.10	2.76

[a]The area percentage relates to the combined area of the peak assigned to CuO and the peak assigned to Cu and Cu_2O.

performed over several particles, with each data point representing an Auger scan of Cu LMM, O KLL, and Ti LMM. The change in intensity was evaluated by integration of the signal; see Figure 8 b. Finally, individual Cu LMM scans on NPs and off NPs were summed to compare their structure; see Figure 8c. In the Cu Auger signal, the intensity increases on particles, whereas the O and Ti signals show peaks between particles, indicating the dominance of the substrate signal. Small variations in Cu signal intensity were observed between different NPs, indicating slight particle-to-particle differences. However, it becomes apparent that the peak structure is the same everywhere. The Cu signal observed between particles can be explained by interparticle distances of approximately 10 nm and an instrument resolution of 8 nm, which prevents Cu-free regions from being resolved. This allows the conclusion that the oxide structure of all NPs is the same and that the different oxide states seen in XPS must exist in a core−shell structure or as an intermixed state.

4. DISCUSSION & CONCLUSION

For the growth of Cu nanoparticles on rutile $TiO_2(110)$ single crystals, we find that the main growth direction is Cu[111] out-of-plane with Cu[110]||TiO_2[001] in-plane epitaxy. This is well in line with existing reports for Cu islands on rutile.[36,37] Moreover, we find distinguishable particles with no tendency to form a thin film, which is consistent with the Volmer−Weber growth mode of Cu reported for several substrates.[32−35] In contrast to a report of the growth of Cu NPs on ZnO(0001),[38,39] we find a monodisperse particle size distribution. In addition to the [111]-oriented Cu particles, we find several other epitaxies but with minor contributions to the amount of particles. Most of these "minor epitaxies" feature the Cu[110]||TiO_2[001] in-plane epitaxy. This is likely due to the good match of the Cu(220) direction with the TiO_2(001) direction on the surface. The former is $a_{Cu} \times 1/\sqrt{2} = 3.615$ Å $\times 1/\sqrt{2} = 2.556$ Å, while the latter is 2.96 Å. Hence, over the distance of three unit cells of Cu, the lattices mismatch only by 3.3%. The growth temperature has no effect on the "minor epitaxies". In addition to the "minor epitaxies", a fraction of the [111]-oriented Cu NPs is tilted 12° in-plane, resulting in a Cu[110]||TiO_2[112] epitaxy instead of the Cu[110]||TiO_2[001] epitaxy. At a 100 °C growth temperature, 7% of the particles grow in this epitaxy. With increasing temperature, we find an increase in this tilted epitaxy, reaching 21% for a growth temperature of 400 °C. The Cu[110] planes have a distance of 2.556 Å, while the TiO_2[112] planes have a distance of 1.346 Å. The resulting mismatch of 5.3% for two TiO_2 planes and one Cu plane is larger than the mismatch of the Cu[110]||TiO_2[001] epitaxy, which likely explains why more of these tilted particles appear at higher growth temperatures. The Cu particles grown at 400 °C feature an aspect ratio H/D of about 0.5, calculated from linescans through the Cu(101) Bragg peak. This agrees with previous reports of Cu on rutile[37] and is in contrast with Cu growth on ZnO(0001), which is known to feature flatter particles.[38] Linescans through the $Cu(113)_s$ Bragg peak feature a slightly larger ratio of H/D ≈ 0.6. The difference can be attributed to strain in the particles, resulting in different peak broadening for different Bragg peaks. Additionally, the $(113)_s$ Bragg peak may be influenced by particles of different sizes compared to the $(101)_s$ Bragg peak, as the overall particle size distribution ranges from 2 to 25 nm. The H/D ratio of 0.5, together with the SEM images (Figure 5), indicates that the particles resemble half-spheres or flattened half-spheres.

The oxidation of the well-defined Cu NPs grown on rutile $TiO_2(110)$ was studied by exposing them to 1 bar O_2. The signal from all minor growth directions is completely lost after 20 min, whereas for samples A and B, the signal from the main growth direction Cu[110]||TiO_2[001] can still be detected. For sample A, the Cu signal can even be detected after 100 min exposure to oxygen, although its intensity is drastically reduced. The signal from the particles 12° tilted away from

https://doi.org/10.1021/acs.jpcc.6c00835
J. Phys. Chem. C 2026, 130, 7136−7147

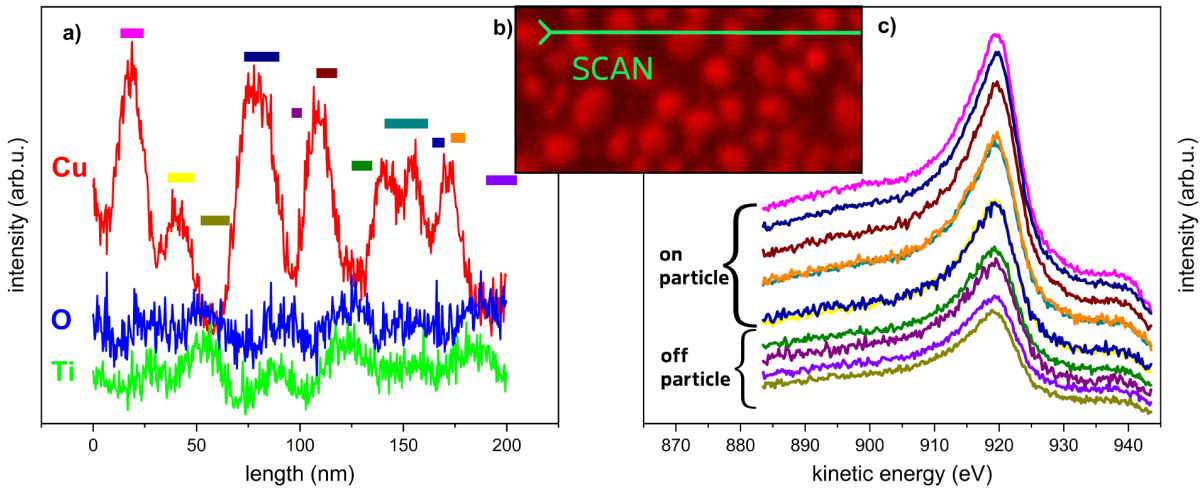


Figure 8. Scanning Auger microscopy measurement of sample B. a) SAM linescans with the corresponding intensities of the Cu, O, and Ti Auger signals. b) The SAM-SEM image with the marked area of the linescan. c) The individual Cu AES scans taken at the positions on the scan indicated with the color bars in a).

the main Cu[110]||TiO_2[001] epitaxy does not oxidize faster than that of the particles of the main growth direction. Heating sample C to 100 °C under 1 bar of oxygen pressure results in the loss of all Cu signals. HEXRD measurements reveal that sample B features metallic Cu NPs of various epitaxies even after exposing it to ambient conditions for 1 week, whereas sample A, which underwent similar treatments, no longer exhibits epitaxial Cu after prolonged exposure to ambient conditions. The oxidation kinetics were investigated by following the Cu Bragg peak intensity as calculated from radial scans; see Figure 2. It can be seen that the decay of the Cu signal follows the inverse logarithmic law described by Cabrera and Mott,[22] indicating the self-passivating oxide shell. At the start of the oxidation (the first 20 min), the Cu signal loss is better described by a linear decay. This suggests that the oxidation kinetics in this regime are controlled by the high surface area and the high amounts of steps and edges of the nanoparticles compared to the thin film in the model by Cabrera and Mott. The stable Cu NPs of sample B, as detected by HEXRD, are larger (~14 nm) than the average Cu NP size detected after growth (~7 nm, based on XRD data), indicating that larger particles are more resistant to oxidation. This also explains the increased stability against oxidation of sample B compared to sample A: Due to its higher Cu growth temperature, sample B features overall larger particles, as shown by the diameter distributions from SEM measurements in Figure S28. Similar size-dependent effects on oxidation states have been reported in the literature for Pd NPs.[41] Moreover, comparing the NP diameter distributions for samples B and C from the GISAXS calculations shows that the coverage plays an important role in determining the resulting NPs: Where sample B was grown at 200 °C with a coverage close to 50%, sample C, which was grown at 400 °C, has only about half of that coverage. Based on growth temperature, sample C would be expected to have larger particles. However, both GISAXS and SEM reveal that sample C actually exhibits smaller NP diameters than sample B, indicating that coverage can outweigh the effect of temperature on particle size. From the GISAXS NP diameter distributions, it can be concluded that sample B is homogeneous across the whole surface, as partial sequences of GISAXS images do not reveal different size distributions. This is not the case for sample C, where some sequences indicate the presence of larger particles (which were not imaged in SEM). This may be attributed to local variances in the heating of the sample during growth or during heating under O_2, resulting in a change in particles sizes. The oxide formed after oxidation is partially epitaxial in the case of Cu_2O, with [111]-orientation, but completely amorphous for CuO. The latter is in line with existing reports of Cu NP oxidation on ZnO(0001).[46] The presence of epitaxial Cu_2O is also expected with respect to this reference, but the extent seen here is much less, indicating that only a minor amount of Cu has formed epitaxial Cu_2O, in contrast to the fully epitaxial NPs reported in the reference.[46] This difference may be attributed to the fact that the nanoparticles studied here are only about one-fifth the size of the NPs reported on ZnO.[46] The distribution of CuO and Cu_2O, as measured with XPS, is similar for samples A and B with both featuring approximately 85% CuO after two months of storage under ambient conditions. In contrast, sample C contains around 90% CuO after annealing in oxygen and two months of storage at ambient conditions. The XPS Cu_2O signal can also contain contributions from positively charged copper that is not part of an oxide. Such states have been reported for the first monolayer of Cu deposited on oxide single crystals and have been attributed to an interaction with oxygen vacancies.[54] In our study, the nanoparticles are several nanometers in height, diminishing the influence of the first layer. Furthermore, XPS measurements do not show any detectable Ti^{3+} signals (Figure S29 in the Supporting Information), which are commonly used as indicators of oxygen vacancies. Therefore, we infer that oxygen vacancies do not play a significant role in the observed behavior of the Cu/TiO_2 nanoparticles. Additionally, it has been shown that Cu interacts only weakly with TiO_2.[35] The oxidation states of all samples remain essentially unchanged after an additional 4−6 months of storage under ambient conditions. As the HEXRD data reveal the presence of stable Cu NPs for sample B and as XPS only probes the uppermost nanometers, whereas hard X-rays fully penetrate the NPs, this indicates that for sample B a copper/copper-oxide core−shell structure has formed. This is not the case for sample A, which can be attributed to the

https://doi.org/10.1021/acs.jpcc.6c00835
J. Phys. Chem. C 2026, 130, 7136−7147

smaller dimensions of the nanoparticles, resulting in full oxidation. The absence of strong signals from epitaxial Cu_2O and the lack of any signal originating from CuO in the HEXRD data indicates that the oxide is mostly amorphous. Furthermore, it could be shown via scanning Auger microscopy that the nanoparticle oxidation state is homogeneous across the whole sample.

In conclusion, the growth temperature of the Cu particles dictates the NP sizes and the amount of tilted Cu[111] epitaxy. Oxidation leads to core−shell metal-oxide structures for sufficiently large particles, whereas smaller particles (below ∼14 nm) fully oxidize. Importantly, the oxidation state of the oxide shell is determined by the oxidation temperature rather than the particle size, with higher temperatures favoring the formation of CuO.

These findings demonstrate the critical role of growth and oxidation behavior in controlling the structure and composition of Cu nanoparticles on TiO_2(110). The oxidation state of Cu determines possible pathways for visible light activity, and thus, the ability to produce different stable oxidation states for the NPs is highly relevant for further studies aimed at identifying the most efficient NP configuration for virus inactivation or organic pollutant degradation.

■ ASSOCIATED CONTENT

Supporting Information

The Supporting Information is available free of charge at https://pubs.acs.org/doi/10.1021/acs.jpcc.6c00835.

The time of sample oxidation for different measurements; XRR data; in-plane rocking scans and fits; HEXRD data; linescans through Bragg peaks and fits; radial scans; SEM images; XPS data; realspace lattice drawings (PDF)

■ AUTHOR INFORMATION

Corresponding Authors

Andreas Stierle − *Centre for X-ray and Nano Science CXNS, Deutsches Elektronen-Synchrotron DESY, Hamburg 22607, Germany; Fachbereich Physik, Universität Hamburg, Hamburg 20355, Germany;* orcid.org/0000-0002-0303-6282; Email: andreas.stierle@desy.de

Heshmat Noei − *Centre for X-ray and Nano Science CXNS, Deutsches Elektronen-Synchrotron DESY, Hamburg 22607, Germany; Fachbereich Physik, Universität Hamburg, Hamburg 20355, Germany;* orcid.org/0000-0003-1294-3527; Email: heshmat.noei@desy.de

Authors

Daniel Silvan Dolling − *Centre for X-ray and Nano Science CXNS, Deutsches Elektronen-Synchrotron DESY, Hamburg 22607, Germany; Fachbereich Physik, Universität Hamburg, Hamburg 20355, Germany;* orcid.org/0000-0002-3723-552X

Miguel Blanco Garcia − *Centre for X-ray and Nano Science CXNS, Deutsches Elektronen-Synchrotron DESY, Hamburg 22607, Germany; Fachbereich Physik, Universität Hamburg, Hamburg 20355, Germany*

Mona Kohantorabi − *Centre for X-ray and Nano Science CXNS, Deutsches Elektronen-Synchrotron DESY, Hamburg 22607, Germany;* orcid.org/0000-0002-4230-8797

Yufeng Zhai − *Deutsches Elektronen-Synchrotron DESY, Hamburg 22607, Germany;* orcid.org/0009-0005-3187-1815

Benedikt Sochor − *Deutsches Elektronen-Synchrotron DESY, Hamburg 22607, Germany*

Mohammad Ebrahim Haji Naghi Tehrani − *Centre for X-ray and Nano Science CXNS, Deutsches Elektronen-Synchrotron DESY, Hamburg 22607, Germany; Fachbereich Physik, Universität Hamburg, Hamburg 20355, Germany*

Jan-Christian Schober − *Centre for X-ray and Nano Science CXNS, Deutsches Elektronen-Synchrotron DESY, Hamburg 22607, Germany; Fachbereich Physik, Universität Hamburg, Hamburg 20355, Germany*

Ming-Chao Kao − *Centre for X-ray and Nano Science CXNS, Deutsches Elektronen-Synchrotron DESY, Hamburg 22607, Germany; Fachbereich Physik, Universität Hamburg, Hamburg 20355, Germany;* orcid.org/0000-0002-6443-214X

Jagrati Dwivedi − *Centre for X-ray and Nano Science CXNS, Deutsches Elektronen-Synchrotron DESY, Hamburg 22607, Germany;* orcid.org/0000-0002-5986-9638

Arno Jeromin − *Centre for X-ray and Nano Science CXNS, Deutsches Elektronen-Synchrotron DESY, Hamburg 22607, Germany*

Olof Gutowski − *Deutsches Elektronen-Synchrotron DESY, Hamburg 22607, Germany;* orcid.org/0000-0001-5514-4480

Dmitri V. Novikov − *Deutsches Elektronen-Synchrotron DESY, Hamburg 22607, Germany*

Thomas F. Keller − *Centre for X-ray and Nano Science CXNS, Deutsches Elektronen-Synchrotron DESY, Hamburg 22607, Germany; Fachbereich Physik, Universität Hamburg, Hamburg 20355, Germany;* orcid.org/0000-0002-3770-6344

Stephan V. Roth − *Deutsches Elektronen-Synchrotron DESY, Hamburg 22607, Germany; KTH Royal Institute of Technology, Department of Fibre and Polymer Technology Division of Fibre Processes, SE-100 44 Stockholm, Sweden*

Complete contact information is available at: https://pubs.acs.org/10.1021/acs.jpcc.6c00835

Notes

The authors declare no competing financial interest.

■ ACKNOWLEDGMENTS

This work is supported by the Initiative and Networking Fund of the Helmholtz Association of German Research Centers (HGF) under the CORAERO project (KA1-Co-06). We acknowledge DESY (Hamburg, Germany), a member of the Helmholtz Association HGF, for the provision of experimental facilities. Parts of this research were carried out at PETRA III beamlines P03, P07-EH2, P23, and at DESY NanoLab. Beamtime was allocated for proposals I-20230640, I-20010075, and I-20230376. We thank Dennis Renner for support in the UHV lab and Simon Geile for support with mobile chambers.

■ REFERENCES

(1) Han, T.; Zhou, D.; Wang, H.; Zheng, X. The Study on Preparation and Photocatalytic Activities of Cu_2O/TiO_2 Nanoparticles. *J. Environ. Chem. Eng.* **2015**, *3*, 2453−2462.

(2) Liu, M.; Sunada, K.; Hashimoto, K.; Miyauchi, M. Visible-Light Sensitive Cu(II)-TiO_2 with Sustained Anti-Viral Activity for Efficient Indoor Environmental Remediation. *J. Mater. Chem. A* **2015**, *3*, 17312−17319.
(3) Mathew, S.; Ganguly, P.; Rhatigan, S.; Kumaravel, V.; Byrne, C.; Hinder, S.; Bartlett, J.; Nolan, M.; Pillai, S. Cu-Doped TiO_2: Visible Light Assisted Photocatalytic Antimicrobial Activity. *Appl. Sci.* **2018**, *8*, 2067.
(4) Méndez-Medrano, M. G.; Kowalska, E.; Ohtani, B.; Bahena Uribe, D.; Colbeau-Justin, C.; Rau, S.; Rodríguez-López, J. L.; Remita, H. Heterojunction of CuO Nanoclusters with TiO_2 for Photo-Oxidation of Organic Compounds and for Hydrogen Production. *J. Chem. Phys.* **2020**, *153*, 034705.
(5) Qiu, X.; Miyauchi, M.; Sunada, K.; Minoshima, M.; Liu, M.; Lu, Y.; Li, D.; Shimodaira, Y.; Hosogi, Y.; Kuroda, Y.; Hashimoto, K. Hybrid Cu_xO/TiO_2 Nanocomposites as Risk-Reduction Materials in Indoor Environments. *ACS Nano* **2012**, *6*, 1609−1618.
(6) Irie, H.; Kamiya, K.; Shibanuma, T.; Miura, S.; Tryk, D. A.; Yokoyama, T.; Hashimoto, K. Visible Light-Sensitive Cu(II)-Grafted TiO_2 Photocatalysts: Activities and X-ray Absorption Fine Structure Analysis. *J. Phys. Chem. C* **2009**, *113*, 10761−10766.
(7) Miyauchi, M.; Sunada, K.; Hashimoto, K. Antiviral Effect of Visible Light-Sensitive Cu_xO/TiO_2 Photocatalyst. *Catalysts* **2020**, *10*, 1093.
(8) Nakano, R.; Yamaguchi, A.; Sunada, K.; Nagai, T.; Nakano, A.; Suzuki, Y.; Yano, H.; Ishiguro, H.; Miyauchi, M. Inactivation of Various Variant Types of SARS-CoV-2 by Indoor-Light-Sensitive TiO_2-Based Photocatalyst. *Sci. Rep.* **2022**, *12*, 5804.
(9) Kohantorabi, M.; Wagstaffe, M.; Creutzburg, M.; Ugolotti, A.; Kulkarni, S.; Jeromin, A.; Krekeler, T.; Feuerherd, M.; Herrmann, A.; Ebert, G.; Protzer, U.; Guédez, G.; Löw, C.; Thuenauer, R.; Schlueter, C.; Gloskovskii, A.; Keller, T. F.; Di Valentin, C.; Stierle, A.; Noei, H. Adsorption and Inactivation of SARS-CoV-2 on the Surface of Anatase TiO_2(101). *ACS Appl. Mater. Interfaces* **2023**, *15*, 8770−8782.
(10) Kohantorabi, M.; Ugolotti, A.; Sochor, B.; Roessler, J.; Wagstaffe, M.; Meinhardt, A.; Beck, E. E.; Dolling, D. S.; Garcia, M. B.; Creutzburg, M.; Keller, T. F.; Schwartzkopf, M.; Vayalil, S. K.; Thuenauer, R.; Guédez, G.; Löw, C.; Ebert, G.; Protzer, U.; Hammerschmidt, W.; Zeidler, R.; Roth, S. V.; Di Valentin, C.; Stierle, A.; Noei, H. Light-Induced Transformation of Virus-Like Particles on TiO_2. *ACS Appl. Mater. Interfaces* **2024**, *16*, 37275−37287.
(11) Blanco Garcia, M.; Perilli, D.; Daldossi, C.; Ugolotti, A.; Giordano, M.; Dolling, D. S.; Wagstaffe, M.; Kohantorabi, M.; Stierle, A.; Di Valentin, C.; Noei, H. Unraveling the Role of the Multifunctional Groups in the Adsorption of L-Cysteine on Rutile TiO_2(110). *J. Am. Chem. Soc.* **2025**, *147*, 40158−40170.
(12) Fujishima, A.; Hond, K. Electrochemical Photolysis of Water at a Semiconductor Electrode. *Nature* **1972**, *278*, 37−38.
(13) Hernández-Ramírez, A.; Medina-Ramírez, I. *Photocatalytic Semiconductors: synthesis, Characterization, and Environmental Applications*; Springer, 2015.
(14) Bundesinstitut für Risikobewertung, *Titanium Dioxide - Are There Health Risks?*; Bundesinstitut für Risikobewertung, 2024, https://www.bfr.bund.de/fragen-und-antworten/thema/titandioxid-gibt-es-gesundheitliche-risiken/.
(15) Micochova, P.; Chadha, A.; Hesseloj, T.; Fraternali, F.; Ramsden, J. J.; Gupta, R. K. Rapid Inactivation of SARS-CoV-2 by Titanium Dioxide Surface Coating. *Wellcome Open Research* **2021**, *6*, 56.
(16) Djellabi, R.; Basilico, N.; Delbue, S.; D'Alessandro, S.; Parapini, S.; Cerrato, G.; Laurenti, E.; Falletta, E.; Bianchi, C. L. Oxidative Inactivation of SARS-CoV-2 on Photoactive AgNPs@TiO_2 Ceramic Tiles. *Int. J. Mol. Sci.* **2021**, *22*, 8836.
(17) Sathish Kumar, P. S.; Sivakumar, R.; Anandan, S.; Madhavan, J.; Maruthamuthu, P.; Ashokkumar, M. Photocatalytic Degradation of Acid Red 88 Using Au-TiO_2 Nanoparticles in Aqueous Solutions. *Water Res.* **2008**, *42*, 4878−4884.
(18) Haynes, W. M.; Lide, D. R.; Bruno, T. J. *CRC Handbook of Chemistry and Physics*; CRC Press, 2016. DOI: .
(19) Osako, K.; Matsuzaki, K.; Hosono, H.; Yin, G.; Atarashi, D.; Sakai, E.; Susaki, T.; Miyauchi, M. Examination of Interfacial Charge Transfer in Photocatalysis Using Patterned CuO Thin Film Deposited on TiO_2. *APL Mater.* **2015**, *3*, 104409.
(20) Lee, B.-H.; Park, S.; Kim, M.; Sinha, A. K.; Lee, S. C.; Jung, E.; Chang, W. J.; Lee, K.-S.; Kim, J. H.; Cho, S.-P.; Kim, H.; Nam, K. T.; Hyeon, T. Reversible and Cooperative Photoactivation of Single-Atom Cu/TiO_2 Photocatalysts. *Nat. Mater.* **2019**, *18*, 620−626.
(21) Wagner, C. Elementarvorgänge bei der Bildung von Metalloxyd aus Metall und Sauerstoff sowie bei verwandten Reaktionen. *Angew. Chem.* **1936**, *49*, 735−740.
(22) Cabrera, N. N. M.; Mott, N. F. Theory of the Oxidation of Metals. *Rep. Prog. Phys.* **1949**, *12* (1), 163.
(23) Rhodin Jr, T. N. Low Temperature Oxidation of Copper. II. Reaction Rate Anisotropy. *J. Am. Chem. Soc.* **1951**, *73*, 3143−3146.
(24) Pinnel, M. R.; Tompkins, H. G.; Heath, D. E. Oxidation of Copper in Controlled Clean Air and Standard Laboratory air at 50°C to 150°C. *Appl. Surface Sci.* **1979**, *2*, 558−577.
(25) Pedersen, D. B.; Wang, S.; Liang, S. H. Charge-Transfer-Driven Diffusion Processes in Cu@Cu-Oxide Core-Shell Nanoparticles: Oxidation of 3.0 ± 0.3 nm Diameter Copper Nanoparticles. *J. Phys. Chem. C* **2008**, *112*, 8819−8826.
(26) Nilsson, S.; Albinsson, D.; Antosiewicz, T. J.; Fritzsche, J.; Langhammer, C. Resolving Single Cu Nanoparticle Oxidation and Kirkendall Void Vormation with In Situ Plasmonic Nanospectroscopy and Electrodynamic Simulations. *Nanoscale* **2019**, *11*, 20725−20733.
(27) Rice, K. P.; Paterson, A. S.; Stoykovich, M. P. Nanoscale Kirkendall Effect and Oxidation Kinetics in Copper Nanocrystals Characterized by Real-Time, In Situ Optical Spectroscopy. *Part. Part. Syst. Charact.* **2015**, *32*, 373−380.
(28) Grant, F. S. Properties of Rutile (Titanium Dioxide). *Rev. Mod. Phys.* **1959**, *31*, 646−654.
(29) Khort, A.; Roslyakov, S.; Loginov, P. Solution Combustion Synthesis of Single-Phase Bimetallic Nanomaterials. *Nano-Struct. Nano-Objects* **2021**, *26*, 100727.
(30) Restori, R.; Schwarzenbach, D. Charge Density in Cuprite, Cu_2O. *Acta Cryst. B* **1986**, *42*, 201−208.
(31) Calos, N. J.; Forrester, J. S.; Schaffer, G. B. A Crystallographic Contribution to the Mechanism of a Mechanically Induced Solid State Reaction. *J. Solid State Chem.* **1996**, *122*, 273−280.
(32) Park, H.; Sun, Y.-M.; Troiani, H.; Santiago, P.; Yacaman, M.; White, J. Growth and Thermal Annealing of Cu on HfO_2. *Surf. Sci.* **2002**, *521*, 1−9.
(33) Qingfeng, G.; Möller, P. J. A Study of Cu Growth on an Yttria-Stabilized ZrO_2(110) Surface. *Thin Solid Films* **1995**, *254*, 10−15.
(34) Wu, Y.; Garfunkel, E.; Madey, T. E. Initial Stages of Cu Growth on Ordered Al_2O_3 Ultrathin Films. *J. Vacuum Sci. Technol. A* **1996**, *14* (3), 1662−1667.
(35) Diebold, U.; Pan, J.-M.; Madey, T. E. Growth Mode of Ultrathin Copper Overlayers on TiO_2(110). *Phys. Rev. B* **1993**, *47*, 3868−3876.
(36) Chen, D.; Bartelt, M.; Hwang, R.; McCarty, K. Self-Limiting Growth of Copper Islands on TiO_2(110)-(1 × 1). *Surf. Sci.* **2000**, *450*, 78−97.
(37) Wilson, A.; Bernard, R.; Vlad, A.; Borensztein, Y.; Coati, A.; Croset, B.; Garreau, Y.; Prévot, G. Epitaxial Growth of Bimetallic Au-Cu Nanoparticles on TiO_2(110) Followed In Situ by Scanning Tunneling Microscopy and Grazing-Incidence X-Ray Diffraction. *Phys. Rev. B* **2014**, *90*, 075416−075426.
(38) Gleißner, R.; Noei, H.; Chung, S.; Semione, G. D. L.; Beck, E. E.; Dippel, A.-C.; Gutowski, O.; Gizer, G.; Vonk, V.; Stierle, A. Copper Nanoparticles with High Index Facets on Basal and Vicinal ZnO Surfaces. *J. Phys. Chem. C* **2021**, *125*, 23561−23569.
(39) Qiu, H.; Gallino, F.; Di Valentin, C.; Wang, Y. Shallow Donor States Induced by In-Diffused Cu in ZnO: A Combined HREELS and Hybrid DFT Study. *Phys. Rev. Lett.* **2011**, *106*, 066401.

(40) Asaduzzaman, A. M.; Krüger, P. Adsorption of 3d Transition Elements on a TiO_2(110) Surface. *J. Phys. Chem. C* **2008**, *112*, 19616−19619.
(41) Nolte, P.; Stierle, A.; Kasper, N.; Jin-Phillipp, N. Y.; Reichert, H.; Rühm, A.; Okasinski, J.; Dosch, H.; Schöder, S. Combinatorial High-Energy X-Ray Microbeam Study of the Size-Dependent Oxidation of Pd Nanoparticles on MgO(100). *Phys. Rev. B* **2008**, *77*, 115444.
(42) Schell, N.; King, A.; Beckmann, F.; Fischer, T.; Müller, M.; Schreyer, A. The High Energy Materials Science Beamline (HEMS) at PETRA III. *Mater. Sci. Forum.* **2013**, *772*, 57−61.
(43) Buffet, A.; Rothkirch, A.; Döhrmann, R.; Körstgens, V.; Abul Kashem, M. M.; Perlich, J.; Herzog, G.; Schwartzkopf, M.; Gehrke, R.; Müller-Buschbaum, P.; Roth, S. V. P03, the Microfocus and Nanofocus X-Ray Scattering (MiNaXS) Beamline of the PETRA III Storage Ring: The Microfocus Endstation. *J. Synchrotron Radiat* **2012**, *19*, 647−653.
(44) Stierle, A.; Keller, T. F.; Noei, H.; Vonk, V.; Roehlsberger, R. DESY NanoLab. *J.Large-Scale Research Facilities JLSRF* **2016**, *2*, A76−A76.
(45) Walton, J.; Wincott, P.; Fairley, N.; Carrick, A. *Peak Fitting with CasaXPS: A Casa pocketbook: A Casa Pocket Book*; Casa XPS pocketbooks; Acolyte Science: Cheshire, 2010.
(46) Gleißner, R.; Chung, S.; Semione, G. D. L.; Jacobse, L.; Wagstaffe, M.; Tober, S.; Neumann, A. J.; Gizer, G.; Goodwin, C. M.; Soldemo, M.; Shipilin, M.; Lömker, P.; Schlueter, C.; Gutowski, O.; Muntwiler, M.; Amann, P.; Noei, H.; Vonk, V.; Stierle, A. Role of Oxidation-Reduction Dynamics in the Application of Cu/ZnO-Based Catalysts. *ACS Appl. Nano Mater.* **2023**, *6*, 8004−8016.
(47) Cullity, B. D.; Stock, S. R. *Elements of X-Ray Diffraction*, Third ed. ed.; Pearson: Essex, 2014.
(48) Chung, S.; Schober, J.-C.; Tober, S.; Schmidt, D.; Khadiev, A.; Novikov, D. V.; Vonk, V.; Stierle, A. Epitaxy and Shape Heterogeneity of a Nanoparticle Ensemble during Redox Cycles. *ACS Nano* **2021**, *15*, 13267−13278.
(49) Chen, C.-H.; Yamaguchi, T.; Sugawara, K.-I.; Koga, K. Role of Stress in the Self-Limiting Oxidation of Copper Nanoparticles. *J. Phys. Chem. B* **2005**, *109*, 20669−20672.
(50) Ghodselahi, T.; Vesaghi, M. A.; Shafiekhani, A.; Baghizadeh, A.; Lameii, M. XPS Study of the Cu@Cu_2O Core-Shell Nanoparticles. *Appl. Surf. Sci.* **2008**, *255*, 2730−2734.
(51) Deroubaix, G.; Marcus, P. X-ray Photoelectron Spectroscopy Analysis of Copper and Zinc Oxides and Sulphides. *Surf. Interface Anal.* **1992**, *18*, 39−46.
(52) Zheng, M.; Wan, Y.; Yang, L.; Ao, S.; Fu, W.; Zhang, Z.; Huang, Z.-H.; Ling, T.; Kang, F.; Lv, R. In Situ Construction of Cu(I)-Cu(II) Pairs for Efficient Electrocatalytic Nitrate Reduction Reaction to Ammonia. *J. Energy Chem.* **2025**, *100*, 106.
(53) Seah, M. P.; Dench, W. A. Quantitative Electron Spectroscopy of Surfaces: A Standard Data Base for Electron Inelastic Mean Free Paths in Solids. *Surf. Interface Anal.* **1979**, *1*, 2−11.
(54) Chen, A.; Yu, X.; Zhou, Y.; Miao, S.; Li, Y.; Kuld, S.; Sehested, J.; Liu, J.; Aoki, T.; Hong, S.; et al. Structure of the Catalytically Active Copper-Ceria Interfacial Perimeter. *Nat. Catal.* **2019**, *2019*, 334−341.



https://doi.org/10.1021/acs.jpcc.6c00835
J. Phys. Chem. C 2026, 130, 7136−7147

5.1 High-Coverage Oxidation

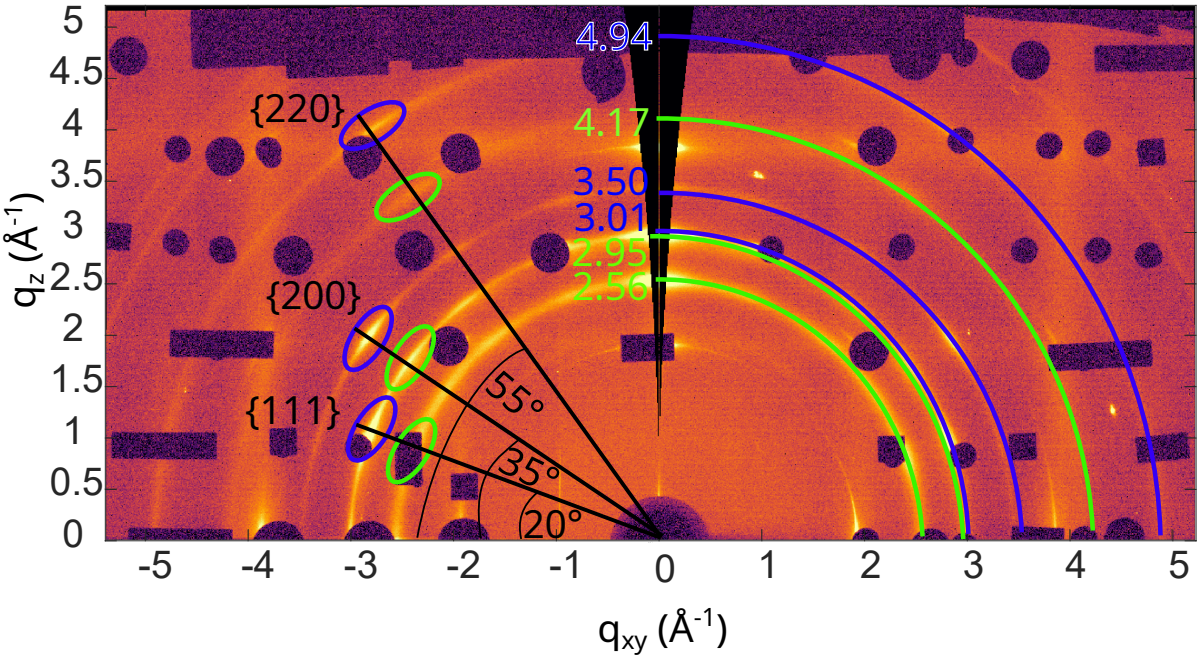


Figure 5.1: HEXRD detector image for a sample grown in similar conditions as sample C from [10]. The image is a sum of all images taken during a sample rotation by 180 ° around the surface normal.

In addition to the studies detailed in the publication above [10], another sample of Cu NPs on rutile TiO_2 was investigated. It was grown similarly to sample C in [10] (400°C substrate temperature during growth, grown in the same mobile chamber), but roughly triple the amount of Cu was deposited. Crucially, it was not heated in O_2 for oxidation, but stored in ambient air at room temperature for about two months. Afterwards, it was measured with atomic force microscopy (AFM) (see Figure 5.2) and HEXRD (see Figure 5.1). The sample exhibits a high NP coverage and particle diameters of about 60 nm (though diameters measured with AFM are prone to overestimation). The HEXRD data show (111)-, (200)- and (220)-type Bragg peaks and powder rings. For a cubic crystal system, the angles between the [111] axis and selected other axes are: $[111]\sphericalangle[\bar{1}11] \simeq 70$ °, $[111]\sphericalangle[200] \simeq 55$ ° and $[111]\sphericalangle[220] \simeq 35$ °. Hence, from the HEXRD data in Figure 5.1 it can be concluded that both the Cu_2O and the Cu NPs are [111]-oriented. Additionally, as both oxide and metallic Cu feature the same epitaxy (seen by the alignment of the peaks), it can be assumed that core-shell particles of Cu/oxide have formed. This measurement complements the results presented in [10], verifying that the large NPs grown at 400 °C can oxidize to epitaxial Cu_2O, not seen for the smaller NPs.

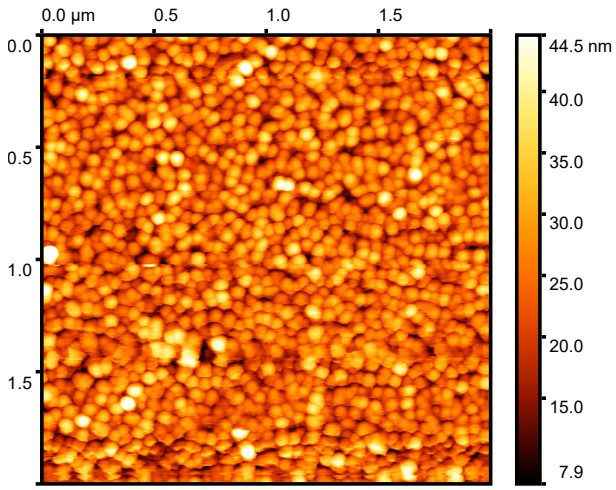


Figure 5.2: AFM image of the sample grown similarly to sample C in [10].

Chapter 6

Article II: Structure and Reactivity of Cu and Cu Oxide Nanoparticles on Anatase $TiO_2(101)$ for Cysteine Degradation

Structure and Reactivity of Cu and Cu Oxide Nanoparticles on Anatase TiO_2(101) for Cysteine Degradation

Daniel Silvan Dolling[1,2*];
Miguel Blanco Garcia[1,2]
Ming-Chao Kao[1,2]
Mona Kohantorabi[1]
Lydia J. Bachmann[1,2]
Luis-Felipe Mochalski[1,2]
Luisa K. Wartner[1,2]
Eleonora Spurio[4,5]
Arti Dangwal[1]
Joris W. Fuchs[1,2]
Mais Jamil A. Ahmad[1]
Arno Jeromin[1]
Ying Kong[6]
Dmitri Novikov[3]
Thomas F. Keller[1,2]
Volkmar Koller[3]
Olof Gutowski[3]
Paola Luches[5]
Vedran Vonk[1]
Andreas Stierle[1,2]
Heshmat Noei[1†]

[1]Centre for X-ray and Nano Science CXNS,
Deutsches Elektronen-Synchrotron DESY,
Notkestr. 85, 22607 Hamburg, Germany

[2]Fachbereich Physik, Universität Hamburg,
Notkestraße 9-11, 22607 Hamburg, Germany

[3]Deutsches Elektronen-Synchrotron DESY,
Notkestr. 85, 22607 Hamburg, Germany

[4] Dipartimento FIM, Università degli Studi di Modena e Reggio Emilia,
Via G. Campi 213/a, 41125 Modena, Italy
[5] Istituto Nanoscienze, CNR (NANO-CNR), Via G. Campi 213/a, 41125 Modena, Italy
[6] Laboratory of Industrial Chemistry, Ruhr-Universität Bochum,
Universitätsstr. 150, 44801 Bochum, Germany

September 23, 2026

Abstract

Copper and copper oxide nanoparticles supported on TiO_2 are of interest for various applications ranging from organic pollutant degradation to photocatalytic virus inactivation. We investigated the growth, structure and heterogeneous oxidation of Cu nanoparticles on anatase $TiO_2(101)$ single crystals as well as the surface reactivity of Cu and Cu-oxide nanoparticles. Thereby, we focused on cysteine adsorption and its photocatalytic degradation, as a biologically relevant sulfur-containing amino acid and model compound for thiol-containing biomolecules. Cu NPs were grown by physical vapor deposition under ultra-high vacuum (UHV) conditions at different growth temperatures and characterized using high-energy X-ray diffraction (HEXRD), grazing-incidence X-ray diffraction (GIXRD), scanning electron microscopy (SEM) and X-ray photoelectron Spectroscopy (XPS). We found out that below 200 °C, no epitaxial particles are formed, whereas higher temperatures (200 °C - 400 °C) lead to well defined epitaxial nanoparticles with $Cu[470]||TiO_2(101)$ out-of-plane and $Cu[100]||TiO_2[010]$ in-plane orientations. The oxidation of Cu NPs was studied by exposing them to 1 bar O_2 at room temperature for up to 2 hours and monitoring the size changes of the NPs. We found that the oxidation is rapid in the first hour and then slows down significantly, allowing metallic Cu to still be detected even after one week of exposure to ambient conditions. Additionally, larger NPs favor the formation of epitaxial Cu_2O shells. The adsorption of cysteine amino acid on the Cu(-oxide) NPs on TiO_2 was investigated using infrared reflection-absorption spectroscopy (IRRAS) and XPS, revealing dissociative adsorption. Sulfur oxidation occurs even under ambient dark conditions, evidencing intrinsic catalytic activity, which is further enhanced under white light and ultraviolet (UV) irradiation. These findings reveal structure–reactivity relationships in Cu/Cu_2O–TiO_2 hetero-structures and underscore their potential for photocatalysis and self-disinfecting surfaces.

1 Introduction

Copper and its oxides are well known for their antiviral and antibacterial properties, more recently including the inactivation of SARS-CoV-2 [18, 47, 33]. The use of nanoparticles (NPs), compared to thin films, offers a higher surface-to-volume ratio and enhances the surface reactivity. In particular, combining Cu oxides with TiO_2 has attracted significant interest due to the dark and photo-reactivity of the resulting heterostructures. The antiviral properties of TiO_2 under UV light are well known [5, 31, 30] and for visible light activity, it has been shown that Cu oxide on TiO_2 is photoactive in the visible light spectrum, deactivating bacteria and degrading organic dyes [36, 37]. In 2022 it was shown that TiO_2 decorated with Cu oxide particles effectively inactivate SARS-CoV-2 [40]. Remarkably, this system exhibits activity not only under visible light but also in the dark, albeit with reduced efficiency compared to illuminated conditions. This activity was attributed to changes in the oxidation state of Cu: A mixture of Cu(I) and Cu(II) was proposed to act as electron storage, being able to either accept photoelectrons by locally reducing, or giving them away by locally oxidizing. The combination of visible light driven activity and catalytic func-

*silvan.dolling@desy.de
†heshmat.noei@desy.de

tionality under dark conditions makes this system highly promising for indoor self-disinfection surfaces. In this context, Cu oxides alone are known to exhibit degradation activity toward organic molecules, both as individual phases and in mixed oxide systems [18, 47].

To systematically study the self-cleaning and antiviral properties of the Cu(-oxide)/TiO_2 system, well defined model systems are required. Here, we present results of metallic Cu NPs grown on atomically flat anatase TiO_2(101) single crystal substrates and their subsequent oxidation. Recently, the growth and oxidation of Cu NPs on rutile TiO_2(110) single crystals were investigated [12]. It was found that the Cu NPs grow predominantly adopt a [111]-oriented, while oxidation at atmospheric pressure (1 bar O_2) leads to the formation of polycrystalline copper oxide. In contrast to rutile, anatase TiO_2 is often considered the more catalytically active polymorph [55, 66]. Moreover, unlike the relatively flat rutile (110) surface, the anatase (101) surface is possesses an intrinsic stepped structure [62]. This stepped topology is expected to influence Cu nanoparticle epitaxy by modifying surface diffusion pathways and nucleation sites [17]. Anatase TiO_2 features a tetragonal unit cell with lattice parameters a = b = 3.78 Å, c = 9.50 Å [7], Cu features a face-centered cubic (fcc) crystal system with the lattice parameter a_{Cu} = 3.62 Å [27] and Cu_2O crystallizes in a body-centered cubic lattice with constant a_{Cu_2O} = 4.26 Å. For all crystal systems, bulk coordinate Miller indices are used. The oxidation of bulk and thin film Cu has been studied since the mid of the last century, dating back to the theoretical investigation of metal oxidation by Cabrera and Mott [39]. It is known that the Cu oxidation is limited by ion transport and electric fields at room temperature and ambient conditions, yielding an inverse logarithmic rate law. The expected thickness of oxide before the surface is passivated is about 2-5 nm at time scales of a few hours, as demonstrated in experiments on bulk Cu, Cu thin films and Cu NPs [35, 58]. In case of nanoparticles, the situation is more complicated, as particle size, the interaction with the substrate and facet distribution influence the oxidation process. In particular, the presence of edges and associated Cu defects accelerates oxidation. It is well established that more defective Cu lattices oxidize more rapidly [51], that the Cu[111] facet is more resistant against oxidation than the Cu[200] and Cu[220] facets [11], and that smaller grains or particles tend to oxidize more readily [11]. At elevated temperatures, Kirkendall void formation has been reported [1, 41, 42]. At room temperature and below 100 °C, stable oxide shells of 3 - 5 nm are typically formed on nanoparticles with sizes of 10-100 nm [42, 49], while even very small Cu NPs of only 3 nm in diameter can develop stable core-shell metal-oxide structures [45]. Most studies show that below 100 °C, Cu_2O is the predominant oxide formed, while CuO formation becomes dominant at higher oxidation temperatures or longer oxidation times at atmospheric conditions [45, 48]. Additionally, Cu_2O can grow epitaxial on the nanoparticle (it expands by intake of oxygen) or the particles fracture, creating a polycrystalline system [16]. Furthermore, the oxidation of Cu nanoparticles can be influenced heavily by the compressive stress of the oxide-copper interface [10].

Considering the antiviral properties of the Cu(-oxide)/TiO_2 system, three main routes towards degradation of organics are possible: (1) Reactive oxygen species (ROS), generated at the surface, attack viruses or bacteria [20]. (2) Direct interactions between adsorbed molecules

and Cu or TiO_2 lead to organic degradation [57]. (3) Cu ions are released, interacting with the virus [60]. For our system, we exclude the latter possibility, as we are investigating a solid model system without a liquid carrier substance for Cu ions. In reports about pure TiO_2 systems for photocatalysis, ROS generation is often considered to be the main mechanism driving the degradation of organic substances [3, 32, 61, 65]. In Cu(-oxide)/TiO_2 systems, recent studies indicate that direct interaction with Cu constitutes the dominant pathway for antiviral activity [21, 57]. To understand the interaction of the nanoparticle system with viruses and bacteria, amino acids can be used as model system. In particular, cysteine is known to be one of the key building blocks of the SARS-Cov-2 spike protein. Moreover, with its three functional groups (amino, thiol and carboxyl), cysteine allows for clear distinction of specific interactions with the surface during adsorption. The adsorption of cysteine on Cu and bare TiO_2 single crystals has been studied. On Cu, it has been reported that cysteine interacts through its amine group, the deprotonated thiol group, and the dissociated sulfur group [26, 29]. On TiO_2, cysteine is known to interact through the carboxyl group and the thiol group, however, several studies report dissociative adsorption through deprotonation of the thiol group [2]. Our recent study combined density functional theory (DFT) with infrared reflection-absorption spectroscopy (IRRAS) and XPS to provide a detailed atomistic picture of cysteine adsorption. The results show that cysteine can adsorb on the surface in four distinct geometries, differing in molecular orientation and binding motifs. Notably, this study also identifies the presence of cystine dimers (two cysteine molecules that are bonded by an S=S bridge), indicating that dimerization via disulfide bond formation can occur alongside molecular adsorption [5]. A similar study was done for the adsorption of cysteine on anatase TiO_2(101) [4]. It was found that cysteine adsorbs primarily in bidentate modes coordinated over Ti atoms: either adsorbing with the deprotonated carboxyl group oxygen (COO^-) and the amino group (NH_2), or adsorbing with thiol group (S-H) and amino group (NH_2). In the latter case, the carboxyl group is found to stay protonated. In contrast to the findings on pristine rutile, protonated amino groups are only a minor contribution. Here, we investigate the adsorption of cysteine on a model system consisting of Cu (-oxide) NPs supported on single crystalline anatase TiO_2(101). This approach enables us to disentangle and distinguish the interaction of the amino acid with both the Cu species and the oxide substrate, in analogy to a recent report on cysteine adsorption on pristine anatase TiO_2(101) [4].

2 Results

For the investigation of Cu NPs on anatase TiO_2(101) single crystals, Cu was deposited by thermal evaporation in an ultra-high vacuum (UHV) chamber with a base pressure of 10^{-10} mbar [56]. To achieve different growth conditions, the substrate temperature during growth was varied for different samples. Oxidation of the NPs was achieved either by flooding a UHV chamber with molecular oxygen or by exposing the samples to air. The interaction with cysteine was investigated by gas-phase adsorption with IRRAS and by XPS. The experiments were performed in three different steps: 1) growth of Cu NPs, 2) their oxidation, and 3) the (photo-)catalytic interaction with cysteine. After the

Table 1: Sample Overview: Coverages and particle sizes are acquired via SEM once the samples had reached a stable oxidation state after several months at ambient conditions. Further details are provided in the SI, see Figures S1 to S4. For sample D, SEM images do not resolve particles. The coverage is estimated based on comparison to the other samples' growth conditions. The samples names are categorized in terms of the substrate temperature during Cu growth: 'A' for 400 °C growth, 'B' for 100 °C growth, 'C' for 200 °C growth and 'D' for 20 °C growth. Samples with the same growth temperature are distinguished by a separate number.

Sample	Growth Temp. [°C]	Coverage [%]	NP diameter [nm]
A1	400	29 ± 2	21.6 ± 7.3
A2	400	52 ± 9	22.9 ± 10.7
A3	400	16 ± 5	22.0 ± 5.0
B1	100	12 ± 2	13.8 ± 5.8
B2	100	31 ± 5	7.9 ± 4.6
B3	100	42 ± 8	11.0 ± 4.3
C	200	64 ± 4	21.7 ± 10.0
D	20	30 ± 20	not resolved

experiments, the samples were characterized using SEM. The resulting coverage and NP diameters are represented in Table 1. Notably, the samples were fully oxidized at the time the SEM images were taken (they were stored at ambient conditions for months). Based on the substrate temperature during Cu growth, the samples are categorized as: 'A' for 400 °C growth, 'B' for 100 °C growth, 'C' for 200 °C growth and 'D' for 20 °C growth, and are subsequently numbered.

2.1 Cu NPs Structure: Epitaxy and Shape

From a detailed analysis of XRD patterns, the epitaxy, average size and the average shape of the NPs can be determined. Samples A1 and B1 were investigated with HEXRD, samples A2, B2 and C were investigated with GIXRD.

Samples A1 and B1 were measured by HEXRD with a 2D detector directly after growth, experiencing only 4 hours of exposure to air prior the measurement. To elucidate the NP epitaxy, in-plane rocking scans over 180° were performed in grazing incidence geometry. The results for sample A1 can be seen in Figure 1 and Table S1, as well as in Figures S5 to S7. The Cu NPs are grown in a tilted epitaxy, aligning the Cu[100] direction with an angle of 8° ± 0.5° to the TiO_2[100] axis, see Figure 1. This can be described as Cu[470]||TiO_2(101). From the positions of the Cu Bragg peaks relative to the TiO_2 substrate, the in-plane NP epitaxy is determined to be Cu[001]||TiO_2[010]. This results in an in-plane lattice mismatch of 4.4% (along TiO_2[010], the lattice constant is 3.78 Å [7] and the lattice constant of Cu is 3.62 Å [6]). Along the the $TiO_2[10\bar{1}]$ direction, the specific tilt of Cu with respect to TiO_2 can be explained by row-matching: The projected lengths of 2.5 times the Cu lattice constant (along Cu[010], 2.5×3.62 Å$/\cos 30° = 10.45$ Å) is very close to the projected distance of the TiO_2 along TiO_2[100] (9.50 Å$/\cos 22° = 10.24$ Å), resulting in a mismatch of only 1.9 %. Similar effects have been seen for Ni on Yttria stabilized zirconia [63]. Similar effects have been seen for Ni on Yttria stabilized zirconia [63].

The NP sizes were calculated via Scherrer's formula for different Bragg peaks (see Table S1). The resulting sizes were used to propose a particle shape based on the sizes along different directions, see Figure 1 c). The same scans were performed for sample B1, but no sign of epitaxial Cu was found, see Figures S5 and S7. The signals seen in the scans for sample B1 are all related

to substrate defects and background (e.g. from scattering from the central beam-block). While XPS confirms the presence of Cu (see Figure 4 and the oxidation discussion later), and SEM clearly demonstrates particle formation (see Figure S3), HEXRD analysis indicates the absence of epitaxial Cu-related reflections. In combination, this leads to the conclusion that the NPs are polycrystalline with small enough grain sizes to not be resolved by HEXRD.

To further investigate the epitaxy and growth, we performed in-situ GIXRD on samples A2 and B2 and C. To elucidate the epitaxy, in-plane rocking scans were performed over a range of 190 ° to detect Cu(111), Cu(200) and Cu(220) planes. The results can be seen in Figures S8 to S10. Sample A2 was found to contain nanoparticles with Cu[111], Cu[100], Cu[110] and Cu[112] orientation in addition to the [470]-oriented NPs, see Figures S8 to S10. By comparing the integrated Bragg peak intensities from the different NP orientations with strongest intensity ([470], [111] and [100]), their relative coverage is determined, see Figure S14 and table S2 and SI (Equations (2) to (4)) for details. It is found that about 54% ± 5% of the Cu is [470]-oriented, roughly 28% ± 5% is [111]-oriented and 18% ± 5% is [100]-oriented. This is in contrast to the HEXRD measurements of sample A1, where only [470]-oriented particles were found. As both samples A1 and A2 were grown at the same conditions and feature particles of similar size, it would be expected to also find the same NP epitaxies. As coverage is the main differentiator of the samples, it can be assumed that all minor epitaxies only form at high coverages (of about 50 %).

By comparing the in-plane rocking scans of sample A2 and C it becomes apparent that both feature the same epitaxies, see Figures S11 to S13. In contrast, sample B2 only features a very weak signal from Cu[470]. This is in line with the HEXRD measurements for samples B1 (which was also grown at 100 °C), which featured no diffraction signal of Cu. The GIXRD finding thus confirm the polycrystalline nature of the Cu NPs grown at 100 °C.

Table 2: Calculated percentage of the different Cu orientations (out-of-plane orientations) for sample A2. The values were determined by comparing in-plane rocking scan peak areas, see Figure S14 and table S2.

Orientation	[470]	[100]	[111]
Percentage	54 ± 6	18 ± 2	28 ± 3

For sample C, radial scans were conducted to determine the sizes of the NPs with different epitaxial orientations. It is found that the [470]-oriented particles exhibit an avarage diameter of 8.7 nm, which is smaller than that of Cu(100), 9 nm and Cu(111), 11 nm, as shown in Figure 2. Compared with SEM (see Table 1), which show a mean NP size of 7.9 nm. These results suggest that the [470] orientation is the main epitaxy, in line with the XRD results.

2.2 Cu NP Oxidation

The oxidation of sample C was studied in detail by GIXRD. The oxidation was performed by flooding the UHV growth chamber with 1 bar O_2 at room temperature. Radial scans through the Cu(200) and Cu(220) peaks belonging to the [470]-, [111]- and [100]-oriented particles were performed. The resulting NP size changes can be seen in Figure 2. The oxidation kinetic is similar for all of epitaxies: After 60 minutes exposure to oxygen the NP diameters decrease by 1-2 nm, but further 60 minutes exposure to O_2 does not change the NP size anymore. The small increase in size seen in Figure 2 after 120 minutes

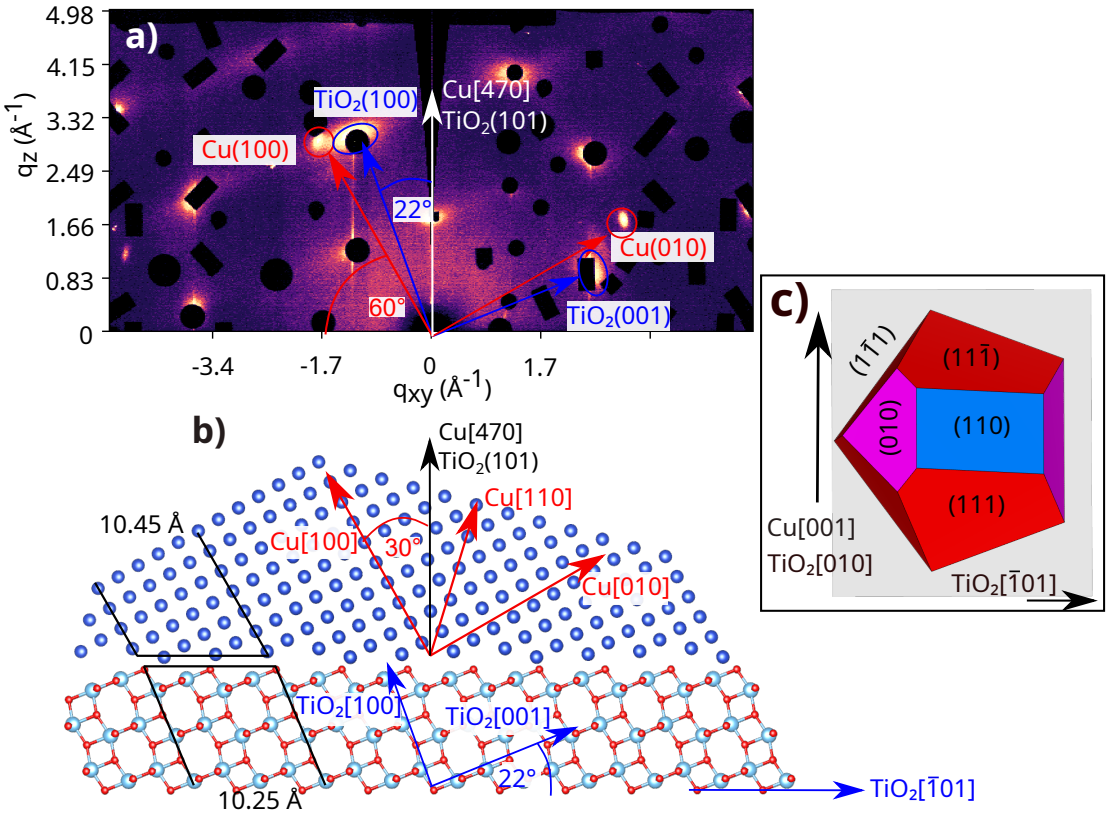


Figure 1: a) HEXRD measurement of sample A1 depicting the HL map $TiO_2(101)$, measured after the sample was exposed to ambient conditions for about 4 hours. The Bragg peaks belonging to the Cu NPs are marked, as well as the $TiO_2(100)$ direction. The image is a sum of 500 individual images taken $\pm 5°$ along the $TiO_2[010]$ axis (with the $TiO_2[101]$ surface normal). b) Schematic depiction of the Cu NPs based on sizes calculated for different Bragg peaks, see Table S1. The calculated NP sizes along different Bragg peaks were used to generate a schematic view of the NP. The NP dimension (number of atoms) was scaled down by a factor of 10. c) Proposed particle shape based on sizes calculated for different Bragg peaks (see Table S1). The different facet types are color labeled: red is [111]-type, blue is [110]-type and purple is [100]-type. They correspond to the Bragg peak that was used to calculate the NP size in the specific direction. The model does not represent the actual facets, but only the general shape of the NPs.

exposure to oxygen is within the error bars of its size after 60 minutes oxidation, thus a constant size can be assumed.

The oxidation of sample A1 was studied by repeating the HEXRD measurements (initially done after 4 hours exposure to air) for a second time after 11 days of exposure to air (264 h total exposure). The resulting average NP diameters calculated from the Bragg peak widths can be found in Table S1 and Figure 2. It can be seen that only minor changes in nanoparticle size occure after 264 hours of air exposure. Notably, the sizes calculated from the $(11\bar{1})$ and the (111) reflections decrease, whereas the size derived from the $(1\bar{1}1)$ reflection remains unchanged. Due to the [470]-particle orientation, the directions are not symmetric. As illustrated by the model in Figure 1 b) and c), the $(1\bar{1}1)$ facet is small and almost vertical to the substrate, whereas the $(11\bar{1})$ and the (111) facets are larger and more parallel to the substrate. Therefore, it can be assumed that the top of the NPs is more readily oxidized than the sides.

Both in the HEXRD data after 4 hours as well as after 264 hours, $Cu_2O(111)$ Bragg peaks from epitaxial Cu_2O are found, see Figure 3: The oxide has the same orientation as the metallic Cu, seen by the radial alignment of the $Cu_2O(111)$ peak with the Cu(111) peak. As it will be discussed later with XPS data, it is assumed that core-shell particles of Cu/Cu_2O are formed. The size of the oxide NPs is calculated to be 10.4 ± 2.9 nm after 4 h and 10.8 ± 2.8 nm after 264 h exposure to air. This size reflects the average size for pure Cu_2O NPs as well as for Cu/Cu_2O core-shell particles. The oxidation is further studied by comparing the ratio of the oxide peak and the metallic Cu peak areas, see Figure 3. It is found that the ratio of Cu oxide/Cu increases after 264 hours oxidation compared to 4 hours oxidation, indicating an ongoing oxidation. As the average particle size barely changes, this highlights that small particles oxidize faster, changing the NP ensemble such that the average diameter does not change.

To evaluate the chemical state of the samples, XPS was employed on sample A1 and B1 after the HEXRD measurements. The resulting Cu 2p spectra can be seen in Figure 4, details on the fitting can be found in Table S7: Both samples feature CuO as well as Cu_2O. The amount of Cu found either as CuO or as Cu and Cu_2O can be determined by fitting the $2p_{3/2}$ peaks, resulting in percentages relative to all available Cu signal. Due to the peak structure, Cu and Cu_2O can not be distinguished. Sample A1 features 41 ± 5 % CuO, sample B1 contains of 54 ± 5 % CuO, indicating that the smaller NPs of sample B1 either feature a faster oxidation kinetic or evolve towards a different end-state of the oxide.

UV-Vis To investigate the interaction with visible light directly, UV visible reflectance spectra (UV-Vis) were taken for samples A1, A2, B2 and C (as well as for clean anatase as reference), after about 6-8 months of exposure to air, see Figure 5. Samples A1 and B2 exhibit no features that would distinguish them from clean anatase. Sample C features a very broad peak, between 600 nm and 1000 nm. In comparison with literature [9, 15, 46, 34] this is consistent with localized surface plasmon resonances (LSPR) from metallic Cu cores of Cu / Cu-oxide core / shell NPs. The broad feature indicates a non-homogeneous size distribution and partial oxidation. Sample A2 has a smaller peak around 450 nm. This can be attributed to Cu_2O excitons, as seen in literature [52, 19, 50]. The UV-Vis measurements were complemented with XPS

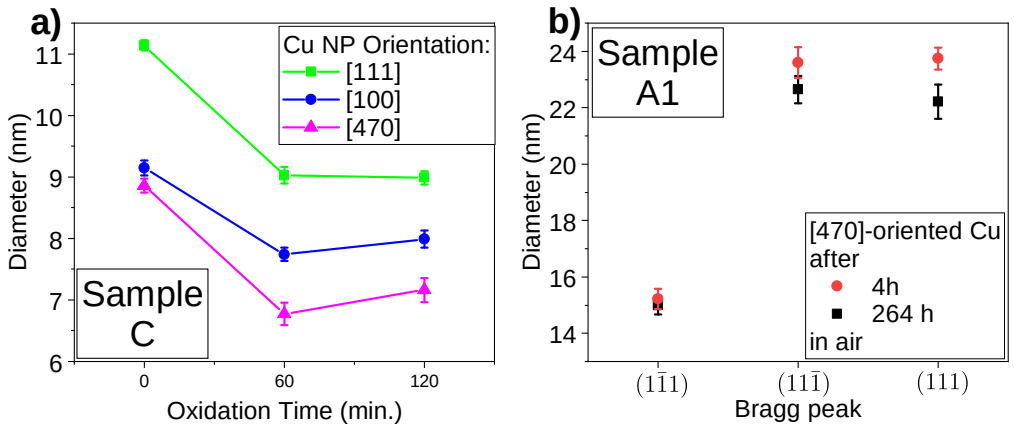


Figure 2: a) NP diameters calculated from radial scans for sample C during different oxidation times for different NP orientations (out-of-plane) after oxidation in 1 bar O_2 at room temperature (see Table S3. b) NP diameters in radial direction for sample A1, for 4 h and 264 h oxidation at room temperature in air, see Table S1.

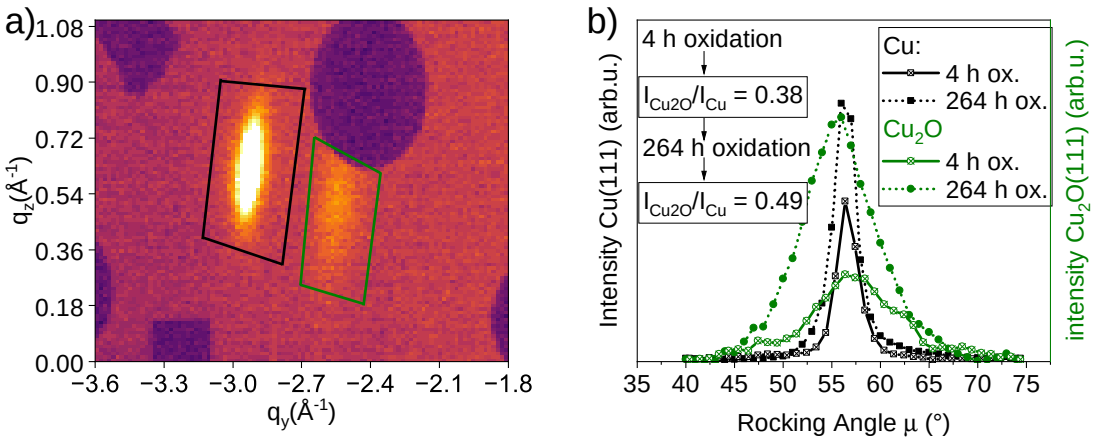


Figure 3: a) HEXRD data for sample A after 4 hours at air, depicting the Cu(111) and Cu_2O(111) Bragg peaks and the regions of interest (ROIs) used to integrate intensity. Both peaks belong to [470]-oriented Cu or Cu_2O NPs. b) Comparison of the integrated intensity for Cu and Cu_2O according to the ROIs in a). The intensity is plotted over 35 ° in-plane rotation. To evaluate the intensity, a linear background was subtracted from the curves and the intensity was integrated.

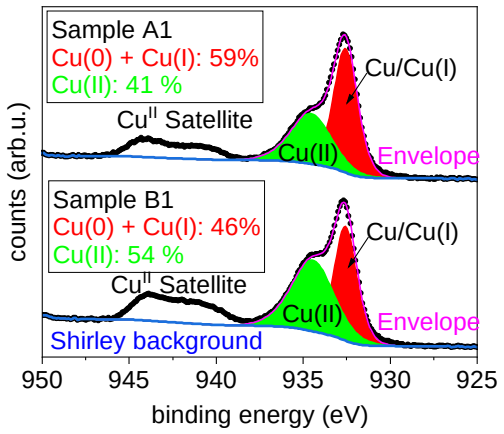


Figure 4: Deconvoluted Cu 2p core-level XP spectra for sample A1 and B1 after 7 h oxidation at ambient conditions, demonstrating the presence of Cu(II), Cu(I) and Cu(0).

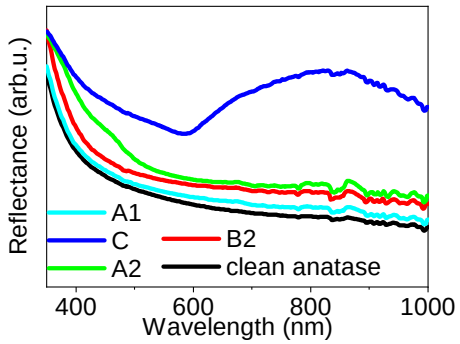


Figure 5: UV-Vis reflectance data for the different samples.

measurements of the samples oxidation state either in the month before or on the months after the UV-Vis measurements. The results can be seen in Figure S18 and Table S8. Within the probing depths of the XPS (3-5 nm), sample A1 features the highest amounts of either metallic Cu or Cu_2O, about 64%. The other samples all feature close to 70% CuO. Considering that sample A1 and A2 are very similar and sample A1 even features less CuO, it is not obvious why only sample A2 exhibits the Cu_2O exciton. Both samples were grown and oxidized under similar conditions and feature similar results in SEM analysis. The main differentiator is the lower coverage for sample A1. This could cause a loss of signal intensity, meaning that a possible Cu_2O peak for sample A1 is lost in the background. Similar reasoning can be applied to the plasmonic resonance of sample C, which also features the highest coverage of all samples (see Table 1). In combination with particles of the same size as for sample A1 and A2, this may lead to detectable plasmonic resonances from metallic Cu cores.

2.3 Cysteine Adsorption, Dark, and Light-Induced Degradation

Amino acids, as the fundamental building blocks of organic matter, serve as important model systems for investigating the interactions of organic compounds with metal-oxide surfaces. Cysteine in particular is known to be abundant in the SARS-CoV-2 spike protein, which is relevant for the infectiousness of the virus.

Adsorption: IRRAS & XPS To investigate the interaction between cysteine and the Cu(-oxide)/TiO_2 system, we employed IRRAS and XPS. Samples A3, B3 and D were used to study the adsorption with IRRAS and XPS and samples A2 and B2 were used to study the N1s spectra in detail with XPS. Samples B3 and D were oxidized for 2 h in 1 bar O_2 at room temperature, whereas sample A3 was not exposed to air prior to cysteine adsorption. Samples A2 and B2

were exposed to air for several weeks before cysteine adsorption. Cysteine was evaporated onto the samples by evaporation in an UHV chamber.

An overview of the samples' state before cysteine exposure can be seen in Figure 7, incorporating the NP characterization measurements from above as well as XPS measurements either directly before adsorption or directly after adsorption (see Figure S19 and Table S10). It is known that sample A2 features epitaxial core-shell particles of oxide and metallic Cu and does not have CuO. Sample A3 is metallic before cysteine deposition and both A2 as well as A3 feature epitaxial NPs of about 20 nm diameter. Samples B2, B3 and D feature polycrystalline NPs with a roughly 50/50 mixture of Cu_2O and CuO and diameters of 7-12 nm.

The IRRAS results for cysteine adsorption on samples A3, B3, D and a clean anatase crystal can be seen in Figures 6 and S21. All measurements were performed at room temperature. After dosing 100 L cysteine, several bands are found: The symmetric and asymmetric stretching vibration of COO^- are seen at 1366 and 1575 cm^{-1} for all samples. A signal from a protonated carboxyl group is only detected on sample A3 at 1740 cm^{-1}. At 1513 and 1610 cm^{-1} the symmetric and asymmetric bending vibrations of NH_3^+ is found on samples A3 and D, whereas the NH_2 stretching band is only found for sample A3 (at 1539 cm^{-1}). Surprisingly, a strong vibrational band is found at 2208 cm^{-1} for sample B3 and D. This wavenumber is characteristic for the C≡N stretching vibration of nitrile. No S-H stretching band was detected, but this may be caused by the low intensity of this vibration. The IRRAS results show that the cysteine molecules predominantly adsorb with their deprotonated carboxyl end-group. Furthermore, samples B3 and D feature significant amounts of nitrile signal. After dosing 550 L cysteine, the NH_3^+ band increases significantly for all samples. Additionally, the NH_2 signal and the CH_2 band also increase. Similar effects have been reported for the adsorption of amino acids on metallic Cu single crystals when going from lower to higher coverages [26, 28, 29]. Two recent studies on cysteine adsorption on clean rutile and anatase highlighted that on anatase, vibrational signals associated with C=O and NH_2 groups dominate over those of COO^- and NH_3^+, while the opposite behavior is observed on rutile [5, 4].

Here, on the Cu oxide/TiO_2 system, however, we observe a mixture of both contributions: Weak signals from from NH_3^+ and C=O and a strong COO^- band. This means that the molecules most likely adsorb with the deprotonated carboxyl group on the copper atoms. The lack of a strong NH_2 band and the appearance of a nitrile signal indicate that the amino group is also interacting with the NPs, and that at least some cysteine molecules are fractured to create nitrile. In combination, this implies that cysteine preferentially binds to the Cu nanoparticles, leaving minimal contribution from direct adsorption on the TiO_2 surface.

After the adsorption of cysteine for the IRRAS measurements, the samples were transferred via UHV to the XPS setup.

The S 2p spectra for the clean reference show two different S $2p_{3/2}$ peaks (see Figure S28 and Table S13) at 161.5 eV and at 163.7 eV. In accordance with literature [5], these peaks are attributed to intact thiol groups (R-S-H, 163.7 eV) and to sulfur adsorbed on Ti (R-S-Ti, 161.5 eV). For the Cu NP samples, cysteine adsorption leads to distinct changes in the core level spectra. In sample B3 in Figure 8, a new peak emerges at 167.1 eV. Although, the features between 165 eV and 160 eV appear similar to those

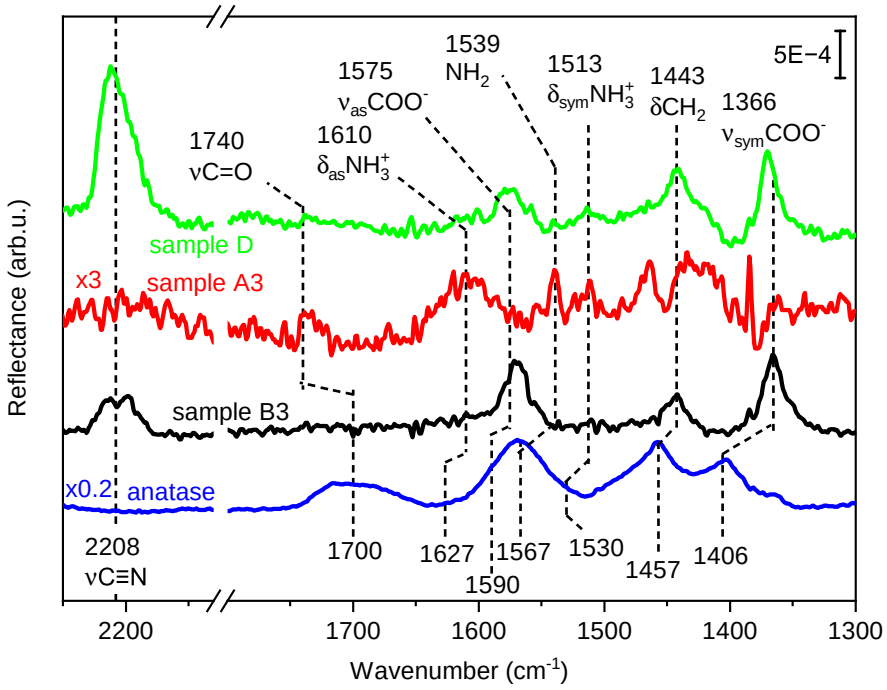


Figure 6: IRRAS measurement of cysteine adsorption on samples A3, B3, D and a clean anatase crystal (withouth NPs). P-polarized spectra [43] are shown after dosing 100 L cysteine (only 5 L on the clean anatase crystal), the full dataset can be found in the SI.

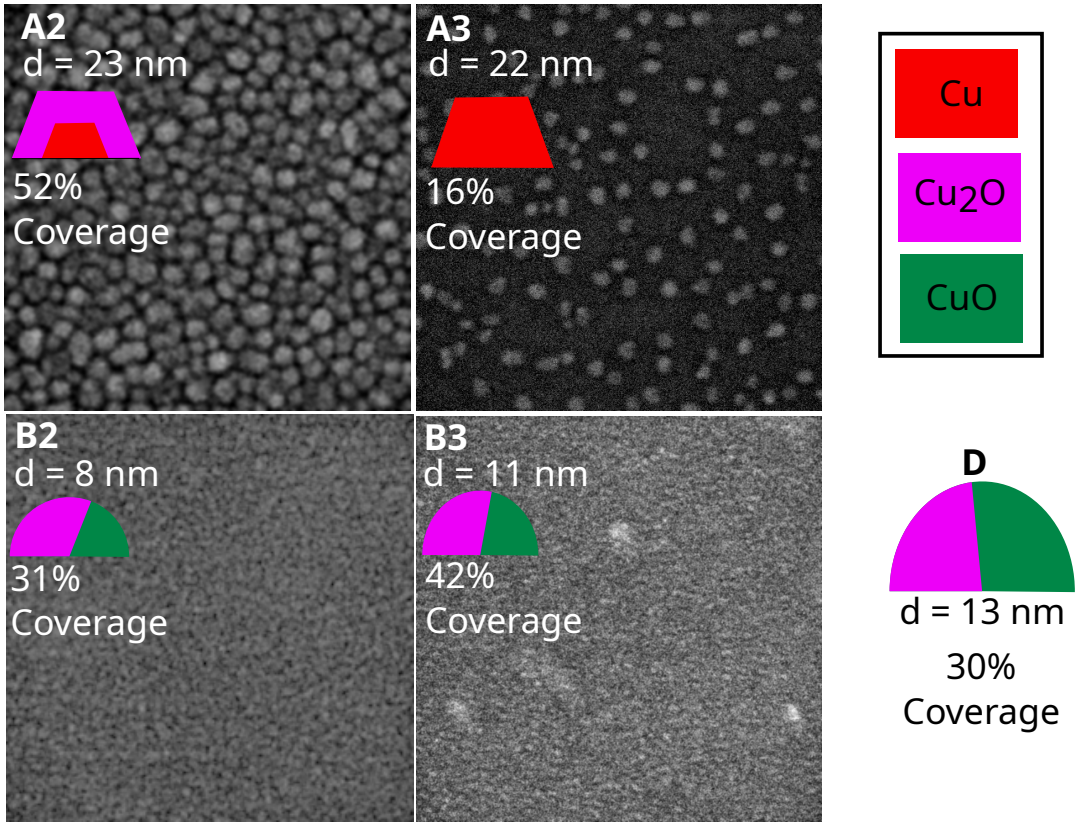


Figure 7: Overview of the samples used for cysteine dosing. The SEM images are 500 nm by 500 nm in size. The drawings represent the different oxidation state (colors) and the polycrystalline or epitaxial state (round shape or angular shape). Detailed information about coverage and particle size can be found in Table 1 and in Table S10 and Figure S19.

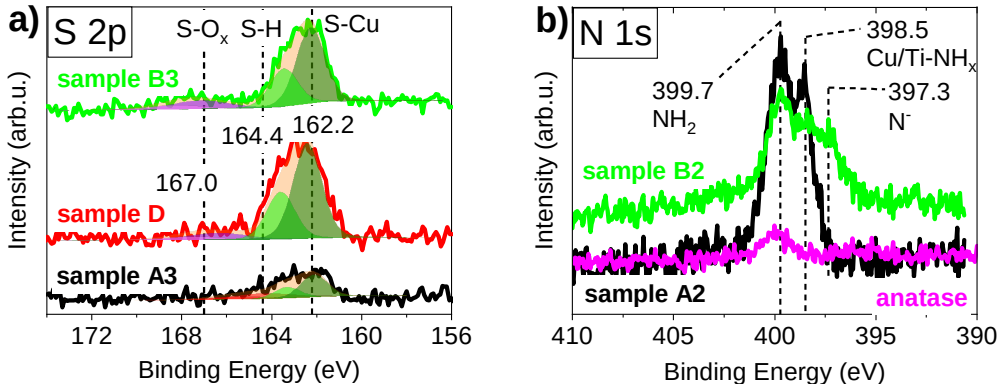


Figure 8: a) S 2p spectra after cysteine adsorption (550 L) with fits: The green doublet belongs to S adsorbed on Cu or Ti, the purple doublet to oxidized sulfur. The envelope is orange. b) The N1s spectrum after cysteine adsorption.

observed for bare TiO_2, they can not be accurately described using the same fitting functions. Further details of the fitting parameters are provided in the supporting information (Figure S20). Within the resolution limits, contributions from S–H and Ti–S species are plausible; however, the dominant feature of the peak is attributed to a new doublet with the S $2p_{3/2}$ component located at 162.3 eV. For the adsorption of amino acids on single crystalline copper, the core level region between 161.8 eV to 162.8 eV is commonly assigned to the interaction of a deprotonated thiol group (thiolate) with Cu atoms (R-S-Cu) [59, 38, 29, 28]. In contrast, a fully dissociated (atomic) sulfur atom bound to Cu would be expected at a lower binding energy of approximately 161 eV. Hence, the present peak is best described as arising from a deprotonated thiol group and still remaining part of the intact cysteine molecule adsorbed to Cu, rather than isolated sulfur atoms. The weak peak at 167.1 eV can be attributed to oxidized forms of sulfur. Due to the large FWHM, the best explanation for this peak is a combination of different oxidation states SO_x (typically fully oxidized sulfate is attributed to binding energies of 168 eV and partial oxidation between 165 eV and 167 eV [22, 4]). Notably, this feature has not been seen for cysteine adsorption on bare anatase and only appears after photocatalytic reaction under UV irradiation in air, following photo-oxidation of cysteine [4]. Sample D exhibits the same features in the S 2p peak after cysteine adsorption as sample B3, with a blue shift in binding energy up to 0.5 eV, which is considered to be due to broad peak shapes and slightly different chemical environments. Sample A3 shows a different behavior. While the S-Cu peak remain unchanged, no oxide-related peak is observed between 166 eV and 169 eV. Instead, a feature at 164.4 eV is detected, attributed to protonated sulfur (R-S-H) (see Table S12), similar to the bare anatase sam-

ple. Since sample A3 was not oxidized prior to cysteine dosing, this behavior can be explained by the limited availability of oxygen for cysteine oxidation via sulfur group. As a result, the surface is characterized by a mixture of S-Cu and protonated thiol groups (R-S-H). The O 1s and C 1s spectra are provided in the SI, while they are not discussed in detail. These data complement the analysis but due to overlapping contributions from Cu oxide, TiO_2 lattice and carboxyl group for O 1s, as well as carbon contamination arising from NP oxidation prior to cysteine dosing, they do not allow for a clear, independent interpretation of the adsorption and photocatalytic processes.

A comparison between the Cu 2p spectra before and after cysteine adsorption reveals a reduction of CuO to Cu and Cu_2O for sample B3 and D, visible in the decrease of the CuO satellite, see Figure S29 and Figure S31. Similar effects have been reported for the adsorption of organics with thiol groups on CuO surfaces [64, 8]. On the reduced surface, thiols form Cu-S bonds, forming self-assembled monolayers. The subsequent formation of sulfur dimers is also reported [64]; however, no corresponding dimer-related peaks are observed in the present data. As sample A3 was not oxidized prior to cysteine adsorption, no reduction can be observed (see Figure S30).

Taken with a laboratory XPS source, the N 1s spectra of samples A3, B3 and D do not feature a good peak-to-noise ratio and do not allow for a full characterization. To investigate the N 1s core level, cysteine was dosed on samples A2, B2 and a clean anatase substrate and their spectra were taken with synchrotron radiation at high energy XPS beamline P22 at PETRA III (details are found in the SI/Methods section). The resulting N 1s spectra can be seen in Figure 8. The clean substrate features only one peak at 399.9 eV, which can be attributed to neutral NH_2 [14, 23, 26, 28, 29, 38, 59]. Notably, a NH_3^+ peak at about 402 eV is missing, in line with recent reports about cysteine adsorption on bare anatase and rutile [5, 4]. Both sample B2 and A2 feature a peak at 399.8 eV, assigned to NH_2 by comparison with the bare anatase. Furthermore, a new peak at 398.4 eV is found and sample B2 features an additional peak at 397.1 eV. An XP peak at 397 eV has been reported as atomic nitrogen impurity for the adsorption of cysteine on Cu [26]. Considering the cleaning of the crystals in HNO_3 before sputtering and annealing, a contribution from such a bulk nitrogen contamination can not be ruled out. On the other hand, XP peaks between 398 eV and 398.6 eV have been reported for unsaturated nitrogen compounds, usually a C=N double bond [14], and a peak at 397.7 eV was reported as a decomposition product of glycine on Cu [13]. Additionally, a similar peak at 398 eV was reported for alanine on Cu after annealing [25], thus also being related to amino acid decomposition. The lack of the signal at 397 eV for sample A2 can be related to variations in particle size and oxidation state, as sample B2 features much smaller NPs than sample A2, see Table 1. Overall, we assume that the N 1s peaks at 398.5 eV and 397.3 eV are related to cysteine decomposition products, as this would correlate with the nitrile signal observed in IRRAS. This further confirms a higher degree of cysteine decomposition on Cu/TiO_2 compared to bare anatase TiO_2, indicating that Cu/TiO_2 is a more efficient catalyst for amino acid decomposition.

In combination, the IRRAS and the XPS results show that cysteine adsorbs dissociatively on the Cu oxide NPs: The presence of a nitrile band in IRRAS as well as the XP peak from

amino group decomposition products reveal a strong interaction between the amino group and the copper NPs. The absence of an IR band associated with the S-H vibration for oxidized NPs, together with S 2p peaks shifted relative to those observed for intact cysteine adsorption on pristine anatase, indicates that most thiol groups are deprotonated and preferentially adsorbed on Cu atoms rather than on TiO_2, thereby inducing partial reduction of copper NPs.

These findings can be compared to the adsorption of cysteine on clean anatase single crystals as reported in [4]. It was found that the N 1s core level spectrum is mostly comprised of NH_2 with only minor NH_3^+ contribution. The S 2p spectra contain both Ti-S and S-H contributions. In contrast, the N 1s features two additional lower binding energy peaks in the Cu NPs system, related to the degradation of cysteine, as well as an additional higher energy S 2p peak, corresponding to oxidized sulfur. In combination, this means that cysteine degrades upon adsorption on the Cu NP system, whereas on the pure TiO_2 single crystal the adsorption leaves the molecule intact and only UV irradiation can denature it.

Photocatalysis To investigate the photocatalytic properties of the system, samples A3, B3, D and a pristine anatase TiO_2(101) crystal (without Cu NPs) were exposed to air and light after the cysteine adsorption. This was done by exposing them to four steps of ambient conditions, each for 30 minutes: without light (dark), with a broadband white LED (450 nm to 800 nm with UV cutoff filter), with UV-A (365 nm) and again with the LED. The XP S 2p spectra were monitored for changes. For the pristine anatase TiO_2 crystal, the S 2p, O 1s and C 1s spectra can be seen in Figures S25, S28 and S35. As discussed above, upon adsorption cysteine is present both in form of intact thiol groups (R-S-H, 163.7 eV) as well as in a Ti-bound state (R-S-Ti, 161.5 eV). After the first ambient exposure (in dark conditions), the Ti-bound cysteine species desorbs completely, and a peak corresponding to oxidized sulfur appears at 167.4 eV. Subsequent exposure to LED light does not lead to significant changes in the spectra. Upon UV light irradiation, the peaks for S-H vanish and the oxide peak shifts to 168.4 eV. As described recently [4], this behavior is explained by the UV-induced oxidation of the thiol group.

For the Cu NP samples, the full spectra for the S 2p evolution can be seen in SI (Figures S26 and S27), as well as the C 1s, O 1s and Cu 2p spectra (Figures S22 to S24 and S29 to S34). The S 2p spectra for sample B3 can be seen in Figure 9: Upon exposure to ambient conditions, the oxide contribution increases over time (see Figure 10 for a comparison of the oxide areas of all samples). It is at 19% of the total peak area directly after adsorption (before exposure to air), rising to 61% oxide peak after all exposure steps. The same behavior is seen for sample D. Samples B3 and D exhibit an approximately linear increase in oxidized sulfur with ambient exposure time (see Figure 10), indicating that sulfur oxidation proceeds independently of light. Sample A3 features a different initial behavior, starting from protonated thiol groups and without detectable copper oxide after dosing cysteine. Sulfur oxide species become detectable after exposure to white light. At the same time, the Cu 2p spectrum clearly shows a CuO signal in Cu 2p core level (Figure S30). These results suggest that the presence of surface oxide is required to activate sulfur oxidation under these conditions.

Comparing the relative amount of SO_x for the

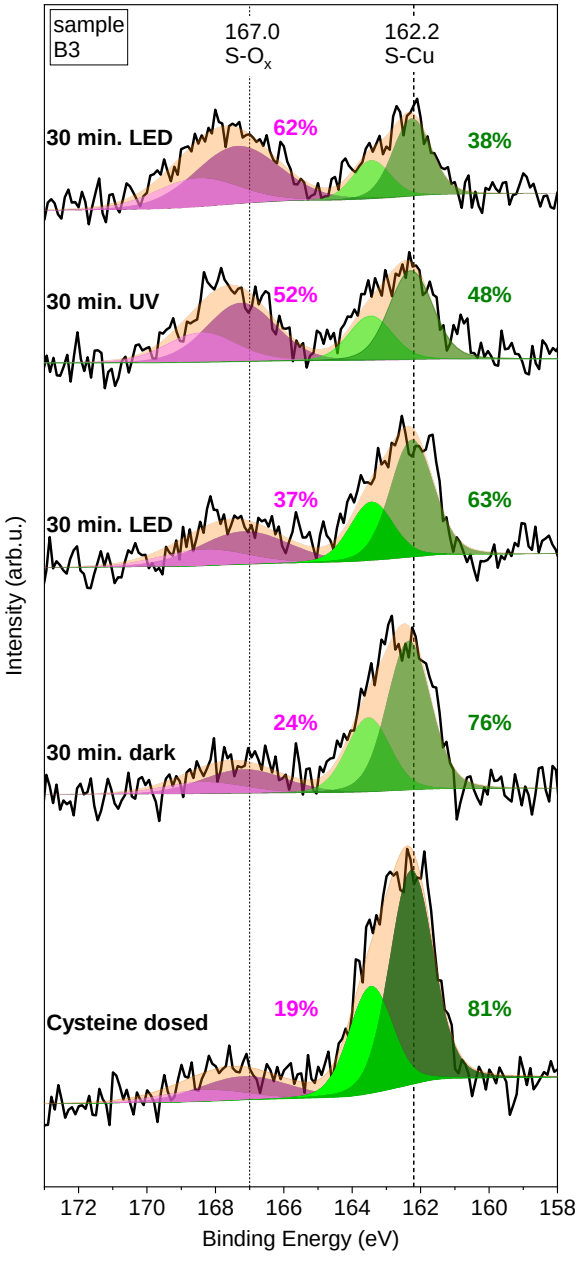


Figure 9: S 2p spectra of sample B3 during photocatalysis measurements. 'oxidized' means the oxidized sample before cysteine dosing. The green shaded are fits for sulfur bound to Cu and Ti, the purple shaded are the doublets for oxidized sulfur.

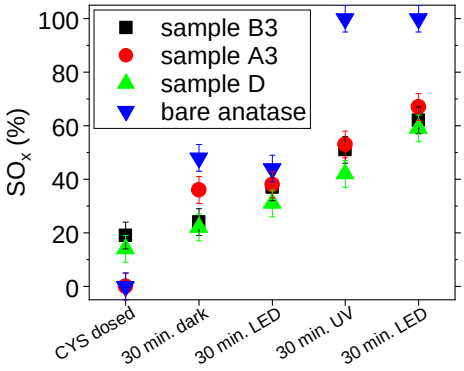


Figure 10: Development of the SO_x signal area compared to the full S 2p signal.

Cu NP samples with the bare anatase sample, we see that the oxidized NPs result in oxidized sulfur upon adsorption. For pristine anatase, about half of the sulfur is oxidized after the first ambient exposure in dark and this does not change with LED exposure. At the same time, the Cu samples have less oxidized sulfur, but the percentage increases with each step. Upon UV light exposure, all sulfur is oxidized on the bare TiO_2, whereas the Cu NP samples continue to oxdize the thiol groups almost linearly with time. In contrast to our previous report on the photocatalytic degradation of cysteine on an anatase single-crystal surface [4], complete oxidation of sulfur is not observed for the Cu NP samples. The Cu 2p core level peak of all samples shows Cu oxidation to CuO upon ambient exposure, as expected for Cu, see SI Figures S29 to S31. The C1s spectra show no changes after light treatment and ambient exposure (see Figures S22 to S25). In our recent publication on anatase TiO_2 [4], it was shown that the thiol group of cysteine undergoes stepwise oxidation under UV irradiation to sulfonic acid (-SO_3H), via the intermediates sulfinic acid (-SO_2H) and sulfenic acid (-SOH). In contrast, the present Cu NP system already induces partial oxidation of the thiol group upon cysteine adsorption. Further oxidation of the thiol group is seen upon ambient exposure, independent of illumination conditions. On the other hand, the Cu NP system does not oxidize all sulfur, but only up to 60 %. This can be related to the strong interaction of the thiol group with copper: About half of the cysteine molecules is either adsorbed with the thiol group or has a dissociated thiol group. These sulfur atoms will not oxidize further. Although the sulfur atoms do not undergo further oxidation, this level of transformation can already denature sulfur-containing viral structures even in the dark. The dissociation of cysteine alone indicates that the molecule is no longer intact in its native form. The other half of the molecules, adsorbed with the carboxylic group, can undergo oxidation similar to our observations on the pristine anatase system.

3 Discussion & Conclusion

We investigated the growth and oxidation of Cu NPs on anatase TiO_2(101) single crystals. The main epitaxy of Cu is found to be Cu[100]||TiO_2[010] in-plane and Cu[470]||TiO_2(101) out-of-plane, similar to reports of Cu growth on vicinal ZnO [17]. Moreover, the presence of several minor NP orientations was identified, including Cu[111] and Cu[200]. This is significantly different to Cu growth on rutile, where Cu[111] is reported to be the main out-of-plain orientation [12]. The dependence of the Cu growth on the substrate temperature revealed that at 100 °C, only polycrystalline Cu NPs are formed, indicated by the lack

of diffraction signal from Cu. In contrast, samples grown at 200 °C and 400 °C feature epitaxial NPs. This is in contrast to the findings on rutile, where the epitaxial Cu with (111) orientation can already be formed at 100 °C[12]. The oxidation of the NPs proceeds relatively fast within the first hour of exposure to air or ambient pressure oxygen, leading to a significant reduction in the Cu NP size as measured by XRD. However, this process slows down afterwards, indicating no further changes in the average Cu size observed during the second hour of oxidation. As the intensity of the Cu peaks continues to decrease, while the average particle diameter remains relatively stable, it can be concluded that small Cu NPs in the ensemble of differently sized particles oxidize faster than larger ones. On the timescale of a week, Cu NPs oxidize further and the ratio of Cu_2O to Cu changes from 0.38 to 0.49, determined by the intensity of the corresponding Cu(111) and Cu_2O(111) Bragg peaks. Cu_2O is found to grow epitaxially, suggesting that the NPs develop an oxide shell that preserves the same epitaxy as the underlying Cu NP core itself. After several months of storage in air, the sample featuring the highest Cu coverage is still found to exhibit plasmonic resonances originating from a metallic Cu cores, indicating resistance to complete oxidation. This was not the case for samples grown at 400 °C, even though average particle size and coverage were similar. These differences highlight the importance of the growth conditions on the final oxidation state of the sample. No epitaxial CuO is found on any sample; however, CuO formation is confirmed in Cu 2p core level spectrum, in particular through the presence of Cu^{II} satellite features, indicating a polycrystalline CuO phase. The amount of CuO depends on the growth temperature and O_2 pressure: The higher the growth temperature, the larger the NPs become and the less CuO (and the more Cu_2O) is formed upon oxidation. Additionally, at a low Cu growth temperature of 100 °C, no epitaxial Cu was observed in X-ray diffraction. In combination with the higher amount of CuO seen in XPS (compared to samples grown at 400 °C) it can be assumed that the polycrystalline Cu is more readily oxidized to CuO, whereas epitaxial NPs preferentially form Cu_2O (see Figure 3).

We investigated the adsorption of the amino acid cysteine on the Cu(oxide) nanoparticle on TiO_2(101) with XPS and IRRAS. Cysteine was found to adsorb exclusively with deprotonated carboxyl group and protonated and amino group. The Cu oxide NPs were reduced by the cysteine adsorption, indicating an interaction between the thiol group and the CuO that results in a Cu-S bond. Both IRRAS and XPS reveal strong signs of decomposition of cysteine upon adsorption for all samples: A nitrile signal is found in the IRRAS spectra, the XPS N 1s spectrum include signals from reduced nitrogen and the S 2p spectrum showed denatured sulfur. In combination, this suggests that cysteine can adsorb in two different configurations: either with the thiol group interacting with Cu atoms, indicated by a Cu-S bond, or by adsorption via the carboxyl group. These findings can be compared to our recent study of the adsorption of cysteine on single crystalline anatase TiO_2[101] [4]: there, cysteine was found to adsorb either in molecular state with the thiol and amino group or with deprotonated carboxyl group by interaction of carboxyl and thiol group with the five fold coordinated Ti atoms. Additionally, photooxidation of the cysteine under air and UV irradiation oxidized the thiol group. Comparing this to the present results of the adsorption of cysteine on the Cu/TiO_2 system reveals similarities in the

absence of NH^{3+} and the presence of a deprotonated carboxyl group. Thus, it can be assumed that cysteine can partially adsorb on the TiO_2 substrate. The differences can be found in the Cu-S bond and the oxidized sulfur in the S 2p spectra. The former indicates the binding of cysteine to Cu NPs. The latter is assumed to be the start of the thiol group oxidation that was seen in [4] during photo-oxidation and only under UV irradiation. This process can occur directly upon adsorption on the Cu NPs, as the formation of Cu-S bonds can promote the reduction of CuO to Cu_2O or metallic Cu, releasing oxygen species that may facilitate the oxidation of thiol groups not bound to Cu. This is backed up by the fact that the sample with only metallic Cu (no oxide) showed no sign of sulfur oxidation prior to air exposure, see Figure 8. The presence of the nitrile signal also suggests that some cysteine molecules are broken upon adsorption, to form the nitrile bond. The photocatalytic properties of the Cu/TiO_2 system were probed by following the evolution of core level spectra obtained by XPS after exposure to ambient conditions in various light environments. The S 2p signal revealed oxidation of the sulfur upon ambient exposure, independent of light conditions, for samples A3, B3 and D with oxidized Cu. A fully oxidative transformation of the thiol group to sulfonic acid (SO_3H) upon UV light exposure has been reported for $TiO_2(101)$ [4] and was also seen here by exposing a pristine anatase $TiO_2(101)$ crystal to UV light. No full oxidation of the sulfur is achieved for the Cu NP samples, however, as parts of the sulfur stay bound to Cu even after all oxidation steps. This can be related to the differences in adsorption configuration on Cu NPs compared to the TiO_2 surface: The cysteine bound with the thiol group to Cu will not undergo oxidation, whereas cysteine that adsorbed on TiO_2 or with a different adsorption orientation will be oxidized.

In conclusion, this study demonstrates that the Cu growth temperature can be used to control the resulting morphology and epitaxy, enabling either epitaxial NPs or highly dispersed polycrystalline Cu. Furthermore, the oxidation state of the NPs evolves only slowly after the initial formation of an oxide layer, remaining largely stable over timescales of up to seven days in air. Additionally, it is found that the growth temperature can be used to engineer NPs that result in Cu/oxide - core/shell particles which are stable on timescales of months.

Cysteine adsorbs either by forming Cu-S bonds or via its deprotonated carboxyl group on $Cu(\text{-oxide})/TiO_2(101)$, similar to the adsorption behavior on pure TiO_2. In the presence of CuO, parts of the cysteine are oxidized upon adsorption in UHV. In under ambient conditions, the sulfur is further oxidized irrespective of light exposure. This highlights the advantages of the usage of Cu NPs on TiO_2 for the degradation of organic matter over pure TiO_2. It remains an open question if the Cu-S bonds would be able to break to free adsorption sites or if the system would be in need of external cleaning.

4 Methods

All experiments were performed at DESY NanoLab [56], PETRA III beamline P23 (proposal R-20240689), PETRA III beamline P22 [54] (proposal R-20250686) and PETRA III beamline P07-DESY [53] (beamtime 11023950).

4.1 Nanoparticle Growth

The nanoparticles were grown in a mobile UHV chamber [44] with an electron beam evaporator using a Cu rod at beamline P23 and in a UHV chamber with an electron beam evaporator using Cu in a Mo crucible at NanoLab. The anatase $TiO_2(101)$ crystals were prepared prepared in the NanoLab UHV system before Cu growth and before being inserted into the mobile UHV chamber. They were cleaned four times in an ultrasonic bath; first in acetone, then in ethanol, afterward in isopropyl, and finally in deionized water and then introduced to a UHV system. They were sputtered at 1kV acceleration voltage and 10 mA emission in 10^{-6} mbar Ar and subsequently annealed first at 400 °C in $2{\cdot}10^{-7}$ mbar O_2 for 10 minutes, then at 650 °C in UHV for 15 minutes. The sputter/anneal cycle was repeated five times. For use in the mobile UHV chamber, the samples were degased and sputter/annealed once after insertion. High-purity oxygen (99.999%) was used for the sample preparation. Oxidation of the samples was achieved either by exposure to air or by exposure to molecular oxygen in a UHV chamber. For the different samples, the oxidation was done differently:

- Sample A1, B1, C were grown with a Cu crucible evaporator, and were transported through air to HEXRD or GISXRD measurements, respectively.
- Samples A2 and B2 were grown in a mobile UHV chamber with a Cu rod evaporator and could be characterized by GIXRD before exposure to oxygen.
- Samples A3, B3 and D were grown with a Cu crucible evaporator and were used for cysteine adsorption measurements. After growth in UHV, samples B3 and D were oxidized at ambient conditions. Sample A3 was not oxidized before cysteine exposure.

4.2 X-Ray Diffraction Measurements

The XRD measurements at beamline P23 were done at a photon energy of 18 keV in grazing-incidence geometry. HEXRD measurements were performed at the PETRA III beamline P07 at 73.34 keV in a grazing incidence geometry (0.03°) at a sample-detector distance of 1.5 m, employing a flat-panel pixel detector. Both methods were used complementary to exploit the high-resolution of the GIXRD and the full reciprocal space imaging of HEXRD.

4.3 XPS

X-ray photo-electron measurements were performed at the dedicated HAXPES beamline (P22) at Petra III, DESY [54] and at DESY NanoLab [56]. At P22, a photon energy of 2.4 kV at an exit angle of 3° was employed. At NanoLab, an Al K_α source was used at 1.486 keV. Both setups employed hemispherical analyzer and all XPS spectra were fitted with CasaXPS software [24] using a Shirley background and a Gaussian-Lorentzian line profile, employing the Marquardt fitting algorithm. Peak position and FWHM were constrained, see SI for details. All spectra are normalized to Ti $2p_{3/2}$ (at 458.7 eV).

4.4 SEM

SEM images were obtained in secondary electron mode with a field emission instrument at an accelerator voltage of 5 kV, providing a nominal lateral resolution of 1.3 nm.

4.5 Cysteine Adsorption & Photocatalysis

Cysteine was dosed in UHV by heating cysteine powder in a glass vial connected to a leak valve to about 140 °C. For samples A3, B3 and D dosing was done in the following steps in a chamber with a base pressure of 10^{-9} mbar:

- 1 L cysteine ($2{\cdot}10^{-8}$ mbar, 66 s)
- +4 L cysteine ($1{\cdot}10^{-7}$ mbar, 53 s)
- +5 L cysteine ($1{\cdot}10^{-7}$ mbar, 66 s)
- +90 L cysteine ($1{\cdot}10^{-6}$ mbar, 60 s)
- +450 L cysteine ($1{\cdot}10^{-5}$ mbar, 60 s)

Samples A3 and B3 were exposed to cysteine in a chamber with a base pressure of 10^{-6} mbar. Cysteine was dosed for 26 minutes at a pressure of 10^{-3} mbar.

The photocatalysis experiments were performed by taking the samples with cysteine out of UHV for 30 minutes and exposing them to different light conditions:

- Dark conditions: The samples were put under a light cover.
- LED: The samples were exposed to a white broadband LED (ThorLabs MBB1L3, 470-850 nm, 80 mW) with a 450 nm highpass filter under a cover to avoid influences of other light sources. The lamp was positioned 10 cm above the sample.
- UV: The samples were exposed to a UV-A lamp (365 nm, 6 W) under a cover to avoid influences of other light sources. The lamp was positioned 10 cm above the sample.

After the 30 minutes exposure, the samples were put in UHV again.

4.6 UV-Vis

UV-Vis spectroscopy measurements were performed employing a xenon lamp for non-polarized white light, an ORIEL-MS257 monochromator and a silicon photodetector. The measurements were done in relfection mode with an incidence angle of 10 °.

5 Acknowledgement

This work is supported by the Initiative and Networking Fund of the Helmholtz Association of German Research Centers (HGF) under the CORAERO project (KA1-Co-06).

We acknowledge DESY (Hamburg, Germany), a member of the Helmholtz Association HGF, for the provision of experimental facilities. Parts of this research were carried out at PETRA III using beamlines P07, P23 and P22 and DESY NanoLab. Beamtime was allocated for proposals R-20250686, R-20240689 and 20010075.

We thank Bastian Mei and Martin Muhler for helpful discussions.

References

[1] David Albinsson, Sara Nilsson, Tomasz J. Antosiewicz, Vladimir P. Zhdanov, and Christoph Langhammer. “Heterodimers for in Situ Plasmonic Spectroscopy: Cu Nanoparticle Oxidation Kinetics, Kirkendall Effect, and Compensation in the Arrhenius Parameters”. In: *The Journal of Physical Chemistry. C, Nanomaterials and Interfaces* 123.10 (2019), pp. 6284–6293. ISSN: 1932-7447. DOI: 10.1021/acs.jpcc.9b00323.

[2] Evren Ataman, Cristina Isvoranu, Jan Knudsen, Karina Schulte, Jesper N. Andersen, and Joachim Schnadt. "Adsorption of L-Cysteine on Rutile TiO_2(110)". In: *Surface Science* 605.1-2 (2011), pp. 179–186. ISSN: 00396028. DOI: 10.1016/j.susc.2010.10.017.

[3] Tadeusz Bak, Janusz Nowotny, Nikolaus J. Sucher, and Eric Wachsman. "Effect of Crystal Imperfections on Reactivity and Photoreactivity of TiO_2 (Rutile) with Oxygen, Water, and Bacteria". In: *The Journal of Physical Chemistry C* 115.32 (2011), pp. 15711–15738. ISSN: 1932-7447. DOI: 10.1021/jp2027862.

[4] Miguel Blanco Garcia, Daniele Perilli, Chiara Daldossi, Aldo Ugolotti, Daniel Dolling, Andreas Stierle, Annabella Selloni, Cristiana Di Valentin, and Heshmat Noei. "Adsorption and Sulphur-Selective Photooxidation of Cysteine on Anatase TiO_2(101)". In: *Accepted for: Journal of the American Chemical Society* tba.tba (2026), tba. DOI: tba.

[5] Miguel Blanco Garcia, Daniele Perilli, Chiara Daldossi, Aldo Ugolotti, Martina Giordano, Daniel Silvan Dolling, Michael Wagstaffe, Mona Kohantorabi, Andreas Stierle, Cristiana Di Valentin, and Heshmat Noei. "Unraveling the Role of the Multifunctional Groups in the Adsorption of L-Cysteine on Rutile TiO_2(110)". In: *Journal of the American Chemical Society* 147.44 (2025), pp. 40158–40170. DOI: 10.1021/jacs.5c07119.

[6] Setia Budi, Wisnu Ari Adi, Yusmaniar, Zahra Fairuza, Imam Basori, and Akrajas Ali Umar. "Structural Analysis of Nanocrystalline Cu_2O Prepared by Electrodeposition at Different Temperatures". In: *International Journal of Electrochemical Science* 17.3 (2022), p. 22033. ISSN: 14523981. DOI: 10.20964/2022.03.08.

[7] Jeremy K. Burdett, Timothy Hughbanks, Gordon J. Miller, James W. Richardson, and Joseph V. Smith. "Structural-Electronic Relationships in Inorganic Solids: Powder Neutron Diffraction Studies of the Rutile and Anatase Polymorphs of Titanium Dioxide at 15 and 295 K". In: *Journal of the American Chemical Society* 109.12 (1987), pp. 3639–3646. ISSN: 0002-7863. DOI: 10.1021/ja00246a021.

[8] L. Carbonell, C. M. Whelan, M. Kinsella, and K. Maex. "A Thermal Stability Study of Alkane and Aromatic Thiolate Self-Assembled Monolayers on Copper Surfaces". In: *Superlattices and Microstructures* 36.1-3 (2004), pp. 149–160. ISSN: 07496036. DOI: 10.1016/j.spmi.2004.08.033.

[9] George H. Chan, Jing Zhao, Erin M. Hicks, George C. Schatz, and Richard P. van Duyne. "Plasmonic Properties of Copper Nanoparticles Fabricated by Nanosphere Lithography". In: *Nano Letters* 7.7 (2007), pp. 1947–1952. ISSN: 1530-6984. DOI: 10.1021/nl070648a.

[10] Chun-Hua Chen, Tomohiko Yamaguchi, Ko-ichi Sugawara, and Kenji Koga. "Role of Stress in the Self-Limiting Oxidation of Copper Nanoparticles". In: *The Journal of Physical Chemistry B* 109.44 (2005), pp. 20669–20672. ISSN: 1520-6106. DOI: 10.1021/jp0546498.

[11] Juan J. Diaz Leon, David M. Fryauf, Robert D. Cormia, Min-Xian Max Zhang, Kathryn Samuels, R. Stanley Williams, and Nobuhiko P. Kobayashi. "Reflectometry-Ellipsometry Reveals Thickness, Growth Rate, and Phase Composition in Oxidation of Copper". In: *ACS Applied Materials & Interfaces* 8.34 (2016), pp. 22337–22344. DOI: 10.1021/acsami.6b06626.

[12] Daniel Silvan Dolling, Miguel Blanco Garcia, Mona Kohantorabi, Yufeng Zhai, Benedikt Sochor, Mohammad Ebrahim Haji Naghi Tehrani, Jan-Christian Schober, Ming-Chao Kao, Jagrati Dwivedi, Arno Jeromin, Olof Gutowski, Dmitri V. Novikov, Thomas F. Keller, Stephan V. Roth, Andreas Stierle, and Heshmat Noei. "In-Situ Growth and Oxidation of Cu Nanoparticles on Rutile TiO_2(110)". In: *The Journal of Physical Chemistry C* 130.20 (2026), pp. 7136–7147. ISSN: 1932-7447. DOI: 10.1021/acs.jpcc.6c00835.

[13] Tugce Eralp, Andrey Shavorskiy, Zhasmina V. Zheleva, Vinod R. Dhanak, and Georg Held. "Hydrogen Bond-Induced Pair Formation of Glycine on the Chiral Cu{531} surface". In: *Langmuir : the ACS Journal of Surfaces and Colloids* 26.13 (2010), pp. 10918–10923. ISSN: 0743-7463. DOI: 10.1021/la1012796.

[14] M. Furukawa, H. Fujisawa, S. Katano, H. Ogasawara, Y. Kim, T. Komeda, A. Nilsson, and M. Kawai. "Geometrical Characterization of Pyrimidine Case Molecules Adsorbed on Cu(110) Surfaces: XPS and NEXAFS Studies". In: *Surface Science* 532-535 (2003), pp. 261–266. ISSN: 00396028. DOI: 10.1016/S0039-6028(03)00464-3.

[15] T. Ghodselahi, H. Zahrabi, M. Heidari Saani, and M. A. Vesaghi. "CO Gas Sensor Properties of Cu@CuO Core–Shell Nanoparticles Based on Localized Surface Plasmon Resonance". In: *The Journal of Physical Chemistry C* 115.45 (2011), pp. 22126–22130. ISSN: 1932-7447. DOI: 10.1021/jp204020j.

[16] Robert Gleißner, Simon Chung, Guilherme D. L. Semione, Leon Jacobse, Michael Wagstaffe, Steffen Tober, A. Joanne Neumann, Gökhan Gizer, Christopher M. Goodwin, Markus Soldemo, Mikhail Shipilin, Patrick Lömker, Christoph Schlueter, Olof Gutowski, Matthias Muntwiler, Peter Amann, Heshmat Noei, Vedran Vonk, and Andreas Stierle. "Role of Oxidation–Reduction Dynamics in the Application of Cu/ZnO-Based Catalysts". In: *ACS Applied Nano Materials* 6.9 (2023), pp. 8004–8016. ISSN: 2574-0970. DOI: 10.1021/acsanm.3c01306.

[17] Robert Gleißner, Heshmat Noei, Simon Chung, Guilherme D. L. Semione, E. Erik Beck, Ann-Christin Dippel, Olof Gutowski, Gökhan Gizer, Vedran Vonk, and Andreas Stierle. "Copper Nanoparticles with High Index Facets on Basal and Vicinal ZnO Surfaces". In: *The Journal of Physical Chemistry C* 125.42 (2021), pp. 23561–23569. ISSN: 1932-7447. DOI: 10.1021/acs.jpcc.1c08008.

[18] Mohsen Hosseini, Alex W. H. Chin, Saeed Behzadinasab, Leo L. M. Poon, and William A. Ducker. "Cupric Oxide Coating That Rapidly Reduces Infection by

SARS-CoV-2 via Solids". In: *ACS Applied Materials & Interfaces* 13.5 (2021), pp. 5919–5928. DOI: 10.1021/acsami.0c19465.

[19] Lei Huang, Feng Peng, Hongjuan Wang, Hao Yu, and Zhong Li. "Preparation and Characterization of Cu_2O/TiO_2 Nano–Nano Heterostructure Photocatalysts". In: *Catalysis Communications* 10.14 (2009), pp. 1839–1843. ISSN: 15667367. DOI: 10.1016/j.catcom.2009.06.011.

[20] James A. Imlay. "Pathways of Oxidative Damage". In: *Annual Review of Microbiology* 57 (2003), pp. 395–418. ISSN: 0066-4227. DOI: 10.1146/annurev.micro.57.030502.090938.

[21] Hiroshi Irie, Kazuhide Kamiya, Toshihiko Shibanuma, Shuhei Miura, Donald A. Tryk, Toshihiko Yokoyama, and Kazuhito Hashimoto. "Visible Light-Sensitive Cu(II)-Grafted TiO_2 Photocatalysts: Activities and X-ray Absorption Fine Structure Analyses". In: *The Journal of Physical Chemistry C* 113.24 (2009), pp. 10761–10766. ISSN: 1932-7447. DOI: 10.1021/jp903063z.

[22] J.A. Reynaud, B. Malfoy, and P. Canesson. "Electrochemical Investigations of Amino Acids at Solid Electrodes: Part I. Sulfur Components: Cystine, Cysteine, Methionine". In: *J. Electroanal. Chem.* 1980.114 (1980), pp. 195–211. DOI: 10.1016/S0022-0728(80)80447-5.

[23] Mark J. Jackman, Karen L. Syres, David J. H. Cant, Samantha J. O. Hardman, and Andrew G. Thomas. "Adsorption of Dopamine on Rutile $TiO_2(110)$: a Photoemission and Near-Edge X-Ray Absorption Fine Structure Study". In: *Langmuir : the ACS Journal of Surfaces and Colloids* 30.29 (2014), pp. 8761–8769. ISSN: 0743-7463. DOI: 10.1021/la501357b.

[24] John Walton, Paul Wincott, Neal Fairley, and Alan Carrick. *Peak Fitting with CasaXPS: A Casa Pocketbook*. Casa XPS pocketbooks. Cheshire: Acolyte Science, 2010. ISBN: 9780954953317. URL: https://permalink.obvsg.at/AC13363835.

[25] G. Jones, L. B. Jones, F. Thibault-Starzyk, E. A. Seddon, R. Raval, S. J. Jenkins, and G. Held. "The Local Adsorption Geometry and Electronic Structure of Alanine on Cu(110)". In: *Surface Science* 600.9 (2006), pp. 1924–1935. ISSN: 00396028. DOI: 10.1016/j.susc.2006.02.033.

[26] Astrid Jürgensen, Hannes Raschke, Norbert Esser, and Roland Hergenröder. "An In Situ XPS Study of L-Cysteine Co-Adsorbed with Water on Polycrystalline Copper and Gold". In: *Applied Surface Science* 435 (2018), pp. 870–879. ISSN: 01694332. DOI: 10.1016/j.apsusc.2017.11.150.

[27] Alexander Khort, Sergey Roslyakov, and Pavel Loginov. "Solution Combustion Synthesis of Single-Phase Bimetallic Nanomaterials". In: *Nano-Structures & Nano-Objects* 26 (2021), p. 100727. ISSN: 2352507X. DOI: 10.1016/j.nanoso.2021.100727.

[28] Jeong Won Kim, Han-Na Hwang, and Chan-Cuk Hwang. "Adsorption of Cysteine on Cu(110) Studied by Core-Level Photoelectron Spectroscopy". In: *The Journal of Physical Chemistry C* 111.35

(2007), pp. 13192–13196. ISSN: 1932-7447. DOI: 10.1021/jp072496d.

[29] Jeong Won Kim, Young Mi Lee, Seung Mi Lee, Min Jung Son, Hyeseung Kang, and Yongsup Park. "Surface Reaction of Sulfur-Containing Amino Acids on Cu(110)". In: *Langmuir : the ACS Journal of Surfaces and Colloids* 26.8 (2010), pp. 5632–5636. ISSN: 0743-7463. DOI: 10.1021/la904496j.

[30] Mona Kohantorabi, Aldo Ugolotti, Benedikt Sochor, Johannes Roessler, Michael Wagstaffe, Alexander Meinhardt, E. Erik Beck, Daniel Silvan Dolling, Miguel Blanco Garcia, Marcus Creutzburg, Thomas F. Keller, Matthias Schwartzkopf, Sarathlal Koyiloth Vayalil, Roland Thuenauer, Gabriela Guédez, Christian Löw, Gregor Ebert, Ulrike Protzer, Wolfgang Hammerschmidt, Reinhard Zeidler, Stephan V. Roth, Cristiana Di Valentin, Andreas Stierle, and Heshmat Noei. "Light-Induced Transformation of Virus-Like Particles on TiO_2". In: *ACS Applied Materials & Interfaces* 16.28 (2024), pp. 37275–37287. DOI: 10.1021/acsami.4c07151.

[31] Mona Kohantorabi, Michael Wagstaffe, Marcus Creutzburg, Aldo Ugolotti, Satishkumar Kulkarni, Arno Jeromin, Tobias Krekeler, Martin Feuerherd, Alexander Herrmann, Gregor Ebert, Ulrike Protzer, Gabriela Guédez, Christian Löw, Roland Thuenauer, Christoph Schlueter, Andrei Gloskovskii, Thomas F. Keller, Cristiana Di Valentin, Andreas Stierle, and Heshmat Noei. "Adsorption and Inactivation of SARS-CoV-2 on the Surface of Anatase $TiO_2(101)$". In: *ACS applied materials & interfaces* 15.6 (2023), pp. 8770–8782. DOI: 10.1021/acsami.2c22078.

[32] Yang Li, Wen Zhang, Junfeng Niu, and Yongsheng Chen. "Mechanism of Photogenerated Reactive Oxygen Species and Correlation with the Antibacterial Properties of Engineered Metal-Oxide Nanoparticles". In: *ACS Nano* 6.6 (2012), pp. 5164–5173. DOI: 10.1021/nn300934k.

[33] Min Liu, Kayano Sunada, Kazuhito Hashimoto, and Masahiro Miyauchi. "Visible-light sensitive Cu(II)-TiO_2 with sustained anti-viral activity for efficient indoor environmental remediation". In: *Journal of Materials Chemistry A* 3.33 (2015), pp. 17312–17319. ISSN: 2050-7488. DOI: 10.1039/C5TA03756E.

[34] Zhonghua Liu, Bin Xu, Yuqing Cheng, Mengting Si, Xiangqian Chu, Mengtao Sun, and Yingcui Fang. "Spectral Analysis of Oxidation on Localized Surface Plasmon Resonance of Copper Nanoparticles Thin Film". In: *Spectrochimica Acta. Part A, Molecular and Biomolecular Spectroscopy* 303 (2023), p. 123202. DOI: 10.1016/j.saa.2023.123202.

[35] M.R. Pinnel, H.G. Tompkins, and D.E. Heath. "Oxidation of Copper in Controlled Clean Air and Standard Laboratory Air at 50°C to 150°C". In: *Applications of Surface Science* 1979.2 (1978), pp. 558–577.

[36] Snehamol Mathew, Priyanka Ganguly, Stephen Rhatigan, Vignesh Kumaravel, Ciara Byrne, Steven Hinder, John Bartlett, Michael Nolan, and Suresh Pillai. "Cu-Doped TiO_2: Visible Light Assisted Photocatalytic Antimicrobial Activity".

In: *Applied Sciences* 8.11 (2018), p. 2067. DOI: 10.3390/app8112067.

[37] Maria Guadalupe Méndez-Medrano, Ewa Kowalska, Bunsho Ohtani, Daniel Bahena Uribe, Christophe Colbeau-Justin, Sven Rau, José Luis Rodríguez-López, and Hynd Remita. "Heterojunction of CuO Nanoclusters with TiO_2 for Photo-Oxidation of Organic Compounds and for Hydrogen Production". In: *The Journal of Chemical Physics* 153.3 (2020), p. 034705. DOI: 10.1063/5.0015277.

[38] Christophe Méthivier, Vincent Humblot, and Claire-Marie Pradier. "l-Methionine adsorption on Cu(110), binding and geometry of the amino acid as a function of coverage". In: *Surface Science* 632 (2015), pp. 88–92. ISSN: 00396028. DOI: 10.1016/j.susc.2014.09.007.

[39] N. Cabrera and N. F. Mott. "Theory of the Oxidation of Metals". In: *Rep. Prog. Phys* 1949.12 (1949).

[40] Ryuichi Nakano, Akira Yamaguchi, Kayano Sunada, Takeshi Nagai, Akiyo Nakano, Yuki Suzuki, Hisakazu Yano, Hitoshi Ishiguro, and Masahiro Miyauchi. "Inactivation of Various Variant Types of SARS-CoV-2 by Indoor-Light-Sensitive TiO_2-Based Photocatalyst". In: *Scientific reports* 12.1 (2022), p. 5804. DOI: 10.1038/s41598-022-09402-7.

[41] Sara Nilsson, David Albinsson, Tomasz J. Antosiewicz, Joachim Fritzsche, and Christoph Langhammer. "Resolving Single Cu Nanoparticle Oxidation and Kirkendall Void Formation with In Situ Plasmonic Nanospectroscopy and Electrodynamic Simulations". In: *Nanoscale* 11.43 (2019), pp. 20725–20733. DOI: 10.1039/c9nr07681f.

[42] Sara Nilsson, Monia Nielsen, Joachim Fritzsche, Christoph Langhammer, and Shima Kadkhodazadeh. *Unravelling Competing Oxidation Mechanisms in Single Cu Nanoparticles*. 2022. DOI: 10.21203/rs.3.rs-1148708/v1.

[43] Heshmat Noei, Marcus Creutzburg, Gregor Vonbun-Feldbauer, and Andreas Stierle. "Revealing Formic Acid Adsorption Geometries on Magnetite (001) and (111) Surfaces by IRRAS Line Shape Analysis". In: *Physical Chemistry Chemical Physics : PCCP* (2026). DOI: 10.1039/d5cp00848d.

[44] P. Nolte, A. Stierle, N. Kasper, N. Y. Jin-Phillipp, H. Reichert, A. Rühm, J. Okasinski, H. Dosch, and S. Schöder. "Combinatorial High-Energy X-Ray Microbeam Study of the Size-Dependent Oxidation of Pd Nanoparticles on MgO(100)". In: *Physical Review B* 77.11 (2008). ISSN: 1098-0121. DOI: 10.1103/PhysRevB.77.115444.

[45] David B. Pedersen, Shiliang Wang, and Septimus H. Liang. "Charge-Transfer-Driven Diffusion Processes in Cu@Cu-Oxide Core−Shell Nanoparticles: Oxidation of 3.0 ± 0.3 nm Diameter Copper Nanoparticles". In: *The Journal of Physical Chemistry C* 112.24 (2008), pp. 8819–8826. ISSN: 1932-7447. DOI: 10.1021/jp710619r.

[46] Vladimir N. Popok, Sergey M. Novikov, Yurij Yu. Lebedinskij, Andrey M. Markeev, Aleksandr A. Andreev, Igor N. Trunkin, Aleksey V. Arsenin, and Va-

lentyn S. Volkov. “Gas-Aggregated Copper Nanoparticles with Long-term Plasmon Resonance Stability”. In: *Plasmonics* 16.2 (2021), pp. 333–340. ISSN: 1557-1955. DOI: 10.1007/s11468-020-01287-4.

[47] Agung Purniawan, Maria Inge Lusida, Royan Wafi Pujiyanto, Aldise Mareta Nastri, Adita Ayu Permanasari, Alfonsus Adrian Hadikusumo Harsono, Nur Hafidzah Oktavia, Sigit Tri Wicaksono, Jezzy Renova Dewantari, Rima Ratnanggana Prasetya, Krisnoadi Rahardjo, Mitsuhiro Nishimura, Yasuko Mori, and Kazufumi Shimizu. “Synthesis and Assessment of Copper-Based Nanoparticles as a Surface Coating Agent for Antiviral Properties Against SARS-CoV-2”. In: *Scientific Reports* 12.1 (2022), p. 4835. DOI: 10.1038/s41598-022-08766-0.

[48] A. E. Rakhshani. “Preparation, Characteristics and Photovoltaic Properties of Cuprous Oxide—a Review”. In: *Solid-State Electronics* 29.1 (1986), pp. 7–17. ISSN: 00381101. DOI: 10.1016/0038-1101(86)90191-7.

[49] Katherine P. Rice, Andrew S. Paterson, and Mark P. Stoykovich. “Nanoscale Kirkendall Effect and Oxidation Kinetics in Copper Nanocrystals Characterized by Real-Time, In Situ Optical Spectroscopy”. In: *Particle & Particle Systems Characterization* 32.3 (2015), pp. 373–380. ISSN: 09340866. DOI: 10.1002/ppsc.201400155.

[50] Antonio Rubino, Robertino Zanoni, Pier G. Schiavi, Alessandro Latini, and Francesca Pagnanelli. “Two-Dimensional Restructuring of Cu_2O Can Improve the Performance of Nanosized n-TiO_2/p-Cu_2O Photoelectrodes under UV-Visible Light”. In: *ACS Applied Materials & Interfaces* 13.40 (2021), pp. 47932–47944. DOI: 10.1021/acsami.1c13399.

[51] S.k. Roy, S.K. Bose, and S.C. Sircar. “Pressure Dependencies of Copper Oxidation for Low- and High-Temperature Parabolic Laws”. In: *Oxidation of Metals* 1991.35 (1990), pp. 1–18.

[52] Sachin S. Sawant, Ashok D. Bhagwat, and Chandrashekhar M. Mahajan. “Synthesis of Cuprous Oxide (Cu_2O) Nanoparticles - a Review”. In: *Journal of Nano- and Electronic Physics* 8.1 (2016), pp. 01035-1-01035–5. ISSN: 20776772. DOI: 10.21272/jnep.8(1).01035.

[53] Norbert Schell, Andrew King, Felix Beckmann, Torben Fischer, Martin Müller, and Andreas Schreyer. “The High Energy Materials Science Beamline (HEMS) at PETRA III”. In: *Materials Science Forum* 772 (2013), pp. 57–61. DOI: 10.4028/www.scientific.net/MSF.772.57.

[54] C. Schlueter, A. Gloskovskii, K. Ederer, I. Schostak, S. Piec, I. Sarkar, Yu. Matveyev, P. Lömker, M. Sing, R. Claessen, C. Wiemann, C. M. Schneider, K. Medjanik, G. Schönhense, P. Amann, A. Nilsson, and W. Drube. “The new dedicated HAXPES beamline P22 at PETRAIII”. In: AIP Conference Proceedings. Author(s), 2019, p. 040010. DOI: 10.1063/1.5084611.

[55] Cláudia Gomes Silva and Joaquim Luís Faria. “Anatase vs. Rutile Efficiency on the Photocatalytic Degradation of Clofibric Acid Under Near UV to Visible Irradiation”. In: *Photochemical & Photobiological Sciences : Official Journal of the European*

Photochemistry Association and the European Society for Photobiology 8.5 (2009), pp. 705–711. ISSN: 1474-905X. DOI: 10.1039/b817364h.

[56] Andreas Stierle, Thomas F. Keller, Heshmat Noei, Vedran Vonk, and Ralf Roehlsberger. "DESY NanoLab". In: *Journal of Large-Scale Research Facilities JLSRF* 2 (2016). DOI: 10.17815/jlsrf-2-140.

[57] Kayano Sunada, Masafumi Minoshima, and Kazuhito Hashimoto. "Highly Efficient Antiviral and Antibacterial Activities of Solid-State Cuprous Compounds". In: *Journal of Hazardous Materials* 235-236 (2012), pp. 265–270. DOI: 10.1016/j.jhazmat.2012.07.052.

[58] T. N. Rhodin Jr. "Low Temperature Oxidation of Copper. II. Reaction Rate Anisotropy". In: *Journal of the American Chemical Society* 73 (1951), pp. 3143–3146. DOI: 10.1021/ja01151a042.

[59] L. Thomsen, M. T. Wharmby, D. P. Riley, G. Held, and M. J. Gladys. "The Adsorption and Stability of Sulfur Containing Amino Acids on Cu(531)". In: *Surface Science* 603.9 (2009), pp. 1253–1261. ISSN: 00396028. DOI: 10.1016/j.susc.2009.03.014.

[60] Robert B. Thurman, Charles P. Gerba, and Gabriel Bitton. "The Molecular Mechanisms of Copper and Silver Ion Disinfection of Bacteria and Viruses". In: *Critical Reviews in Environmental Control* 18.4 (1989), pp. 295–315. ISSN: 1040-838X. DOI: 10.1080/10643388909388351.

[61] Yimin Tong, Gansheng Shi, Gaowei Hu, Xiaoyou Hu, Lin Han, Xiaofeng Xie, Yongfen Xu, Rong Zhang, Jing Sun, and Jin Zhong. "Photo-Catalyzed TiO_2 Inactivates Pathogenic Viruses by Attacking Viral Genome". In: *Chemical engineering journal (Lausanne, Switzerland : 1996)* 414 (2021), p. 128788. ISSN: 1385-8947. DOI: 10.1016/j.cej.2021.128788.

[62] Jon P. W. Treacy, Hadeel Hussain, Xavier Torrelles, David C. Grinter, Gregory Cabailh, Oier Bikondoa, Christopher Nicklin, Sencer Selcuk, Annabella Selloni, Robert Lindsay, and Geoff Thornton. "Geometric Structure of Anatase $TiO_2(101)$". In: *Physical Review B* 95.7 (2017). ISSN: 2469-9950. DOI: 10.1103/PhysRevB.95.075416.

[63] V. Vonk, N. Khorshidi, and A. Stierle. "Structure and Oxidation Behavior of Nickel Nanoparticles Supported by YSZ(111)". In: *The Journal of Physical Chemistry C, Nanomaterials and Interfaces* 121.5 (2017), pp. 2798–2806. ISSN: 1932-7447. DOI: 10.1021/acs.jpcc.6b11342.

[64] Yiwen Wang, Jisun Im, Jason W. Soares, Diane M. Steeves, and James E. Whitten. "Thiol Adsorption on and Reduction of Copper Oxide Particles and Surfaces". In: *Langmuir : The ACS Journal of Surfaces and Colloids* 32.16 (2016), pp. 3848–3857. ISSN: 0743-7463. DOI: 10.1021/acs.langmuir.6b00651.

[65] X. Sang and T.G. Phan and F. Yagyu and S. Okitsu and N. Maneekarn and W.E. Müller and H. Ushijima. "Photocatalytic Inactivation of Diarrheal Viruses by Visible-Light-Catalytic Titanium Dioxide". In: *Clin Lab.* 2007.53 (2007), pp. 413–421.

[66] Mingchun Xu, Youkun Gao, Elias Martinez Moreno, Marinus Kunst, Martin Muhler, Yuemin Wang, Hicham Idriss, and Christof Wöll. "Photocatalytic Activity of Bulk TiO_2 Anatase and Rutile Single Crystals Using Infrared Absorption Spectroscopy". In: *Physical Review Letters* 106.13 (2011), p. 138302. DOI: 10.1103/PhysRevLett.106.138302.

Chapter 7

Article III: Cysteine Degradation Facilitated by Cu Nanoparticles Supported on TiO_2(110)

Cysteine Degradation Facilitaded by Cu Nanoparticles Supported on TiO_2(110)

Daniel Silvan Dolling[1,2*];
Miguel Blanco Garcia[1,2]
Arno Jeromin[1]
Thomas F. Keller[1]
Andreas Stierle[1,2]
Heshmat Noei[1†]
[1]Centre for X-ray and Nano Science CXNS,
Deutsches Elektronen-Synchrotron DESY,
Notkestr. 85, 22607 Hamburg, Germany

[2]Fachbereich Physik, Universität Hamburg,
Notkestr. 9-11, 22607 Hamburg, Germany

September 21, 2026

Abstract

Copper and cpper oxide nanoparticles supported on TiO_2 are of interest for various applications ranging from organic pollutant degradation to photocatalytic virus inactivation. We investigated the adsorption of cysteine amino acid via infrared reflection-absorption spectroscopy (IRRAS) and X-ray photoelectron spectroscopy (XPS) on five different samples of Cu(-oxide) nanoparticles (NPs) supported on rutile TiO_2(110) single crystals. The NP morphologies, coverages, size distribution and local composition are characterized by scanning electron microscopy (SEM) and scanning auger microscopy (SAM). We find that different NP configurations in terms of coverage and oxidation state lead to different adsorption behavior, ranging from almost inactive surfaces to strong bonds between sulfur and copper (Cu-S). Furthermore, the oxidation of the adsorbed thiol group is used as a

*silvan.dolling@desy.de
†heshmat.noei@desy.de

measure of catalytic activity. The activity is tested in air under different light exposures. Our results demonstrate that the activity is both influenced by Cu coverage and oxidation state, with a high-coverage CuO sample exhibiting the strongest catalytic properties.

1 Introduction

Copper and its oxides are well known for their antiviral and antibacterial properties, more recently including the inactivation of SARS-CoV-2 [8, 19, 13]. The use of nanoparticles (NPs), compared to thin films, offers a higher surface-to-volume ratio and enhances the surface reactivity. In particular, combining Cu oxides with TiO_2 has attracted significant interest due to their higher activity, even under dark conditions. It has been shown that Cu oxide on titanium oxide is photoactive in the visible light spectrum, deactivating bacteria and degrading organic dyes [15, 16]. In 2022 it was shown that TiO_2 decorated with Cu oxide particles effectively inactivate SARS-CoV-2 [17]. Remarkably, this system is active not only under visible light but also in the dark, although with reduced efficiency compared to illumination. This activity was attributed to changes in the oxidation state of Cu: A mixture of Cu(I) and Cu(II) was estimated to act as an 'electron storage', being able to either accept photo-electrons by locally reducing Cu(II) to Cu(I), or giving them away by locally oxidizing C(I) to Cu(II). The combination of activity under visible light and the availability of catalytic effects under dark conditions makes this system very interesting for indoor self-disinfection surfaces. To systematically study the self-cleaning and antiviral properties of the Cu(-oxide)/TiO_2 system, well-defined model systems are required.

To understand the interaction of the nanoparticle system with virus and bacteria, amino acids can be used as model system. Cysteine in particular is known to be one of the main building blocks of the spike protein in SARS-Cov-2. Moreover, with its three functional groups (amino, thiol and carboxyl), cysteine allows for clear distinction of specific interactions with the surface during adsorption. The adsorption of cysteine on Cu and TiO_2 single crystals has been studied before. On Cu, it has been reported that cysteine interacts through its amine group, the deprotonated thiol group, and also the deprotonated carboxyl group [11, 12, 14]. On TiO_2, cysteine is known to interact through the carboxyl and the thiol groups, though some studies reported dissociative adsorption (deprotonation) of the thiol group [1]. A recent study employed both DFT as well as IRRAS and XPS to get a full atomistic understanding of the adsorption of intact cysteine on rutile [3]. Different adsorption geometries were found: cysteine adsorbs with

a deprotonated carboxyl group either via both oxygen atoms bridging two Ti atoms or through a bridging configuration involving the carboxyl group paired with either the amino or thiol group interacting with Ti. Moreover, the presence of water molecules, even residual amounts in UHV, leads to the stabilization of the zwitterionic state of cysteine (deprotonated carboxyl group and protonated amino group). A similar study was conducted for the adsorption of cysteine on anatase TiO_2(101) [2]. In contrast to the adsorption on rutile, cysteine was found to favor adsorption with the amino group, either in a bridging adsorption configuration via amino and sulfur groups, or via the deprotonated carboxylic group and the amino group. Upon exposure of the system to air and UV light, the thiol group of the cysteine is stepwise oxidized to sulfonic acid (-SO_3H), complete oxidation is reached after 30 minutes. Another study investigated the adsorption and degradation of cysteine on Cu(-oxide) NPs supported on anatase TiO_2(101) [7]. It was found that cysteine adsorbs exclusively with deprotonated carboxyl group and protonated amino group and that the Cu-oxide NPs were reduced upon adsorption. Moreover, a fraction of the cysteine thiol groups is oxidized upon adsorption and evidence for the decomposition of cysteine directly upon adsorption is found. Following light and air exposure, it was observed that the thiol group of cysteine is further oxidized, but also that no complete oxidation of all thiol groups is achieved due to the strong Cu-S bond. Thus, the adsorption and degradation of cysteine has been studied in detail on bare anatase and rutile substrates, as well as on Cu NPs supported on anatase TiO_2. To complete the picture, the investigation of cysteine adsorption on Cu NPs supported on rutile TiO_2 is needed. This is particularly relevant, as commonly used commercial TiO_2 powder for photocatalysis is typically comprised of 25% rutile [5, 18]. Here, we aim to close this missing link and adsorb cysteine on Cu (oxide) NPs on single crystalline rutile TiO_2(110) to elucidate the interaction of the amino acid with both the NPs and the substrate.

2 Results

2.1 NP Characterization

Five different Cu/TiO_2 samples and an additional TiO_2(110) crystal without NPs were investigated in total. An overview of the sample parameters can be seen in Table 1 and the individual SEM images are found in Figures S1 to S4. Samples C, D, and E feature homogeneous particle distributions across the whole surface at a coverage close to 50 %, whereas samples A and B consist

Table 1: *Comparison of the different samples. The coverage and mean diameter were calculated from SEM. The relative Cu deposition is the amount of Cu deposited initially, compared to the other samples. All samples were oxidized under ambient conditions at various temperatures. The Cu(II) percentage is calculated from XPS fits, see Figure S12. As the XPS probing depth is limited to the first nanometers of the NPs, these percentages only display the oxidation state of the outer layers.*

Sample	Coverage [%]	NP diameter [nm]	Relative Cu Deposition	Oxidation Temperature [°C]	Cu(II) [%]
A	7 ± 3	117 ± 37 6 ± 3	1	200	75
B	9 ± 7	59 ± 24 16 ± 6	1	800	100
C	42 ± 8	4.7 ± 2.6	1	20	63
D	55 ± 4	10.6 ± 3.6	4	20	42
E	60 ± 4	15.1 ± 5.3	5	200	71

of combinations of large and small NPs at coverages of roughly 10 %. A comparison of the Cu oxidation states was done using XPS. The results can be seen in Figure S12, Figure S41 and in Table 1. In the Cu 2p core level, it is found that samples A, C and E feature both Cu(I) & Cu(0) as well as Cu(II). CuO is dominant, making up about 70 % of the Cu 2p signal. Sample D features only about 40 % Cu(II) and sample B consists exclusively of Cu(II). From the Cu LMM spectra, which allow for distinguishing Cu(0) from Cu(I), it is seen that sample D and sample E feature metallic Cu. Considering the probing depths of about 3-5 nm for XPS, these results reflect the outer shell and not the core of the NPs, as most NPs are larger than 5 nm.

For samples A and B, the annealing procedure at air might have caused strong metal-support interaction (SMSI), leading to an overgrowth of the Cu(-Oxide) NPs with TiO_2 [23]. To investigate this, scanning Auger microscopy (SAM) images were taken for sample A, see Figure 1. The line scan reveals that all particles seen in SEM are Cu(-Oxide) NPs and that there is no Ti on the NPs after annealing in air. Additionally, a comparison of individual Cu LMM spectra at different positions along the line scan reveals that the NPs are all composed of the same oxide (see Figure S48). This rules out SMSI effects for sample A. By analogy to sample A, it can be assumed that the oxidation state of sample B is homogeneous too. For samples C, D, and E, survey spectra were taken, comparing larger and smaller

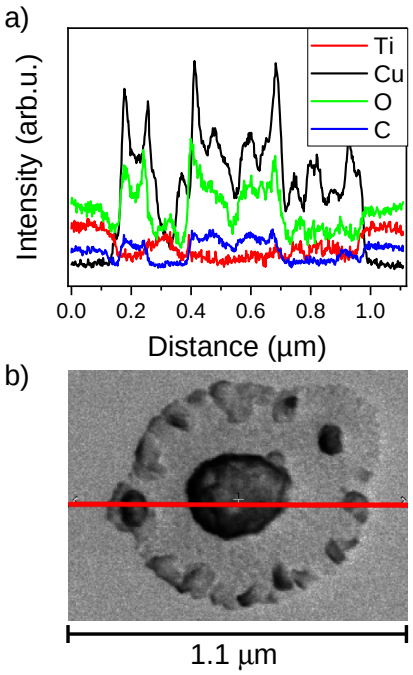


Figure 1: *SAM line scan through a representative NP of sample A. a) Intensity of the elements measured for the line scan. The distance is along the line scan. b) SEM image of the line scan - the actual scan area is marked red.*

NPs, see Figures S49 to S51 . It can be seen that all NPs feature the same elements, thus confirming the homogeneity of these samples.

2.2 Cysteine Adsorption

Cysteine was deposited on all samples via vapor exposure in the IRRAS UHV chamber. The resulting IR spectra can be seen in Figure 2 and Figures S7 to S11, the band assignments in Table S1.

The IRRAS results are compared to our recent data obtained for the adsorption of cysteine on clean rutile $TiO_2(110)$ in the same setup [3]. On $TiO_2(110)$, a combination of strong IRRAS signals for a protonated amino group ($-NH_3^+$) was found, with the symmetric stretching vibration δ_{sym} at 1513 cm^{-1} and the asymmetric stretching vibration δ_{as} at 1610 cm^{-1}. Additionally, it was seen that the IR bands from the carboxyl group are related

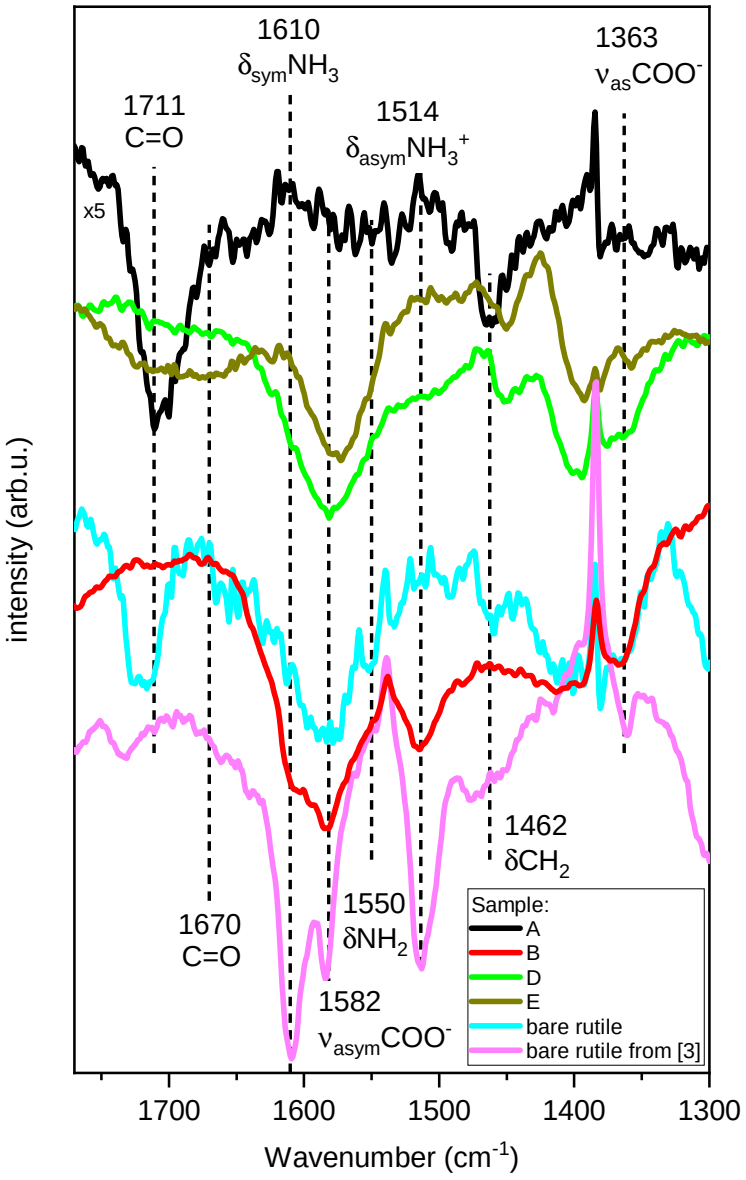


Figure 2: *IRRAS spectra of all samples after exposure to 190 L cysteine at room temperature. Additionally, the spectrum for bare rutile TiO_2(110) (with 8 L cysteine dosed) reproduced from [3] is included (with permission).*

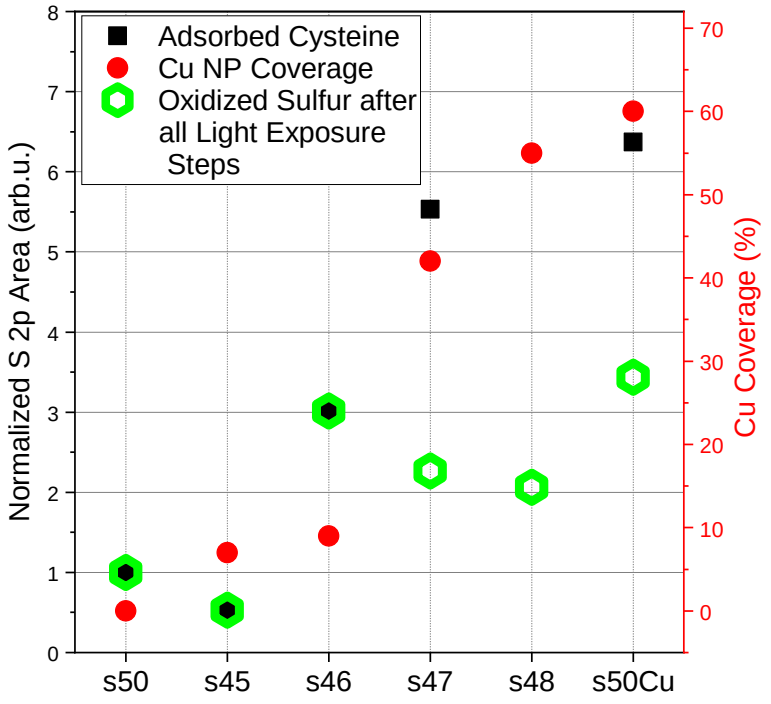


Figure 3: *Comparison of the S $2p_{3/3}$ area after cysteine adsorption, the Cu NP coverage and the normalized amount of oxdized sulfur after all light exposure steps. Details on the normalization can be found in the SI.*

to a deprotonated state (-COO^-), with the symmetric stretching band ν_{sym} at 1363 cm^{-1} and the asymmetric stretching band at 1585 cm^{-1}. C=O double bonds were only found for low coverage of cysteine.

In the present study, a rutile TiO_2(110) crystal without NPs was measured in addition to the Cu/TiO_2 samples. In comparison to the experiment conducted in [3], significantly more cysteine was dosed (190 L instead of 8 L). Moreover, the crystal was exposed to high background pressure to mimic contamination from air exposure, before dosing cysteine. The crystal exhibits the same adsorption bands as reported in [3], but the NH_3^+ bands are significantly weaker. This means that less zwitterionic cysteine exists.

Moreover, a strong C=O band at 1718 cm^{-1} is found, indicative of non-dissociated adsorption of carboxyl groups. These differences compared to the cysteine adsorption reported in [3] can be explained by partially hydroxylated surface caused by exposure to non-UHV pressures prior to cysteine dosing. As less adsorption sites are present, adsorption via the thiol group (either R-S-Ti or R-S-H-O) may become sterically favored compared to bridging configurations.

For sample A, only two bands are observed: the δCH_2 band at 1462 cm^{-1} and a strong νC=O band at 1711 cm^{-1}. The latter is very similar to the C=O stretching band observed on bare rutile without Cu NPs and is thus similarly attributed to cysteine adsorption in monodentate configuration, without interaction of the carboxyl group to the surface. Similar to the C=O found on the rutile sample, its existence can be explained by the carbon contamination of the sample and thus the sterically favored upright adsorption (all Cu NP samples were oxidized at air and feature carbon contamination, see Figures S18 to S23). In contrast to the rutile crystal without NPs, no other signal indicative of a different adsorption geometry is found.

Sample B exhibits almost exactly the same adsorption bands as pristine rutile in [3]. This indicates that Cu on the sample is not interacting with cysteine. In contrast to sample A, this also means that the main adsorption geometries are the ones described in [3], a deprotonated carboxyl group and bridging adsorption of two of the functional groups to Ti atoms.

Sample C shows similar adsorption bands to those of sample B, but the bands corresponding to NH_3^+ are much weaker and broader. Considering the much higher Cu coverage of sample C compared with sample B, it can be assumed that the interactions with the surface are the same as seen for sample B, but the actual geometry leads to band broadening.

Sample E features no signal from NH_3^+, but both COO^- bands (ν_{sym} at 1392 cm^{-1} and ν_{asym} 1582 cm^{-1}), as well as the C=O band at 1710 cm^{-1}, though the latter is much broader than it is for sample A. Again, this is an indicator of adsorption of cysteine with protonated and intact carboxyl group. In addition to these peaks, a new peak at 2208 cm^{-1} (see Figures S6 and S10) is found. A peak in this region is not typically seen for cysteine, but it can be attributed to a C≡N triple-bond (nitrile). A similar signal was found for the adsorption of cysteine on Cu NPs on anatase TiO_2 recently [6]. For a nitrile group to form, the cysteine molecule has to fracture. Hence, this can be taken as an indicator for cysteine degradation.

In addition to the IRRAS measurements, XPS S 2p spectra were taken after cysteine adsorption for all samples, see Figures 5 and S24 to S28. On

the bare rutile crystal without NPs, sulfur is bound to Ti (S-Ti) at 161.6 eV, but mostly in protonated form (S-H) at 163.8 eV. For the NP samples, sulfur is predominantly found bound to Cu (S-Cu) at 162.4-163.4 eV and in molecular form (S-H) at 163.8 eV. All samples feature both sulfur bound to Cu (S-Cu) and molecular thiol groups (S-H), but the amount of S-H is much lower for sample D compared to the other samples. Comparing the samples, the only clear differentiator between sample D and the other samples is the lower amount of CuO in sample D. As a result, a correlation between the presence of high percentage of Cu_2O in XPS spectra and an increased adsorption of cysteine is assumed. The low signal-to-noise ratio of the S 2p spectra for samples A and B hinders a precise study of the peak components. Though the spectra of sample B were fitted both with molecular thiol groups and sulfur bound to copper, it is possible to model the peak with only one of both components. Hence, this is compatible with SMSI overgrowth of the Cu NPs for sample B, indicated by the similarity of the IRRAS bands with those reported in [3]. In addition to the S-Cu and S-H peaks, all Cu NP samples feature partially oxidized thiol groups (S-O_x) directly after adsorption, leading to peaks between 166 eV and 169 eV. An exception to this are sample E (only 2 % oxide) and the bare rutile crystal. A detailed comparison of the S 2p peaks after adsorption can be seen in Figure 4. In that figure, the S 2p spectra from [7] for cysteine on Cu(-oxide)/TiO_2(101) are included. It can be seen that cysteine adsorption on Cu/anatase does not feature strong S-H signal and that it is compatible with adsorption via S-Cu and S-Ti. The data from the present study of the Cu/rutile system, in contrast, features a clear signal of S-H (except for sample D) and no sign of S-Ti (except for sample B). These differences suggest different adsorption configurations, indicating less S-Cu and S-Ti interactions for the rutile substrates and thus lead to the assumption that adsorption with the amino group or the carboxyl group is favored, in line with the IRRAS data.

A comparison of the amounts of deposited cysteine is done by comparing the XPS S 2p spectra after adsorption, see Figure 3. It can be seen that the S 2p signal intensity scales linearly with the Cu coverage. Compared to a bare rutile crystal, the surface area of the NP samples is increased. Considering the NPs as half-spheres, the gain in surface area is equal to the NP coverage (see SI for details). Even though this is a very simplified consideration, it yields an estimate on the maximum increase in adsorption that can be attributed to pure geometric factors. For all samples except sample A, the increase in adsorption of cysteine compared to bare rutile is $\gtrsim 2$, indicating an increase in adsorption that has to be attributed to

Cu-cysteine interaction (as the Cu coverage does not exceed 60%).

The most cysteine is found on sample D (about 13 times the amount found on bare rutile), followed by sample E and sample C, both featuring roughly six times that amount. Even though the IRRAS adsorption bands for sample B are similar to those seen for bare rutile, about 3 times the amount of cysteine is adsorbed.

For all samples except E, a reduction of Cu-oxide oxidation state can be seen upon adsorption of cysteine, see Figures S13 to S17. This has been reported for the adsorption of thiol-containing organics on Cu surfaces [21, 4] and recently for the adsorption of cysteine on Cu(-oxide) NPs supported by anatase TiO_2(101) [7]. It is attributed to the formation of Cu-S bonds and the subsequent reduction of surface oxide.

SAM measurements, taken after the photocatalysis experiments, reveal that carbon adsorbs mostly on Cu NPs and not on substrate TiO_2, see Figure S48.

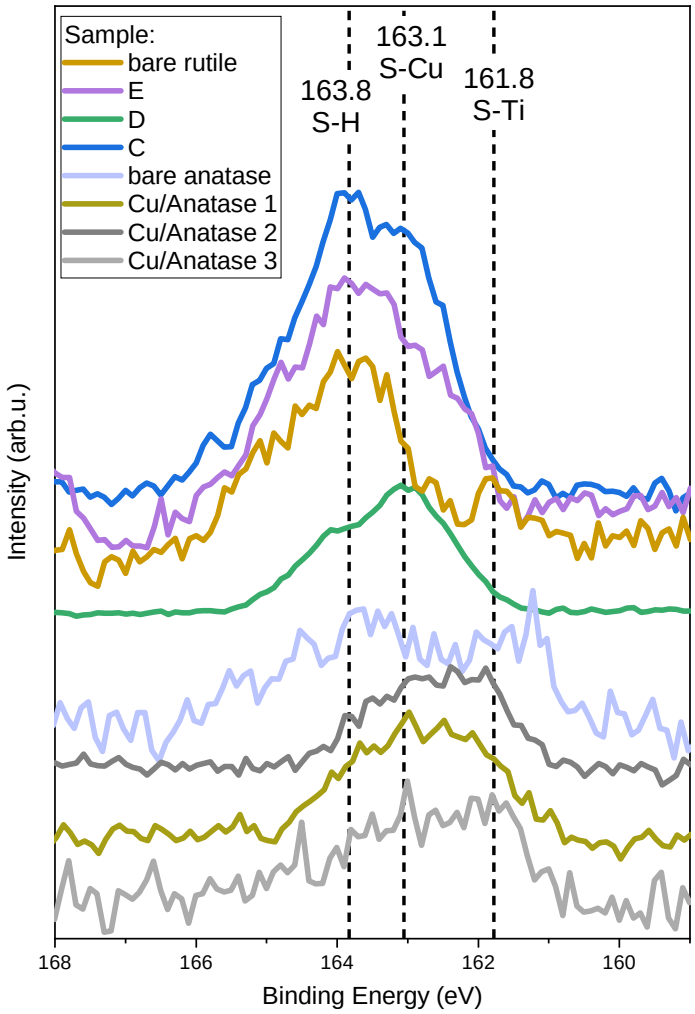


Figure 4: *Comparison of S 2p peaks for the different samples, as well as for adsorption on anatase and on Cu NPs on anatase TiO_2(101), reproduced from [7].*

2.3 Cysteine Degradation

To investigate the effect of light on cysteine adsorbed on different Cu/TiO_2 samples, they were exposed to ambient conditions under light and XPS was measured at different times. Similar to a recent publication about cysteine on $Cu/TiO_2(101)$ [7], the S 2p core level is used as an indicator for cysteine degradation: By exposure to light in air, the thiol group is oxidized, forming a mixture of several oxide states SO_x. A fully oxidized thiol group ($R\text{-}SO_3^-$ or SO_4) is attributed to binding energies of 168 eV and partial oxidation ($R\text{-}SO_x$) is attributed to binding energies between 165 eV and 167 eV [9, 2]. The first ambient exposure was done under dark conditions, the second and third under a broad-band white-light LED exposure and the fourth under UV light exposure. Each exposure took 30 minutes. The S 2p spectra for all samples for different steps can be seen in Figures S24 to S27 and Figure 5.

For the rutile crystal without NPs, exposure to ambient conditions leads to a loss of all sulfur bound to Ti (S-Ti) and to the rise of a sulfur oxide peak around 166 eV. Upon the second and third exposure to ambient conditions under white LED light, the amount of sulfur oxide grows up to 56 % (of all sulfur), and reaches 100 % after exposure to UV light. For sample A, the percentage of oxidized sulfur is increasing with each exposure to air, similar to pristine anatase, reaching 100 % after UV irradiation. Sample B has a high amount of oxidized sulfur directly after adsorption (almost half of all sulfur from the cysteine is directly oxidized). The ambient condition treatments increase the amount of SO_x to 100 % after UV light exposure. A similar pattern is seen for the oxidation of the thiol on sample C. The main difference between the cysteine degradation on sample B and samples A and B is that only about 40 % of all sulfur is oxidized on sample C. The same can be seen for sample D, where even less oxidation is found, reaching roughly 15 % of the thiol signal. In contrast, sample E oxidizes about 54 % of all sulfur. As the samples feature different amounts of adsorbed cysteine, it is also useful to look at the amount of oxidized sulfur scaled with the amount of cysteine adsorbed, see Figure 3. It is found that sample A produces less sulfur oxide than bare rutile. Sample B produces about 3 times the amount of SO_x compared to clean rutile, as well as sample C and D. The most oxide is produced by sample E, featuring about 3.4 times the SO_x created by pristine rutile.

The effect of light on the sulfur oxidation is evaluated by studying the percentage of $S\text{-}O_x$ on the whole S 2p signal during the different light and air treatments, see Figure 6. It is found that the increase in oxidized thiol groups is increasing linearly with the amount of time at air, regardless of

the light condition, for almost all samples. The exception to this is sample E, for which the oxide only starts to be formed after exposure to white light.

3 Discussion & Conclusion

Five samples of Cu(-Oxide) NPs on TiO_2(110) were prepared and characterized, revealing different NP sizes, coverages and oxidation states. The interaction of these samples with cysteine was studied by IRRAS and XPS. It is found that the adsorption of the amino acid strongly depends on the sample: It is known that on pristine rutile crystals the adsorption is dominated by the presence of a deprotonated carboxyl group (-COO^-) and a protonated amino group (-NH_3^+), with several possible adsorption geometries [3]. Almost the exact same IRRAS bands are seen for sample B. As XPS and SEM clearly reveal the presence of CuO NPs, it can be assumed that the particles are covered in a thin shell of TiO_2 via strong metal support interaction (SMSI). This has been reported to occur for Cu/TiO_2 systems under conditions similar to the 800 °C anneal used for sample B [22]. This is confirmed by the S 2p XP spectra, which show adsorption of sulfur on Ti, not seen for any other sample with Cu NPs. Even though the adsorption is very similar to a bare rutile crystal, sample B produces about three times the amount of SO_x, indicating the increased activity due to the buried Cu NPs. On sample A, on the other hand, which features very similar NPs from a morphological point of view, the adsorption of cysteine is significantly different. Instead of the adsorption modes reported in [3], only one mode of adsorption is found, involving a molecular carboxyl group (COOH). Moreover, whereas relatively large amounts of cysteine are found on sample B, sample A features even less cysteine than the pristine rutile sample. The differences in adsorption mode can be explained by the SMSI overgrowth of the Cu NPs on sample B, which is not present on sample A. Furthermore, it can be assumed that sample B features only little contamination, as it would otherwise not exhibit the same adsorption modes as are reported for a thoroughly cleaned rutile TiO_2 crystal [3]. This is an indicator of self-cleaning properties of the sample. Sample C and D, both featuring NPs that were oxidized at room temperature, exhibit very similar IRRAS adsorption bands to those found for bare rutile, but only very weak signs of NH_3^+ vibrations. Additionally, from XPS it is known that the thiol group can be adsorbed on Cu (S-Cu) or exist in molecular form (S-H) on both samples, but that sample D features significantly less S-H signal. This is attributed to the higher amount of Cu_2O present on sample D, which may favor direct Cu-S

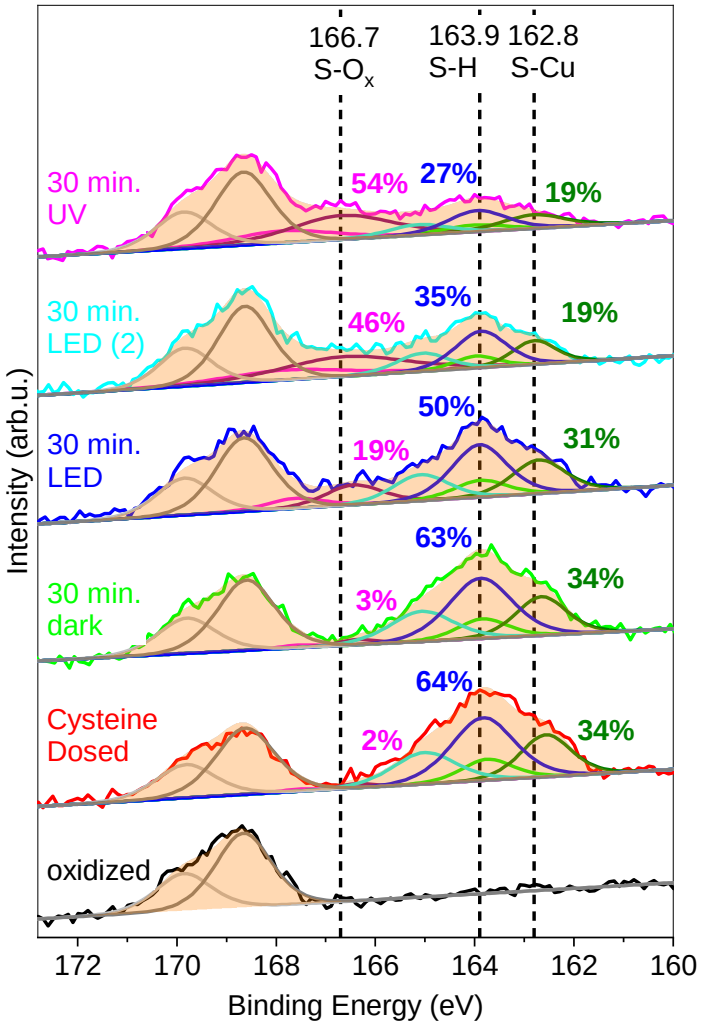


Figure 5: *S 2p spectra for sample E for different steps of exposure to ambient conditions and light. 'Oxidized' means that the Cu NPs are oxidized, but no cysteine is deposited. The spectra were fitted with a doublet corresponding to sulfur bound to Cu (green), a doublet for the molecular thiol group S-H (blue), and a doublet for oxidized sulfur (purple). The envelope of the fit is displayed as orange shade. Additionally, a double for contamination prior to cysteine dosing had to be added (grey). The contamination was assumed to stay constant.*

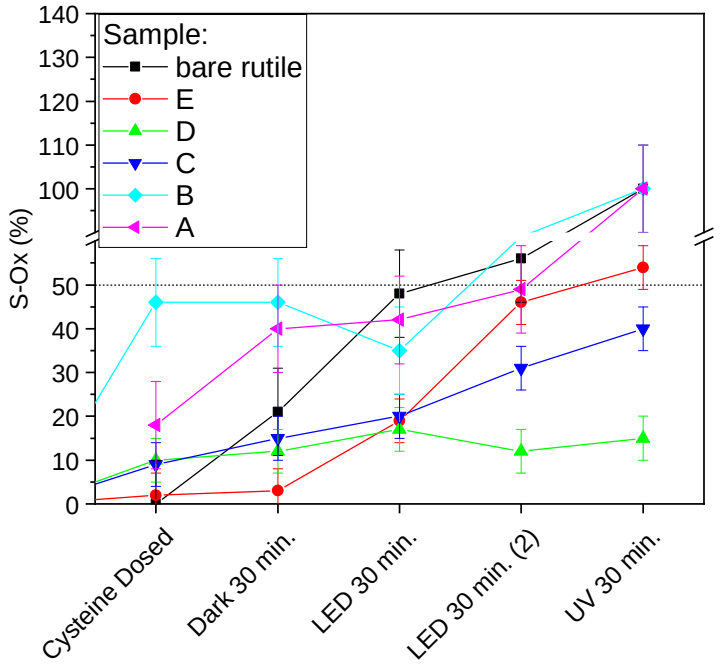


Figure 6: *Comparison of the percentages of oxidized sulfur from the whole S 2p signal for all samples during different stages of exposure to air and light.*

interaction. It can be assumed that the main adsorption modes are similar to those found on pristine rutile [2] (bridging adsorption with two functional groups), but that adsorption with the amino group is favored, resulting in less signal from NH_3^+. Though both samples feature high Cu coverages and as a result high amounts of adsorbed cysteine, the amount of oxidized sulfur after all exposures to air and light is relatively low compared to the amount of cysteine. This is especially visible for sample D, featuring by far the most cysteine adsorption, but the lowest percentage of oxidized sulfur. This highlights the competition between the strong adsorption with S-Cu bonds and the degradation.

Sample E, featuring a high coverage of high-temperature annealed NPs (CuO), shows adsorption similar to samples C and D, but includes a strong C=O band, indicative of cysteine adsorption with protonated carboxyl group. This sample adsorbed about 6 times the amount of cysteine compared to bare rutile and produced roughly 3.4 times the amount of oxide after all light and air exposures. Significantly, it is the only sample that exhibited a

response to light for the oxidation of the thiol group, whereas all other Cu NP samples oxidized the sulfur linearly with time, independent of light.

In conclusion, we found that cysteine adsorbs on Cu(-oxide)/TiO_2(110) systems in similar configurations as seen for pristine rutile crystals [3], highlighted by the similarities in IRRAS and XPS data. Differences to adsorption on bare rutile crystals are found in the fact that strong Cu-S bonds are formed, especially when high amounts of Cu_2O are present. These lead to high amounts of cysteine adsorption, but also block the oxidation of the thiol group. In contrast to the adsorption on Cu/anatase systems [7], there is no indicator of S-Ti bonds. Moreover, S-H bonds, present for the rutile system, were not seen on the Cu/anatase system. This means that the choice of substrate for the NPs influences the interaction with the cysteine, either favoring direct bonds of the thiol group to the surface (in the case of anatase) or also allowing for other adsorption configurations with non-interacting thiol group. Two samples were found most effective for cysteine degradation as measured by the amount of oxidized cysteine (compared to the amount found on bare rutile): a sample with low NP coverage and SMSI overgrowth (sample B) featured a high amount of adsorbed cysteine and high oxide conversion rate. A sample with high Cu coverage and high amounts of CuO on the surface (but still metallic Cu signal present) featured the highest amount of oxidized cysteine (sample E). In addition, it was the only sample that explicitly exhibited a response to visible light (regarding the oxidation of cysteine). In total, these findings highlight the influence of the substrate, the oxidation state and the nanoparticle coverage on the adsorption and degradation of cysteine on Cu/TiO_2 systems.

4 Methods

All experiments were performed at DESY Nanolab [20].

4.1 Nanoparticle Preparation

The nanoparticles were grown in a UHV chamber with an electron beam evaporator using a Cu crucible, similar to the procedure described in a previous publication [6]. The rutile TiO_2(110) crystals were cleaned four times in an ultrasonic bath; first in acetone, then in ethanol, afterward in isopropyl, and finally in deionized water and then introduced to a UHV system. They were sputtered at 1 kV acceleration voltage, 10 mA emission current and 10^{-6} mbar Ar and subsequently annealed at 800 °C for six times: Three times with UHV annealing, once with annealing in 10^{-6} mbar

O_2, once with annealing in UHV and finally once with annealing in UHV and cool down in 10^{-6} mbar O_2. Afterwards, the sample was flashed to 420 °C in UHV. High-purity oxygen (99.999%) was used for the sample preparation.

To oxidize the Cu NPs, the samples were taken out of UHV to ambient conditions. The exact oxidation procedure differs for the samples:

- samples A and B were oxidized at room temperature for several months. Then, they were annealed in UHV to 700 °C for 10 minutes. Afterwards, both samples were annealed in air (at ambient conditions) for 1 hour: sample A at 200 °C, sample B at 800 °C.
- sample C was stored at ambient conditions for two days.
- sample D was stored at ambient conditions for four days.
- sample E was stored at ambient conditions for two days and then annealed for 1 hour at 800 °C in air.

4.2 XPS

X-ray photo-electron measurements were performed at DESY NanoLab [20]. An Al Kα source was used at 1.486 keV. Both setups employed a hemispherical analyzer and all XPS spectra were fitted with CasaXPS software [10] using Shirley or linear backgrounds and Gaussian-Lorentzian line profiles, employing the Marquardt fitting algorithm. Peak position and FWHM were constrained, see SI for details. All spectra are normalized to Ti $2p_{3/2}$ (at 458.7 eV).

4.3 SEM

Scanning electron microscopy (SEM) images were obtained in secondary electron mode with a field emission instrument at an accelerator voltage of 5 kV, providing a nominal lateral resolution of 1.3 nm.

4.4 Cysteine Adsorption & Photocatalysis

Cysteine was dosed in UHV by heating cysteine powder in a glass vial connected to a leak valve to about 130 °C. Dosing was done in a chamber with a base pressure of 2×10^{-9} mbar in the following steps:

- 0.5 L cysteine (1E-8 mbar, 66 s), total 0.5 L
- +1.5 L cysteine (1E-7 mbar, 20 s), total 2 L

- +3 L cysteine (1E-7 mbar, 40 s), total 5 L
- +5 L cysteine (1E-7 mbar, 66 s), total 10 L
- +90 L cysteine (1E-6 mbar, 120 s), total 100 L
- +90 L cysteine (1E-6 mbar, 120 s), total 190 L

The photocatalysis experiments were performed by taking the samples with cysteine out of UHV for 30 minutes and exposing them to different light conditions:

- Dark conditions: The samples were put under a light cover.
- LED: The samples were exposed to a white broadband LED (ThorLabs MBB1L3, 470-850 nm, 80 mW) with a 450 nm highpass filter under a cover to avoid influences of other light sources. The lamp was positioned 10 cm above the sample. This step was repeated once.
- UV: The sampels were exposed to a UV-A lamp (365 nm, 6 W) under a cover to avoid influences of other light sources. The lamp was positioned 10 cm above the sample.

After each step of 30 minutes exposure to air (and light), the samples were re-introduced to UHV for XPS measurements.

4.5 SAM

Scanning Auger Microscopy (SAM) measurements were done using a PHI 710 Scanning Auger Nanoprobe instrument at an acceleration voltage of 20 kV with a nominal lateral resolution of 8 nm.

5 Acknowledgement

This work is supported by the Initiative and Networking Fund of the Helmholtz Association of German Research Centers (HGF) under the CORAERO project (KA1-Co-06).

We acknowledge DESY (Hamburg, Germany), a member of the Helmholtz Association HGF, for the provision of experimental facilities. Parts of this research were carried out at PETRA III using DESY NanoLab.

References

[1] Evren Ataman et al. “Adsorption of L-cysteine on rutile TiO_2(110)”. In: *Surface Science* 605.1-2 (2011), pp. 179–186. ISSN: 00396028. DOI: 10.1016/j.susc.2010.10.017.

[2] Miguel Blanco Garcia et al. “Adsorption and Sulfur-Selective Photooxidation of Cysteine on Anatase TiO_2(101)”. In: *Journal of the American Chemical Society* tba.tba (2026). DOI: 10.1021/jacs.6c07370.

[3] Miguel Blanco Garcia et al. “Unraveling the Role of the Multifunctional Groups in the Adsorption of l-Cysteine on Rutile TiO_2(110)”. In: *Journal of the American Chemical Society* 147.44 (2025), pp. 40158–40170. DOI: 10.1021/jacs.5c07119.

[4] L. Carbonell et al. “A Thermal Stability Study of Alkane and Aromatic Thiolate Self-Assembled Monolayers on Copper Surfaces”. In: *Superlattices and Microstructures* 36.1-3 (2004), pp. 149–160. ISSN: 07496036. DOI: 10.1016/j.spmi.2004.08.033.

[5] Ulrike Diebold. “The surface science of titanium dioxide”. In: *Surface Science Reports* 48.5-8 (2003), pp. 53–229. ISSN: 01675729. DOI: 10.1016/S0167-5729(02)00100-0.

[6] Daniel Silvan Dolling et al. “In-Situ Growth and Oxidation of Cu Nanoparticles on Rutile TiO 2 (110)”. In: *The Journal of Physical Chemistry C* 130.20 (2026), pp. 7136–7147. ISSN: 1932-7447. DOI: 10.1021/acs.jpcc.6c00835.

[7] Daniel Silvan Dolling et al. “Structure and Reactivity of Cu and Cu Oxide Nanoparticles on Anatase TiO2(101) for Cysteine Degradation”. In: *tba* tba.tba (2026). DOI: tba.

[8] Mohsen Hosseini et al. “Cupric Oxide Coating That Rapidly Reduces Infection by SARS-CoV-2 via Solids”. In: *ACS applied materials & interfaces* 13.5 (2021), pp. 5919–5928. DOI: 10.1021/acsami.0c19465.

[9] J.A. Reynaud, B. Malfoy, and P. Canesson. “Electrochemical Investigations of Amino Acids at Solid Electrodes: Part I. Sulfur Components: Cystine, Cysteine, Methionine”. In: *J. Electroanal. Chem.* 1980.114 (1980), pp. 195–211. DOI: 10.1016/S0022-0728(80)80447-5.

[10] John Walton et al. *Peak Fitting with CasaXPS: A Casa pocketbook: A Casa Pocket Book*. Casa XPS pocketbooks. Cheshire: Acolyte Science, 2010. ISBN: 9780954953317. URL: https://permalink.obvsg.at/AC13363835.

[11] Astrid Jürgensen et al. “An in situ XPS study of L-cysteine co-adsorbed with water on polycrystalline copper and gold”. In: *Applied Surface Science* 435 (2018), pp. 870–879. ISSN: 01694332. DOI: 10.1016/j.apsusc.2017.11.150.

[12] Jeong Won Kim et al. “Surface reaction of sulfur-containing amino acids on Cu(110)”. In: *Langmuir : the ACS journal of surfaces and colloids* 26.8 (2010), pp. 5632–5636. ISSN: 0743-7463. DOI: 10.1021/la904496j.

[13] Min Liu et al. “Visible-light sensitive Cu(II)-TiO_2 with sustained antiviral activity for efficient indoor environmental remediation”. In: *Journal of Materials Chemistry A* 3.33 (2015), pp. 17312–17319. ISSN: 2050-7488. DOI: 10.1039/C5TA03756E.

[14] E. Mateo Marti, Ch Methivier, and C. M. Pradier. “(S)-cysteine chemisorption on Cu110, from the gas or liquid phase: an FT-RAIRS and XPS study”. In: *Langmuir : the ACS journal of surfaces and colloids* 20.23 (2004), pp. 10223–10230. ISSN: 0743-7463. DOI: 10.1021/la048952w.

[15] Snehamol Mathew et al. “Cu-Doped TiO_2: Visible Light Assisted Photocatalytic Antimicrobial Activity”. In: *Applied Sciences* 8.11 (2018), p. 2067. DOI: 10.3390/app8112067.

[16] Maria Guadalupe Méndez-Medrano et al. “Heterojunction of CuO nanoclusters with TiO_2 for photo-oxidation of organic compounds and for hydrogen production”. In: *The Journal of chemical physics* 153.3 (2020), p. 034705. DOI: 10.1063/5.0015277.

[17] Ryuichi Nakano et al. “Inactivation of various variant types of SARS-CoV-2 by indoor-light-sensitive TiO_2-based photocatalyst”. In: *Scientific reports* 12.1 (2022), p. 5804. DOI: 10.1038/s41598-022-09402-7.

[18] B. Ohtani et al. “What is Degussa (Evonik) P25? Crystalline Composition Analysis, Reconstruction from Isolated Pure Particles and Photocatalytic Activity Test”. In: *Journal of Photochemistry and Photobiology A: Chemistry* 216.2 (2010). 3rd International Conference on Semiconductor Photochemistry, SP-3, April,2010, Glasgow UK, pp. 179–182. ISSN: 1010-6030. DOI: https://doi.org/10.1016/j.jphotochem.2010.07.024. URL: https://www.sciencedirect.com/science/article/pii/S1010603010002959.

[19] Agung Purniawan et al. “Synthesis and assessment of copper-based nanoparticles as a surface coating agent for antiviral properties against SARS-CoV-2”. In: *Scientific reports* 12.1 (2022), p. 4835. DOI: 10.1038/s41598-022-08766-0.

[20] Andreas Stierle et al. “DESY NanoLab”. In: *Journal of large-scale research facilities JLSRF* 2 (2016). DOI: 10.17815/jlsrf-2-140.

[21] Yiwen Wang et al. “Thiol Adsorption on and Reduction of Copper Oxide Particles and Surfaces”. In: *Langmuir : the ACS journal of surfaces and colloids* 32.16 (2016), pp. 3848–3857. ISSN: 0743-7463. DOI: 10.1021/acs.langmuir.6b00651.

[22] Chenchen Zhang et al. “Oxygen vacancies in Cu/TiO_2 boost strong metal-support interaction and CO2 hydrogenation to methanol”. In: *Journal of Catalysis* 413 (2022), pp. 284–296. ISSN: 00219517. DOI: 10.1016/j.jcat.2022.06.026.

[23] Ziyu Zhang. “Surface chemistry and growth of oxide supported metal nanoparticles”. PhD thesis. Louisiana, USA: Louisiana State University and Agricultural and Mechanical College, 2014.

Chapter 8

Conclusions

In this thesis, the growth and oxidation of Cu nanoparticles on anatase $TiO_2(101)$ and rutile $TiO_2(110)$ single crystals were investigated. Additionally, the interaction of these systems with cysteine (an amino acid) was studied. The starting point of this endeavor was the open questions that were detailed in the introductory sections. Though not all of these questions could be answered, the understanding of the Cu/TiO_2 system with respect to NP growth, oxidation and the interaction with cysteine amino acid could be improved significantly. The main conclusions are:

Cu NPs are (mostly) (111)-Oriented on Rutile $TiO_2(110)$ It was found that Cu on rutile $TiO_2(110)$ features several orientations and epitaxies, including [111]-, [100]- and [112]-oriented NPs. [111]-oriented NPs are the majority, featuring a $Cu[110]||TiO_2[001]$ epitaxy.

On Anatase $TiO_2(101)$, Cu NPs are [470]-Oriented Similar to the growth of Cu NPs on rutile, several NP orientations were found on anatase $TiO_2(101)$ single crystals. In contrast to rutile, the majority of the NPs were not [111]-oriented, but [470]-oriented, featuring a $Cu[001]||TiO_2[010]$ epitaxy. This high-index orientation is explained by row-matching of the Cu[100] and the $TiO_2[100]$ rows, which have a mismatch of only 2.7 %.

The Cu Growth Temperature Affects the Epitaxy For both rutile and anatase, the temperature of the substrate during Cu evaporation affects the epitaxy and particle size. In general, higher growth temperatures lead to larger particles. For rutile, this has been reported in literature [56, 9]. Our measurements confirm the same pattern for the growth of Cu on anatase $TiO_2(101)$: at 400 °C growth temperature, the NPs had diameters of about 22 nm, irrespective of the coverage, whereas diameters only ranged between 8-14 nm for NPs grown at 100 °C. For rutile, the growth temperature was also found to influence the epitaxy: with increasing growth temperature, an increasing fraction of the [111]-oriented NPs featured not the $Cu[110]||TiO_2[001]$ epitaxy, but the 12° rotated $Cu[110]||TiO_2[112]$ epitaxy. In relative terms, about 7 % of the [111]-oriented Cu NPs were of that tilted epitaxy for growth at 100 °C, whereas 22 % of all [111]-oriented NPs featured that epitaxy for growth at 400 °C.

The Oxidation State Depends on the NP Size For Cu NPs on rutile TiO_2, the oxidation in 1 bar O_2 was found to proceed rapidly for the first 60 minutes, leading to a loss of about 90 % of the Cu signal intensity. The signal loss slowed down afterwards, following an inverse logarithmic growth law for the oxide. Nevertheless, XRD signal corresponding to metallic Cu was still found after one week of exposure to air for NPs grown at 200 °C. This was not the case for the sample grown at 100 °C. As the growth temperature influences the NP size, it was concluded that the increased size causes the stability against full oxidation. After being exposed to air for two months, the final oxidation state of the NPs was reached, as it was shown that the analysis of the Cu 2p XP spectra after two months and after eight months resulted in the same oxidation state.

For the Cu NPs grown on anatase $TiO_2(101)$, the time evolution of the oxidation was studied by following the (metallic) Cu NP size. The size of the metallic Cu NPs was found to decrease significantly after exposure to 1 bar O_2 for 60 minutes, but then not to change after another 60 minutes of oxidation. The comparison of the oxide Bragg peak intensity with the metallic Cu Bragg peak intensity showed that oxidation is still ongoing after one week of air exposure. Thus, it can be considered to happen on similar time-frames as the oxidation of Cu NPs on rutile.

Cu NPs on rutile and anatase single crystals formed mixtures of CuO and Cu_2O when exposed to ambient pressure of oxygen at room temperature. The ratio of CuO and Cu_2O was found to scale inversely with NP size on anatase substrates, resulting in less Cu_2O for smaller NPs, as detected by XPS.

CuO is Always Polycrystalline or Amorphous On all samples investigated, CuO was always found to be polycrystalline or amorphous (no XRD signal of epitaxial CuO or powder CuO, but CuO signal in XPS). For Cu_2O, the appearance of epitaxial structure was found to depend on the NP size. For relatively small NPs (roughly below 15 nm diameter), no signal of epitaxial oxide was found. For large Cu NPs, however, epitaxial Cu_2O was found on both rutile and anatase substrates. The epitaxial oxide featured the same epitaxy and orientation as the Cu NPs had before oxidation ([111]-orientation for rutile substrates and [470]-orientation for anatase substrates). Thus, it is also assumed that Cu/oxide core-shell particles are formed.

The Adsorption of Cysteine Depends on the Substrate, Cu NP Coverage and Oxidation State Cysteine was found to adsorb differently on Cu/TiO_2 systems, depending on the oxidation state of the Cu NPs and the TiO_2 polymorph (rutile or anatase). For systems of Cu(-oxide) NPs on anatase $TiO_2(101)$, the interaction is dominated by the formation of bonds between the deprotonated cysteine sulfur group and Cu (S-Cu). Moreover, the amino group is interacting with the surface, as IRRAS signal corresponding to NH_3^+ is suppressed in comparison to cysteine adsorption on bare TiO_2. The carboxyl group is deprotonated for all NP configurations for anatase substrates. For Cu NPs supported on rutile $TiO_2(110)$, the adsorption behavior is slightly different. As for the adsorption on Cu NPs supported on anatase, interaction between the cysteine thiol group and the Cu as well as interaction between the surface and the amino group were found. In addition, however, the thiol group and the carboxyl group are also present in their molecular form (S-H and COOH). This indicates different adsorption modes, possibly due to weaker interactions with the surface. The absolute amount of adsorbed cysteine was found to scale linearly with the Cu NP coverage. Moreover, it was found that higher amounts of Cu_2O (determined by XPS) correlate with an increased cysteine adsorption. For all substrates, the thiol group of cysteine was partially oxidized directly upon adsorption, as long as Cu-oxide and not only metallic Cu was present. Further signs of cysteine decomposition were found in the presence of a nitrile signal in IRRAS data after cysteine adsorption.

In total, this shows that cysteine adsorbs on the Cu/TiO_2 system through interaction with the amino group and the deprotonated carboxyl group, and by Cu-S bond formation, depending on the oxidation state and the substrate.

The Choice of Substrate Changes the Adsorption, not the Photocatalytic Activity The amount of adsorbed cysteine was found to scale linearly with the Cu NP coverage. Different Cu epitaxies and geometries were probed by investigating both rutile and anatase substrates. The adsorption was found to differ on both substrates, featuring more or less pronounced interactions of the thiol group with the Cu. The photocatalytic activity, measured by the amount of oxidized sulfur after exposure to light and air, was found to be independent of the choice of TiO_2 substrate, thus ruling out strong effects of epitaxy and geometry.

CuO is Beneficial for Photocatalysis It was shown that purely metallic Cu NPs lead to lower photocatalytic activity. Samples with a high amount of Cu_2O featured a high amount of adsorbed cysteine, but their catalytic performance was found to be relatively low, indicating competition between Cu-S bonds and thiol group oxidation. On samples featuring higher amounts of CuO, the highest amounts of cysteine oxidation were achieved.

High-Coverage CuO is Most Active Combining all the information, it can be concluded that high coverages of CuO NPs (or NPs with a high percentage of CuO) are most effective for the degradation of

cysteine.

For most NPs, the degradation of cysteine was independent of the light conditions and progressed linearly with exposure time to air, indicating a high catalytic activity. A notable exception is a sample with a high coverage of CuO NPs on rutile TiO_2, which showed thiol group oxidation only under visible light and UV light, not in darkness. On the one hand, this means that the sample is less active than the other ones in dark conditions. On the other hand, this was the sample with the highest absolute amount of oxidized cysteine, indicating strong catalytic activity in visible light.

Outlook While many of the initial questions were resolved, new questions arose: It was seen that cysteine strongly binds via Cu-S bonds, but it is not clear if these bonds will be weak enough for the molecules to desorb at some point. If not, the first layer of adsorbates will block all activity of the system. Moreover, as the degradation of the thiol group was used as a tool to identify the activity of the system, the research here remains blind to catalytically induced changes that occur to the other functional groups of cysteine. An exception to this is the nitrile bond found after adsorption and the N 1s peaks attributed to reduced nitrogen. Both hint at further interactions between the NPs and the cysteine molecules. Finally, it is not clear if the results from studying cysteine as a test molecule can carry over one-to-one to larger molecules and viruses. Thus, for the future, it would be of interest to study the interaction of the system with larger molecules as well as the desorption of bound cysteine.

Bibliography

[1] Amira Y. Ahmed et al. "Photocatalytic Activities of Different Well-defined Single Crystal TiO_2 Surfaces: Anatase versus Rutile". In: *The Journal of Physical Chemistry Letters* 2.19 (2011), pp. 2461–2465. ISSN: 1948-7185. DOI: 10.1021/jz201156b.

[2] Akira Fujishima and Kenichi Hond. "Electrochemical Photolysis of Water at a Semiconductor Electrode". In: *Nature* 1972.238 (1972), pp. 37–38.

[3] Aracely Hernández-Ramírez and Iliana Medina-Ramírez. *Photocatalytic Semiconductors: Synthesis, Characterization, and Environmental Applications*. Springer, 2015.

[4] Tadeusz Bak et al. "Effect of Crystal Imperfections on Reactivity and Photoreactivity of TiO_2 (Rutile) with Oxygen, Water, and Bacteria". In: *The Journal of Physical Chemistry C* 115.32 (2011), pp. 15711–15738. ISSN: 1932-7447. DOI: 10.1021/jp2027862.

[5] Miguel Blanco Garcia et al. "Adsorption and Sulfur-Selective Photooxidation of Cysteine on Anatase TiO_2(101)". In: *Journal of the American Chemical Society* tba.tba (2026). DOI: 10.1021/jacs.6c07370.

[6] Miguel Blanco Garcia et al. "Unraveling the Role of the Multifunctional Groups in the Adsorption of l-Cysteine on Rutile TiO_2(110)". In: *Journal of the American Chemical Society* 147.44 (2025), pp. 40158–40170. DOI: 10.1021/jacs.5c07119.

[7] Jeremy K. Burdett et al. "Structural-Electronic Relationships in Inorganic Solids: Powder Neutron Diffraction Studies of the Rutile and Anatase Polymorphs of Titanium Dioxide at 15 and 295 K". In: *Journal of the American Chemical Society* 109.12 (1987), pp. 3639–3646. ISSN: 0002-7863. DOI: 10.1021/ja00246a021.

[8] O. CARP. "Photoinduced Reactivity of Titanium Dioxide". In: *Progress in Solid State Chemistry* 32.1-2 (2004), pp. 33–177. ISSN: 00796786. DOI: 10.1016/j.progsolidstchem.2004.08.001.

[9] D.A. Chen et al. "Self-Limiting Growth of Copper Islands on TiO_2(110)-(1x1)". In: *Surface Science* 2000.450 (1999), pp. 78–97.

[10] Daniel Silvan Dolling et al. "In-Situ Growth and Oxidation of Cu Nanoparticles on Rutile TiO_2(110)". In: *The Journal of Physical Chemistry C* 130.20 (2026), pp. 7136–7147. ISSN: 1932-7447. DOI: 10.1021/acs.jpcc.6c00835.

[11] Howard A. Foster et al. "Photocatalytic Disinfection Using Titanium Dioxide: Spectrum and Mechanism of Antimicrobial Activity". In: *Applied Microbiology and Biotechnology* 90.6 (2011), pp. 1847–1868. DOI: 10.1007/s00253-011-3213-7.

[12] Robert Gleißner et al. "Copper Nanoparticles with High Index Facets on Basal and Vicinal ZnO Surfaces". In: *The Journal of Physical Chemistry C* 125.42 (2021), pp. 23561–23569. ISSN: 1932-7447. DOI: 10.1021/acs.jpcc.1c08008.

[13] Robert Gleißner et al. “Role of Oxidation-Reduction Dynamics in the Application of Cu/ZnO-Based Catalysts”. In: *ACS Applied Nano Materials* 6.9 (2023), pp. 8004–8016. ISSN: 2574-0970. DOI: 10.1021/acsanm.3c01306.

[14] Xue-Qing Gong et al. “Small Au and Pt Clusters at the Anatase TiO_2(101) Surface: Behavior at Terraces, Steps, and Surface Oxygen Vacancies”. In: *Journal of the American Chemical Society* 130.1 (2008), pp. 370–381. DOI: 10.1021/ja0773148.

[15] Tiehu Han et al. “The Study on Preparation and Photocatalytic Activities of Cu_2O/TiO_2 Nanoparticles”. In: *Journal of Environmental Chemical Engineering* 3.4 (2015), pp. 2453–2462. ISSN: 22133437. DOI: 10.1016/j.jece.2015.09.020.

[16] Kazuhito Hashimoto, Hiroshi Irie, and Akira Fujishima. “TiO_2 Photocatalysis: A Historical Overview and Future Prospects”. In: *Japanese Journal of Applied Physics* 44.12 (2005), pp. 8269–8285. ISSN: 0021-4922. DOI: 10.1143/JJAP.44.8269.

[17] Herolab GmbH Laborgeräte. *UV Analysis Lamps (Hand Lamps)*. Manufacturer brochure, accessed 21.06.2026. 2024. URL: https://www.herolab.de/wp-content/uploads/2025/03/Analysis-Lamps-EN.pdf.

[18] James A. Imlay. “Pathways of Oxidative Damage”. In: *Annual Review of Microbiology* 57 (2003), pp. 395–418. ISSN: 0066-4227. DOI: 10.1146/annurev.micro.57.030502.090938.

[19] Hiroshi Irie et al. “Visible Light-Sensitive Cu(II)-Grafted TiO_2 Photocatalysts: Activities and X-ray Absorption Fine Structure Analyses”. In: *The Journal of Physical Chemistry C* 113.24 (2009), pp. 10761–10766. ISSN: 1932-7447. DOI: 10.1021/jp903063z.

[20] Astrid Jürgensen et al. “An In-Situ XPS Study of L-Cysteine Co-Adsorbed with Water on Polycrystalline Copper and Gold”. In: *Applied Surface Science* 435 (2018), pp. 870–879. ISSN: 01694332. DOI: 10.1016/j.apsusc.2017.11.150.

[21] Kayano Sunada et al. “Bactericidal and Detoxification Effects of TiO_2 Thin Film Photocatalysts”. In: *Environmental science & technology* 1998.32 (). ISSN: 0013-936X.

[22] Jeong Won Kim, Han-Na Hwang, and Chan-Cuk Hwang. “Adsorption of Cysteine on Cu(110) Studied by Core-Level Photoelectron Spectroscopy”. In: *The Journal of Physical Chemistry C* 111.35 (2007), pp. 13192–13196. ISSN: 1932-7447. DOI: 10.1021/jp072496d.

[23] Jeong Won Kim et al. “Surface Reaction of Sulfur-Containing Amino Acids on Cu(110)”. In: *Langmuir : the ACS Journal of Surfaces and Colloids* 26.8 (2010), pp. 5632–5636. ISSN: 0743-7463. DOI: 10.1021/la904496j.

[24] Mona Kohantorabi et al. “Adsorption and Inactivation of SARS-CoV-2 on the Surface of Anatase TiO_2(101)”. In: *ACS Applied Materials & Interfaces* 15.6 (2023), pp. 8770–8782. DOI: 10.1021/acsami.2c22078.

[25] Mona Kohantorabi et al. “Light-Induced Transformation of Virus-Like Particles on TiO_2”. In: *ACS Applied Materials & Interfaces* 16.28 (2024), pp. 37275–37287. DOI: 10.1021/acsami.4c07151.

[26] Yang Li et al. “Mechanism of Photogenerated Reactive Oxygen Species and Correlation with the Antibacterial Properties of Engineered Metal-Oxide Nanoparticles”. In: *ACS Nano* 6.6 (2012), pp. 5164–5173. DOI: 10.1021/nn300934k.

[27] Michele S. de Lima et al. “Visible Light-Driven Photocatalysis and Antibacterial Performance of a Cu-TiO2 Nanocomposite”. In: *ACS Omega* 9.47 (2024), pp. 47122–47134. DOI: 10.1021/acsomega.4c07515.

[28] Min Liu et al. "Visible-Light Sensitive Cu(II)-TiO_2 with Sustained Anti-Viral Activity for Efficient Indoor Environmental Remediation". In: *Journal of Materials Chemistry A* 3.33 (2015), pp. 17312–17319. ISSN: 2050-7488. DOI: 10.1039/C5TA03756E.

[29] M.R. Pinnel, H.G. Tompkins, and D.E. Heath. "Oxidation of Copper in Controlled Clean Air and Standard Laboratory air at 50°C to 150°C". In: *Applications of Surface Science* 1979.2 (1979), pp. 558–577.

[30] Maria Guadalupe Méndez-Medrano et al. "Heterojunction of CuO Nanoclusters with TiO_2 for Photo-Oxidation of Organic Compounds and for Hydrogen Production". In: *The Journal of Chemical Physics* 153.3 (2020), p. 034705. DOI: 10.1063/5.0015277.

[31] Masahiro Miyauchi, Kayano Sunada, and Kazuhito Hashimoto. "Antiviral Effect of Visible Light-Sensitive Cu_xO/TiO_2 Photocatalyst". In: *Catalysts* 10.9 (2020), p. 1093. DOI: 10.3390/catal10091093.

[32] Masahiro Miyauchi et al. "Visible-Light-Sensitive Photocatalysts: Nanocluster-Grafted Titanium Dioxide for Indoor Environmental Remediation". In: *The Journal of Physical Chemistry Letters* 7.1 (2016), pp. 75–84. DOI: 10.1021/acs.jpclett.5b02041.

[33] Ryuichi Nakano et al. "Inactivation of Various Variant Types of SARS-CoV-2 by Indoor-Light-Sensitive TiO_2-Based Photocatalyst". In: *Scientific Reports* 12.1 (2022), p. 5804. DOI: 10.1038/s41598-022-09402-7.

[34] Sara Nilsson et al. "Resolving Single Cu Nanoparticle Oxidation and Kirkendall Void Vormation with In Situ Plasmonic Nanospectroscopy and Electrodynamic Simulations". In: *Nanoscale* 11.43 (2019), pp. 20725–20733. DOI: 10.1039/c9nr07681f.

[35] Sara Nilsson et al. *Unravelling Competing Oxidation Mechanisms in Single Cu Nanoparticles*. 2022. DOI: 10.21203/rs.3.rs-1148708/v1.

[36] Yoshio Nosaka and Atsuko Y. Nosaka. "Generation and Detection of Reactive Oxygen Species in Photocatalysis". In: *Chemical Reviews* 117.17 (2017), pp. 11302–11336. DOI: 10.1021/acs.chemrev.7b00161.

[37] K. Osako et al. "Examination of Interfacial Charge Transfer in Photocatalysis Using Patterned CuO Thin Film Deposited on TiO_2". In: *APL Materials* 3.10 (2015), p. 104409. DOI: 10.1063/1.4926934.

[38] David B. Pedersen, Shiliang Wang, and Septimus H. Liang. "Charge-Transfer-Driven Diffusion Processes in Cu@Cu-Oxide Core−Shell Nanoparticles: Oxidation of 3.0 ± 0.3 nm Diameter Copper Nanoparticles". In: *The Journal of Physical Chemistry C* 112.24 (2008), pp. 8819–8826. ISSN: 1932-7447. DOI: 10.1021/jp710619r.

[39] Xiaoqing Qiu et al. "Hybrid Cu_xO/TiO_2 Nanocomposites as Risk-Reduction Materials in Indoor Environments". In: *ACS Nano* 6.2 (2012), pp. 1609–1618. DOI: 10.1021/nn2045888.

[40] A. E. Rakhshani. "Preparation, Characteristics and Photovoltaic Properties of Cuprous Oxide - A Review". In: *Solid-State Electronics* 29.1 (1986), pp. 7–17. ISSN: 00381101. DOI: 10.1016/0038-1101(86)90191-7.

[41] Katherine P. Rice, Andrew S. Paterson, and Mark P. Stoykovich. "Nanoscale Kirkendall Effect and Oxidation Kinetics in Copper Nanocrystals Characterized by Real-Time, In Situ Optical Spectroscopy". In: *Particle & Particle Systems Characterization* 32.3 (2015), pp. 373–380. ISSN: 09340866. DOI: 10.1002/ppsc.201400155.

[42] Norbert Schell et al. "The High Energy Materials Science Beamline (HEMS) at PETRA III". In: *Materials Science Forum* 772 (2013), pp. 57–61. DOI: 10.4028/www.scientific.net/MSF.772.57.

[43] C. Schlueter et al. “The new dedicated HAXPES beamline P22 at PETRAIII”. In: AIP Conference Proceedings. Author(s), 2019, p. 040010. DOI: 10.1063/1.5084611.

[44] A. Sclafani and J. M. Herrmann. “Comparison of the Photoelectronic and Photocatalytic Activities of Various Anatase and Rutile Forms of Titania in Pure Liquid Organic Phases and in Aqueous Solutions”. In: *The Journal of Physical Chemistry* 100.32 (1996), pp. 13655–13661. ISSN: 0022-3654. DOI: 10.1021/jp9533584.

[45] M. P. Seah and W. A. Dench. “Quantitative Electron Spectroscopy of Surfaces: A Standard Data Base for Electron Inelastic Mean Free Paths in Solids”. In: *Surface and Interface Analysis* 1.1 (1979), pp. 2–11. ISSN: 0142-2421. DOI: 10.1002/sia.740010103.

[46] Andreas Stierle et al. “DESY NanoLab”. In: *Journal of Large-Scale Research Facilities JLSRF* 2 (2016). DOI: 10.17815/jlsrf-2-140.

[47] Kayano Sunada, Masafumi Minoshima, and Kazuhito Hashimoto. “Highly Efficient Antiviral and Antibacterial Activities of Solid-State Cuprous Compounds”. In: *Journal of Hazardous Materials* 235-236 (2012), pp. 265–270. DOI: 10.1016/j.jhazmat.2012.07.052.

[48] Thorlabs, Inc. *MBB1L3 LED Emission Spectrum Data*. Excel file downloaded from the Thorlabs website, accessed 21.06.2026. 2026. URL: https://www.thorlabs.com/mounted-leds?pn=MBB1L3&tabName=Overview.

[49] Robert B. Thurman, Charles P. Gerba, and Gabriel Bitton. “The Molecular Mechanisms of Copper and Silver Ion Disinfection of Bacteria and Viruses”. In: *Critical Reviews in Environmental Control* 18.4 (1989), pp. 295–315. ISSN: 1040-838X. DOI: 10.1080/10643388909388351.

[50] Yimin Tong et al. “Photo-Catalyzed TiO_2 Inactivates Pathogenic Viruses by Attacking Viral Genome”. In: *Chemical engineering journal (Lausanne, Switzerland : 1996)* 414 (2021), p. 128788. ISSN: 1385-8947. DOI: 10.1016/j.cej.2021.128788.

[51] U. Diebold, J.-M. Pan, and and T. E. Madey. “Growth Mode of Ultrathin Copper Overlayers on TiO_2(110)”. In: *Physical Review B* 1993.47 (1993), pp. 3868–3876. ISSN: 0163-1829. DOI: 10.1103/PhysRevB.47.3868.

[52] U.S. Geological Survey. *Mineral Commodity Summaries 2024*. Tech. rep. 2024. 212 p. U.S. Geological Survey, 2024. DOI: 10.3133/mcs2024. URL: https://pubs.usgs.gov/publication/mcs2024.

[53] Carl Wagner. “Elementarvorgänge bei der Bildung von Metalloxyd aus Metall und Sauerstoff sowie bei verwandten Reaktionen”. In: *Angewandte Chemie* 49.41 (1936), pp. 735–740. ISSN: 0044-8249. DOI: 10.1002/ange.19360494102.

[54] Daji Wang et al. “TiO2 supported single Ag atoms nanozyme for elimination of SARS-CoV2”. In: *Nano Today* 40 (2021), p. 101243. ISSN: 1748-0132. DOI: https://doi.org/10.1016/j.nantod.2021.101243. URL: https://www.sciencedirect.com/science/article/pii/S1748013221001687.

[55] Yiwen Wang et al. “Thiol Adsorption on and Reduction of Copper Oxide Particles and Surfaces”. In: *Langmuir : the ACS Journal of Surfaces and Colloids* 32.16 (2016), pp. 3848–3857. ISSN: 0743-7463. DOI: 10.1021/acs.langmuir.6b00651.

[56] A. Wilson et al. “Epitaxial Growth of Bimetallic Au-Cu Nanoparticles on TiO_2(110) Followed In Situ by Scanning Tunneling Microscopy and Grazing-Incidence X-Ray Diffraction”. In: *Physical Review B* 90.7 (2014), pp. 075416–075426. ISSN: 0163-1829. DOI: 10.1103/PhysRevB.90.075416.

[57] X. Sang and T.G. Phan and F. Yagyu and S. Okitsu and N. Maneekarn and W.E. Müller and H. Ushijima. "Photocatalytic Inactivation of Diarrheal Viruses by Visible-Light-Catalytic Titanium Dioxide". In: *Clin Lab.* 2007.53 (2007), pp. 413–421.

[58] Yun Zhou et al. "Growth of Pt Particles on the Anatase TiO_2(101) Surface". In: *The Journal of Physical Chemistry C* 116.22 (2012), pp. 12114–12123. ISSN: 1932-7447. DOI: 10.1021/jp302273m.

Chapter 9

SI Article I

Supplementary Information: In-Situ Growth and Oxidation of Cu Nanoparticles on Rutile TiO_2(110)

Daniel Silvan Dolling[1,2]
Miguel Blanco Garcia[1,2]
Mona Kohatorabi[1]
Yufeng Zhai[3]
Benedikt Sochor[3]
Mohammad Ebrahim Haji Naghi Tehrani[1,2]
Jan-Christian Schober[1,2]
Ming-Chao Kao[1,2]
Jagrati Dwivedi[1]
Arno Jeromin[1]
Olof Gutowski[3]
Dmitri V. Novikov[3]
Thomas F. Keller[1,2]
Stephan V. Roth[3,4]
Andreas Stierle[1,2*]
Heshmat Noei[1,2†]

[1]Centre for X-ray and Nano Science CXNS,
Deutsches Elektronen-Synchrotron DESY,
Notkestr. 85, 22607 Hamburg, Germany

[2]Fachbereich Physik, Universität Hamburg,
Jungiusstrasse 11, 20355 Hamburg, Germany

[3]Deutsches Elektronen-Synchrotron DESY,
Notkestr. 85, 22607 Hamburg, Germany

[4]KTH Royal Institute of Technology,
Department of Fibre and Polymer Technology,
Division of Fibre Processes,
Teknikringen 56, SE-100 44 Stockholm, Sweden

April 23, 2026

1 Oxidation Time

Table S1: The oxidation time for the samples. Each step gives the time between two measurements.

sample	time at 1 bar O_2 during the first oxidation	time at 1 bar O_2 during the second oxidation	time at ambient condition before HEXRD	time at ambient condition before XPS	time before second XPS measurement
A	20 min	80 min	30 min	62 days	6 months
B	36 min	-	8d 15h	62 days	6 months
C	30 min	270 min	4d 20h	62 days	

2 XRR Data

*andreas.stierle@desy.de
†heshmat.noei@desy.de

Table S2: The coverage and the nominal thickness of Cu and Cu oxide, obtained from fitted XRR data. The XRR measurement after oxidation for sample A, XRR was done after 100 minutes at 1 bar O_2, for sample C XRR was done after 5 h at 1 bar O_2 and heating to 100 °C.

	before oxidation		after oxidation at 1 bar O_2	
	coverage [%]	nominal thickness [nm]	coverage [%]	nominal thickness [nm]
sample A	44	1.2	48	1.7
sample B	38	0.7		
sample C	10	0.3	11	0.5

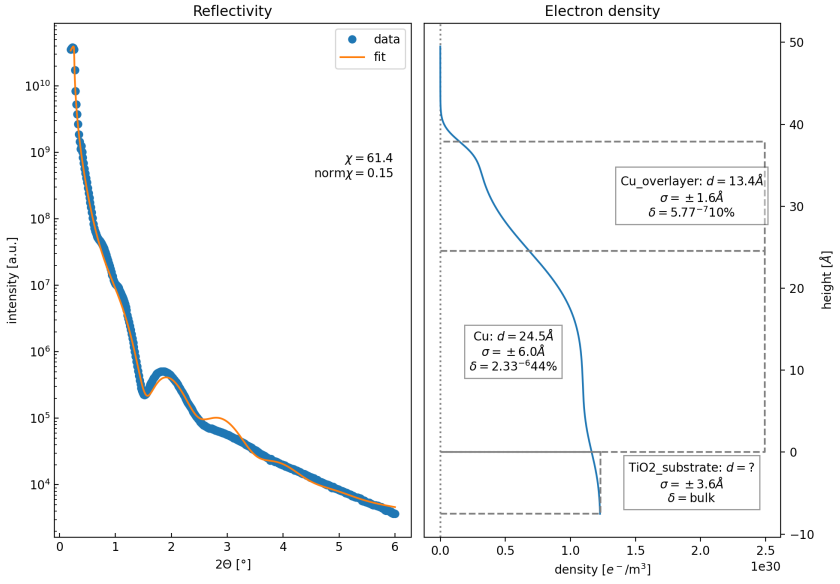


Figure S1: XRR data and fit for sample A, before oxidation.

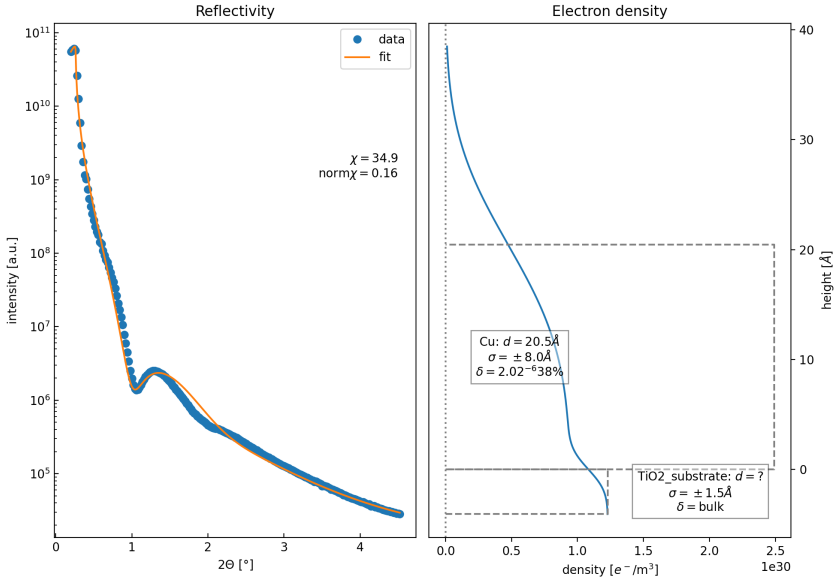


Figure S2: XRR data and fit for sample B, before oxidation.

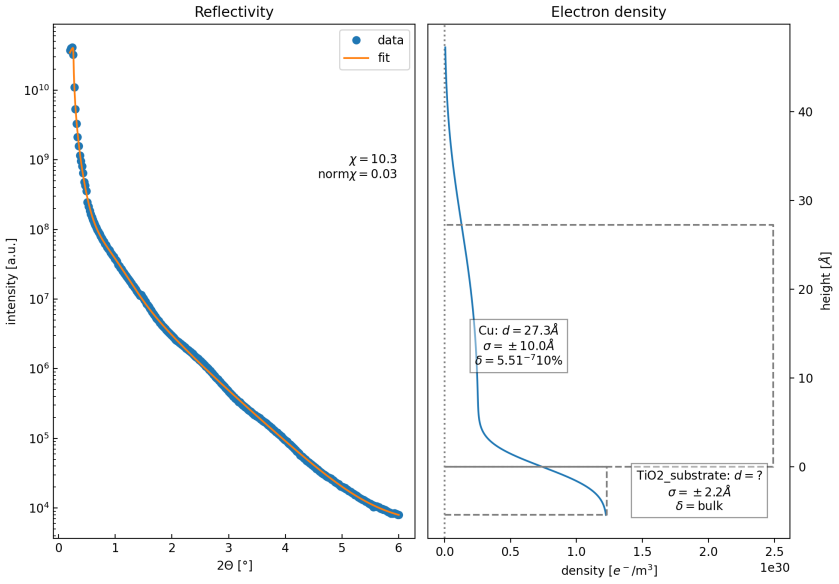


Figure S3: XRR data and fit for sample C, before oxidation.

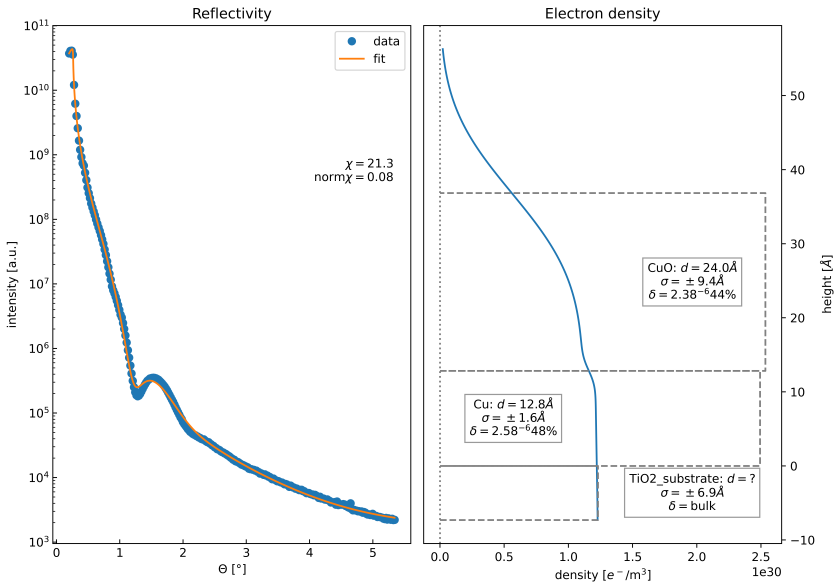


Figure S4: XRR data and fit for sample A, after oxidation (100 minutes at 1 bar O_2).

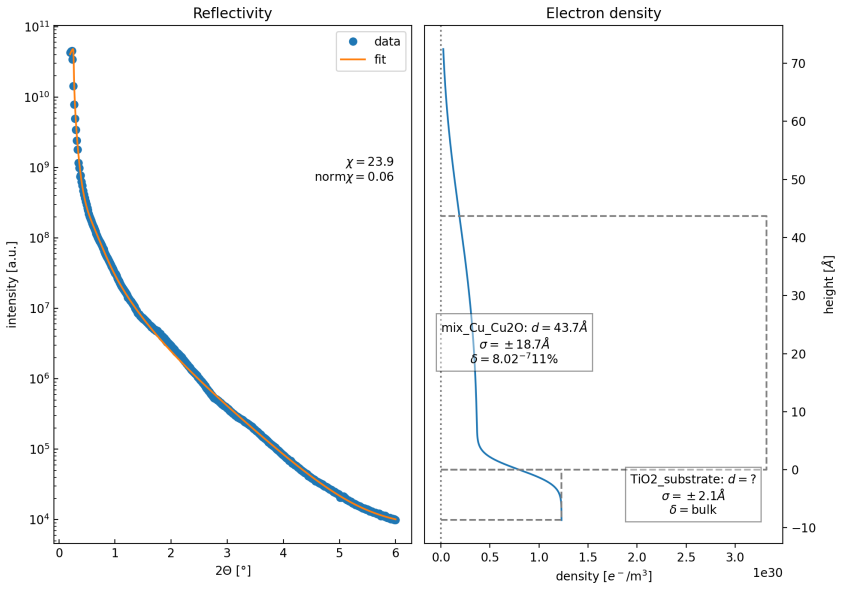


Figure S5: XRR data and fit for sample C, after oxidation (5 h at 1 bar O_2).

3 In-plane Rocking Scans Before Oxidation

The in-plane scans sensitive to Cu(200) and Cu(220) reveal two different in-plane epitaxies for Cu[100] out-of-plane orientation, see Figure S10: $Cu[2\bar{2}0]||TiO_2[1\bar{1}0]$ and both directions of a 24° tilt away from this epitaxy. The in-plane scans sensitive to Cu(220), Cu(111) and Cu(002) reveal Cu[110] out-of-plane oriented NPs with $Cu[220]||TiO_2[002]$ epitaxy. A graphical representation of the epitaxy assignment and the reciprocal map can be seen in Figure S9.

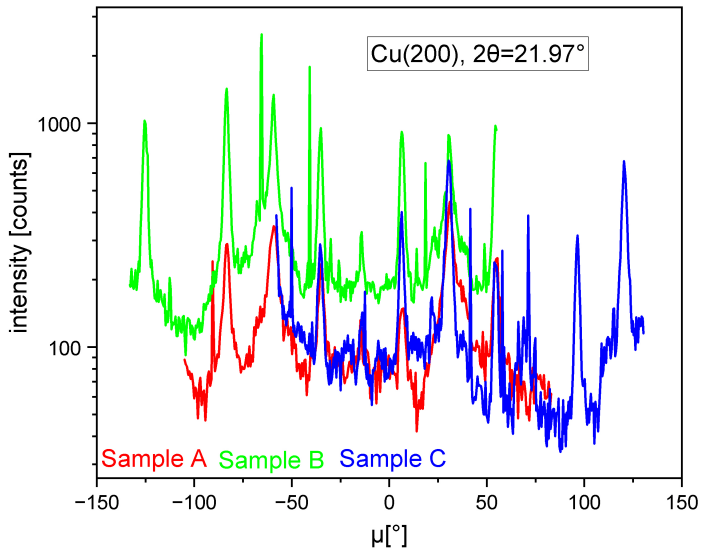


Figure S6: In-plane rocking scans of the samples before oxidation. The scans were set to detect Cu(200) planes.

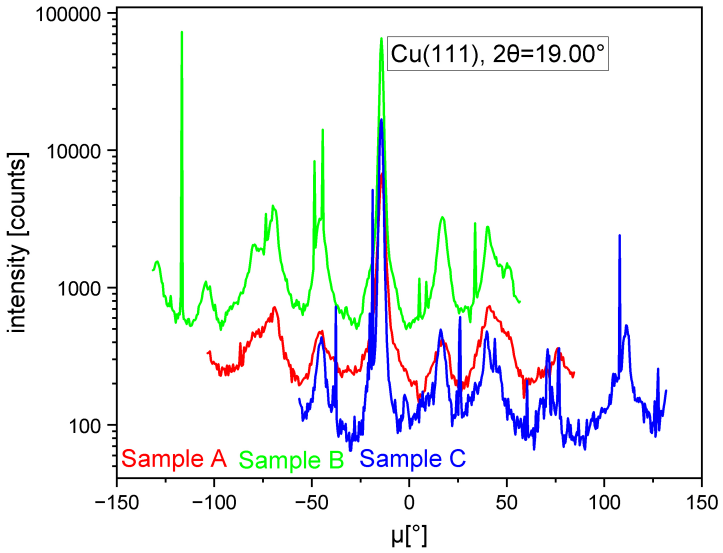


Figure S7: In-plane rocking scans of the samples before oxidation. The scans were set to detect Cu(111) planes.

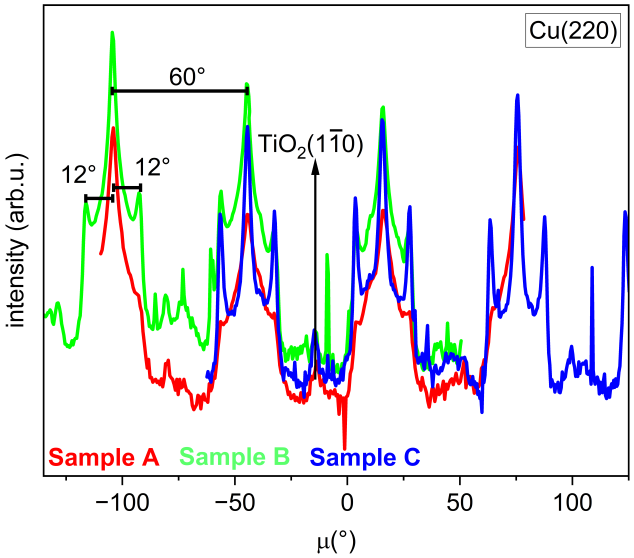


Figure S8: In-plane rocking scans of the samples before oxidation. The scans were set to detect Cu(220) planes.

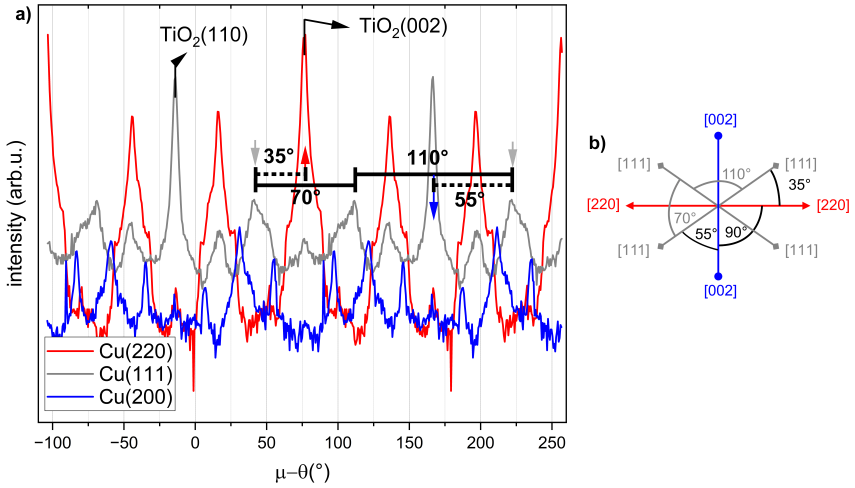


Figure S9: a) In-plane rocking scans set to detect Cu(111), Cu(220), and Cu(200) planes on sample A before oxidation. The measurement was only done over 180° (from -110° to 70°), the higher angle data is a duplicate of the lower angle data used to make pattern recognition easier. $\mu - \theta$ is the in-plane angle with subtracted Bragg angle, such that the positions of peaks for different scans can be compared. b) Schematic drawing of the angles between different in-plane diffraction peaks for Cu NPs with [110] out-of-plane orientation, in line with the markings in a). From the scans, it can be seen that [110] oriented Cu exists in Cu[110]||TiO_2[001] epitaxy.

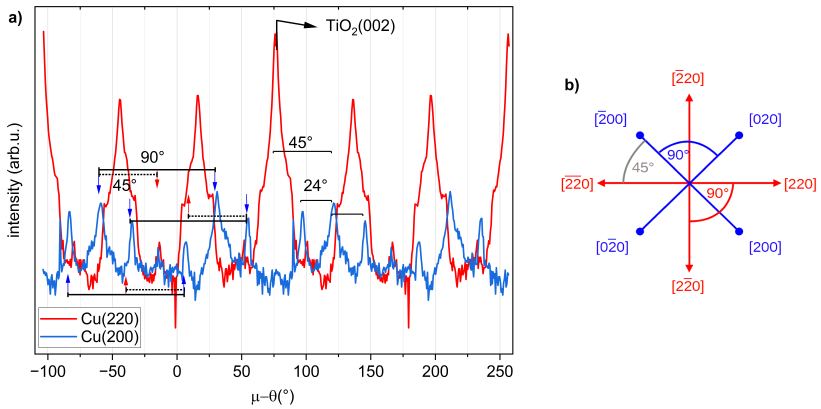


Figure S10: a) In-plane rocking scans set to detect Cu(220) and Cu(200) planes on sample A before oxidation. The measurement was only done over 180° (from -110° to 70°), the higher angle data is a duplicate of the lower angle data used to make pattern recognition easier. $\mu - \theta$ is the in-plane angle with subtracted Bragg angle, such that the positions of peaks for different scans can be compared. b) Schematic drawing of the angles between different in-plane diffraction peaks for Cu NPs with [100] out-of-plane orientation. From the scans, it can be seen that two different epitaxies with this orientation exist, Cu[110]||±24° TiO_2[001].

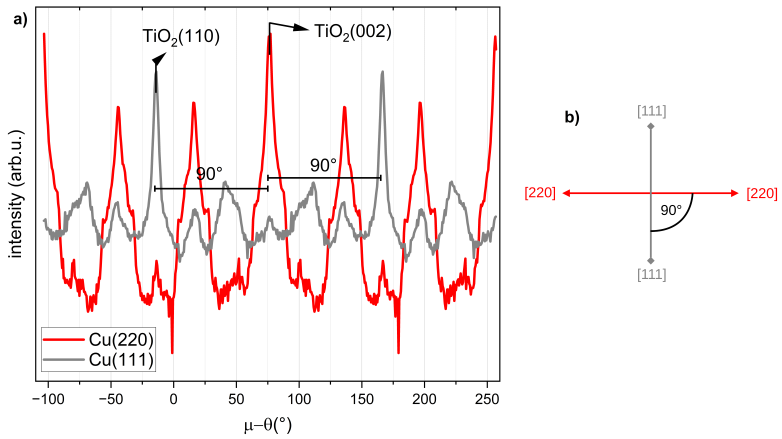


Figure S11: a) In-plane rocking scans set to detect Cu(111) and Cu(220) planes on sample A before oxidation. The measurement was only done over 180° (from -110° to 70°), the higher angle data is a duplicate of the lower angle data used to make pattern recognition easier. $\mu - \theta$ is the in-plane angle with subtracted Bragg angle, such that the positions of peaks for different scans can be compared. b) Schematic drawing of the angles between different in-plane diffraction peaks for Cu NPs with [112] out-of-plane orientation. From the scans, it can be seen that such an out-of-plane epitaxy with Cu[110]||TiO_2[001] in-plane epitaxy exists.

4 In-plane Rocking Scans After/during Oxidation

S15

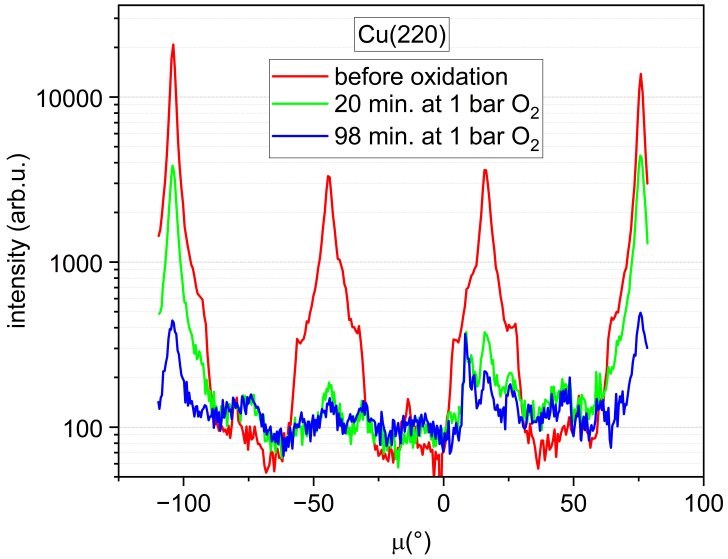


Figure S12: In-plane rocking scans sensitive to Cu(220) planes before and after oxidation of sample A. The measurements were taken at an 18 keV photon energy.

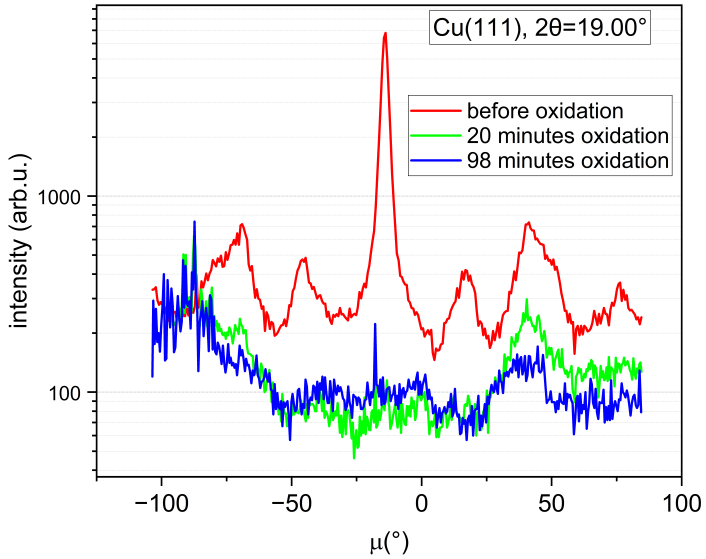


Figure S13: In-plane rocking scans sensitive to Cu(111) planes before and after oxidation of sample A. The measurements were taken at an 18 keV photon energy.

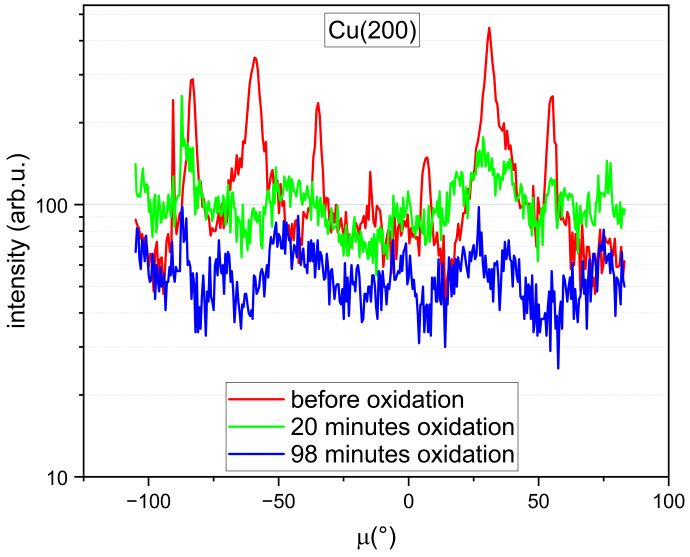


Figure S14: In-plane rocking scans sensitive to Cu(200) planes before and after oxidation of sample A. The measurements were taken at an 18 keV photon energy.

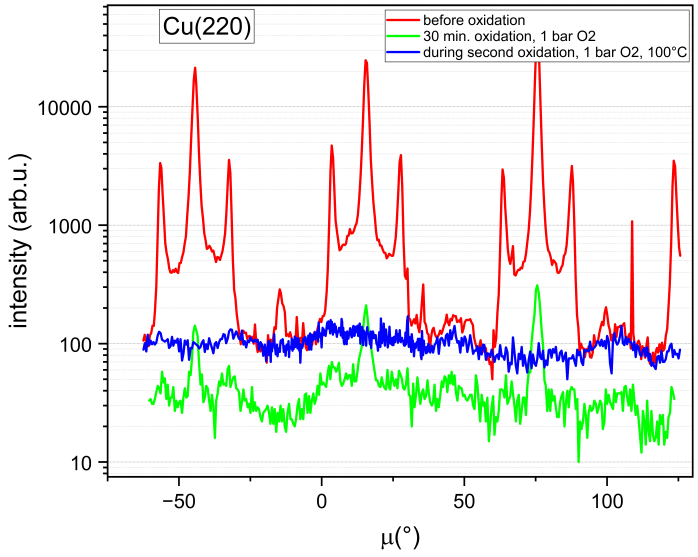


Figure S15: In-plane rocking scans sensitive to Cu(220) planes before and after oxidation of sample C, as well as during a second oxidation at 100 °C. The measurements were taken at an 18 keV photon energy.

5 In-plane Rocking Scans for Oxides

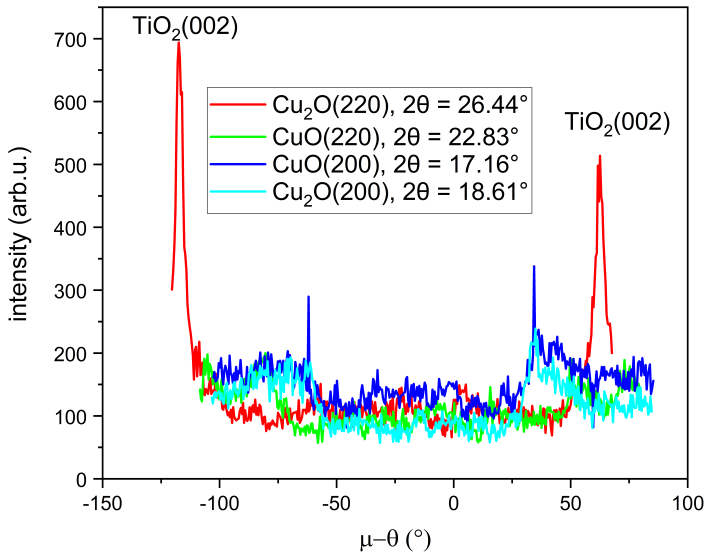


Figure S16: In-plane rocking scans for sample A set to detect epitaxial oxides with various orientations. The scans were done after the first oxidation step at atmospheric pressure. $\mu - \theta$ is the in-plane angle with subtracted Bragg angle, such that the positions of peaks for different scans can be compared.

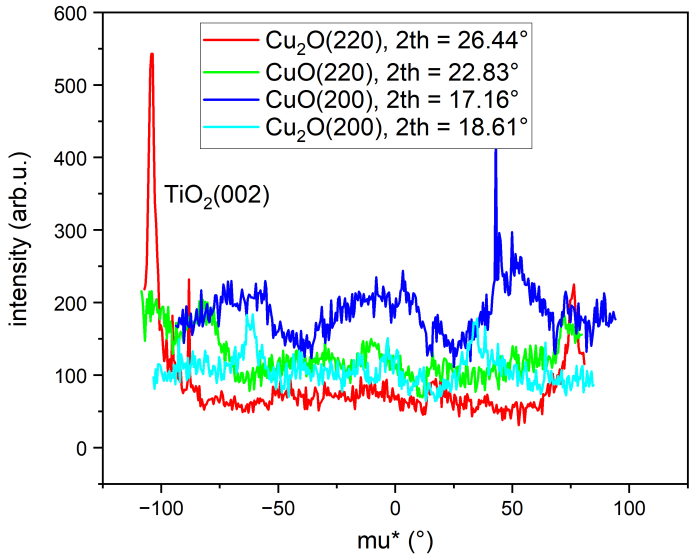


Figure S17: In-plane rocking scans for sample A set to detect epitaxial oxides with various orientations. The scans were done after the second oxidation step at atmospheric pressure.

6 HEXRD Data

Table S3: Found peaks and corresponding particle sizes calculated from line cuts for sample B. Due to weak signal or background noise, not all peaks that were found could be used for fitting. Details can be found in the SI.

Bragg Reflex	in-plane angle μ [°]	out-of-plane angle ϕ [°]	out-of-plane orientation	mean diameter [nm]	mean diameter error [nm]	mean height [nm]	mean height error [nm]
Cu(200)	59	36	111	14.92	0.79	7.15	0.68
Cu(200)	119	35	111				
Cu(200)	179	35	111				
Cu(200)	120	54	111				
Cu(220)	62	54	111				
Cu(220)	1	35	111				
Cu(200)	130	35	111	9.39	1.45	8.89	3.59
Cu(200)	110	35	111				
Cu(200)	50	35	111				
Cu(111)	110	27	112	15.62	2.75	8.08	1.48
Cu(111)	65	27	112				
Cu(200)	128	23	112				
Cu(200)	1	54	112				
Cu(200)	171	54	112				
Cu(111)	171	50	109	9.43	1.58	10.67	1.65
Cu(111)	1	50	109				
Cu(200)	171	73	109				
Cu(200)	5	73	109				
Cu(111)	100	34	200	16.88	1.74	10.58	2.66
Cu(111)	78	34	200				
Cu(200)	44	11	high index	12.94	1.44	7.22	1.08
Cu(200)	132	11	high index				

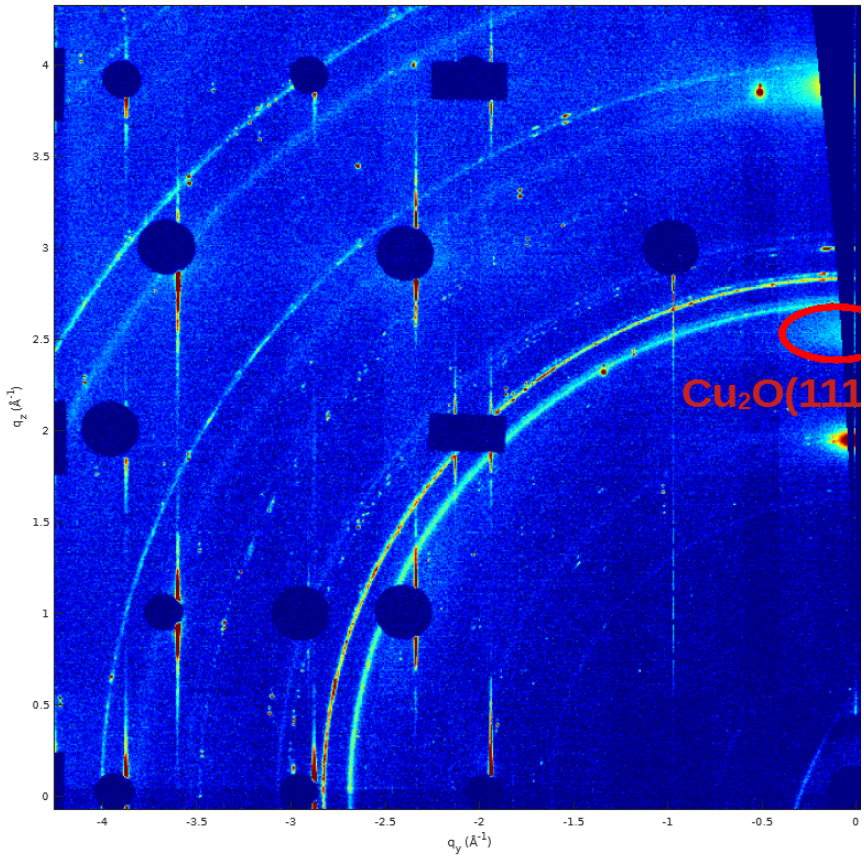


Figure S18: HEXRD data for sample A with a photon energy of 73.34 keV. The sample was turned 180° while measuring an image every 0.025°. The shown graphic is a sum of all images.

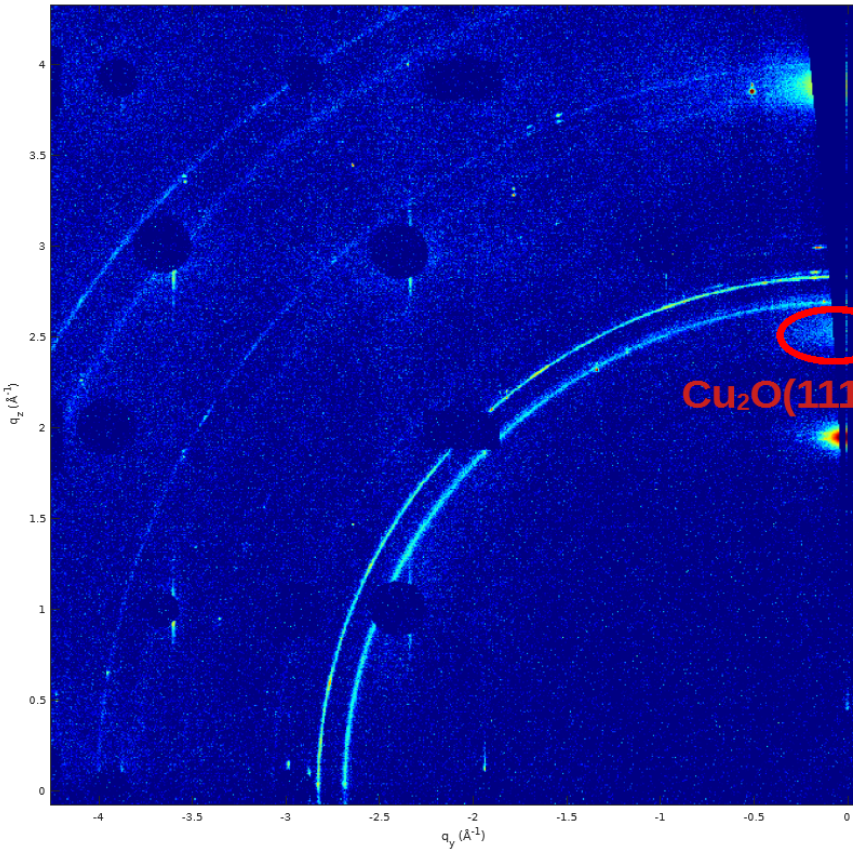


Figure S19: HEXRD data for sample C with a photon energy of 73.34 keV. The sample was turned 180° while measuring an image every 0.025°. The shown graphic is a sum of all images.

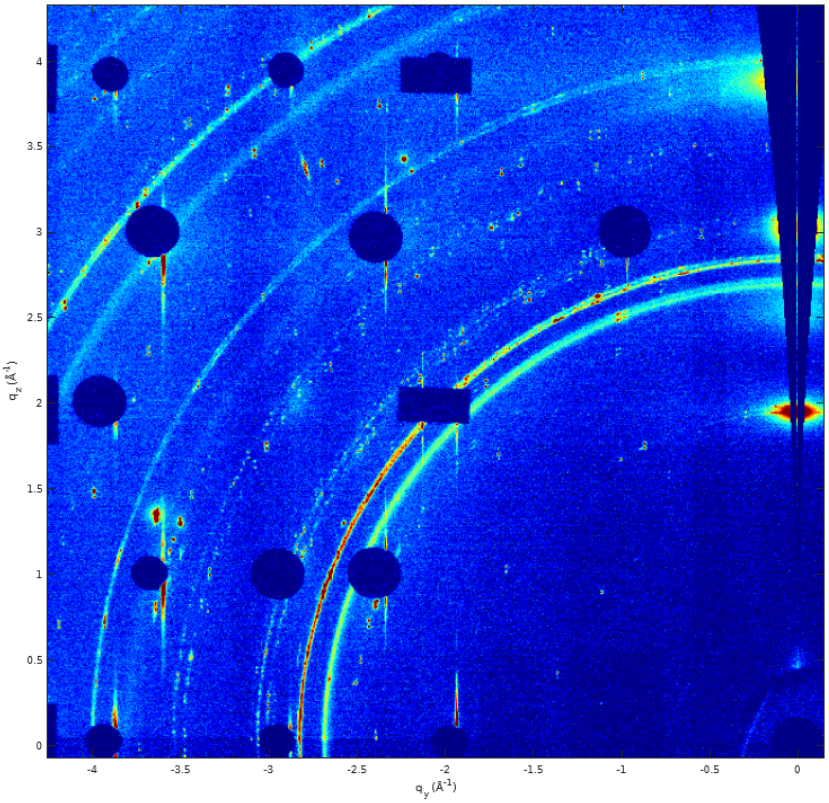


Figure S20: HEXRD data for sample B with a photon energy of 73.34 keV. The sample was turned 1° while measuring an image every 0.025°. he shown graphic is a sum of all images.

7 Line Scans through Bragg Peaks

Line scans have been done through Bragg peaks to calculate the particle diameters in in-plane and out-of-plane direction. The scans have been done along reciprocal lattice directions. The resulting curves were fitted with Pseudovoigt profiles. To calculate the corresponding particle sizes, Scherrer's Formula Scherrer's formula

$$D = \frac{2\pi}{\Delta \mathrm{Q}} \tag{1}$$

is used for the case of a (111)-oriented fcc surface (ΔQ is the FWHM momentum transfer). With the lattice constant of Cu, a_{Cu} the formula can be applied to calculate in-plane particle sizes D from scans in in-plane direction and out-of-plane particle sizes L from out of plane scan directions to be:

$$D = \sqrt{\frac{3}{8}} \times \frac{a_{\mathrm{Cu}}}{\mathrm{FWHM}} \tag{2}$$

$$L = \frac{\sqrt{3} a_{\mathrm{Cu}}}{\mathrm{FWHM}} \tag{3}$$

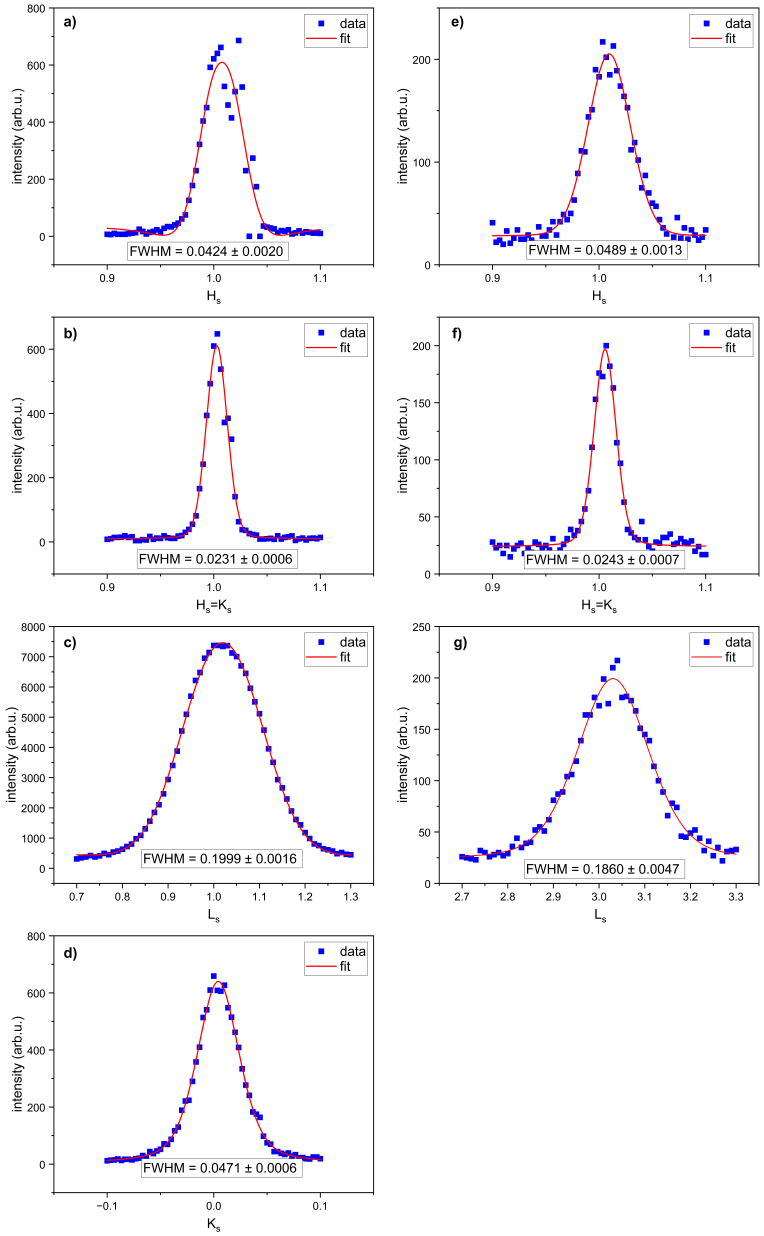


Figure S21: Line scans through the Bragg peak Cu(11$\bar{1}$) (a-d) and through the Bragg peak Cu(113) (e-g).

8 Line Scans After Oxidation

S30

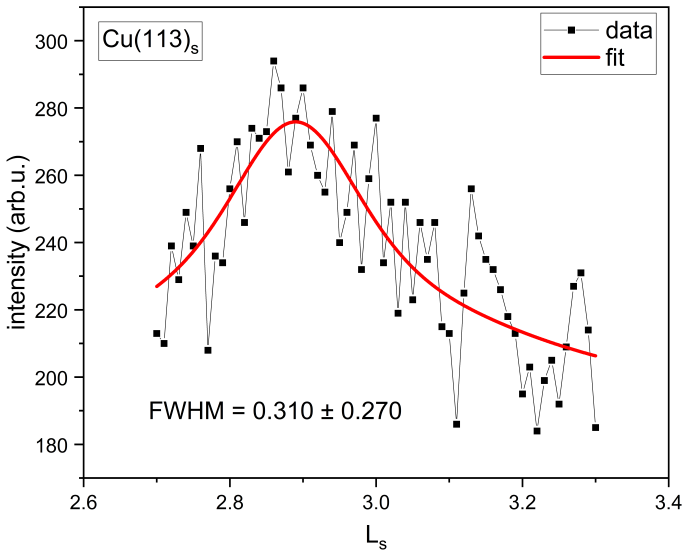


Figure S22: Line scan of sample A after the first oxidation (at 1 bar oxygen pressure) through the $Cu(113)_s$ peak.

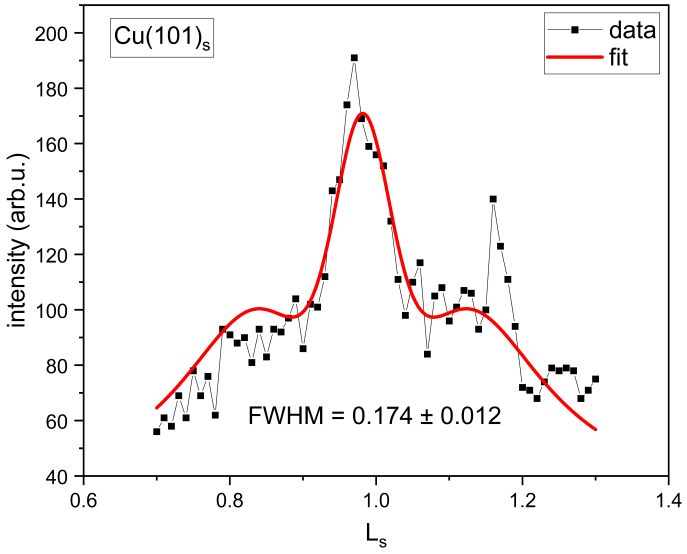


Figure S23: Line scan of sample A after the first oxidation (at 1 bar oxygen pressure) through the $Cu(101)_s$ peak.

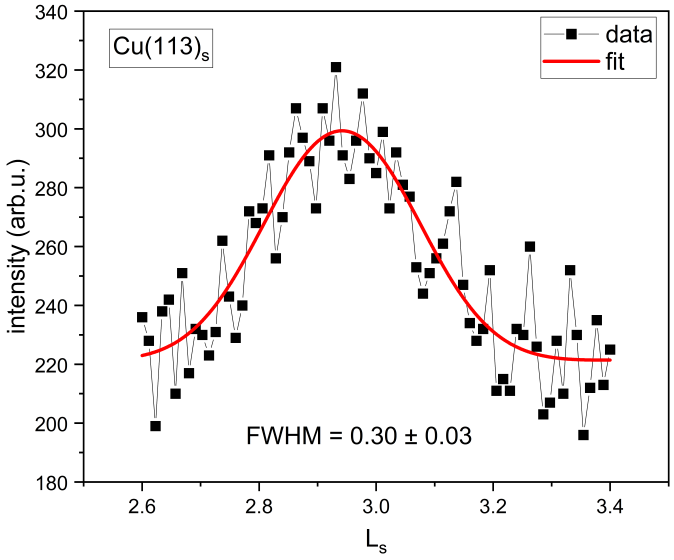


Figure S24: Line scan of sample A after the second oxidation (at 1 bar oxygen pressure) through the $Cu(113)_s$ peak.

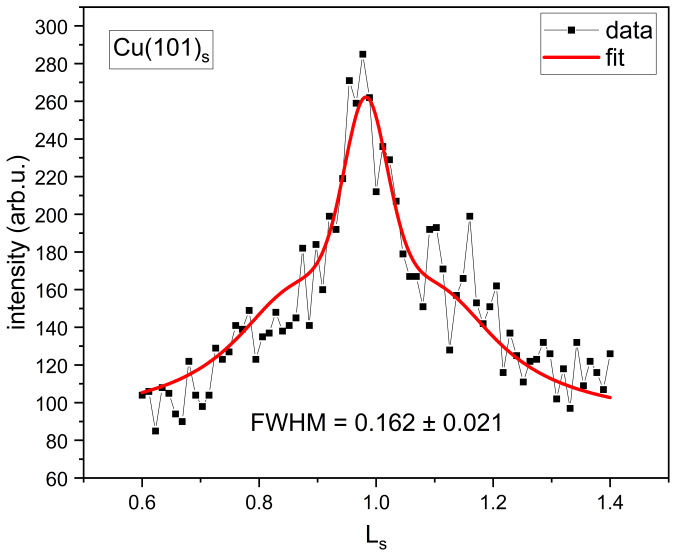


Figure S25: Line scan of sample A after the second oxidation (at 1 bar oxygen pressure) through the $Cu(101)_s$ peak.

9 Radial Scans Before Oxidation

Radial in-plane scans were fitted with Pseudovoigt profiles. From the fits, the FWHM was used to calculate the corresponding particle size (in-plane) with Scherrer's formula (with the wavelength λ and the Bragg angle θ:

$$D = \frac{0.9 \times \lambda}{\mathrm{FWHM}_{\mathrm{radians}} \times \cos\theta} \tag{4}$$

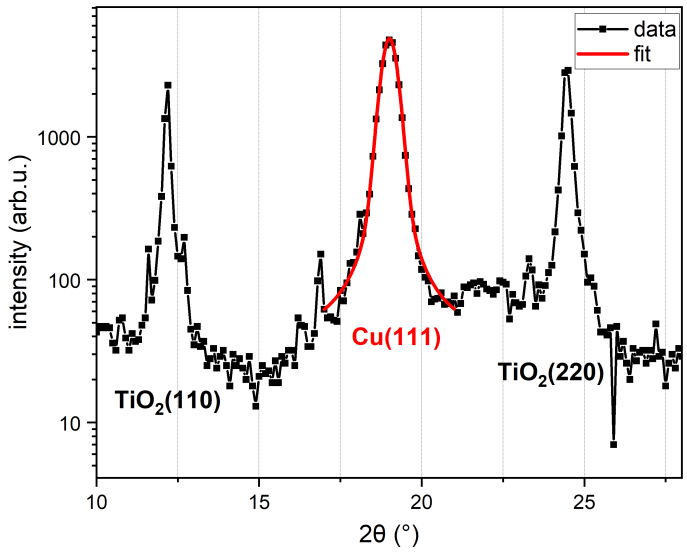


Figure S26: Radial scan through the Cu(111) peak of sample A before oxidation.

10 Radial Scans after Oxidation

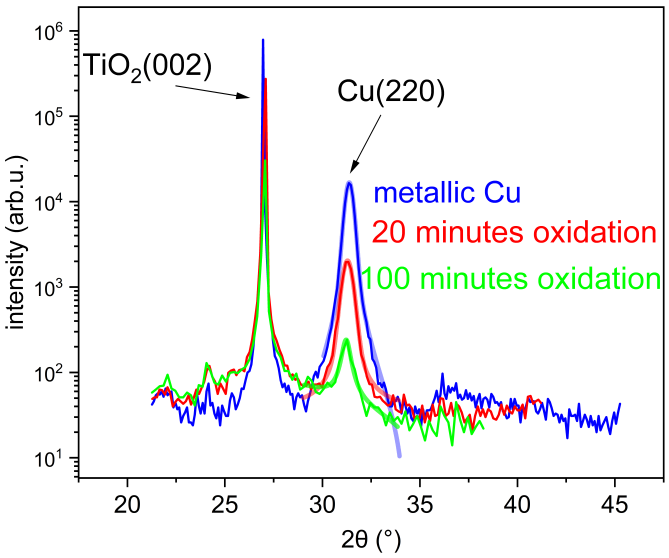


Figure S27: Radial scans through the Cu(220) in-plane peak of sample A before oxidation and after oxidation with fits.

11 SEM

S39

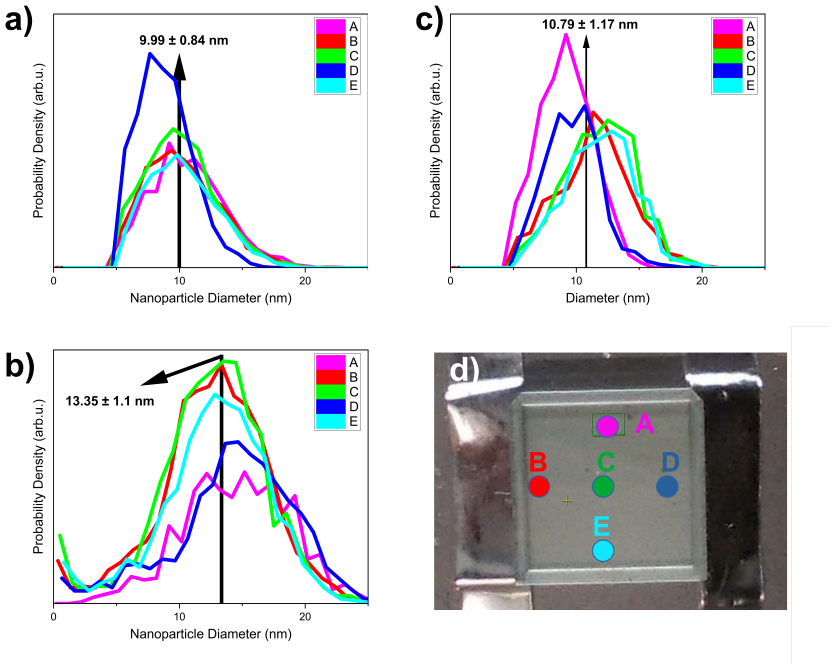


Figure S28: Histogram plots for the size distributions of the NPs on the different samples: a) Sample A, b) sample B and c) sample C. d) shows the positions of the SEM measurements on sample C - similar positions where used for all samples (position C was always in the middle).

12 XPS Fitting

The XP spectra were analysed with the CasaXPS software. They were normalized by fitting a step-down function to the Fermi edge and equating it to zero. All peaks were fitted with Gaussian-Lorentzian functions and a Shirley background, employing the Marquardt fitting algorithm. The resulting chi-squared values can be found in S4.

Table S4: Reduced chi-squared values for the fits of the XPS data.

	reduced chi-squared value		
oxidation time	Sample A	Sample B	Sample C
2 months	2.269	1.692	2.894
8 months	1.630	0.971	2.214

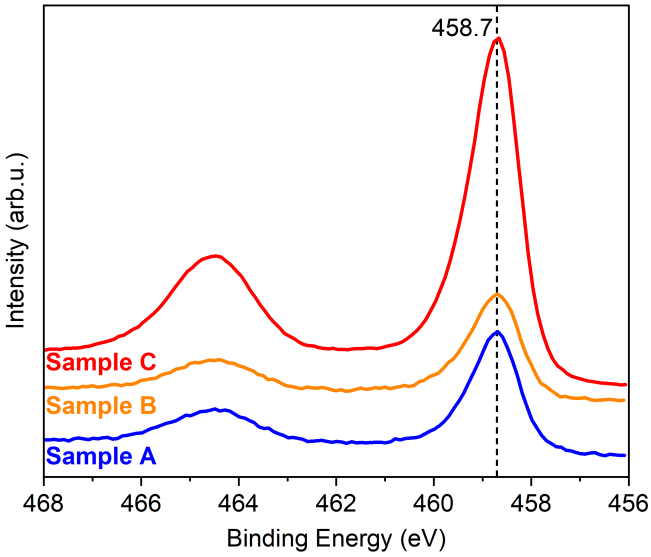


Figure S29: Ti 2p spectra of the samples after two months at air. All XPS spectra were normalized to have the Ti $2p\frac{3}{2}$ peak at 458.7 eV. No sign of Ti^{3+} is found.

13 XPS after 8 Months

Table S5: Parameters from fitting the Cu $2p_{3/2}$ XPS peak after the samples were stored at ambient conditions for eight months. The area percentage relates to the combined area of the peak assigned to CuO and the peak assigned to Cu and Cu_2O.

sample	CuO			Cu & Cu2O		
	Binding Energy [eV]	FWHM [eV]	Area [%]	Binding Energy [eV]	FWHM [eV]	Area [%]
A	933.10	2.90	85.48	931.62	1.40	14.52
B	933.26	2.88	81.64	931.34	1.36	18.36
C	933.00	2.80	88.70	931.52	1.40	11.30

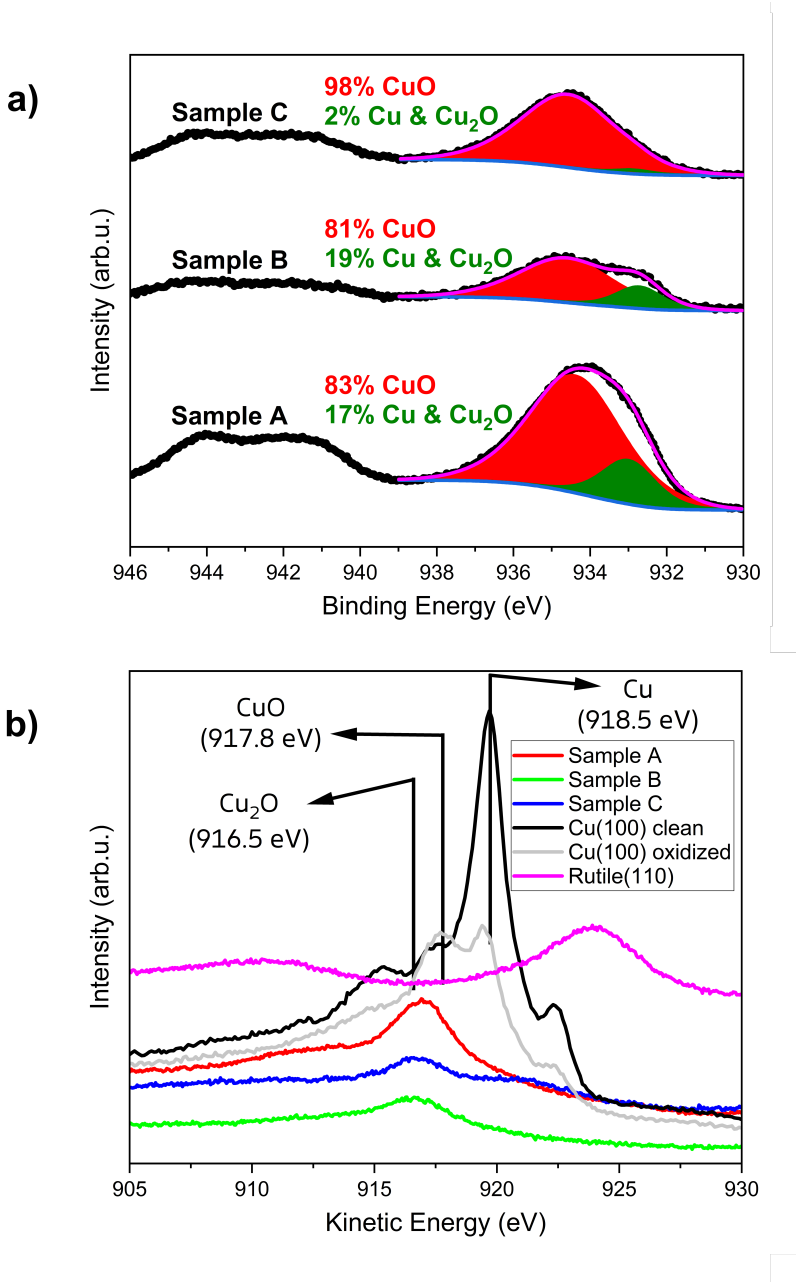


Figure S30: Cu 2p spectra measured via XPS after the samples had been stored at ambient conditions for ~~8~~ 44 months. The area percentage assigned to the fits is with respect to the total area covered by the fits.

14 GISAXS

Synthetic GISAXS Data Generation We generated a library of 2D GISAXS patterns for spherical Cu nanoparticles supported on a TiO_2 substrate using the distorted wave Born approximation (DWBA) [1] implementation in BornAgain [2]. The X-ray wavelength was set to 0.1025 nm and the incidence angle for the scattering simulation to 0.4°. Refractive indices (real decrement δ, absorption β) were $(\delta, \beta)_{\mathrm{Cu}} = (1.154 \times 10^{-5}, 9.6949 \times 10^{-7})$ and $(\delta, \beta)_{\mathrm{TiO_2}} = (5.82 \times 10^{-6}, 1.41 \times 10^{-7})$. The nanoparticle form factor was a hemisphere with in-plane radius R and out-of-plane height h. Detector geometry followed the experimental PILATUS-2M pixel size (172 μm) and the same field of view after cropping. Starting from the native 1475×1679 px detector, we applied a crop [left, up, down, right] = [300, 800, 440, 700] and simulated a 256×256 grid that covers the corresponding physical dimensions. The sample–to–detector distance was 4177.3 mm. For reciprocal-space conversion, we used the same distance (4177.3 mm) and an incident angle of α_i = 0.4° in the geometry module, ensuring that the (q_y, q_z) grid is consistent across all simulated frames and with the experimental preprocessing. We discretized (R, h) on a 30×30 grid over [0.05, 20] nm for both axes. For each grid point we ran BornAgain and stored the resulting intensity image I_{HR} . Each image was divided by R^4h^2 (the leading volume factors of the spheroidal form factor).

Stochastic Size Distributions and Forward Model Each synthetic training pattern was generated as a mixture of the precomputed patterns. We sampled a 2-component Gaussian mixture over normalized $(R, h) \in [0, 1]^2$: for component k we drew a random mean and a covariance (with random correlation), forming a 2D Gaussian g_k. Mixture weights ωk were drawn from a uniform Dirichlet(1, 1, 1) and the mixture $p(R, h) \propto \Sigma_k \omega_k g_k$ was normalized to unit sum on the 30×30 grid. The "form-factor-only" intensity was the weighted sum $I_{\mathrm{FF}} = \Sigma_{\mathrm{i,j}} p(R_i, h_j) I_{\mathrm{HR}}(q; R_i, h_j)$.

To emulate lateral correlations, we multiplied I_{FF} by a Gaussian paracrystal structure factor [3] $S(q_y; D, \sigma_D)$. For each frame we derived a soft constraint on the most likely radius from the horizontal marginal $p(R) = \Sigma_h p(R, h)$; let R_{mode} be the bin with maximal p(R). The interparticle distance D was drawn from a truncated normal with mean $\mu = R_{\mathrm{mode}}$, standard deviation $(40 - R_{\mathrm{mode}})/4$, and support $\max(R_{\mathrm{mode}}, 5), 40]$ nm. The positional disorder was sampled as $\sigma_D \propto$ Uniform(0.05D, 0.3D). To mimic vertical roughness, we included a Debye–Waller attenuation $G(q) = \exp -\sigma_z^2 q_z^2$ with σ_z drawn uniformly from [0, 0.3]. The final synthetic intensity for each frame was

$$I(q) = I_{\mathrm{FF}}(q)S(q_y; D, \sigma_D)G(q).$$

Physical Background Synthesis A physically inspired background was added to each synthetic GISAXS frame prior to noise injection. The background model combined several components that mimic characteristic experimental scattering features: a specular ridge, Yoneda band, anisotropic Guinier–Porod wedge, and a smooth planar gradient with a constant offset. The total background intensity was expressed as

$$I_{\mathrm{bg}}(q_y, q_z) = I_{\mathrm{spec}}(q_y, q_z) + I_{\mathrm{Yoneda}}(q_y, q_z) + I_{\mathrm{GP}}(q_y, q_z) + I_{\mathrm{plane}}(q_y, q_z) \quad (5)$$

The specular pillar represents the mirror-like reflection streak along q_z, with a Lorentzian profile in q_y, whose width increases linearly with

$$I_{\mathrm{spec}}(q_y, q_z) = A_{\mathrm{spec}} e^{-q_z/\lambda} \left(\frac{1}{1 + (\frac{q_y}{\sigma_0 + k_s q_z})^2}\right)^{\nu} \quad (6)$$

Here, the parameter ranges where $[A_{\mathrm{spec}} \in (0.5, 2.0), \sigma_0 \in (0.002, 0.006), k_s \in (0.02, 0.08), \lambda \in (0.03, 0.12), \nu \in (1.2, 2.2)]$ to keep the training set background within a reasonable range. The Yoneda component accounts for the enhanced scattering near the critical angle α_c:

$$I_{\mathrm{Yoneda}}(q_y, q_z) = A_y \exp[-\frac{1}{2}(\frac{q_z - q_{z,0}}{\sigma_z})^2] \exp[-(\frac{q_y}{\xi})^2] \quad (7)$$

Here, the parameters were$[A_{\mathrm{y}} \in (0.1, 0.6), q_{\mathrm{z},0} \in (0.5, 0.7), \sigma_z \in (0.005, 0.02), \xi \in (0.01, 0.8)]$. To represent diffuse scattering at larger angles, an anisotropic Guinier-Porod term was used,

$$I_{\mathrm{GP}}(q_y, q_z) = A_w(\exp[\frac{R_g^2 q_{\mathrm{eff}}^2}{3}] + q_{\mathrm{eff}}^{-m}) \quad (8)$$

with $q_{\mathrm{eff}}^2 = q_y^2 + \gamma q_z^2$. Here, the exponential term dominates at low q_{eff} (Guinier regime) and the power-law term at high q_{eff} (Porod regime). The used parameter are: $[A_{\mathrm{w}} \in (0.05, 0.5), R_g \in (20.0, 80.0), m \in (2.0, 3.8), \gamma \in (0.6, 2.0)]$

A slow illumination gradient and uniform background were added,

$$I_{\mathrm{plane}}(q_y, q_z) = a_x q_y + a_z q_z + c_0 \quad (9)$$

where a_x and a_z mimic smooth intensity slopes due to beam footprint and detector illumination imbalance, and c_0 represents the isotropic background (air scattering, fluorescence, dark current). The ranges used here are $[a_x \in (-0.002, 0.002), a_z \in (-0.002, 0.002), c_0 \in (0.0, 0.05)]$

Noise, Masking and Normalization We first added additive Poisson noise to the simulated images. We then applied the same binary mask used for experimental preprocessing (beamstop, gaps, shadows; masked pixels set to a sentinel value), followed by a logarithmic transform and normalization to $(-\inf, 1]$. Finally, we performed the same post-crop as in the experimental pipeline so that all inputs are 256×256 arrays on a common (q_y, q_z) window. Masked pixels remain at the sentinel value throughout training. We generated 200,000 synthetic frames. For each frame we stored: (i) the input image (256×256) after masking, log-scaling and normalization; (ii) the target size distribution p(R, h) (30×30) for training the form-factor (FF) network.

Neural Network and Training To predict the joint size distribution p(R, h) from a single preprocessed GISAXS frame, we used a compact CNN, see Figure S31:

- Input: $256 \times 256 \times 1$
- Backbone: four Conv–BatchNorm–ReLU blocks with 3×3 kernels, stride 2, channels $32 \to 64 \to 128 \to 256$
- Head: Flatten $\to$ Dense(2048, ReLU) $\to$ Dropout(0.5) $\to$ Dense(900, softmax) $\to$ Reshape(30, 30)

The model training was carried out using TensorFlow/Keras. The input consisted of 256×256 reprocessed GISAXS patterns, and the output was the corresponding two-dimensional particle size distributions on a 30×30 grid [4, 5]. The network was trained with mean squared error (MSE) loss between predicted and ground truth distributions. Optimization was performed using the Adam optimizer with an initial learning rate of 1×10^{-4}.

Reciprocal Space Grid Consistency To ensure 1:1 comparability between synthetic and experimental inputs, we matched the detector field-of-view, beam center, and sample–detector distance in simulation to those used by the experimental geometry step, and we applied the same post-crop and mask when forming inputs. The (q_y, q_z) conversion employed the same distance (4177.3 mm) and the incident-angle setting used by the geometry module (0.4°), so that the synthetic inputs align with the experimental preprocessing pipeline.

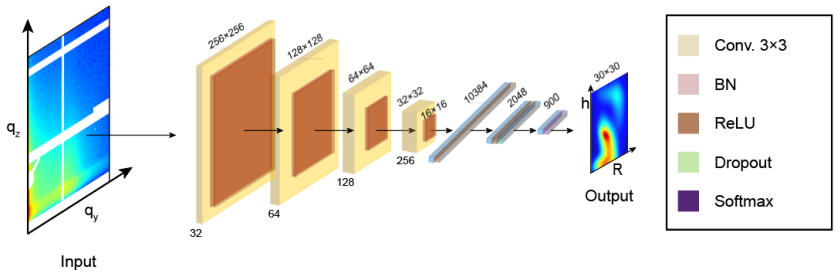


Figure S31: Working Scheme of the CNN.

15 Oxidation Kinetics

Table S6: Fitting Parameters for the linear decay fit for the Cu signal loss during oxidation, see Figure 2.

Equation	y = a + b*t
a	0.43509 ± 1.56875
b	0.56071 ± 0.07536
Residual Sum of Squares	2.65028
Pearson's r	0.99109
R-Square (COD)	0.98226
Adj. R-Square	0.96451

Table S7: Fitting Parameters for the inverse logarithmic fit for the Cu signal loss during oxidation, see Figure 2.

Equation	1/(A+B*ln(x))+C
A	0.66889 ± 0.13241
B	-0.26795 ± 0.0455
C	20.43689 ± 0.30423
Reduced Chi-Sqr	0.0203
R-Square (COD)	0.99953
Adj. R-Square	0.99939

16 Surface Coordinates

The hexagonal surface coordinates are connected to the bulk Cu coordinates by:

$$(\mathrm{HKL})_s = (\mathrm{HKL}) \times M \tag{10}$$

with the transformation matrix M:

$$\begin{pmatrix} a_{0.5} & a_{-0.5} & a_1 \\ a_0 & a_{0.5} & a_{21} \\ a_{-0.5} & a_0 & a_1 \end{pmatrix} \tag{11}$$

Table S8: Different Bragg peaks in bulk and surface coordinates.

surface coordinates	bulk coordinates
(113)	$(13\bar{1})$
(101)	$(11\bar{1})$

References

(1) Vineyard, G. H. Grazing-Incidence Diffraction and the Distorted-Wave Approximation for the Study of Surfaces. *Physical Review B* **1982**, *26*, 4146, DOI: 10.1103/PhysRevB.26.4146.

(2) Pospelov, G.; Van Herck, W.; Burle, J.; Carmona Loaiza, J. M.; Durniak, C.; Fisher, J. M.; Ganeva, M.; Yurov, D.; Wuttke, J. BornAgain: Software for Simulating and Fitting Grazing-Incidence Small-Angle Scattering. *Applied Crystallography* **2020**, *53*, 262–276, DOI: 10.1107/S1600576719016789.

(3) Bonart, R.; Hosemann, R.; McCullough, R. The Influence of Particle Size and Distortions upon the X-Ray Diffraction Patterns of Polymers. *Polymer* **1963**, *4*, 199–211, DOI: 10.1016/0032-3861(63)90026-0.

(4) Yager, K. G.; Zhang, Y.; Lu, F.; Gang, O. Periodic Lattices of Arbitrary Nano-Objects: Modeling and Applications for Self-Assembled Systems. *Applied Crystallography* **2014**, *47*, 118–129, DOI: 10.1107/S160057671302832X.

(5) Maes, J.; Castro, N.; De Nolf, K.; Walravens, W.; Abécassis, B.; Hens, Z. Size and Concentration Determination of Colloidal Nanocrystals by Small-Angle X-Ray Scattering. *Chemistry of Materials* **2018**, *30*, 3952–3962, DOI: 10.1021/acs.chemmater.8b00903.

Chapter 10

SI Article II

Supplementary Information: Structure and Reactivity of Cu and Cu Oxide Nanoparticles on Anatase TiO_2(101) for Cysteine Degradation

Daniel Silvan Dolling[1,2]*;
Miguel Blanco Garcia[1,2]
Ming-Chao Kao[1,2]
Mona Kohantorabi[1]
Lydia J. Bachmann[1,2]
Luis-Felipe Mochalski[1,2]
Luisa K. Wartner[1,2]
Eleonora Spurio[4,5]
Arti Dangwal[1]
Joris W. Fuchs[1,2]
Mais Jamil A. Ahmad[1]
Arno Jeromin[1]
Ying Kong[6]
Dmitri Novikov[3]
Thomas F. Keller[1,2]
Volkmar Koller[3]
Olof Gutowski[3]
Paola Luches[5]
Vedran Vonk[1]
Andreas Stierle[1,2]
Heshmat Noei[1†]

[1]Centre for X-ray and Nano Science CXNS,
Deutsches Elektronen-Synchrotron DESY,
Notkestr. 85, 22607 Hamburg, Germany

[2]Fachbereich Physik, Universität Hamburg,
Notkestraße 9-11, 22607 Hamburg, Germany

[3]Deutsches Elektronen-Synchrotron DESY,
Notkestr. 85, 22607 Hamburg, Germany

[4] Dipartimento FIM, Università degli Studi di Modena e Reggio Emilia,
Via G. Campi 213/a, 41125 Modena, Italy
[5] Istituto Nanoscienze, CNR (NANO-CNR), Via G. Campi 213/a, 41125 Modena, Italy
[6] Laboratory of Industrial Chemistry, Ruhr-Universität Bochum,
Universitätsstr. 150, 44801 Bochum, Germany

June 2, 2026

Anatase TiO_2 features a tetragonal unit cell with lattice parameters a = b = 3.78 Å, c = 9.50 Å [1], space group $I4_1/amd$. Cu features a face-centered cubic (fcc) crystal system with the lattice parameter a_{Cu} = 3.62 Å [2], space group $Fm\bar{3}m$. Cu_2O crystallizes in a body-centered cubic lattice, where oxygen atoms are at the lattice points and the Cu atoms form an inset fcc lattice shifted by $(\frac{1}{4},\frac{1}{4},\frac{1}{4})$ (cuprite structure), space group $Pn\bar{3}m$. The lattice constant is a_{Cu_2O} = 4.26 Å. For all crystal systems, bulk coordinate Miller indices are used.

SEM

*silvan.dolling@desy.de
†heshmat.noei@desy.de

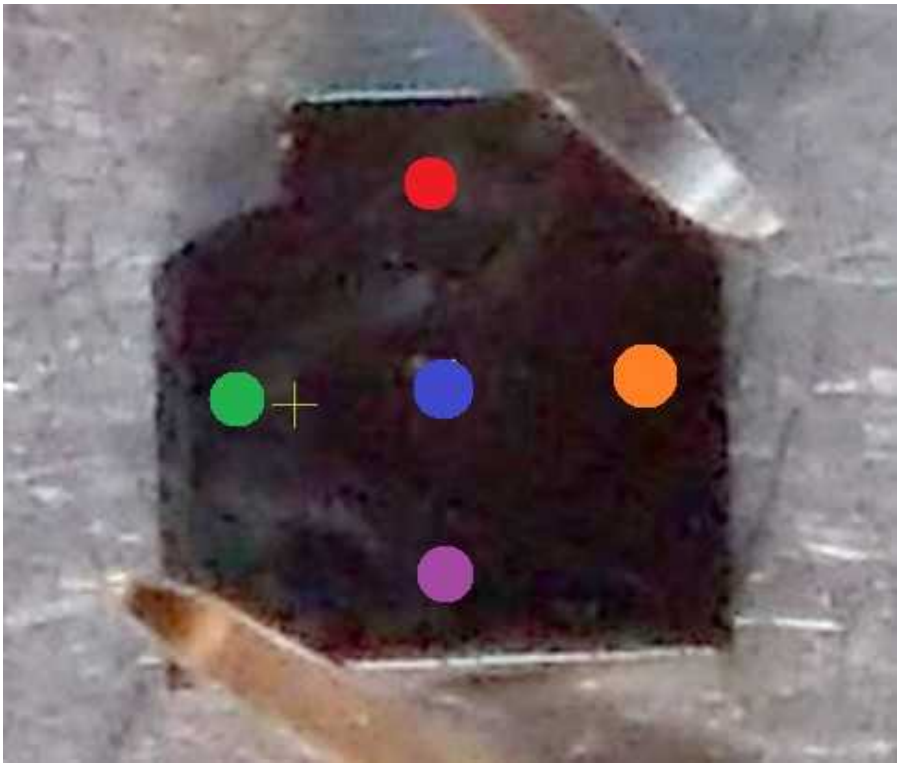


Figure S1: Sample with marked positions for the SEM measurements.

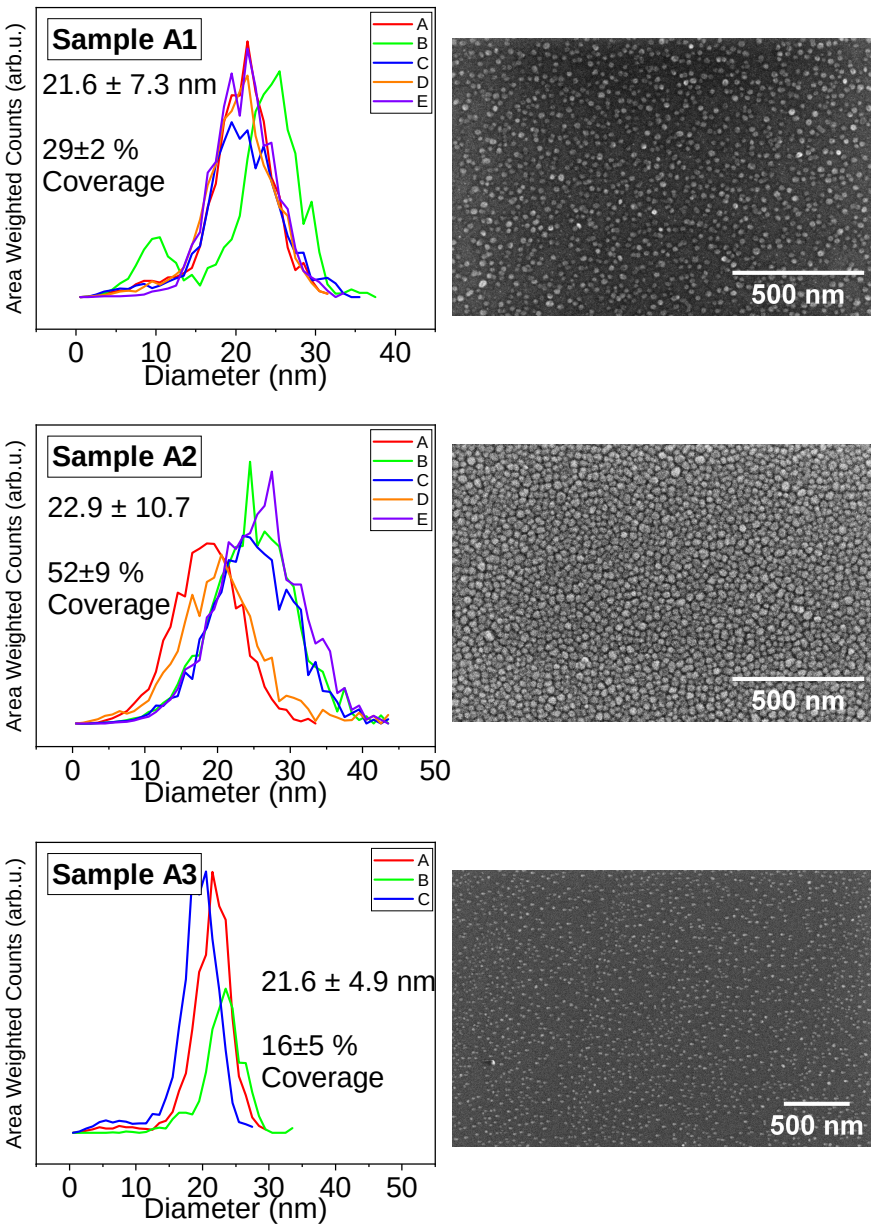


Figure S2: SEM size distributions and SEM images for samples A1, A2 and A3. Each size distribution curve is extracted from an SEM image taken at a different position on the sample, see Figure S1. An exemplary SEM image for each sample is shown.

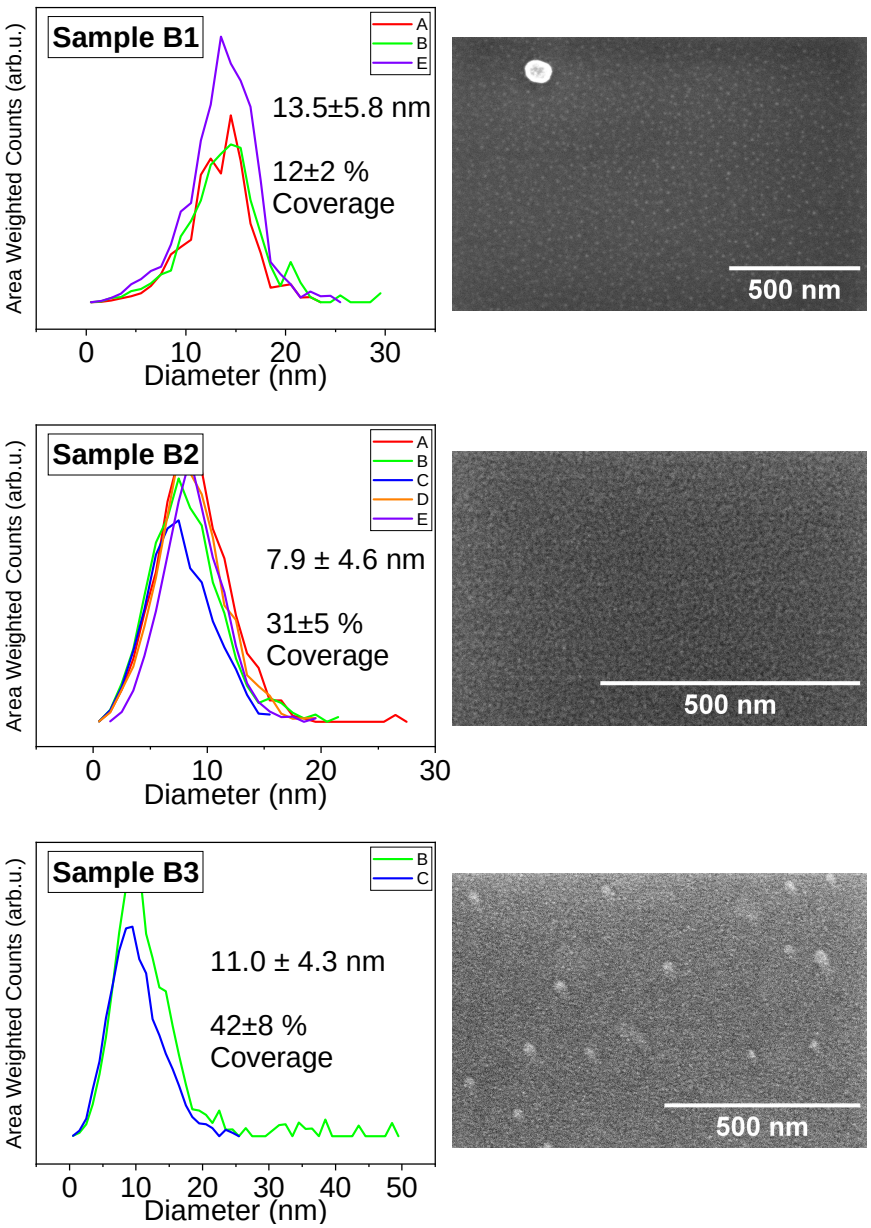


Figure S3: SEM size distributions and SEM images for samples B1, B2 and B3. Each size distribution curve is extracted from an SEM image taken at a different position on the sample, see Figure S1. An exemplary SEM image for each sample is shown.

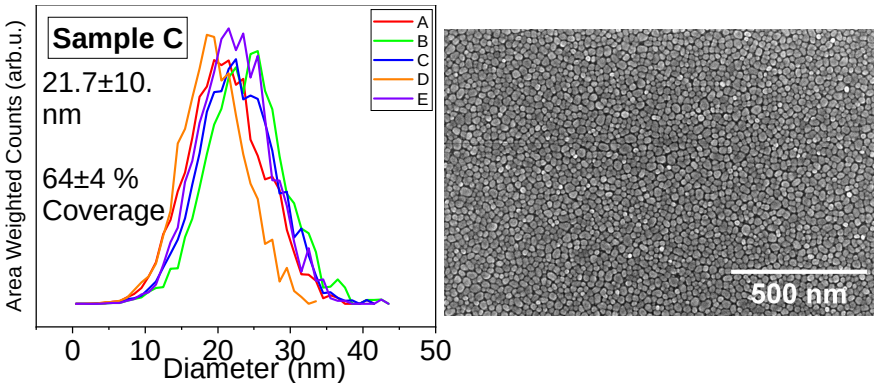


Figure S4: SEM size distributions and SEM images for sample C. Each size distribution curve is extracted from an SEM image taken at a different position on the sample, see Figure S1. An exemplary SEM image is shown.

HEXRD

Particle sizes were calculated by using line profiles through Bragg peaks and employing Scherrer's formula

$$D = \frac{2\pi}{\Delta Q} \quad (1)$$

where D is the particle size and ΔQ is the full width half maximum of the peak in Q-space. The line profiles are measured along radial direction.

Table S1: Average Cu NP sizes estimated in different directions from specific Bragg peaks for sample A1 (from HEXRD data). The sizes were determined from line profiles in the radial direction (through the 'short' axis of the peaks, see e.g. Figure S6). The sample was measured twice, with a 260 hour oxidation period under ambient conditions between the measurements. Due to different geometries, both measurements feature different Bragg peaks.

			4 h oxidation		264 h oxidation	
H	K	L	size (nm)	size error (nm)	size (nm)	size error (nm)
1	-1	1	15.21	0.36	15.00	0.34
1	1	1	23.74	0.38	22.21	0.61
1	1	-1	23.60	0.55	22.64	0.48
2	0	2	16.26	1.14	–	–
0	-2	0	19.04	1.32	18.75	0.51
2	-2	0	10.31	1.42	–	–
3	1	1	17.29	1.71	18.43	5.58
2	0	-2	13.81	1.97	–	–
1	-1	3	12.32	3.04	–	–
3	1	-1	17.90	5.46	16.04	1.56
1	-3	1	16.98	5.51	14.16	1.98
1	-3	-1	–	–	16.60	4.22
1	-1	-1	–	–	15.25	0.50
2	0	0	–	–	17.13	1.08
2	2	0	–	–	20.96	1.13

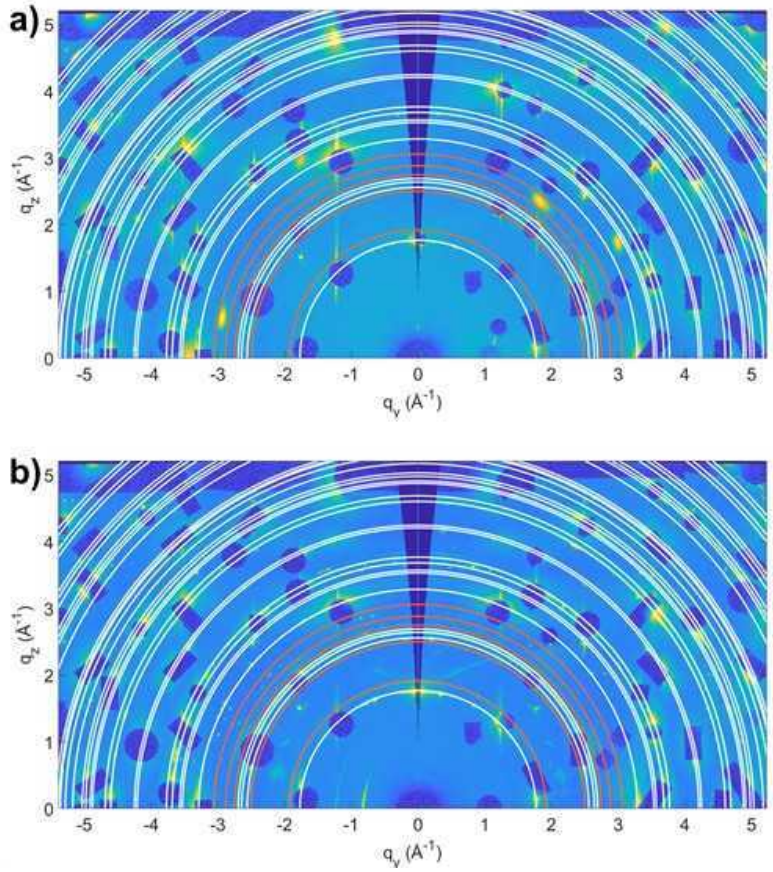


Figure S5: Maximum-intensity images for a) sample A1 and b) sample B1. The white rings correspond to Anatase TiO_2 peaks, the orange rings to rutile TiO_2 peaks. The images were taken by a full 180° rotation of the sample along the surface normal (9000 images, summed in bunches of 50, then combined in a maximum intensity image).

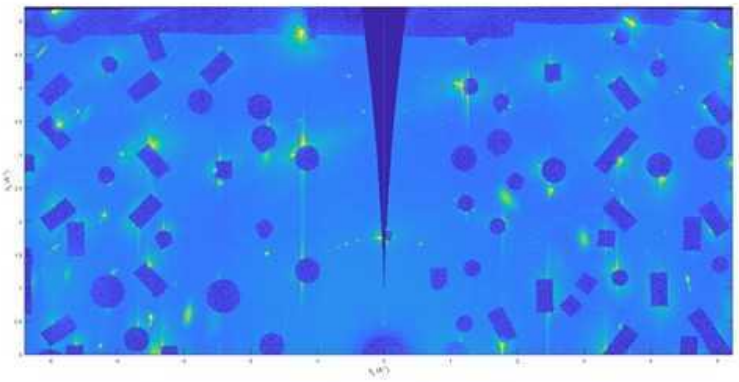


Figure S6: HEXRD measurement of sample A1, depicting a maximum pixel image of a full 180° rotation of the sample along the surface normal (9000 images, summed in bunches of 50, then combined in a maximum intensity image).

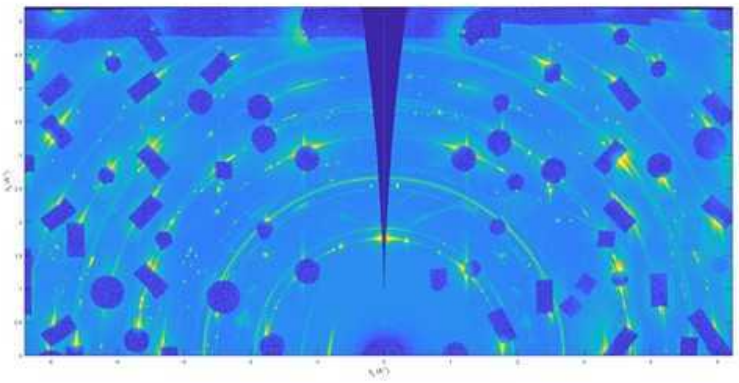


Figure S7: HEXRD measurement of sample B1, depicting a maximum pixel image of a full 180° rotation of the sample along the surface normal (9000 images, summed in bunches of 50, then combined in a maximum intensity image). All peaks and signals seen here are attributed to substrate crystallites and backgrond signal.

In-plane Rocking Scans

Epitaxy Assignment

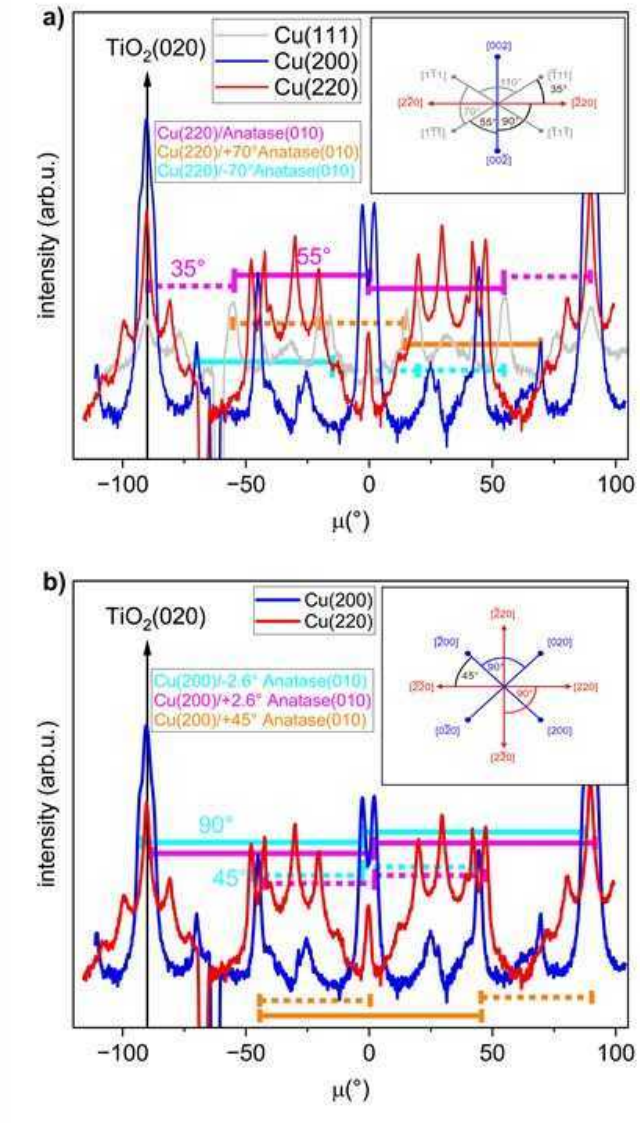


Figure S8: In-plane rocking scans for sample A2, depicting the assingment of (110)-oriented Cu in a) and (100)-oriented Cu in b). The bars indicate the positions of the peaks belonging to the epitaxy. The relationship if the angles is depicted in the right upper corner inset of each graph, displaying an in-plane rotation and the corresponding Bragg peaks.

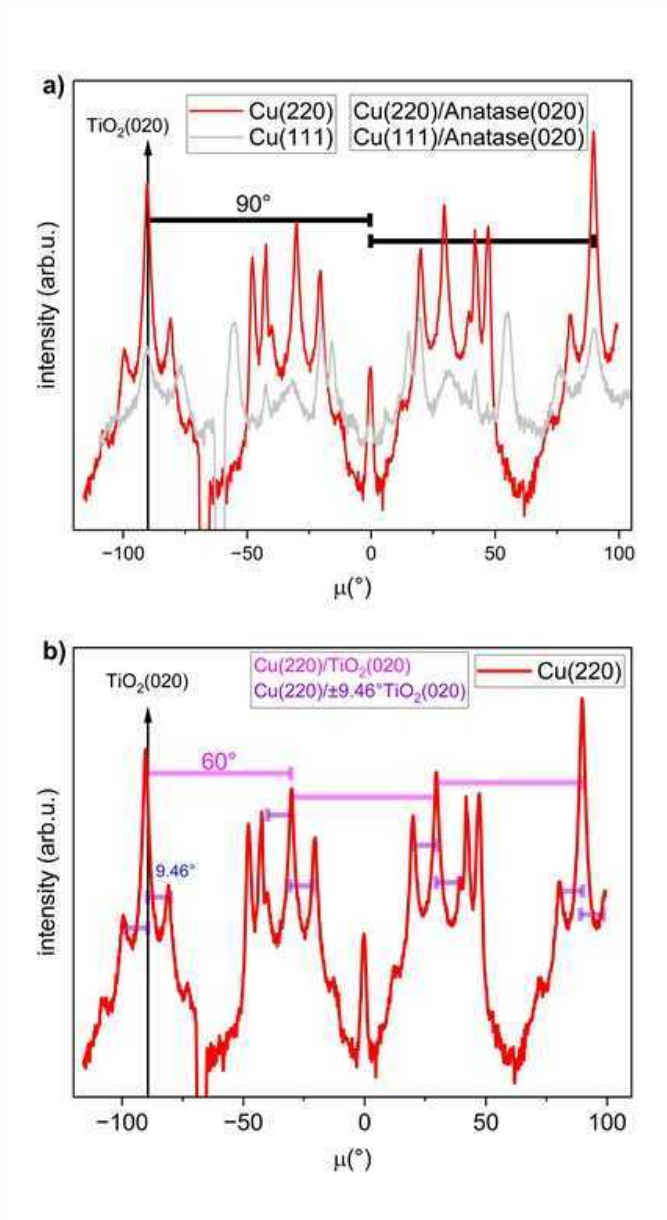


Figure S9: In-plane rocking scans for sample A2, depicting the assingment of (111)-oriented Cu in a) and (112)-oriented Cu in b). The bars indicate the positions of the peaks belonging to the epitaxy.

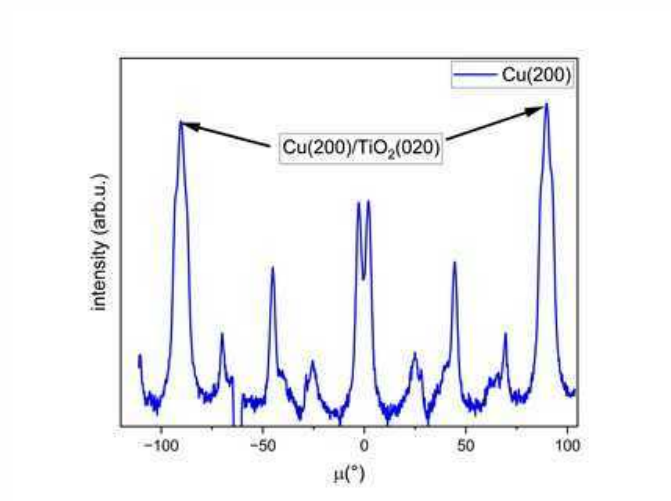


Figure S10: In-plane rocking scan for sample A2, highlighting the two Cu(200) peaks that are assigned to (470)-oriented Cu.

Sample Comparison

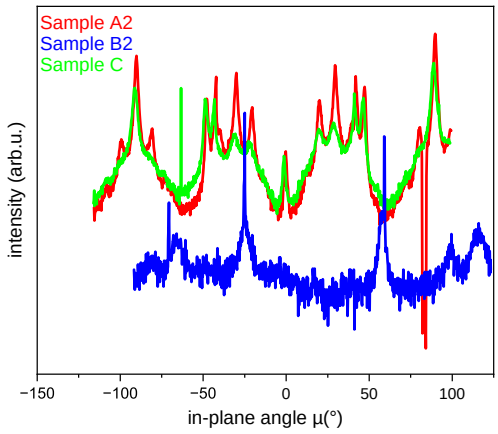


Figure S11: Comparison of the in-plane rocking scans set to detect Cu(220) for samples A2, B2 and C. Samples A2 and C were oxidized for 60 min in 1 bar O_2, sample B2 was exposed to ambient conditions for 60 minutes.

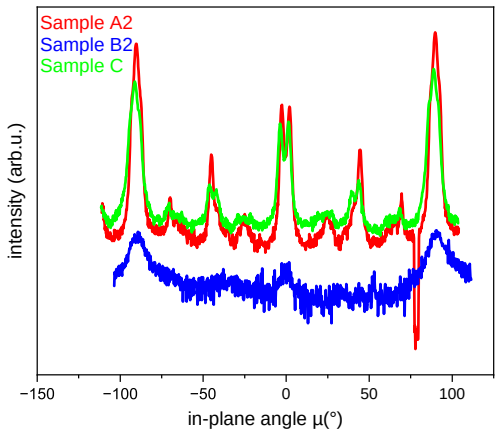


Figure S12: Comparison of the in-plane rocking scans set to detect Cu(200) for samples A2, B2 and C. Samples A2 and C were oxidized for 60 min in 1 bar O_2, sample B2 was exposed to ambient conditions for 60 minutes.

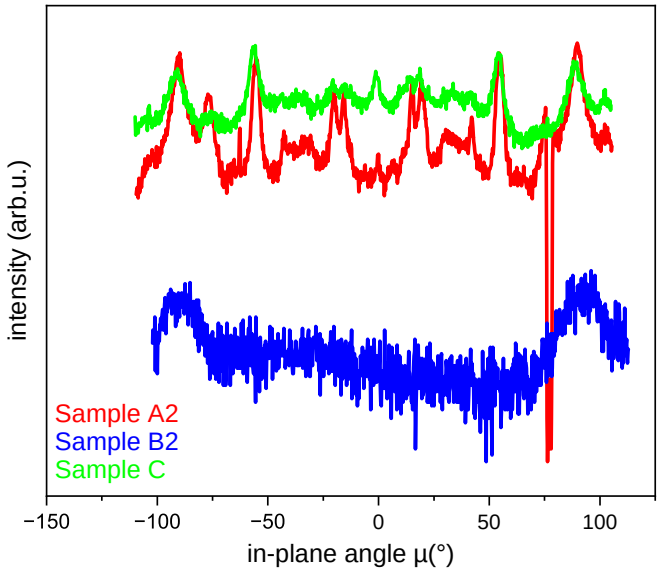


Figure S13: Comparison of the in-plane rocking scans set to detect Cu(111) for samples A2, B2 and C. Samples A2 and C were oxidized for 60 min in 1 bar O_2, sample B2 was exposed to ambient conditions for 60 minutes.

Quantification of In-Plane Scans

The extend of the different epitaxies on sample A* was quantified by integrating the peaks for Cu[470], Cu[111] and Cu[100] in the in-plane rocking scans for Cu(200) and Cu(220). All peaks belonging to other epitaxies were ignored. From the 'trident' side peaks of two middle peaks the [111]-oriented Cu in the Cu(220) rocking scan, one side peak was ignored as it heavily overlapped with the Cu[100] signal and was significantly weaker. The area of all peaks belonging to an epitaxy was added and then divided by the multiplicity of the peak. The corresponding intensities were used to calculate the following ratios (each only related to one in-plane rocking scan):

$$\frac{I_{\mathrm{Cu[470]}}}{I_{\mathrm{Cu[100]}}} = 2.96 \tag{2}$$

$$\frac{I_{\mathrm{Cu[100]}}}{I_{\mathrm{Cu[111]}}} = 0.66 \tag{3}$$

With the additional assumption

$$I_{\mathrm{Cu[470]}} + I_{\mathrm{Cu[100]}} + I_{\mathrm{Cu[111]}} = 1 \tag{4}$$

The percentages of the different epitaxies could be calculated. A gaussian was used for fitting:

$$y = I_0 + \frac{A}{w \times \sqrt{2\pi}} \times \exp -2 \times (x - x_c)^2 \tag{5}$$

Table S2: Fitting parameters for the fit of the Cu(220) in-plane rocking scan. The fitting function is Equation (5).

	I_0	x_c	w	A
Peak 1	24.64525	-97.81964	4	138.23481
error	0.82023	0.49218	0.99848	30.65711
Peak 2	24.64525	-90.24446	2.15123	895.99904
error	0.82023	0.02957	0.06012	21.84151
Peak 3	24.64525	-81.6297	4	239.49766
error	0.82023	0.28147	0.56976	30.41744
Peak 4	24.64525	-47.76719	1.62902	292.44403
error	0.82023	0.06	0.12056	18.96997
Peak 5	24.64525	-42.54669	2.23602	410.50899
error	0.82023	0.06844	0.13866	22.32139
Peak 6	24.64525	-30.14004	2.44007	592.49173
error	0.82023	0.05398	0.10925	23.34065
Peak 7	24.64525	-20.57446	2.4408	332.13679
error	0.82023	0.09699	0.19528	23.45646
Peak 8	24.64525	20.08392	2.70867	403.53346
error	0.82023	0.09282	0.18756	24.66927
Peak 9	24.64525	29.61954	2.68285	761.80379
error	0.82023	0.04819	0.09813	24.47083
Peak 10	24.64525	41.98974	2.72903	487.84327
error	0.82023	0.07775	0.16068	24.91117
Peak 11	24.64525	47.06714	1.74332	402.57907
error	0.82023	0.04898	0.09944	19.99685
Peak 12	24.64525	81.08908	4	235.10365
error	0.82023	0.28706	0.58316	30.49438
Peak 13	24.64525	89.71654	1.86658	1329.15457
error	0.82023	0.01622	0.03266	20.39545
Peak 14	24.64525	97	4	161.38291
error	0.82023	0.50763	1.16271	38.21904

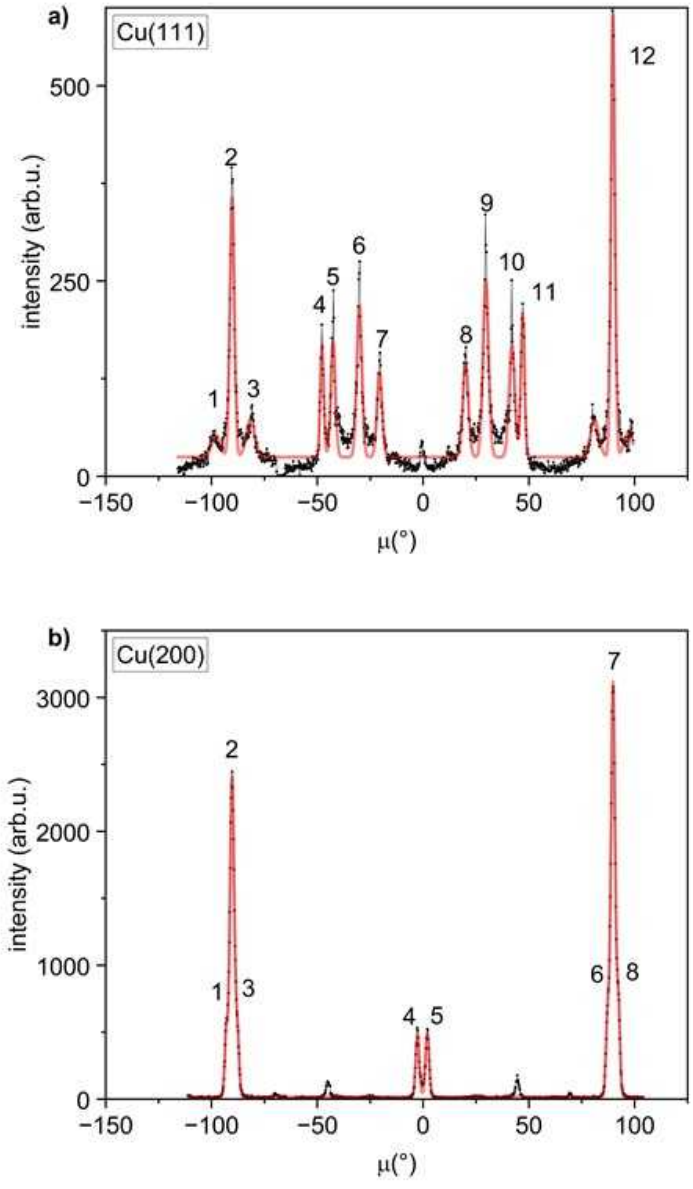


Figure S14: In-plane rocking scans for sample A2, with fits for the peaks. The Cu(220) scan is fitted in a), the Cu(200) scan is fitted in b). The number markings correspond to the peaks and fitting parameters from Table S2.

	I_0	x_c	w	A
Peak 1	16.62136	-93.0077	1.46871	900.2164
error	0.66315	0.03028	0.05269	37.19661
Peak 2	16.62136	-90.30033	2.01641	6043.49249
error	0.66315	0.0106	0.03094	92.91349
Peak 3	16.62136	-87.83481	1.73747	1048.12034
error	0.66315	0.05779	0.08038	71.25873
Peak 4	16.62136	-2.62277	1.75117	1018.04991
error	0.66315	0.01942	0.03918	19.81812
Peak 5	16.62136	1.96966	1.77451	1061.31268
error	0.66315	0.01899	0.03827	19.93352
Peak 6	16.62136	87.33487	1.76433	1414.59365
error	0.66315	0.04512	0.06436	70.16338
Peak 7	16.62136	89.76793	1.86995	7214.43297
error	0.66315	0.00751	0.02637	107.66504
Peak 8	16.62136	92.2131	1.60042	1441.67074
error	0.66315	0.03088	0.04717	55.28734

Radial Scans

Table S3: Nanoparticle sizes calculated from fits of radial scans through Bragg peaks for sample B2 via Scherrer's formula. The fits can be seen in Figures S15 to S17.

	Cu[111]		Cu[100]		Cu[470]	
	size (nm)	STD (nm)	size (nm)	STD (nm)	size (nm)	STD (nm)
clean Cu	11.137	0.084	9.148	0.12	8.858	0.113
60 min. O_2	9.025	0.134	7.741	0.11	6.772	0.181
120 min. O_2	8.986	0.108	7.99	0.14	7.161	0.195

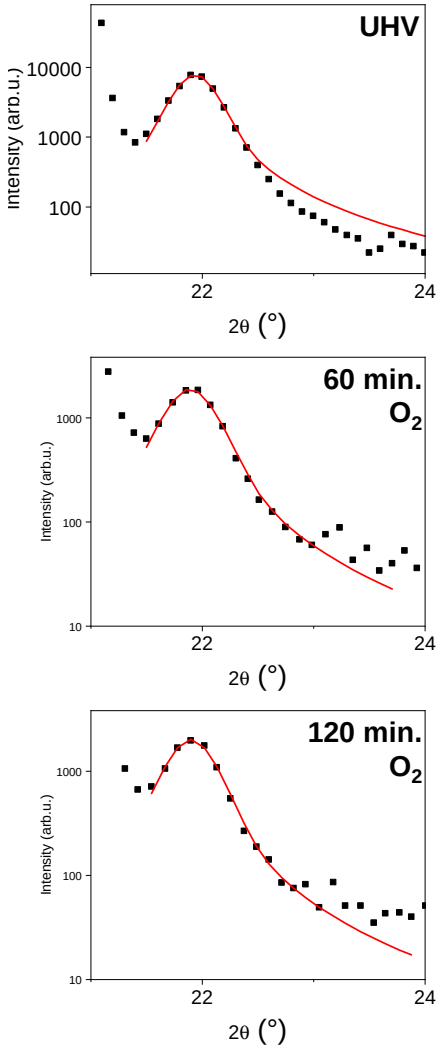


Figure S15: Fits for radial scans through a Cu(200) Bragg peak corresponding to [470]-oriented Cu for sample B2. Data is represented by black boxes, the fit by the red curve.

Table S4: FWHM and center peak position fitting parameters for the radial scans through a Cu(200) Bragg peak corresponding to [470]-oriented Cu, see Figure S15

	2θ (°)	$STD_{2\theta}$ (°)	FWHM (°)	STD_{FWHM} (°)
UHV	21.933	0.002	0.408	0.005
60 min. O_2	21.890	0.004	0.534	0.014
120 min. O_2	21.900	0.004	0.505	0.014

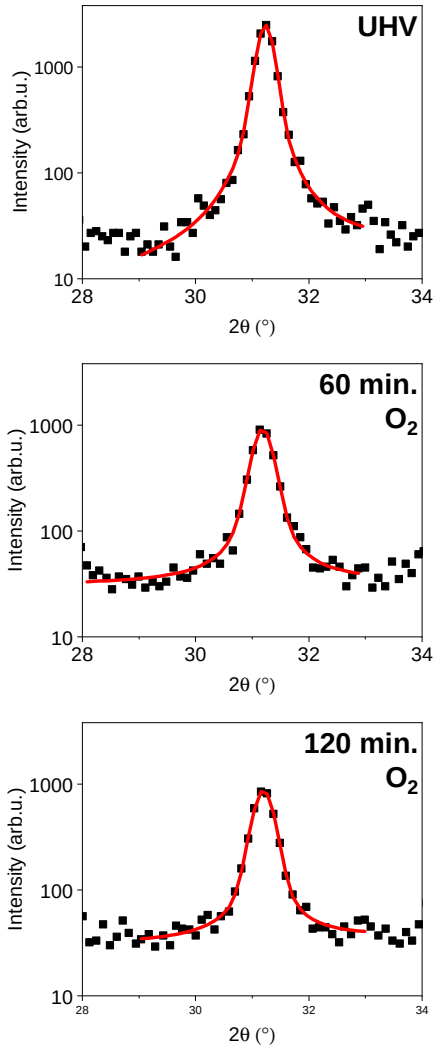


Figure S16: Fits for radial scans through a Cu(220) Bragg peak corresponding to [111]-oriented Cu for sample B2. Data is represented by black boxes, the fit by the red curve.

Table S5: FWHM and center peak position fitting parameters for the radial scans through a Cu(220) Bragg peak corresponding to [111]-oriented Cu, see Figure S16

	2θ (°)	$STD_{2\theta}$ (°)	FWHM (°)	STD_{FWHM} (°)
UHV	31.232	0.001	0.331	0.002
60 min. O_2	31.184	0.002	0.409	0.003
120 min. O_2	31.120	0.002	0.410	0.005

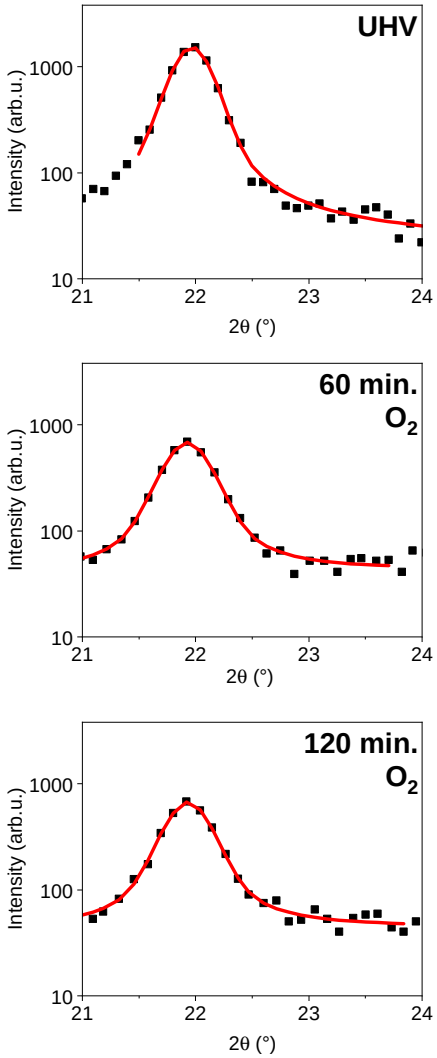


Figure S17: Fits for radial scans through a Cu(200) Bragg peak corresponding to [100]-oriented Cu for sample B2. Data is represented by black boxes, the fit by the red curve.

Table S6: FWHM and center peak position fitting parameters for the radial scans through a Cu(200) Bragg peak corresponding to [100]-oriented Cu, see Figure S17

	2θ (°)	$STD_{2\theta}$ (°)	FWHM (°)	STD_{FWHM} (°)
UHV	21.966	0.000	0.340	0.005
60 min. O_2	21.927	0.002	0.467	0.007
120 min. O_2	21.932	0.002	0.453	0.008

XPS

Table S7: XPS fitting data for the measurements of the Cu oxidation state of sample A1 and B1. GL(50) lineshapes were used.

Sample	$Cu\&Cu_2O$		CuO		RMS
	Binding Energy (eV)	FWHM (eV)	Binding Energy (eV)	FWHM (eV)	
A1	932.5	1.6	934.5	2.8	24193
B1	932.6	1.5	934.5	2.9	51677

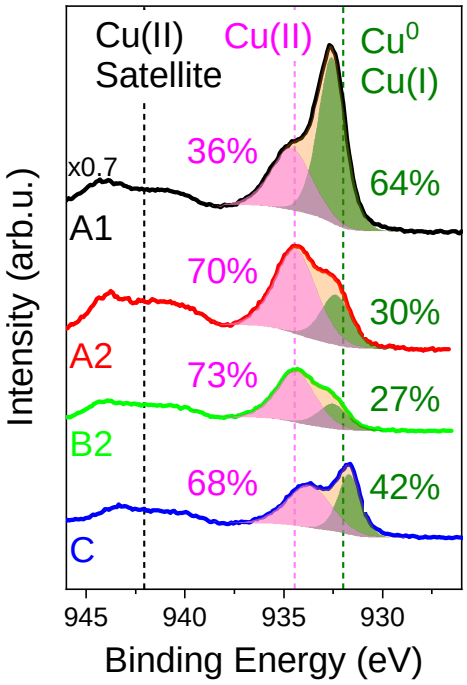


Figure S18: Cu S2p spectra shortly before or after the UVVIS measurements. Details on the fitting can be found in Table S8.

Table S8: Fitting parameters for the XPS Cu 2p spectra of samples A1, A2, B2 and C shortly before / after UVVIS measurements.

Sample	Cu&Cu_2O		CuO		RMS
	Binding Energy (eV)	FWHM (eV)	Binding Energy (eV)	FWHM (eV)	
A1	932.6	1.6	934.6	2.4	3385
A2	932.4	1.8	934.4	2.5	1408
B2	932.5	1.8	934.4	2.3	1629
C	931.7	1.4	933.7	2.6	3151

Table S9: Percentage of CuO and Cu/Cu_2O for samples A1, A2, B2 and C shortly before / after UVVIS measurements. See Table S8 for details on the fitting.

Sample	%∼Cu&Cu_2O	%∼CuO
A1	64	36
A2	30	70
B2	27	73
C	41	59

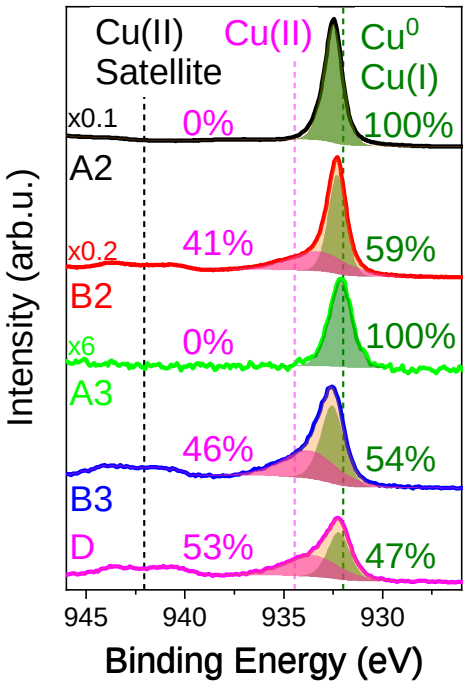


Figure S19: Cu 2p spectra with fits of samples B2 and D directly before dosing cysteine and for samples A2, B2 and A3 directly after dosing cysteine. The green shaded area is the Cu & Cu_2O fit, the pink shaded are is the CuO fit and the orange shaded are is the envelope. Details of the fits are found in Table S10

Table S10: XPS fitting parameters for the Cu 2p spectra of samples B2 and D directly before dosing cysteine and of samples A2, B2 and A3 directly after dosing cysteine. The fits can be seen in Figure S19.

Sample	$Cu\&Cu_2O$		CuO		RMS
	Binding Energy (eV)	FWHM (eV)	Binding Energy (eV)	FWHM (eV)	
A2	932.5	1.2	-	-	25175
B2	932.3	1.0	933.3	3.6	3045
A3	932.1	1.4	-	-	404
B3	932.6	1.4	933.7	3.3	932.3
D	932.2	1.3	933.6	3.3	484

Table S11: Percentages of CuO and Cu/Cu_2O for samples B2 and D directly before dosing cysteine and for samples A2, B2 and A3 directly after dosing cysteine.

Sample	$\%\sim Cu\&Cu_2O$	$\%\sim CuO$
A2	100	0
B2	59	41
A3	100	0
B3	54	46
C	47	53

XPS and IRRAS

Adsorption

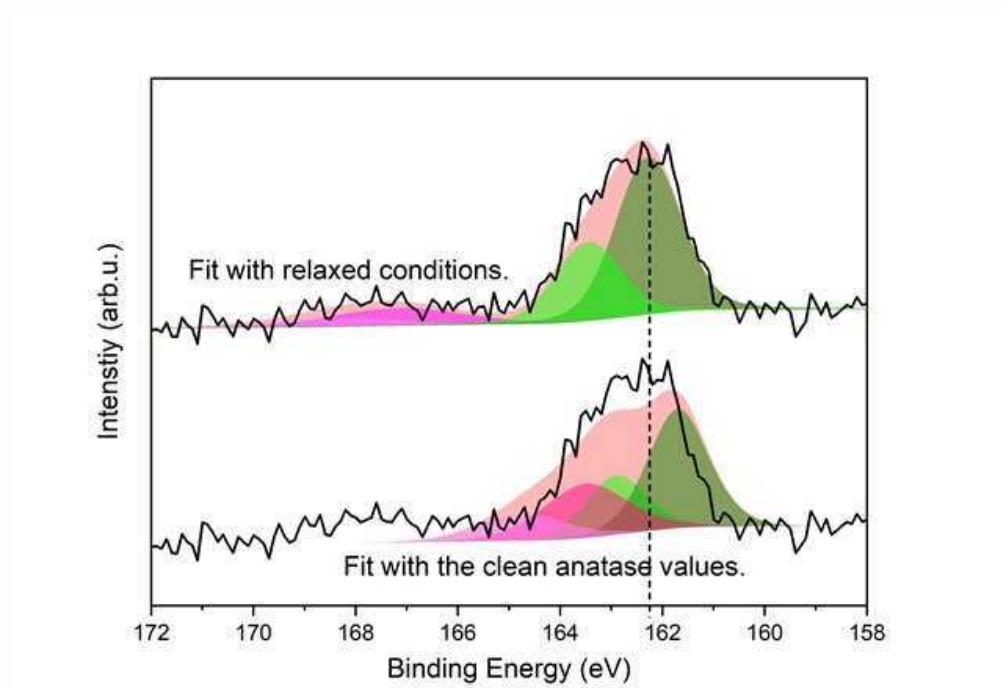


Figure S20: Comparison of the fits for S 2p of sample B3: Employing the same fit conditions as for the clean anatase reference, it does not produce a good fit. When relaxing the conditions, the peaks are allowed to shift. This shows the necessary shift for the S-Ti bond (green doublet), highlighting that it is a S-Cu bond for the NP sample.

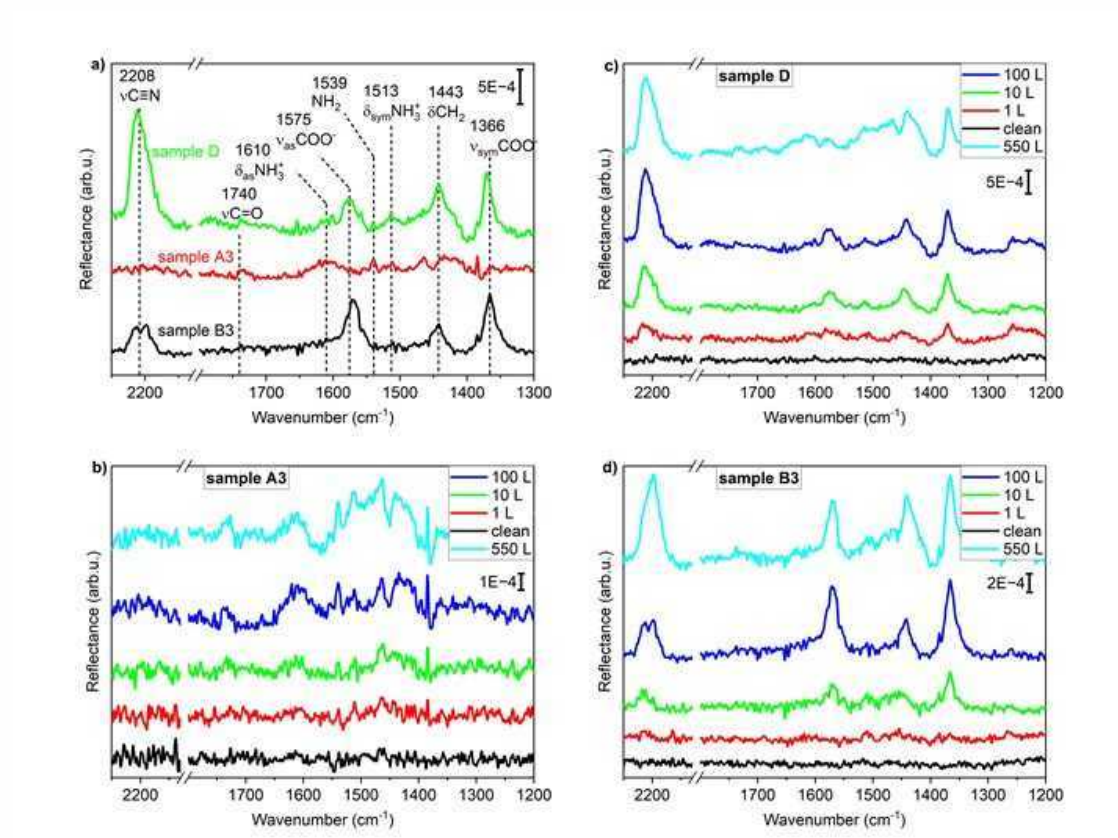


Figure S21: P-polarized spectra of a) sample A3, B3 and D after 100 L cysteine dosing, b) sample A3, c) sample D and D) sample B3.

Photocatalysis

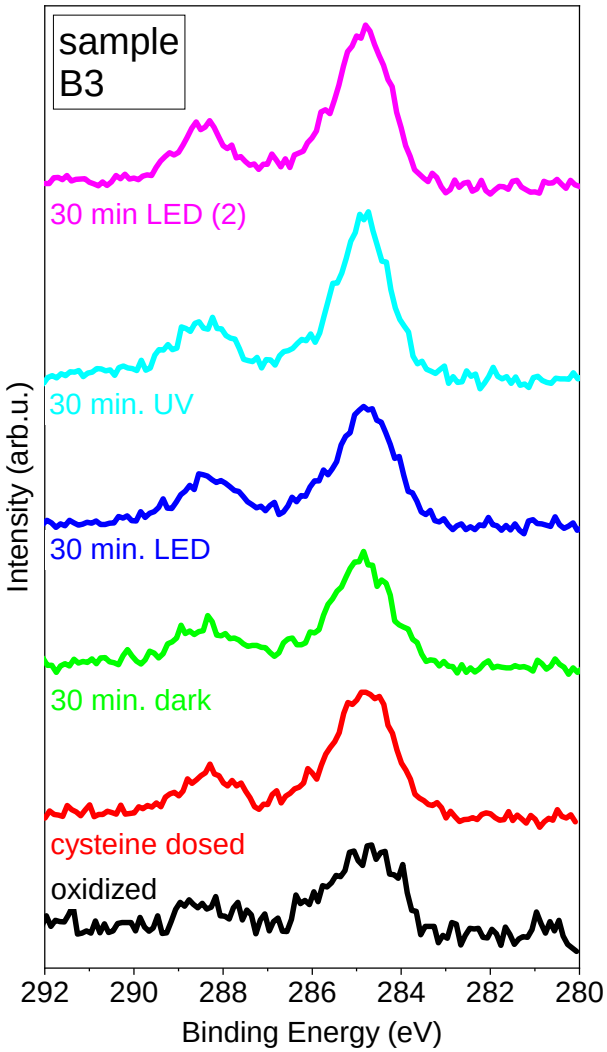


Figure S22: C 1s XP spectra of sample B3 during photocatalysis measurements. 'oxidized' means the oxidized sample before cysteine dosing.

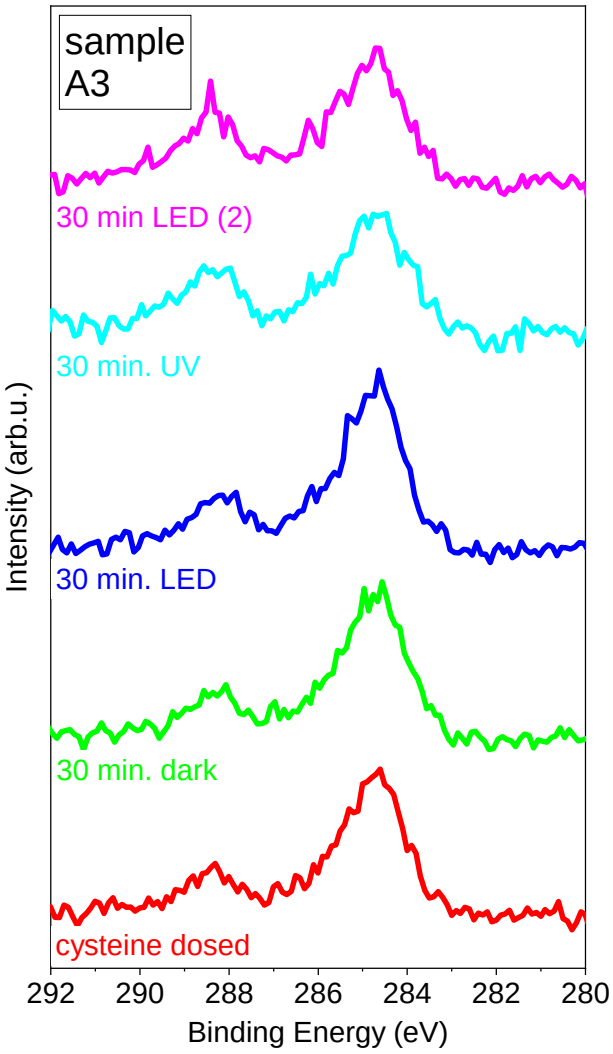


Figure S23: C1s spectra of sample A3 during photocatalysis measurements.

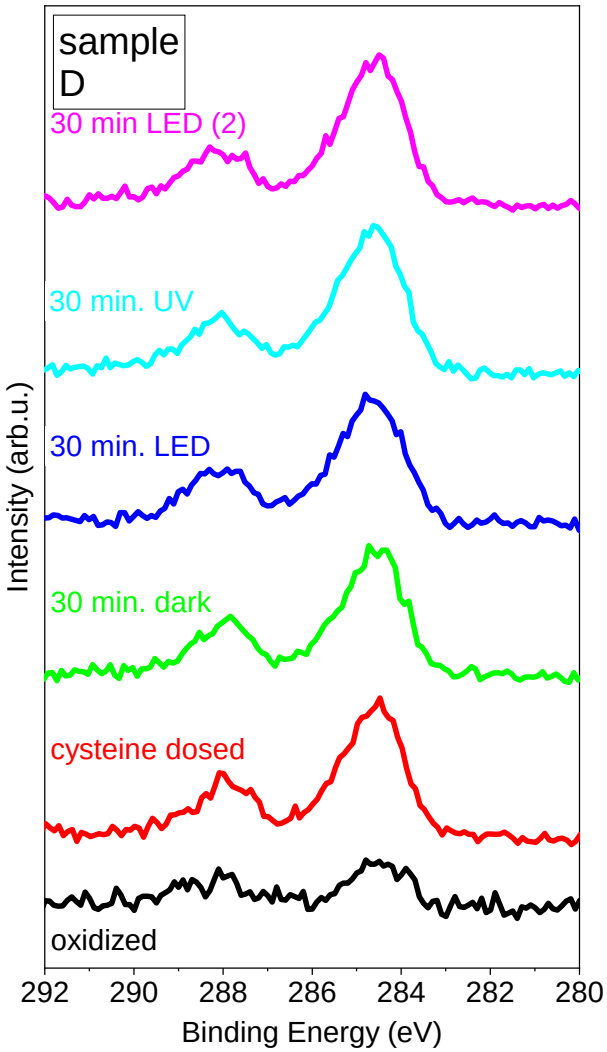


Figure S24: C1s spectra of sample D during photocatalysis measurements. 'oxidized' means the oxidized sample before cysteine dosing.

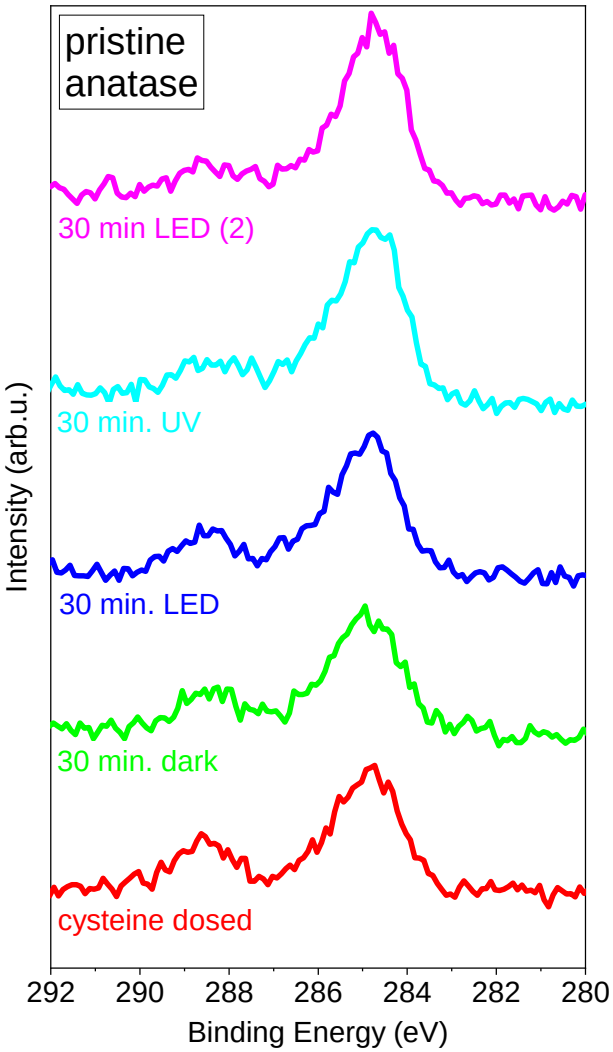


Figure S25: C1s spectra of the pristine anatase TiO_2(101) crystal during photocatalysis measurements.

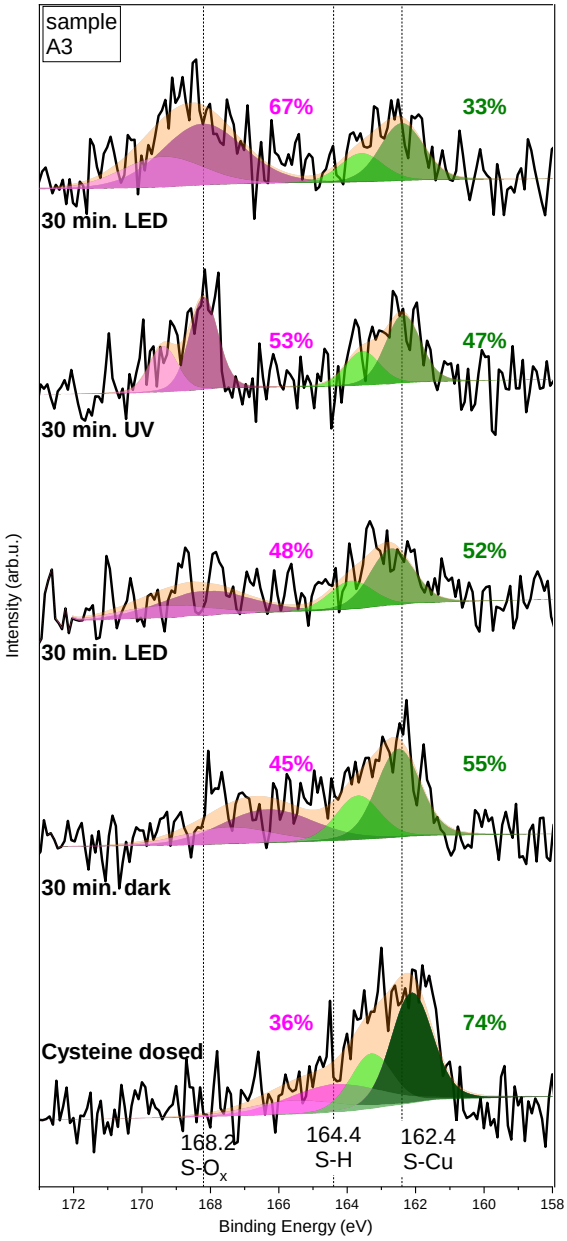


Figure S26: S 2p spectra of sample A3 during photocatalysis measurements. The green shaded area are fits for sulfur bound to Cu and Ti, the purple shaded are the doublets for oxidized sulfur.

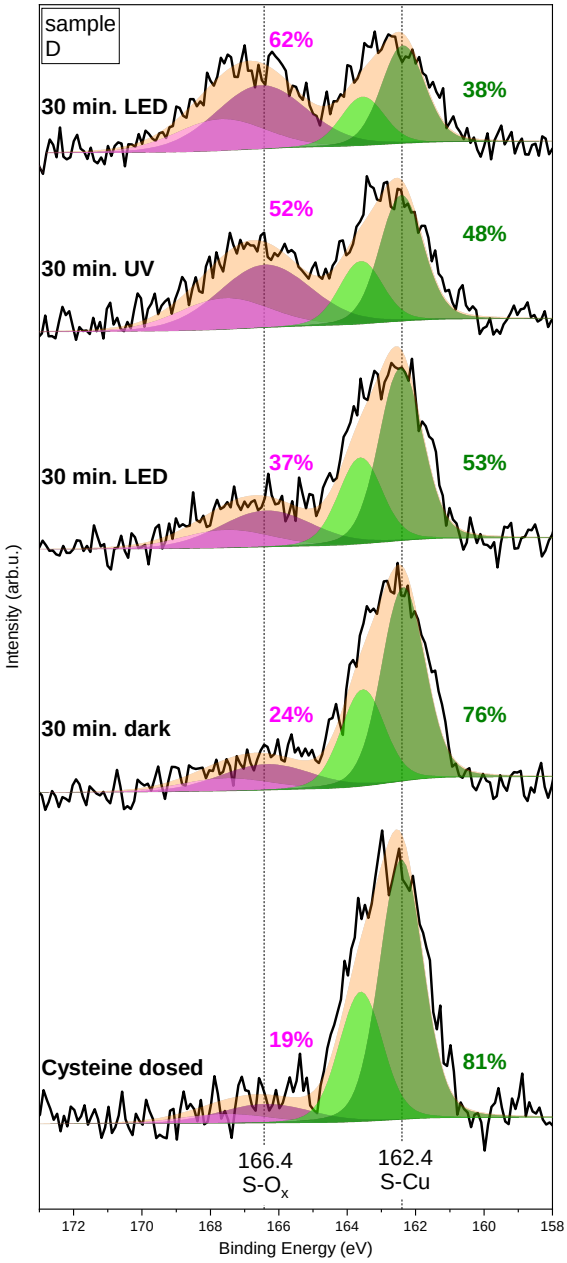


Figure S27: S 2p spectra of sample D during photocatalysis measurements. The green shaded area are fits for sulfur bound to Cu and Ti, the purple shaded are the doublets for oxidized sulfur.

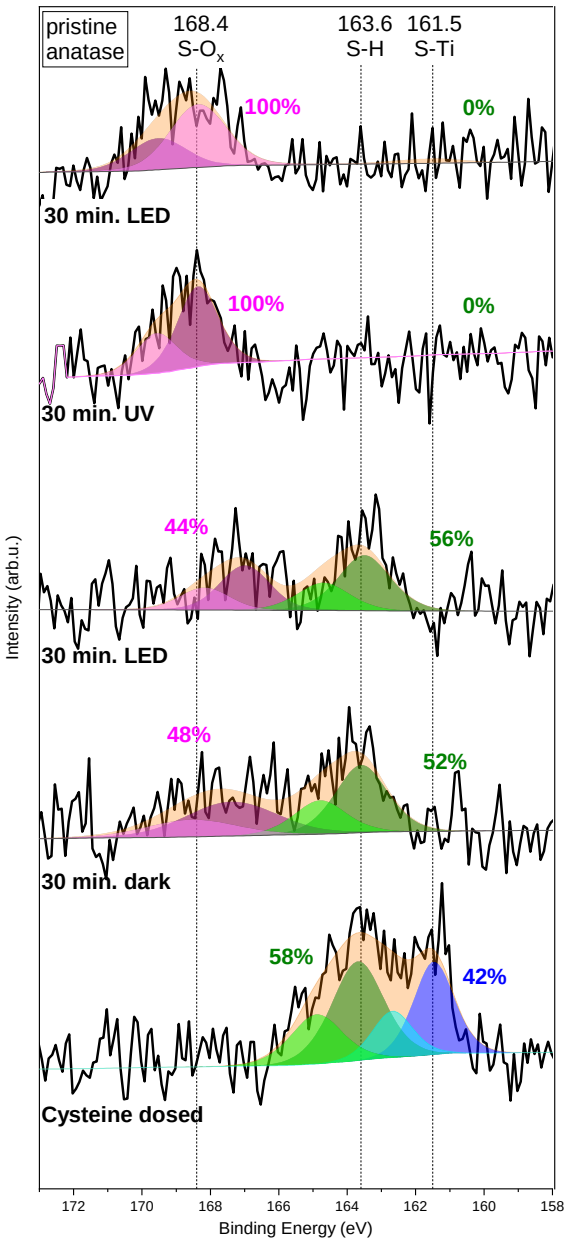


Figure S28: S 2p spectra of the pristine anatase TiO_2 crystal during photocatalysis measurements. The green shaded areas are fits for intact thiol groups R-S-H, the purple shaded are the doublets for oxidized sulfur and the blue shaded doublets are for sulfur bound to Ti.

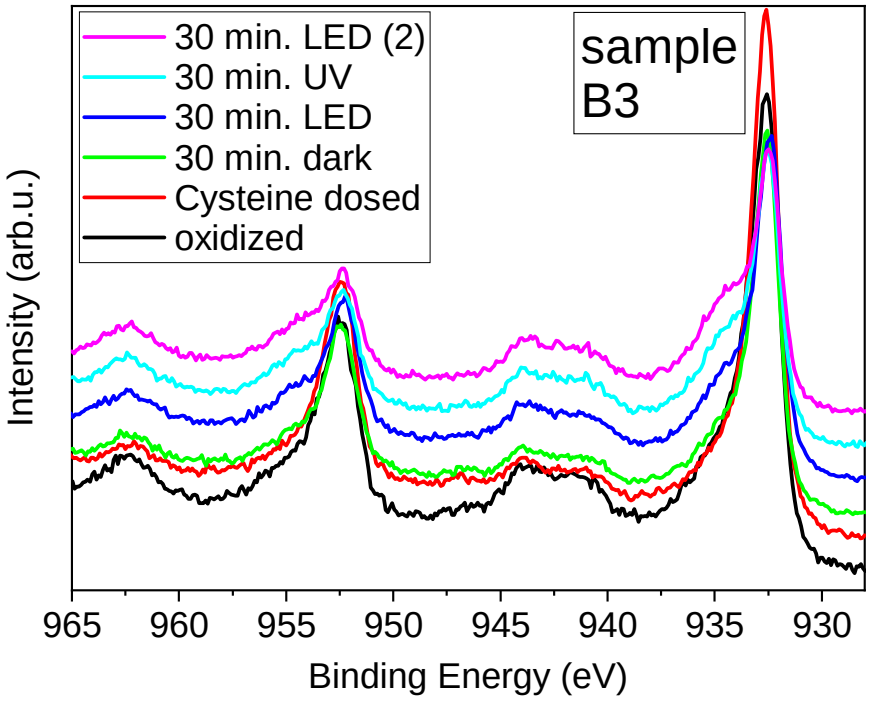


Figure S29: Cu 2p spectra of sample B3 during photocatalysis measurements. 'oxidized' means the oxidized sample before cysteine dosing.

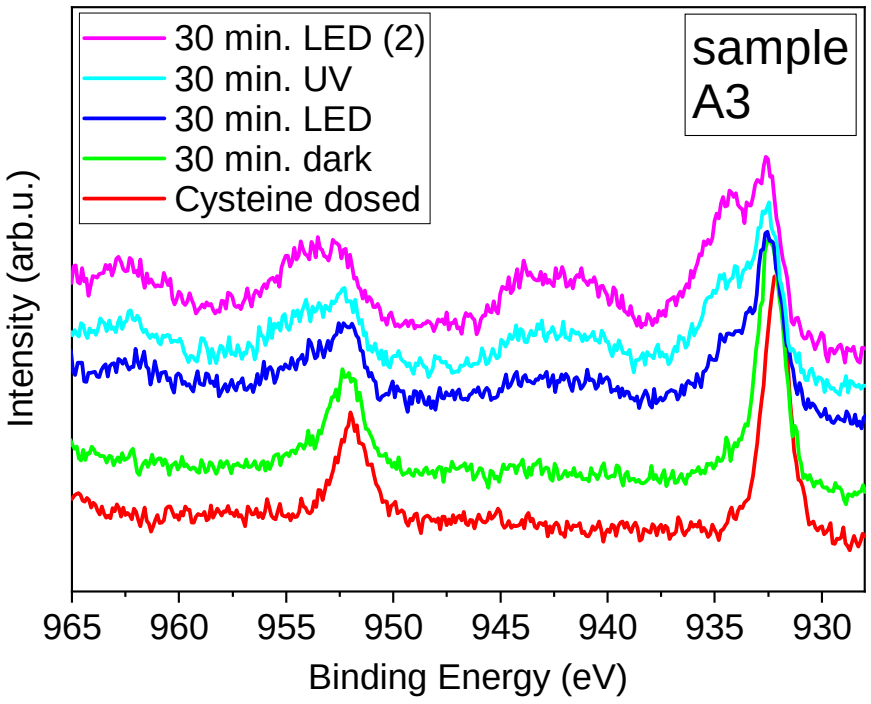


Figure S30: Cu 2p spectra of sample A3 during photocatalysis measurements.

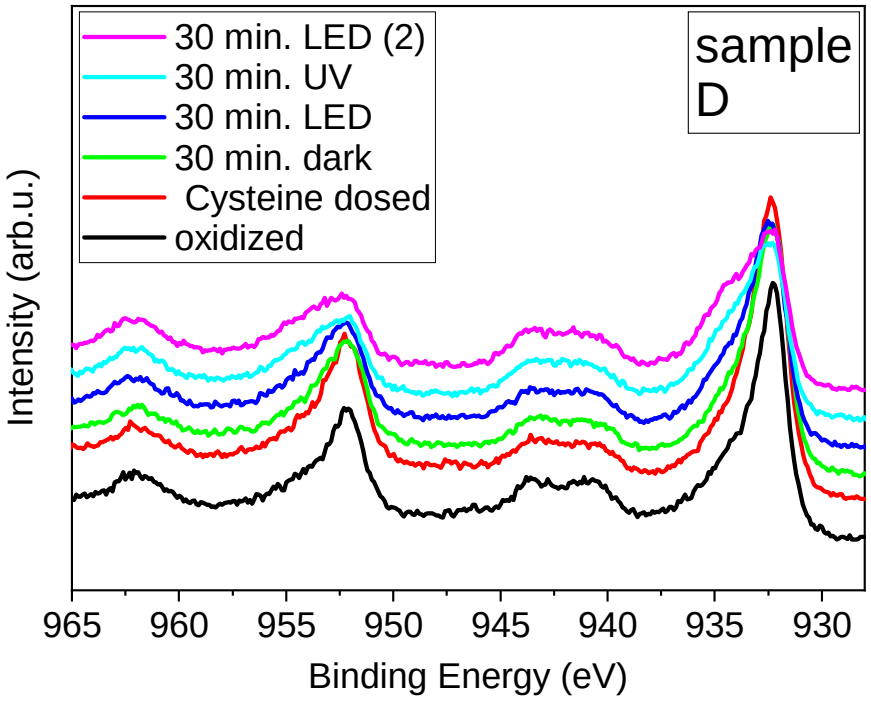


Figure S31: Cu 2p spectra of sample D during photocatalysis measurements. 'oxidized' means the oxidized sample before cysteine dosing.

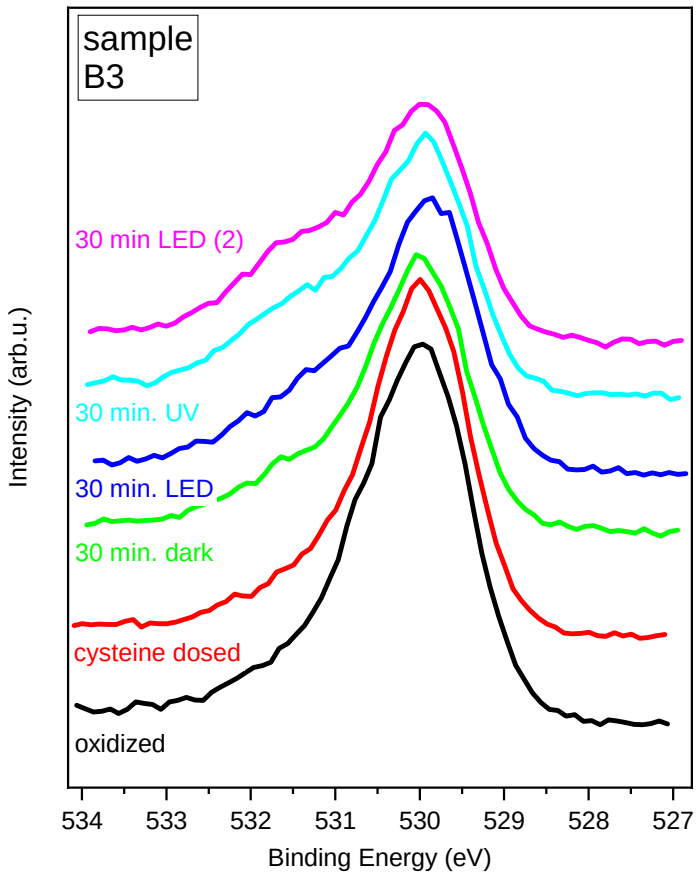


Figure S32: O1s spectra of sample B3 during photocatalysis measurements. 'oxidized' means the oxidized sample before cysteine dosing.

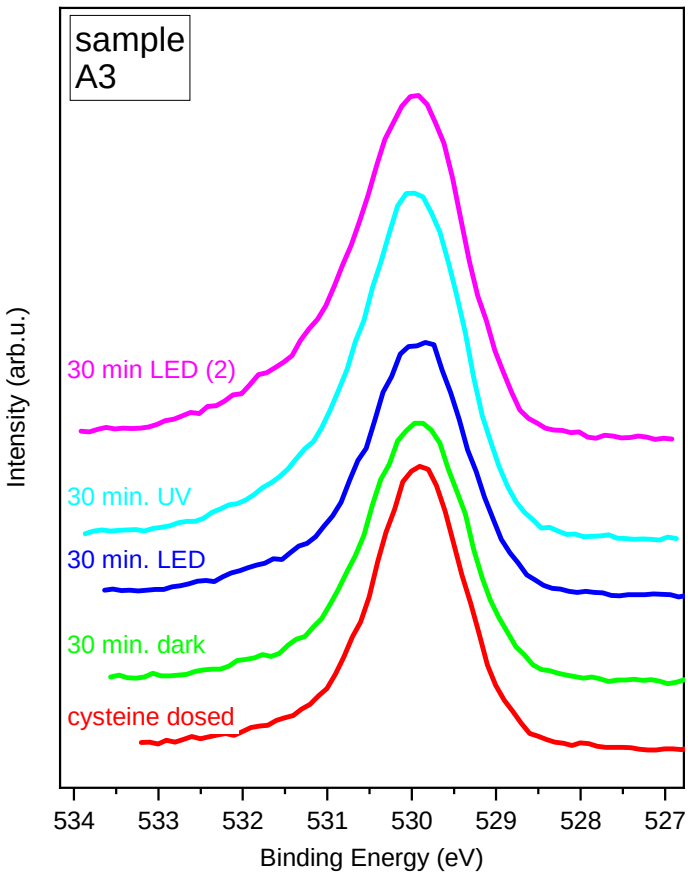


Figure S33: O1s spectra of sample A3 during photocatalysis measurements.

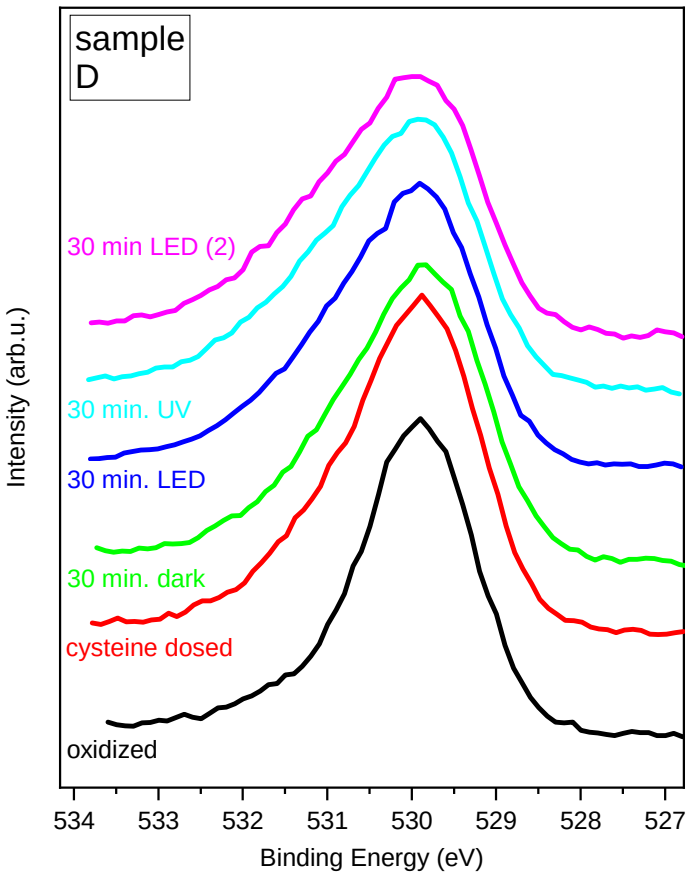


Figure S34: O1s spectra of sample D during photocatalysis measurements. 'oxidized' means the oxidized sample before cysteine dosing.

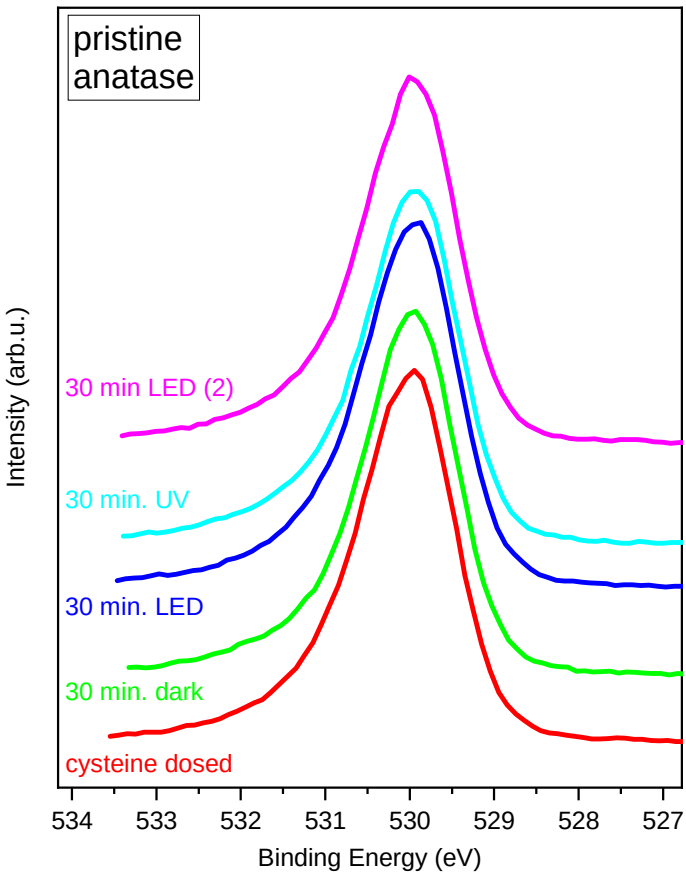


Figure S35: O1s spectra of the pristine anatase TiO_2(101) crystal during photocatalysis measurements.

Table S12: Fitting parameters for the S 2p XP spectra for samples A1, B3 and D, see Figures S26 and S27. GL(50) Lineshapes were used for fitting. The S $2p_{\frac{3}{2}}$ peak was fixed at a binding energy 1.18 eV below the $2p_{\frac{1}{2}}$ peak and at double the area. The FWHM of both peak components was fixed to be the same. For the S-Cu peak, the FWHM was allowed to vary between [1.4,1.8] while the binding energy did not need to be constrained. For the oxide / S-H peak, the FWHM was allowed to vary between [0.3, 3.2] and its binding energy was allowed to vary between [168.5, 166.2].

Sample		S-Cu		S-O_x / S-H		RMS
		Binding Energy (eV)	FWHM (eV)	Binding Energy (eV)	FWHM (eV)	
A1	Cysteine Dosed	162.1	1.4	164.4	3.2	260
	30 min. dark	162.5	1.5	166.3	3.2	154
	30 min. LED	162.7	1.5	168.2	3.2	142
	30 min. UV	162.4	1.2	168.2	1.0	346
	30 min. LED	162.4	1.5	168.2	2.8	333
B3	Cysteine Dosed	162.3	1.5	167.2	3.1	159
	30 min. dark	162.4	1.5	167.2	2.9	409
	30 min. LED	162.3	1.5	167.2	3.1	393
	30 min. UV	162.3	1.5	167.2	2.4	381
	30 min. LED	162.3	1.3	167.4	2.9	139
D	Cysteine Dosed	162.4	1.5	166.4	3.2	176
	30 min. Dark	162.4	1.5	166.4	3.2	536
	30 min. LED	162.4	1.5	166.4	3.2	536
	30 min. UV	162.4	1.5	166.4	3.2	487
	30 min. LED	162.4	1.5	166.5	3.2	148

Table S13: 2p XP spectra for the pristine anatase TiO_2(101) crystal dosed with cysteine, see Figure S28. GL(50) Lineshapes were used for fitting. The S $2p_{\frac{3}{2}}$ peak was fixed at a binding energy 1.2 eV below the $2p_{\frac{1}{2}}$ peak and at double the area. The FWHM of both peak components was fixed to be the same. For the S-H peak, the FWHM was allowed to vary between [1.8,2.5] while the binding energy was constrained to [164.7, 165.1]. For the oxide / S-Ti peak neither binding energy nor FWHM were constrained.

	S-H		S-Ti / S-O_x		
Exposure to Air	Binding Energy (eV)	FWHM (eV)	Binding Energy (eV)	FWHM (eV)	RMS
Cysteine Dosed	163.7	1.8	161.5	1.4	329
30 min. Dark	163.6	1.8	167.4	3.2	330
30 min. LED	163.5	1.8	167	1.7	336
30 min. UV	-	-	168.4	1.4	296
30 min. LED	-	-	168.4	2	309

References

(1) Burdett, J. K.; Hughbanks, T.; Miller, G. J.; Richardson, J. W.; Smith, J. V. Structural-Electronic Relationships in Inorganic Solids: Powder Neutron Diffraction Studies of the Rutile and Anatase Polymorphs of Titanium Dioxide at 15 and 295 K. *Journal of the American Chemical Society* **1987**, *109*, 3639–3646, DOI: 10.1021/ja00246a021.

(2) Khort, A.; Roslyakov, S.; Loginov, P. Solution Combustion Synthesis of Single-Phase Bimetallic Nanomaterials. *Nano-Structures & Nano-Objects* **2021**, *26*, 100727, DOI: 10.1016/j.nanoso.2021.100727.

Chapter 11

SI Article III

Supporting Information: Cysteine Degradation Facilitaded by Cu Nanoparticles Supported on TiO_2(110)

Daniel Silvan Dolling[1,2]*;
Miguel Blanco Garcia[1,2]
Arno Jeromin[1]
Thomas F. Keller[1]
Andreas Stierle[1,2]
Heshmat Noei[1]†
[1]Centre for X-ray and Nano Science CXNS,
Deutsches Elektronen-Synchrotron DESY,
Notkestr. 85, 22607 Hamburg, Germany
[2]Fachbereich Physik, Universität Hamburg,
Notkestr. 9-11, 22607 Hamburg, Germany

September 21, 2026

*silvan.dolling@desy.de
†heshmat.noei@desy.de

1 SEM

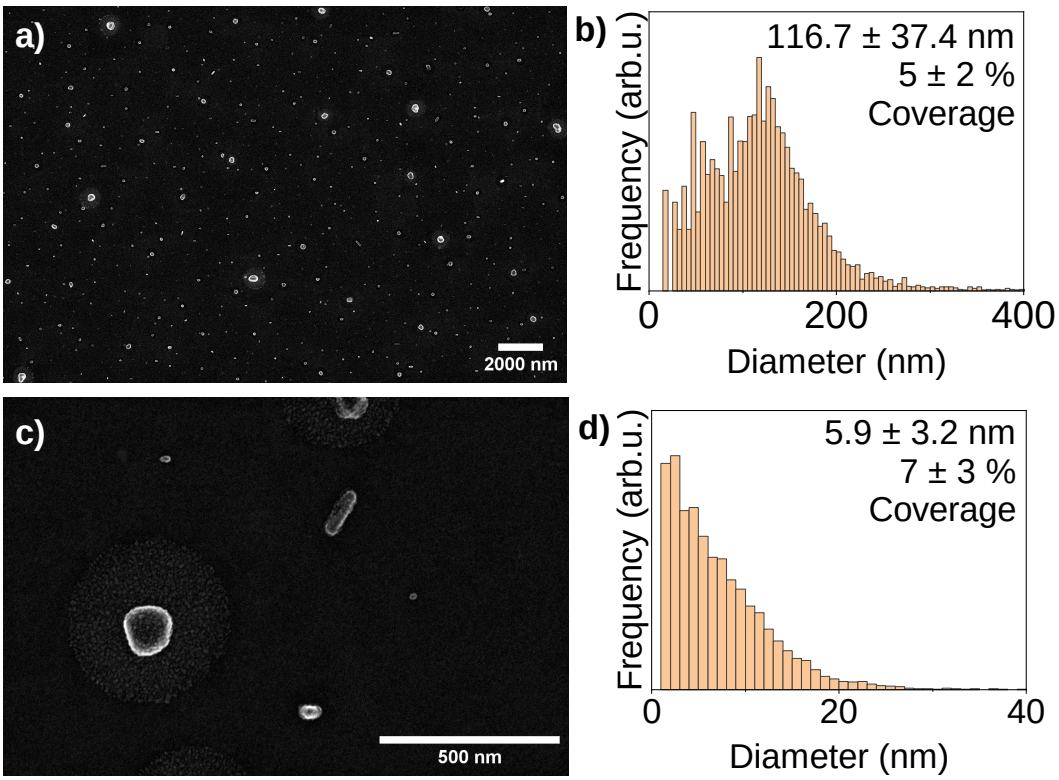


Figure S1: *SEM images (a) and c)) of Sample A and corresponding nanoparticle size distribution (b) and d)). The sizes were calculated assuming a circular NP shape and the size distributions include data from several SEM images, see SI. Two different size distributions were created, as larger scale images mainly depict large NPs, whereas higher resolution images show mainly smaller NPs.*

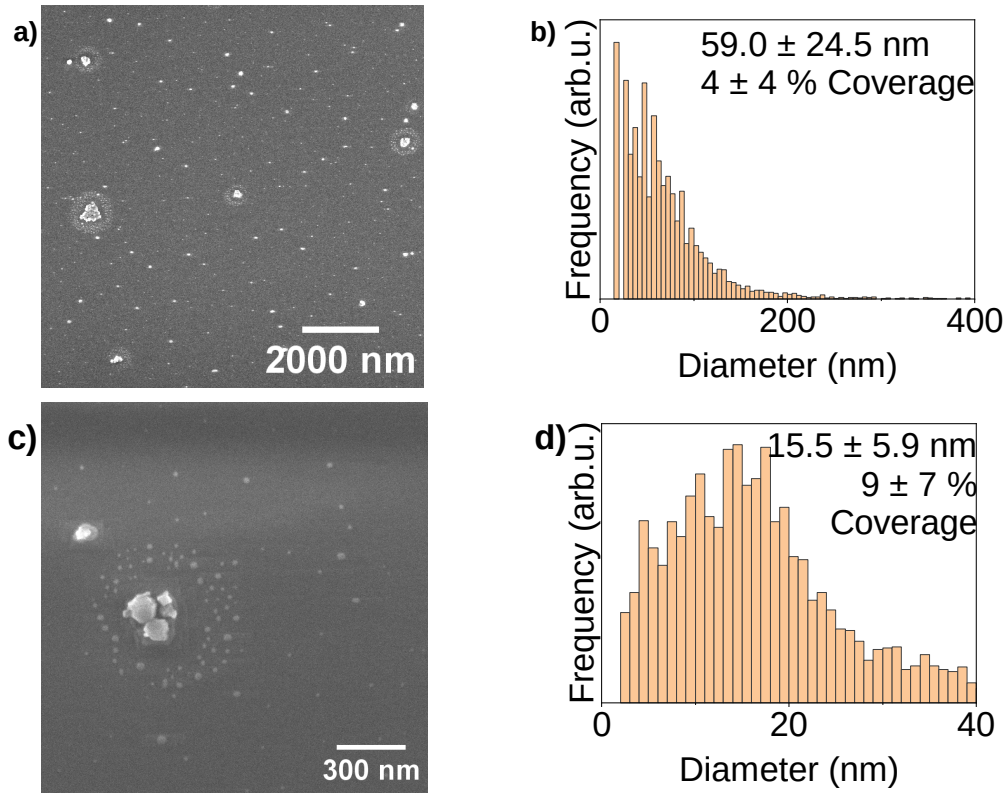


Figure S2: *SEM images (a) and c)) of Sample B and corresponding nanoparticle size distribution (b) and d)). The sizes were calculated assuming a circular NP shape and the size distributions include data from several SEM images, see SI. Two different size distributions were created, as larger scale images mainly depict large NPs, whereas higher resolution images show mainly smaller NPs.*

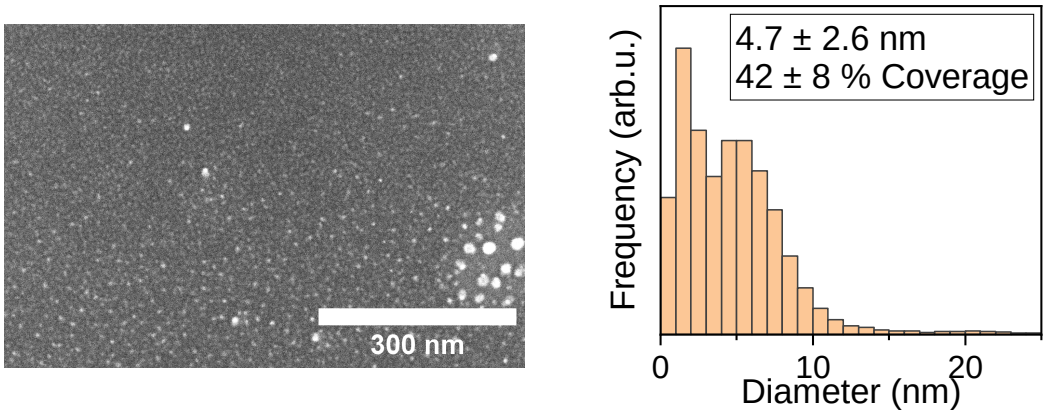


Figure S3: *SEM image and size particle size distribution for sample C.*

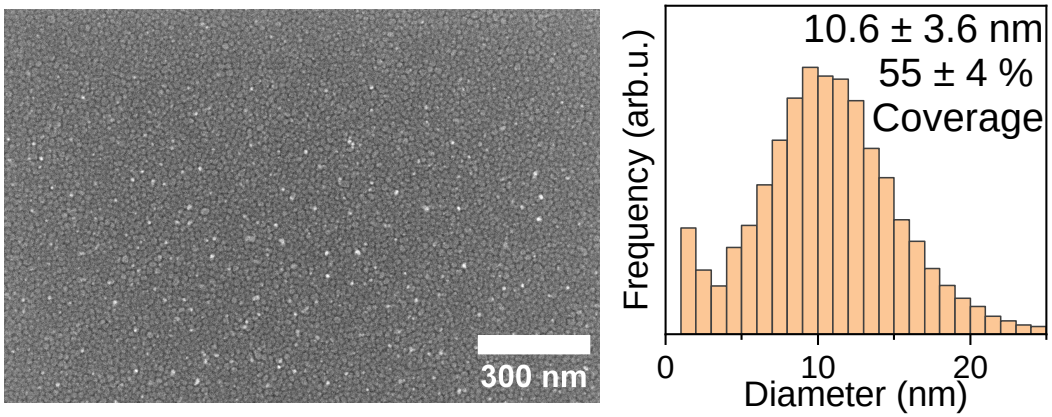


Figure S4: *SEM image and size particle size distribution for sample D.*

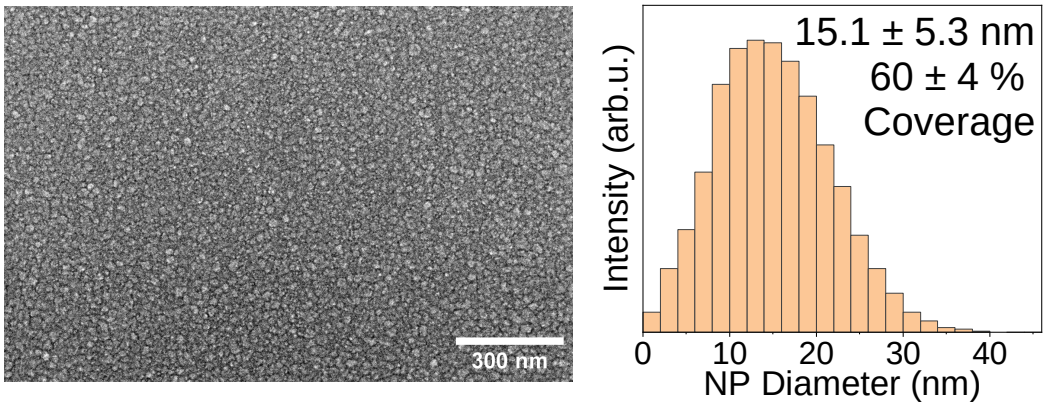


Figure S5: *SEM image and size particle size distribution for sample E.*

1.1 Surface Area Gain

The analysis of the SEM images considers the particles to be 2-dimensional circles. To estimate how much extra surface area is gained by having NPs on the single crystal, a geometric estimation can be made: assuming that the NPs are half-spheres of the same radius as the measured 2-dimensional circles from SEM, and assuming a NP coverage of $\%_{\mathbf{coverage}}$, the increase in area $A_{\mathbf{increase}}$ is:

$$\begin{gathered} A_{\text{increase}} = \\ (2 \times \%_{\text{coverage}}) + (100\% - \%_{\text{coverage}}) - 100\% = \\ 2 \times \%_{\text{coverage}} - \%_{\text{coverage}} = \\ \%_{\text{coverage}} \end{gathered} \tag{1}$$

2 IRRAS

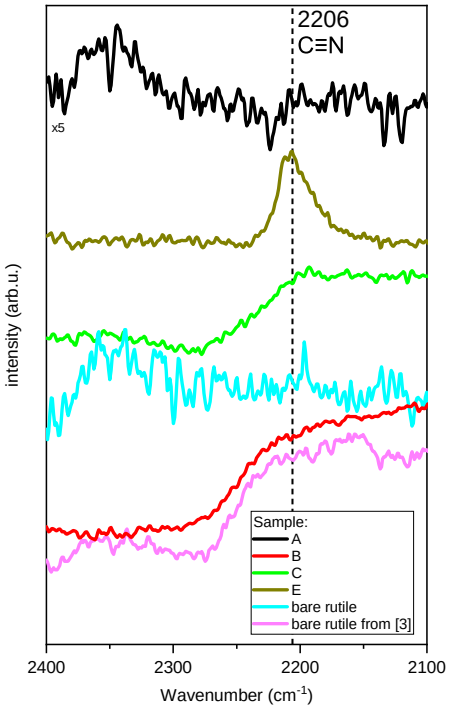


Figure S6: *Comparison of the IRRAS bands for the 2200 cm−1 region.*

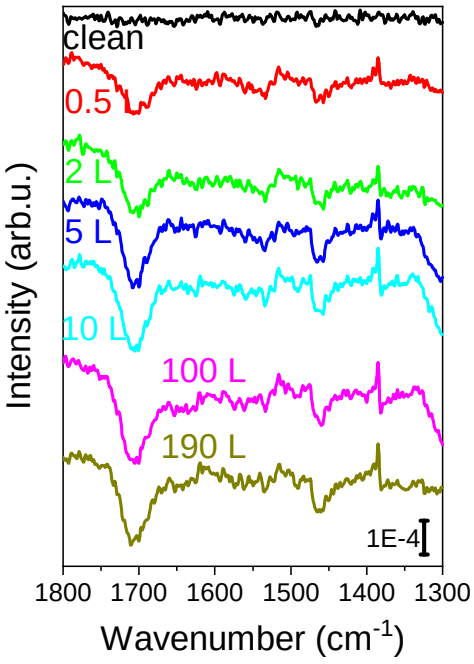


Figure S7: *IRRAS data for sample A (non polarized, at room temperature).*

Table S1: *IRRAS band positions for the different samples.*

	Sample					
Vibration Band	A	B	C	49	E	bare rutile
$\nu_{sym}COO^-$		1363	1363	1392	1392	1364
δCH_2	1462		1451	1450	1450	1462
$\delta_{sym}NH_3^+$		1514	1503			
δNH_2		1550	1550	1550	1550	1550
$\nu_{as}COO^-$		1582	1582	1582	1582	1578
$\delta_{as}NH_3^+$		1610	1610	1610	1610	1608
$\nu C{=}O$				1670	1670	1657
$\nu C{=}O$	1711			1710	1710	1718
$C{\equiv}N$					2206	

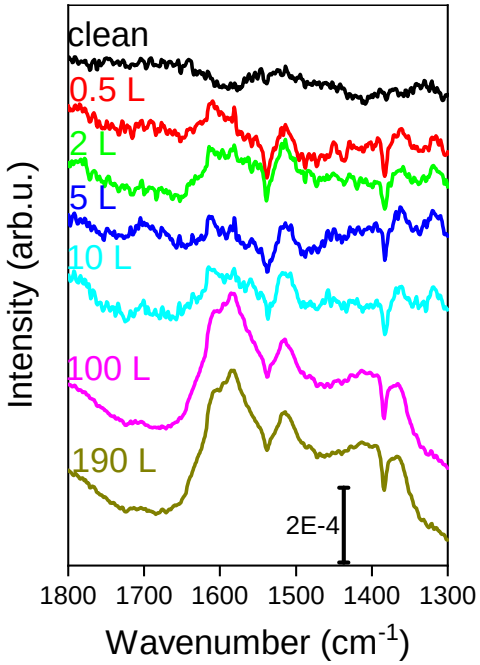


Figure S8: *IRRAS data for sample B (non polarized, at room temperature).*

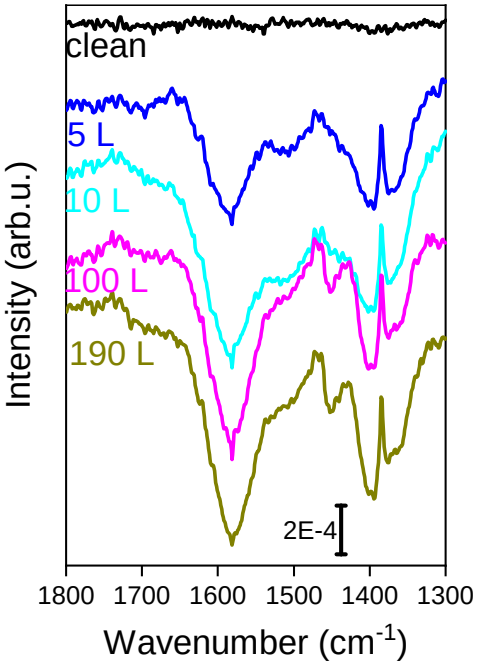


Figure S9: *IRRAS data for sample C (non polarized, at room temperature).*

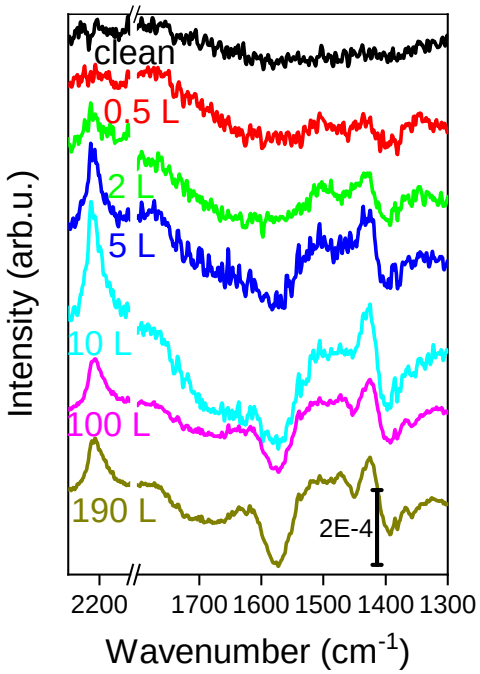


Figure S10: *IRRAS data for sample E (non polarized, at room temperature).*

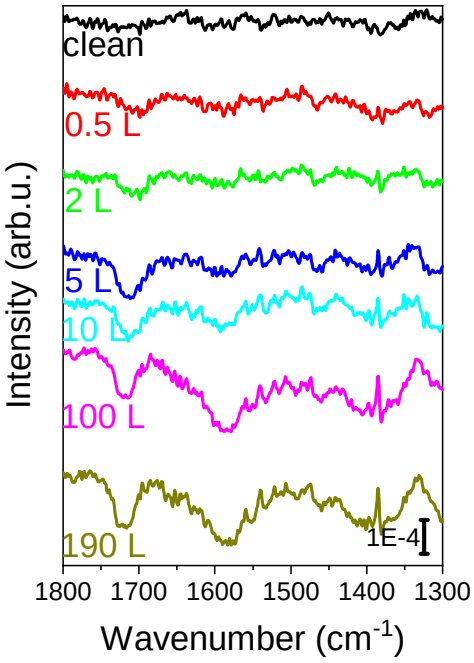


Figure S11: *IRRAS data for the bare rutile crystal (non polarized, at room temperature).*

3 XPS

3.1 Adsorption Quantification

The adsorption of cysteine was quantified by taking the area of the S 2p peak for the different samples. The intensity is normalized with the area A of the Cu $2p_{3/2}$ peak and the Ti $2p_{3/2}$ as follows:

$$I_{norm} = \frac{A_{S2p/RSF_S}}{A_{Cu2p_{3/2}}/RSF_{Cu} + A_{Ti2p_{3/2}}/RSF_{Ti}} \quad (2)$$

The relative sensitivity factors (RSF) used here are 7.94 for Ti, 37.62 for Cu and 1.81 for S. The values for the areas can be found in Table S2. The resulting values are normalized to the value from bare rutile TiO_2. Furthermore, the amount of oxidized sulfur is then quantified by multiplying the normalized intensity of the adsorbed sulfur with the percentage of oxidized sulfur after all light treatments, see Figures 3 and S12.

Table S2: *Area values for the different samples after cysteine adsorption. The unit of the areas is given in counts per second (CPS). For samples 56 and E, S-contamination was seen prior to cysteine dosing. The peak corresponding to the contamination was not taken into account for the S 2p peak area. The corresponding spectra can be seen in Figures 5, S13 to S17, S24 to S28 and S35 to S40.*

Sample	Ti $2p_{3/2}$ Area (CPS)	Cu $2p_{3/2}$ Area (CPS)	S 2p Area (CPS)	Normalized S 2p Area
A	54521	11735	239	0.5
B	11511	21922	421	3.0
C	27261	90734	2041	5.5
D	11711	160661	4984	13.7
E	2030	132299	1516	6.4
bare rutile	70673	0	562	1.0

3.2 Cu 2p

Table S3: *XP fitting parameters for the Cu 2p spectra of all samples before cysteine adsorption. The Cu(II) FWHM was constrained between [2, 3.5], the Cu(II) position between [933.5, 9.4.0] and the Cu(0) & Cu(I) position between [932, 933]. The rest of the parameters was unconstrained. For sample B, the Cu(II) position was set to be [935.5, 936].*

Sample	$Cu\&Cu_2O$		CuO	
	Binding Energy (eV)	FWHM (eV)	Binding Energy (eV)	FWHM (eV)
A	932.8	2.1	934.0	3.4
B	-	-	935.6	3.5
C	932.6	1.2	934.5	3.5
D	932.7	1.3	933.7	3.3
bare rutile	933.5	1.9	934.7	3.5

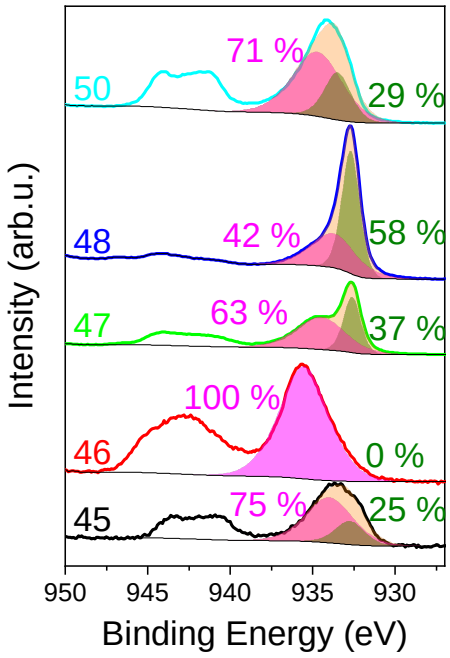


Figure S12: *Cu 2p XP spectra for all samples before cysteine deposition. The peak is decomposed into CuO (pink) and Cu&Cu$_2$O (green), the envelope being beige. Details for the fits are found in Table S3.*

3.3 C 1s

3.4 S 2p Photocatalysis

Fitting Protocol The S 2p spectra were fitted with a Gaussian-Lorentzian GL(50) lineshape in CasaXPS [1]. The line-splitting was fixed to 1.18 eV, and the $2p_{3/2}$ area was fixed to be twice the area of the $2p_{1/2}$ peak. The FWHM of the $2p_{1/2}$ peak and the $2p_{3/2}$ peak were fixed to be the same. The S-Cu $2p_{3/2}$ peak position was varied between [162.82, 162.32] eV with a FWHM between [0.5, 1.5] eV, the S-H $2p_{3/2}$ peak position was varied between [164.02, 163.52] eV with a FWHM between [0.9, 1.5] eV and the $2p_{3/2}$ peak position for oxidized sulfur S-O_x was varied between [167.82, 166.37] eV with a FWHM between [0.37, 3.0] eV. For the bare rutile crystal, the S-Ti $2p_{3/2}$ peak position was varied between [162.9, 161.3] eV with a FWHM between [1.4, 1.8] eV. The contamination doublets used for the fits of samples B and E were fixed to their peak position and FWHM before cysteine dosing within ±0.1 eV, assuming that these peaks do not change or interact.

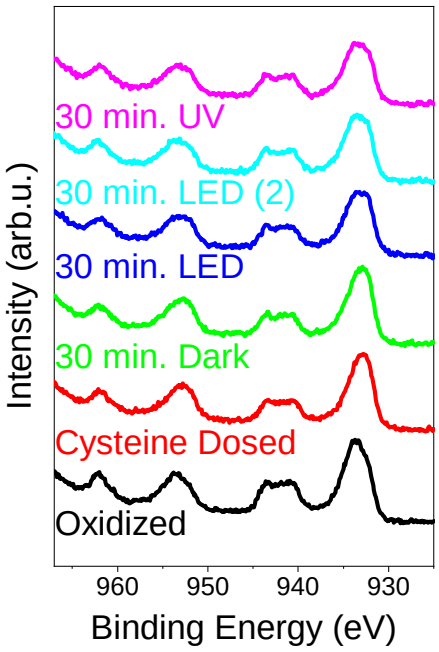


Figure S13: *Cu 2p XP spectra for sample A.*

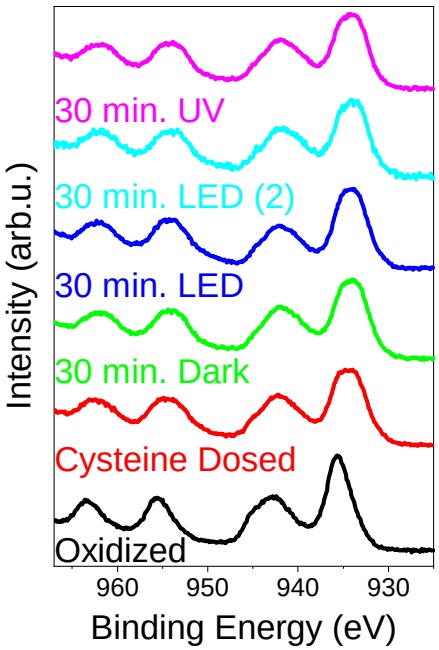


Figure S14: *Cu 2p XP spectra for sample B.*

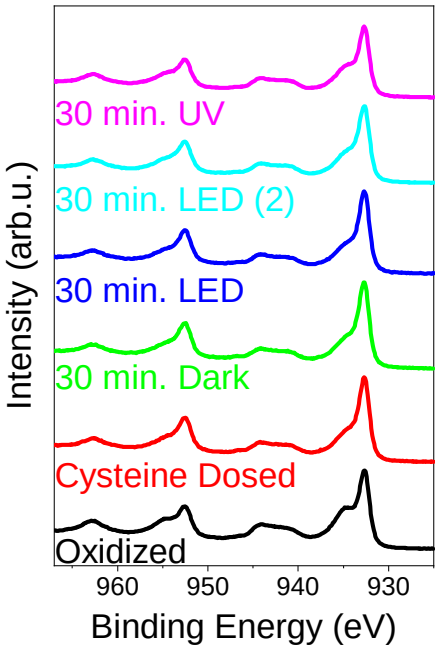


Figure S15: *Cu 2p XP spectra for sample C.*

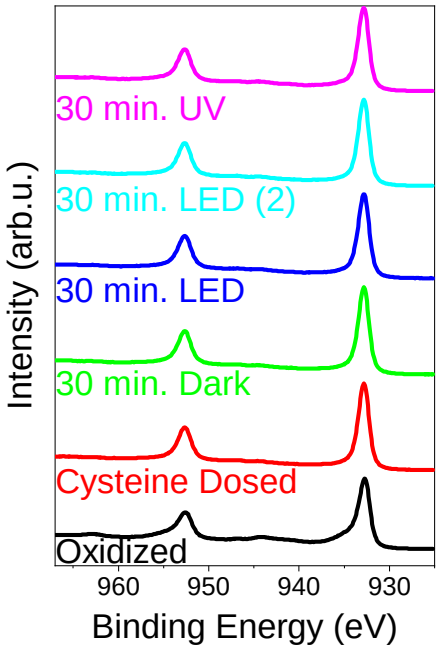


Figure S16: *Cu 2p XP spectra for sample D.*

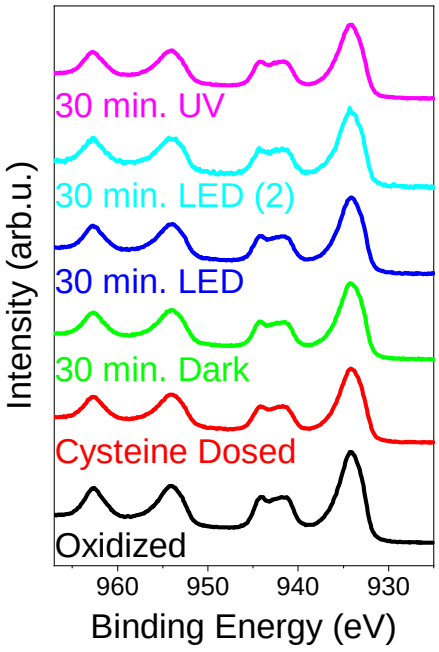


Figure S17: *Cu 2p XP spectra for sample E.*

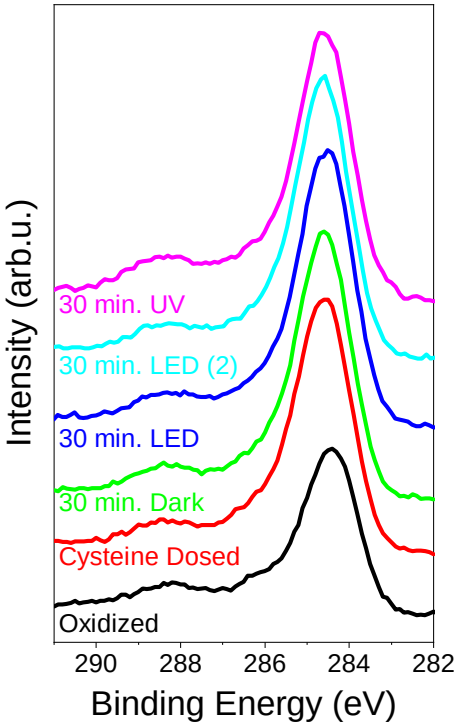


Figure S18: *C 1s spectra for sample A. 'Oxidized' means that the Cu NPs were oxidized, but cysteine is not yet deposited.*

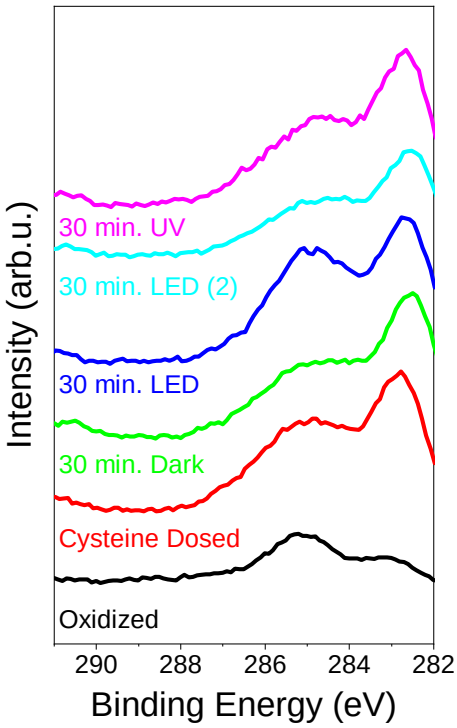


Figure S19: *C 1s spectra for sample B. 'Oxidized' means that the Cu NPs were oxidized, but cysteine is not yet deposited. The sample exhibited charging during the XPS measurement, resulting in additional peaks.*

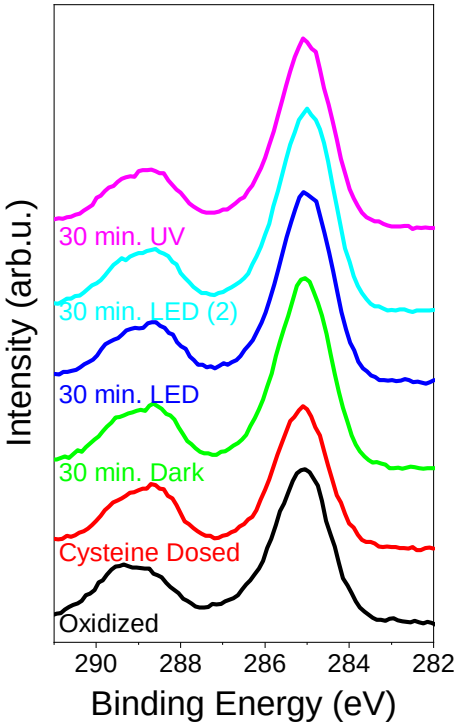


Figure S20: *C 1s spectra for sample C. 'Oxidized' means that the Cu NPs were oxidized, but cysteine is not yet deposited.*

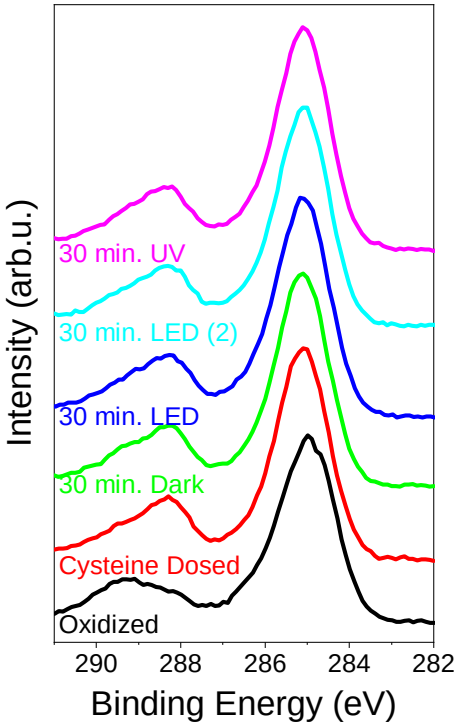


Figure S21: *C 1s spectra for sample D. 'Oxidized' means that the Cu NPs were oxidized, but cysteine is not yet deposited.*

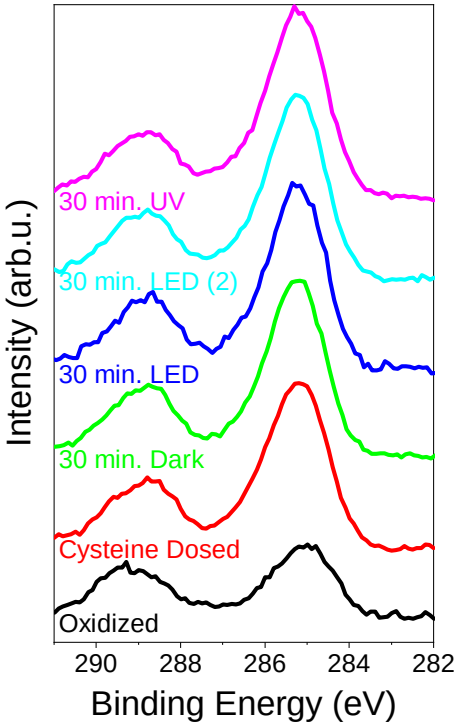


Figure S22: *C 1s spectra for sample E. 'Oxidized' means that the Cu NPs were oxidized, but cysteine is not yet deposited.*

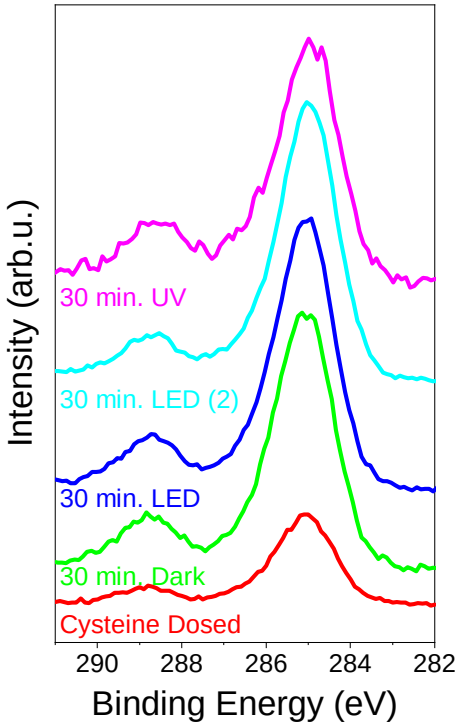


Figure S23: *C 1s spectra for the bare rutile sample.*

Table S4: *S $2p_{3/2}$ fitting values for sample A, see Figure S24.*

	Peak	Binding Energy (eV)	FWHM (eV)
Cysteine Dosed	S-Ox	167.67	1.32
	S-Cu	162.32	1.03
	S-H	163.65	1.50
30 min. Dark	S-Ox	167.10	3.00
	S-Cu	162.41	1.42
	S-H	163.58	1.50
30 min. LED	S-Ox	167.44	3.00
	S-Cu	162.45	1.50
	S-H	164.02	0.90
30 min. LED (2)	S-Ox	167.76	2.73
	S-Cu	162.75	1.50
	S-H	164.02	0.98
30 min. UV	S-Ox	167.82	3.00

Table S5: *S $2p_{3/2}$ fitting values for sample B, see Figure S25. "Cont" is the fit for the contamination present prior to cysteine dosing.*

	Peak	Binding Energy (eV)	FWHM (eV)
Oxidized	Cont.	168.27	3.00
Cysteine Dosed	S-Ox	166.37	3.00
	S-Cu	162.32	1.50
	S-H	164.02	0.90
	Cont.	168.30	3.00
30 min. Dark	S-Ox	166.37	3.00
	S-Cu	162.32	1.50
	S-H	164.02	1.50
	Cont.	168.30	3.00
30 min. LED	S-Ox	166.42	3.00
	S-Cu	162.32	1.50
	S-H	164.02	1.50
	Cont.	168.30	3.00
30 min. LED (2)	S-Ox	166.37	1.61
	S-Cu	162.32	1.33
	S-H	163.52	0.90
	Cont.	168.30	3.00
30 min. UV	S-Ox	166.37	2.88
	Cont.	168.20	3.00

Table S6: *S $2p_{3/2}$ fitting values for sample C, see Figure S26.*

	Peak	Binding Energy (eV)	FWHM (eV)
Cysteine Dosed	S-Ox	166.67	3.00
	S-Cu	162.82	1.14
	S-H	163.83	1.35
30 min. Dark	S-Ox	166.67	3.00
	S-Cu	162.82	1.22
	S-H	163.85	1.55
30 min. LED	S-Ox	166.67	3.00
	S-Cu	162.76	1.28
	S-H	163.82	1.42
30 min. LED (2)	S-Ox	166.67	3.00
	S-Cu	162.70	1.30
	S-H	163.76	1.41
30 min. UV	S-Ox	166.67	3.00
	S-Cu	162.67	1.39
	S-H	163.68	1.41

Table S7: *S $2p_{3/2}$ fitting values for sample D, see Figure S27.*

	Peak	Binding Energy (eV)	FWHM (eV)
Cysteine Dosed	S-Ox	167.43	3.00
	S-Cu	162.82	1.24
	S-H	163.52	1.50
30 min. Dark	S-Ox	167.15	3.00
	S-Cu	162.80	1.29
	S-H	163.52	1.50
30 min. LED	S-Ox	167.04	3.00
	S-Cu	162.78	1.41
	S-H	163.65	1.50
30 min. LED (2)	S-Ox	167.09	3.00
	S-Cu	162.73	1.40
	S-H	163.74	1.50
30 min. UV	S-Ox	166.98	3.00
	S-Cu	162.68	1.43
	S-H	163.52	1.50

Table S8: *S $2p_{3/2}$ fitting values for sample E, see Figure 5. "Cont." is the fit for the contamination prior to cysteine dosing.*

	Peak	Binding Energy (eV)	FWHM (eV)
Oxidized	Cont.	168.66	1.31
Cysteine Dosed	S-Ox	166.39	0.81
	S-Cu	162.57	1.20
	S-H	163.83	1.49
	Cont.	168.62	1.40
30 min. Dark	S-Ox	166.37	0.91
	S-Cu	162.66	1.20
	S-H	163.88	1.50
	Cont.	168.60	1.37
30 min. LED	S-Ox	166.44	1.35
	S-Cu	162.70	1.25
	S-H	163.90	1.31
	Cont.	168.65	1.32
30 min. LED (2)	S-Ox	166.63	2.92
	S-Cu	162.80	1.03
	S-H	163.87	1.21
	Cont.	168.63	1.26
30 min. UV	S-Ox	166.67	2.41
	S-Cu	162.82	1.50
	S-H	163.95	1.41
	Cont.	168.66	1.34

Table S9: *S $2p_{3/2}$ fitting values for the bare rutile crystal, see Figure S28.*

	Peak	Binding Energy (eV)	FWHM (eV)
Cysteine Dosed	S-Ti	161.61	1.40
	S-H	163.75	1.80
30 min. Dark	S-Ti	161.30	1.46
	S-H	163.85	1.80
	S-Ox	167.02	1.40
30 min. LED	S-H	163.68	1.80
	S-Ox	168.03	1.80
30 min. LED (2)	S-H	163.50	2.21
	S-Ox	168.31	1.80
30 min. UV	S-Ox	168.85	1.80

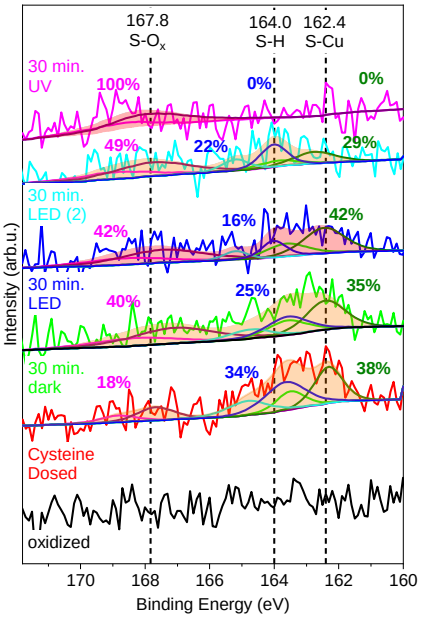


Figure S24: *S 2p spectra for sample A for different steps of exposure to ambient conditions and light. 'Oxidized' means that the Cu NPs are oxidized, but no cysteine is deposited. The spectra were fitted with a doublet corresponding to sulfur bound to Cu S-Cu (green), a doublet for oxidized sulfur (purple) and a doublet for molecular thiol groups (S-H) in blue. The envelope of the fit is displayed as orange shade.*

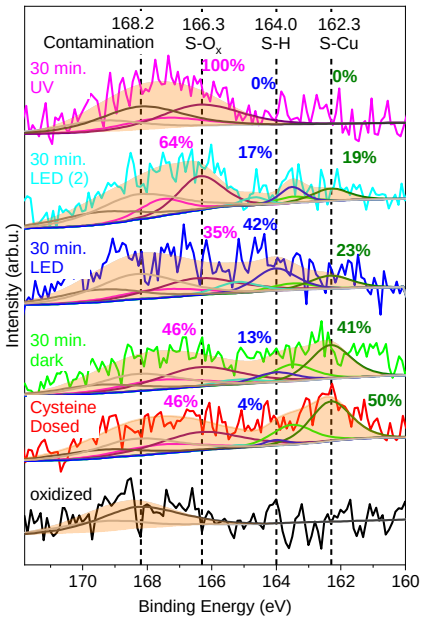


Figure S25: *S 2p spectra for sample B for different steps of exposure to ambient conditions and light. 'Oxidized' means that the Cu NPs are oxidized, but no cysteine is deposited. The spectra were fitted with a doublet corresponding to sulfur bound to Ti (green), a doublet corresponding to oxidized sulfur (purple) and a doublet corresponding to molecular thiol groups (S-H) in blue. Additionally, a doublet for contamination prior to cysteine dosing was needed (grey). The percentages give the amount of cysteine in the specific chemical state. It is assumed that the overall amount of cysteine does not change, such that the percentage of the contamination is constant. After light exposure, some of the cysteine enters the same chemical state as the contaminant. The envelope of the fit is displayed as orange shade.*

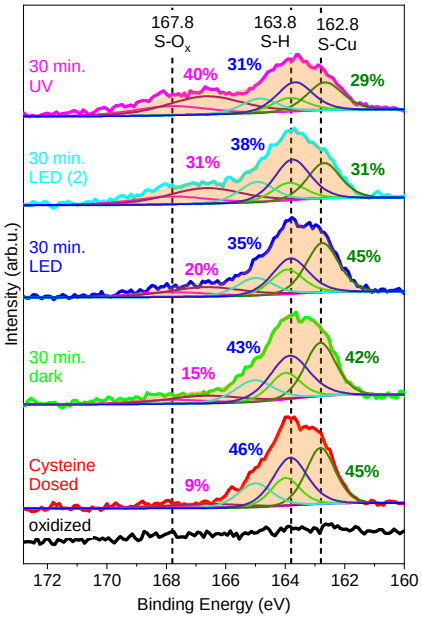


Figure S26: *S 2p spectra for sample C for different steps of exposure to ambient conditions and light. 'Oxidized' means that the Cu NPs are oxidized, but no cysteine is deposited. The spectra were fitted with a doublet corresponding to sulfur bound to Cu (green), a doublet for the molecular thiol group S-H (blue), and a doublet for oxidized sulfur (purple). The envelope of the fit is displayed as orange shade.*

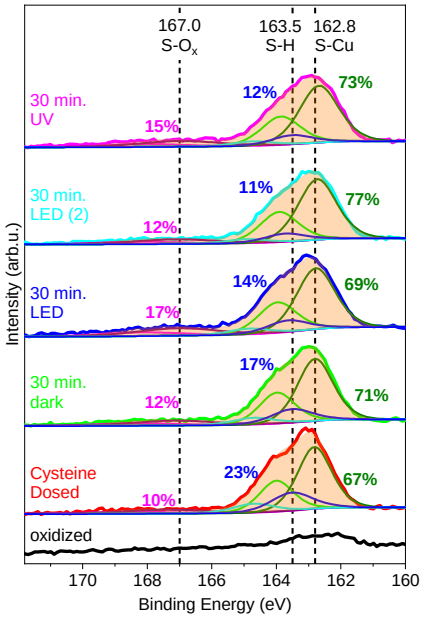


Figure S27: *S 2p spectra for sample D for different steps of exposure to ambient conditions and light. 'Oxidized' means that the Cu NPs are oxidized, but no cysteine is deposited. The spectra were fitted with a doublet corresponding to sulfur bound to Cu S-Cu (green), a doublet for oxidized sulfur (purple) and a doublet for thiol groups in molecular form (S-H) in blue. The envelope of the fit is displayed as orange shade.*

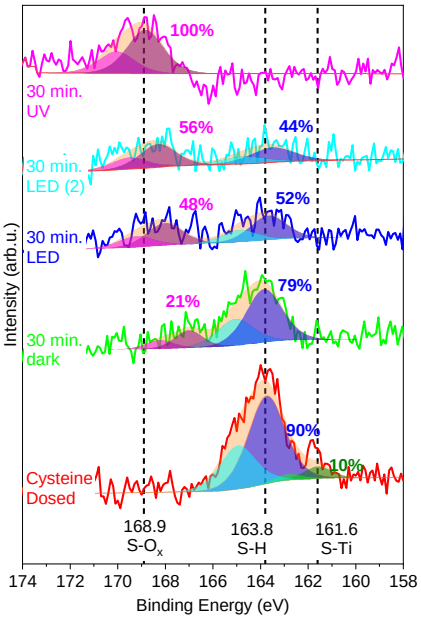


Figure S28: *S 2p spectra for the bare rutile crystal for different steps of exposure to ambient conditions and light. The spectra were fitted with a doublet corresponding to sulfur bound to Ti (green), a doublet for oxidized sulfur (purple) and a doublet for molecular thiol groups (S-H) in blue. The envelope of the fit is displayed as orange shade.*

3.5 O 1s

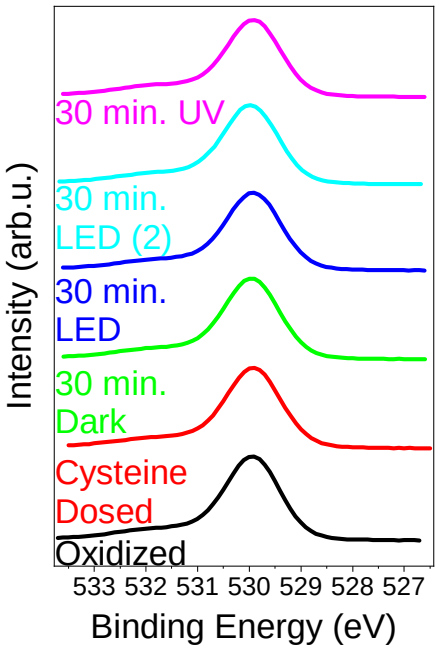


Figure S29: *O 1s XP spectra of sample A.*

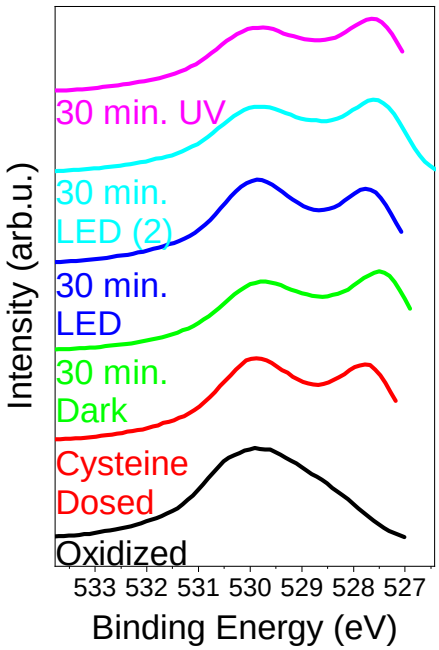


Figure S30: *O 1s XP spectra of sample B. The additional peak visible at low binding energy is a charging artifact.*

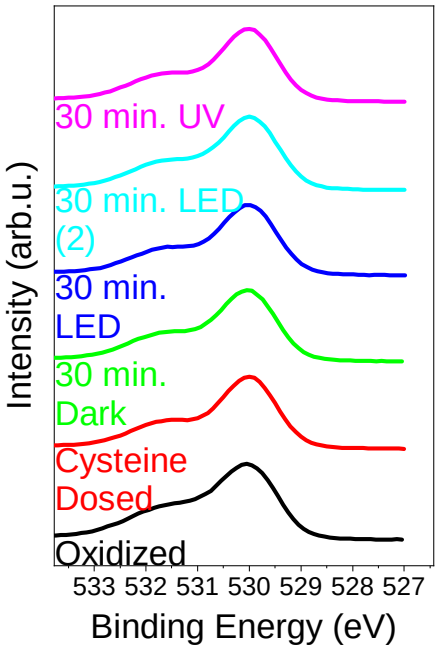


Figure S31: *O 1s XP spectra of sample C.*

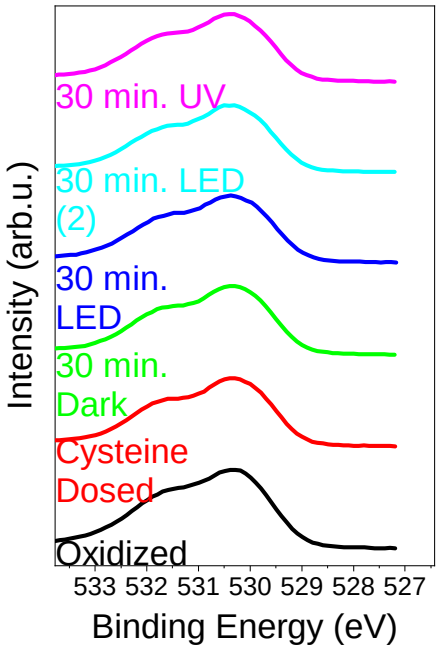


Figure S32: *O 1s XP spectra of sample D.*

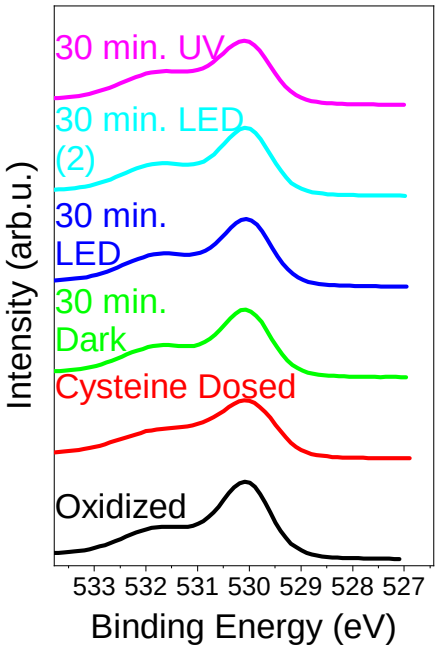


Figure S33: *O 1s XP spectra of sample E.*

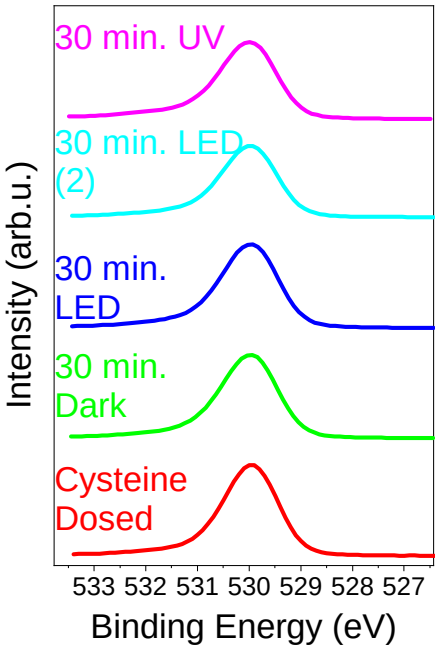


Figure S34: *O 1s XP spectra of the bare rutile crystal.*

3.6 Ti 2p

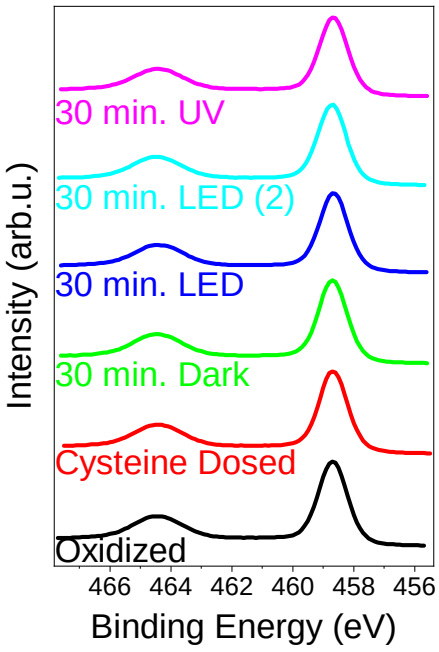


Figure S35: *Ti 2p XP spectra of sample A.*

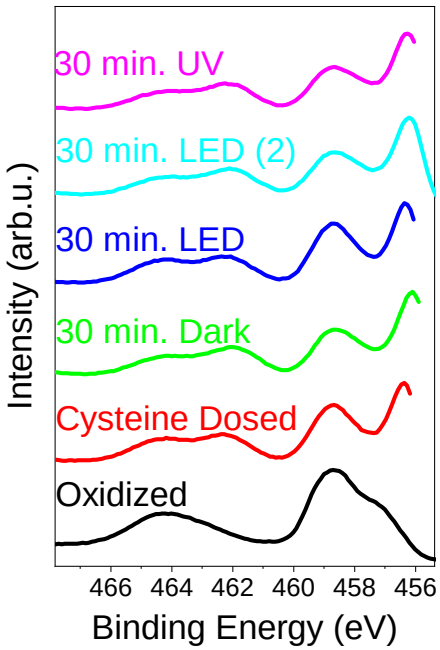


Figure S36: *Ti 2p XP spectra of sample B. The additional peaks are attributed to charging artifacts.*

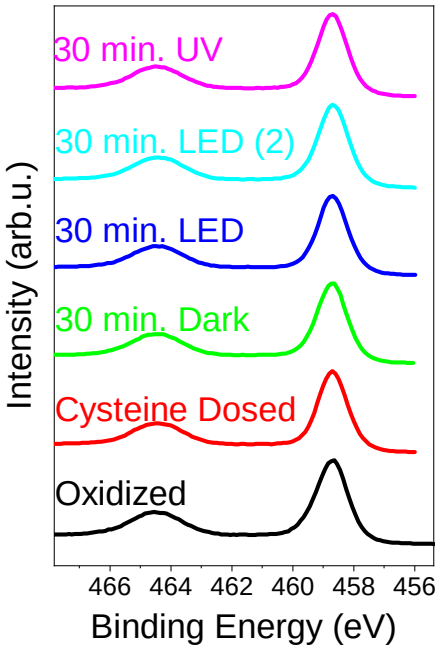


Figure S37: *Ti 2p XP spectra of sample C.*

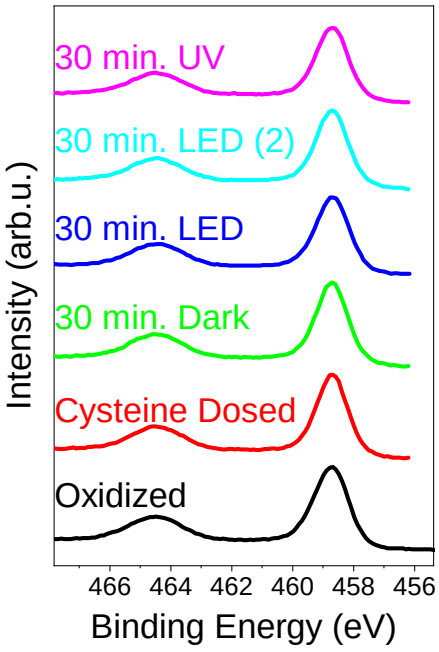


Figure S38: *Ti 2p XP spectra of sample D.*

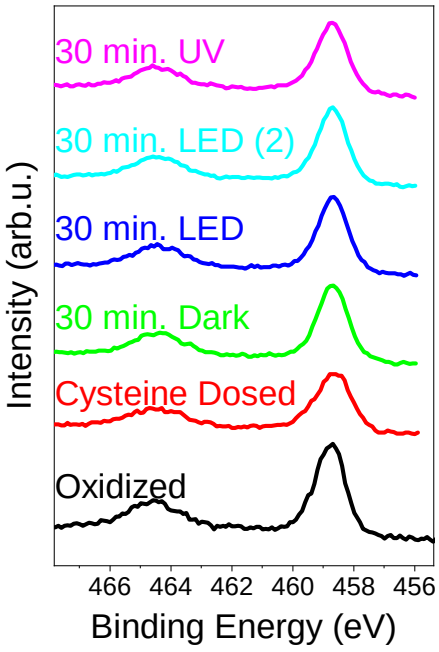


Figure S39: *Ti 2p XP spectra of sample E.*

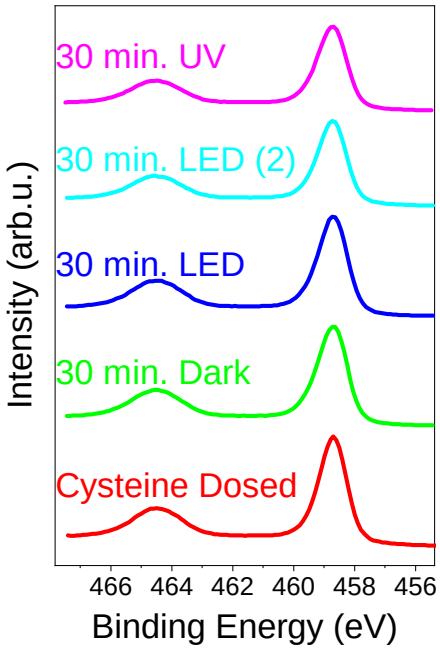


Figure S40: *Ti 2p XP spectra of the bare rutile crystal.*

3.7 Cu LMM

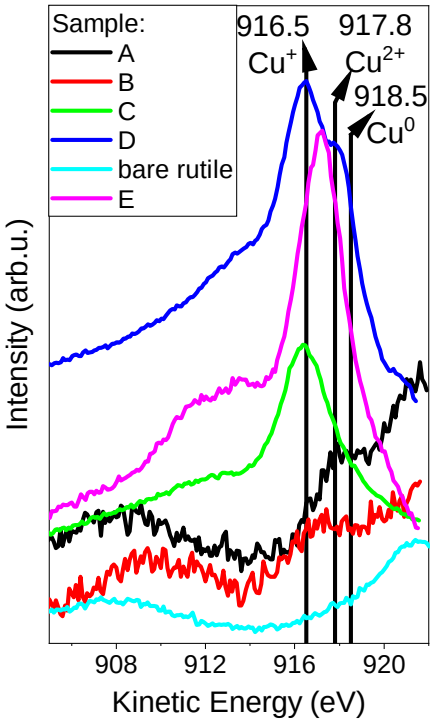


Figure S41: *Cu LMM XP spectra of all samples before cysteine deposition (except for the bare rutile sample, which is shown after cysteine deposition). The intensity differences are attributed to differences in NP coverage.*

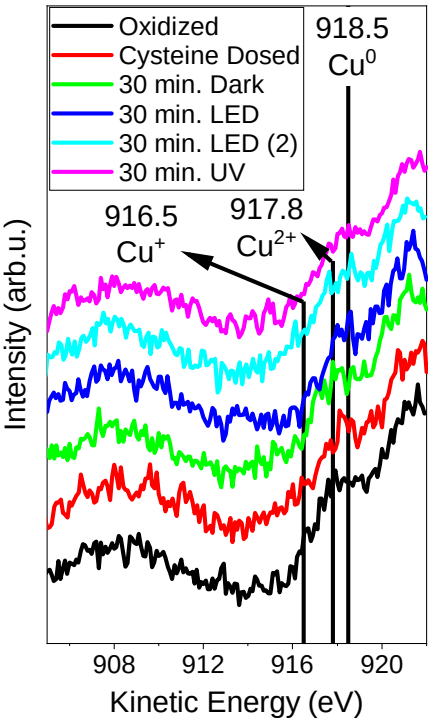


Figure S42: *Cu LMM XP spectra of sample A.*

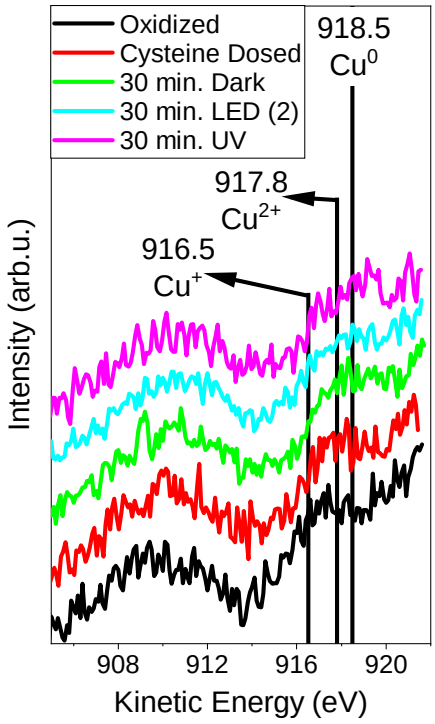


Figure S43: *Cu LMM XP spectra of sample B.*

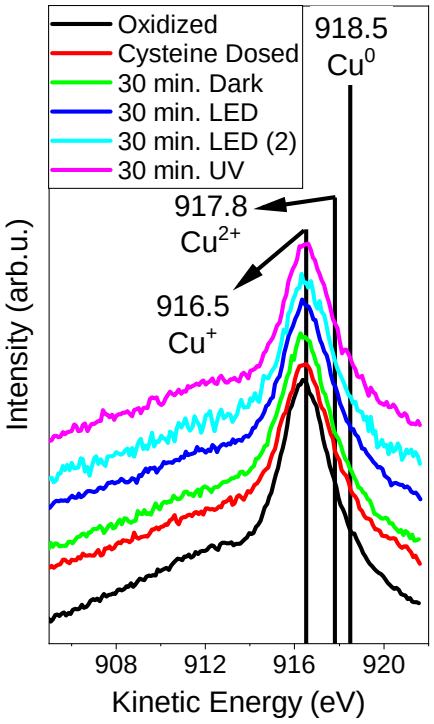


Figure S44: *Cu LMM XP spectra of sample C.*

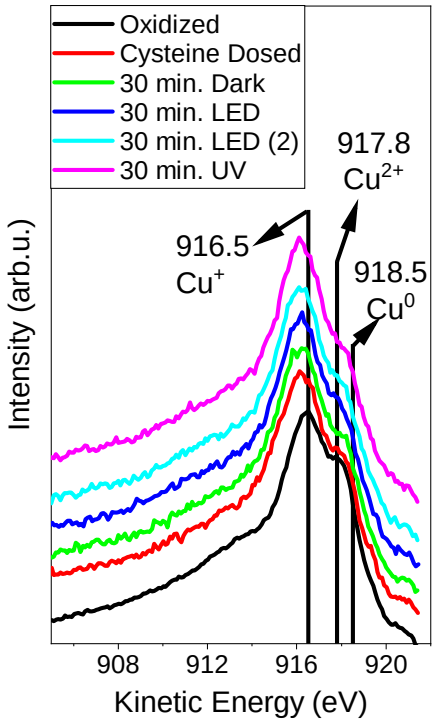


Figure S45: *Cu LMM XP spectra of sample D.*

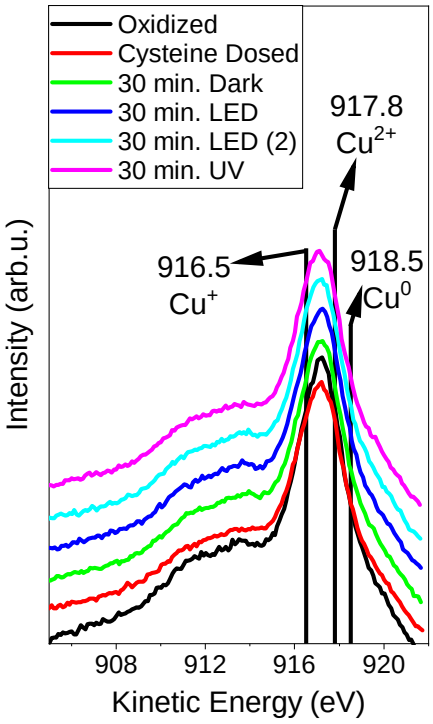


Figure S46: *Cu LMM XP spectra of sample E.*

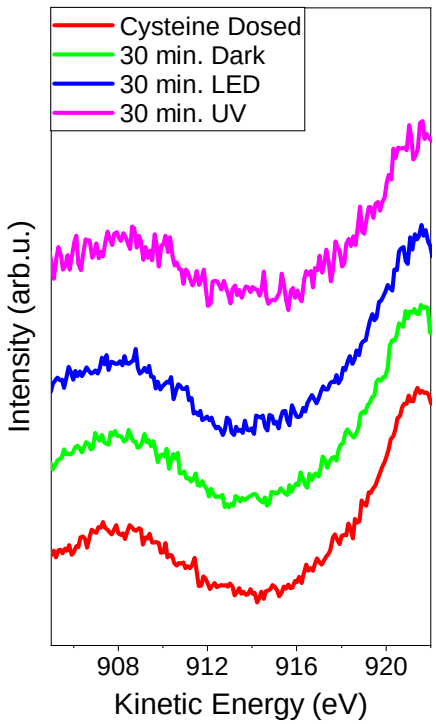


Figure S47: *Cu LMM XP spectra of the bare rutile crystal.*

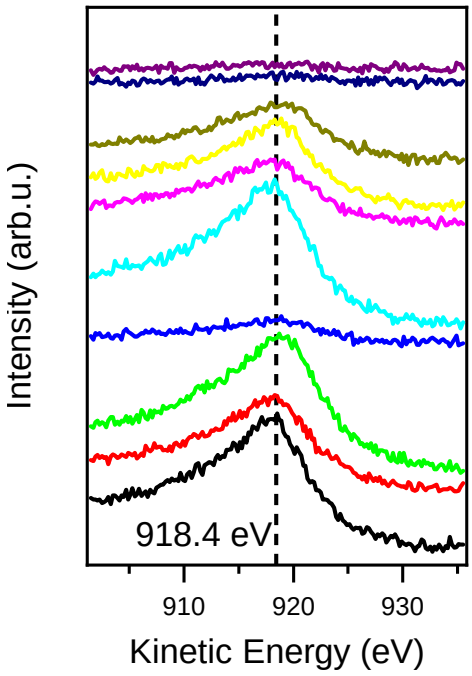


Figure S48: *Individual Cu LMM Auger scans for sample A, extracted at different positions along the line scan, see Figure 1, both on and off the NPs.*

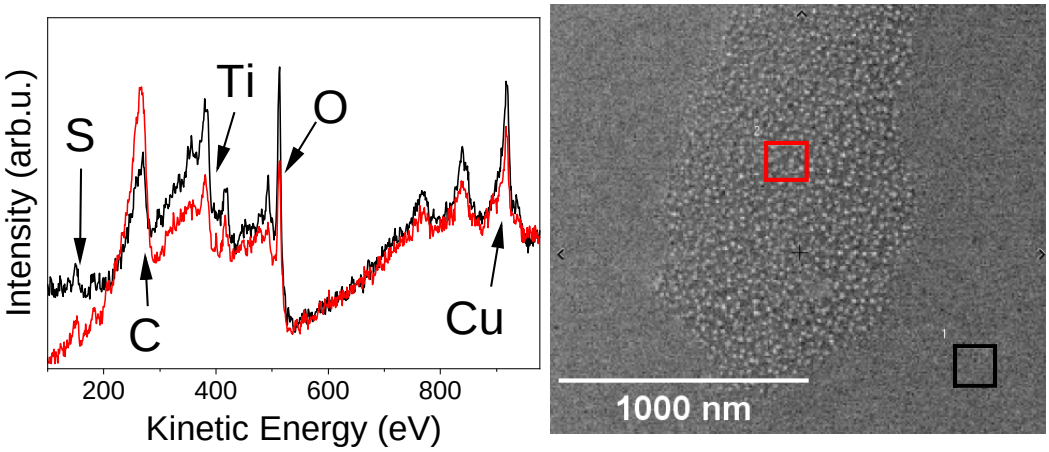


Figure S49: *SAM measurement of sample C. Left: Spectra at two different positions. Right: SEM image with the measurement positions.*

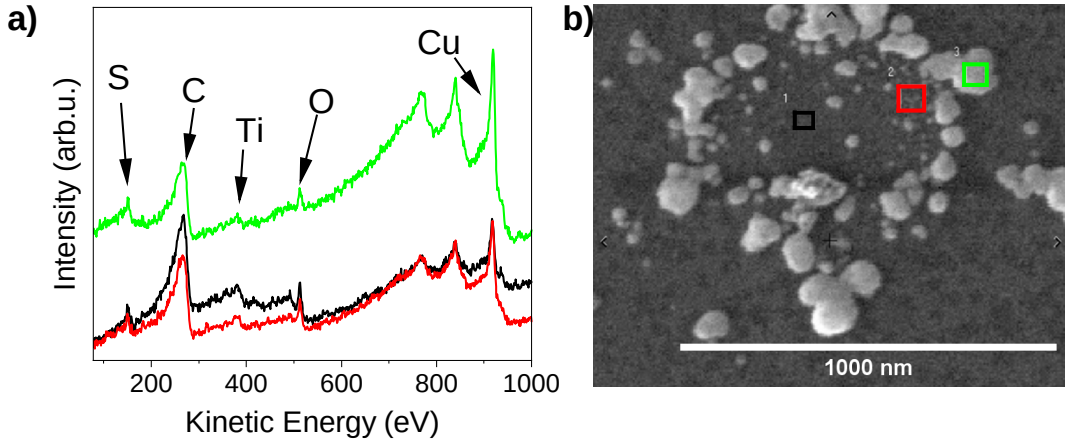


Figure S50: *SAM measurement of sample D. a) Spectra at different positions. b) SEM image with the measurement positions.*

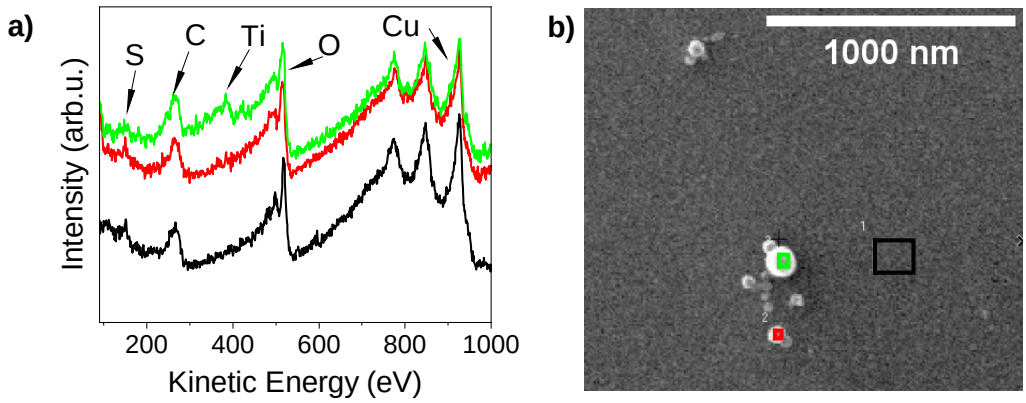


Figure S51: *SAM measurement of sample E. a) Spectra at different positions. b) SEM image with the measurement positions.*

Bibliography

[3] Miguel Blanco Garcia et al. "Uraveling the Role of Multifunctional Groups in the Adsorption of L-Cysteine on Rutile TiO_2(110)". In: *Journal of the American Chemical Society* 147.44 (2025), pp. 40158-40170. DOI: 10.1021/jacs.5c07119